

THESE DE DOCTORAT DE

L'ÉCOLE NATIONALE D'INGÉNIEURS DE BREST

ÉCOLE DOCTORALE N° 601
*Mathématiques et Sciences et Technologies
de l'Information et de la Communication*
Spécialité : Télécommunications

Par
Igor A. GLUKHOV

Manipulation of electromagnetic waves in the visible, IR and microwave domains using plasmonic heterostructures and beam properties

Thèse présentée et soutenue à Brest le 5 décembre 2022
Unité de recherche : Lab-STICC, UMR CNRS 6285
Thèse N° :

Rapporteurs avant soutenance :

Rapporteur :	André NICOLET	Professeur des Universités – Aix-Marseille Université, Marseille, France
Rapporteur :	Anatole LUPU	DR CNRS – Université Paris-Saclay, Palaiseau, France

Composition du Jury :

Président :		
Rapporteur :	André NICOLET	Professeur des Universités – Aix-Marseille Université, Marseille, France
Rapporteur :	Anatole LUPU	DR CNRS – Université Paris-Saclay, Palaiseau, France
Examinatrice :	Nathalie DESTOUCHES	Professeure des Universités – U. Jean Monnet, Saint-Etienne, France
Examinatrice :	Rozenn PIRON	Maîtresse de Conférences – INSA, Rennes, France
Dir. de thèse :	Florian BENTIVEGNA	Maître de Conférences – École Nationale d'Ingénieurs de Brest, France
Dir. de thèse :	Sergey MOISEEV	Associate Professor – U. d'État d'Ulyanovsk, Fédération de Russie
Co-encadrante :	Yuliya DADOENKOVA	Dr, HDR – École Nationale d'Ingénieurs de Brest, France

This research is supported in part by the funding the Ministry of Science and Higher Education of the Russian Federation (project 075-15-2021-581), and by Conseil Régional de Bretagne, France (Project PhotoMag).



ACKNOWLEDGEMENTS

This dissertation is the result of four years of hard and persistent work that could not have been completed without the support of several people.

First of all, I would like to thank my supervisors, Florian F. L. BENTIVEGNA and Sergey G. MOISEEV, and my co-supervisor Yuliya S. DADOENKOVA. Without their support and valuable advice this thesis would not have been possible.

I am also very grateful for all the love and support of my family, in particular my parents, my brother Anton and my aunts Ludmila DANILINA and Irina DANILINA. They were always there for me.

I would like to thank my research mates and colleagues Jacqueline SIME, Dimitrios KASTRITSIS, Abdelouahid BENTAMOU, Noor HAMDASH, Adan Omar ARELLANES and Romildo DE SOUZA.

I wish to expand my special thanks to the entire École Nationale d'Ingénieurs de Brest and Ulyanovsk State University teams: the professors, the technicians, and the administration for their help and support.

Finally, if I have forgotten anyone, I apologize!

RÉSUMÉ

Mes travaux de thèse sont consacrés au développement de méthodes de contrôle des ondes électromagnétiques dans les domaines des fréquences visibles, du proche infra-rouge ou des micro-ondes, par le biais d'hétérostructures photoniques et/ou plasmoniques ou *via* la manipulation des propriétés de l'onde elle-même.

Comme indiqué en **Introduction**, la plus grande partie de ce manuscrit est consacrée à l'étude de quelques hétérostructures qui combinent propriétés photoniques et plasmoniques et à leur utilisation dans la conception de polariseurs et de filtres (neutres ou amplificateurs) sensibles à la polarisation. Ces structures exploitent les réponses d'empilements unidimensionnels multicouches (cristaux photoniques unidimensionnels) et les interférences qui y prennent place entre les ondes réfléchies et réfractées à chaque interface, ainsi que les excitations plasmoniques induites dans des réseaux bidimensionnels ou des distributions tridimensionnelles de nanoparticules métalliques. Une telle combinaison offre en particulier la possibilité d'un contrôle spectralement sélectif et dépendant de la polarisation des ondes des propriétés de réflexion et de transmission de ces structures.

Dans le chapitre I du manuscrit, les principes généraux et les méthodes de calcul utilisés pour la modélisation des propriétés des structures photoniques/plasmoniques étudiées sont décrits. La première partie du chapitre est consacrée aux généralités sur les cristaux photoniques. Dans une définition large, un cristal photonique est un matériau ou une structure multi-matériaux avec une permittivité changeant périodiquement dans une, deux ou trois directions spatiales. On parle alors de cristal photonique unidimensionnel (1D), bidimensionnel (2D) ou tridimensionnel (3D). Dans les chapitres II à IV du manuscrit, ce sont des exemples de cristaux photoniques 1D qui sont considérés. Lorsqu'une onde électromagnétique pénètre une telle structure en incidence normale ou oblique par rapport aux interfaces, chaque interface réfléchit une partie du champ. Si l'épaisseur optique de chaque couche est choisie de manière appropriée, les champs réfléchis peuvent se combiner en phase, entraînant des interférences constructives et une forte réflectivité, dans un processus également appelé réflexion de Bragg. De ce fait, le spectre de transmission de telles structures présente de larges gammes de longueur d'onde (ou de fréquence) pour lesquelles la transmissivité est quasi nulle. Ces régions sont connues sous le nom de bandes interdites photoniques, en référence aux bandes interdites électroniques dans les cristaux, de même que

le terme « cristal photonique » a été inventé pour décrire ces structures en référence aux solides cristallins. Par ailleurs, la présence d'un défaut dans la structure, c'est-à-dire d'une couche qui, du fait de son épaisseur ou de la nature du milieu qui la constitue, rompt la périodicité spatiale de la structure, conduit à l'apparition d'une bande de transmission très étroite à l'intérieur de la bande interdite, que l'on appelle un mode de défaut. Dans les chapitres II à IV, le formalisme des matrices de transfert est utilisé pour la détermination de la réponse optique de telles structures. Les principes généraux de cette méthode et son application à divers types de couches sont décrits au chapitre I.

Afin d'obtenir la dépendance à la polarisation de la réponse des structures décrites dans les chapitres II à IV, des distributions aléatoires tridimensionnelles ou des couches ordonnées bidimensionnelles de nanoparticules métalliques ont été insérées dans les cristaux photoniques. Elles donnent lieu à des résonances plasmoniques de surface. Lorsqu'une onde électro-magnétique interagit avec une nanoparticule métallique, son champ électrique déplace le nuage d'électrons libres de conduction du métal par rapport au réseau atomique. Le déséquilibre qui en résulte dans la répartition des charges à la surface de la particule (avec un excès de charges négatives d'un côté et une déplétion en charges négatives de l'autre côté) crée un champ local de restauration à l'intérieur de la particule qui est proportionnel au déplacement du nuage d'électrons par rapport au réseau atomique. Lorsque le champ électrique de l'onde électromagnétique oscille, il en va de même pour les mouvements des charges et pour le champ de restauration qui en résulte. L'oscillation conjointe des charges des particules et du champ électromagnétique constitue ce que l'on appelle un plasmon de surface localisé. Ce phénomène est un phénomène résonant, et la résonance de ces oscillations est appelée résonance plasmonique de surface localisée. L'excitation d'un plasmon de surface localisé conduit à une forte augmentation des champs électriques près de la surface des particules métalliques et à une forte augmentation de l'absorption de l'onde par ces particules. Le pic d'absorption correspondant est observé à la longueur d'onde de la résonance plasmonique, qui dépend de plusieurs paramètres. Les principaux paramètres influençant la longueur d'onde de résonance plasmonique de surface localisée sont : la dispersion spectrale de la permittivité diélectrique du métal et du milieu dans lequel les particules métalliques sont placées, ainsi que la forme de la particule. À titre d'exemple, dans le cas de particules anisotropes de forme ellipsoïdale (qui sont précisément le type de particules envisagées dans ce manuscrit), la position de la résonance spectrale diffère de la valeur obtenue pour une particule isotrope de forme sphérique et dépend du rapport entre les longueurs des axes

principaux de la particule. Par rapport à la longueur d'onde de résonance plasmonique des particules sphériques, la longueur d'onde de résonance plasmonique des particules ellipsoïdales présente un décalage vers le rouge pour une polarisation de l'onde électromagnétique excitatrice parallèle au grand axe de l'ellipsoïde et un décalage vers le bleu pour une polarisation parallèle à son petit axe, d'où une dépendance de la réponse plasmonique vis-à-vis de la polarisation de l'onde. La description des propriétés optiques de métacouches incluant des nanoparticules métalliques a été faite dans le cadre d'une approximation de milieu effectif et du formalisme des dipôles couplés. Dans le chapitre I, plusieurs approches usuelles de l'approximation de milieu effectif (modèles de Maxwell Garnett et de Bruggeman) sont brièvement décrites et comparées, pour une utilisation dans le cadre de l'étude décrite au chapitre II. Les principes généraux de la méthode des dipôles couplés ont également été décrits, qui seront appliqués aux études qui font l'objet des chapitres III et IV.

Le chapitre II du manuscrit est consacré à l'étude du principe de l'utilisation d'un film composite (constitué d'une matrice diélectrique dans laquelle sont distribuées aléatoirement des nanoparticules métalliques de forme asphérique) comme polariseur amplificateur. Dans la gamme spectrale de la résonance plasmonique des inclusions métalliques, un tel film composite métal-diélectrique d'épaisseur inférieure à la longueur d'onde peut présenter une sélectivité de polarisation élevée aussi bien en réflexion qu'en transmission, tout en maintenant une absorption modérée. Dès lors, les résonances plasmoniques de telles couches nanocomposites peuvent être exploitées pour supprimer les modes de résonance (modes de défaut) des cristaux photoniques dans lesquels elles sont insérées, ce qui rend les spectres de réflexion ou de transmission de telles structures fortement sensibles à la polarisation. De même, on peut s'attendre à pouvoir obtenir une amplification des bords de la bande interdite photonique, si les structures sont actives, qui soit elle aussi sélective en polarisation.

Spécifiquement, la section II.2 de ce chapitre présente la géométrie et les paramètres structurels de la structure étudiée. Elle consiste en une microcavité constituée de deux réflecteurs de Bragg symétriques de structures $(AB)^N$ et $(BA)^N$ entourant une couche de défaut nanocomposite, le tout étant entouré d'air. Chaque cristal photonique (réflecteur de Bragg) consiste en un nombre N de répétitions du motif de base (AB) formé de deux couches juxtaposées de matériaux A et B (respectivement l'arséniure de gallium-indium GaInAs et l'arséniure de gallium GaAs) d'épaisseurs respectives d_A et d_B . Ces milieux semi-conducteurs sont non-magnétiques et optiquement isotropes. La dispersion chromatique des permittivités

diélectriques relatives de tous les milieux est prise en compte dans les calculs. Dans ce chapitre, la lumière est supposée se propager sous incidence normale par rapport aux interfaces séparant les couches de la structure. La couche nanocomposite qui forme une couche défaut placée entre les deux réflecteurs de Bragg est, elle, constituée d'une matrice de matériau semi-conducteur hébergeant des nanoparticules métalliques uniformément réparties dans la matrice, de forme anisotrope sphéroïdale et d'orientations identiques.

La section II.3 du chapitre détaille les résultats des calculs des propriétés spectrales de la structure dans le proche infrarouge. Dans la sous-section II.3.1, les spectres de transmission et de réflexion de la seule couche composite, ainsi que leur dépendance vis-à-vis des paramètres structuraux de cette couche, sont présentés. La sous-section II.3.2 est consacrée à la réponse spectrale de l'ensemble de la structure et offre une discussion détaillée de sa dépendance vis-à-vis des paramètres structurels de la couche défaut.

La section II.4 met en évidence les conclusions de ce chapitre, résumées ci-après.

En raison de la forme sphéroïdale des inclusions métalliques et de leur orientation uniforme, la couche nanocomposite présente une anisotropie optique prononcée. La dépendance de ses caractéristiques spectrales vis-à-vis du facteur de forme (le rapport des longueurs des grand et petit axes de chaque nanoparticule) des inclusions métalliques et de la fraction volumique qu'elles occupent dans le composite a été établie et quantifiée. La dépendance de ces réponses spectrales vis-à-vis de l'épaisseur de la couche nanocomposite a également été discutée.

En termes polarimétriques, l'étude a permis de prédire les conditions d'obtention d'une amplification d'un bord de la bande interdite photonique de la structure (ici, situé à la longueur d'onde télécom 1550 nm) qui soit sensible à l'état de polarisation de l'onde incidente, en raison de l'anisotropie d'absorption (*via* l'excitation plasmonique) due à la forme des particules métalliques. Dès lors, la structure permet de séparer, à la fréquence de résonance plasmonique, deux états de polarisation mutuellement orthogonaux, l'un étant absorbé, l'autre étant au contraire amplifié. Ce type de structure peut trouver des applications par exemple pour le contrôle de l'état de polarisation de l'émission de diodes laser à cavité verticale émettant par la surface (VCSELs).

Dans le chapitre III du manuscrit, l'amplification d'un mode de défaut contrôlée par la polarisation de l'onde incidente est obtenue *via* l'insertion, dans un cristal photonique unidimensionnel, d'un ou plusieurs réseau(x) périodiques bidimensionnels de particules métalliques.

Un des objectifs de l'étude est de déterminer l'emplacement optimal du ou des réseau(x) de particules au sein de la structure.

À nouveau, les caractéristiques spectrales et polarimétriques de l'hétérostructure sont calculées à l'aide du formalisme des matrices de transfert. Ici, un réseau bidimensionnel de nanoparticules métalliques est traité comme une interface, et le calcul des éléments de la matrice de transfert associée est réalisé dans le cadre du formalisme des dipôles couplés. L'influence de la géométrie et de l'emplacement du ou des réseau(x) de nanoparticules sur l'efficacité de l'amplification du mode de défaut et sur son contrôle par l'état de polarisation de l'onde fait l'objet d'une discussion détaillée.

Après une introduction des objectifs recherchés, la section III.2 présente la géométrie de la structure photonique et définit ses paramètres constitutifs. Comme au chapitre précédent, elle est constituée de deux réflecteurs de Bragg distribués (DBRs) entourant une microcavité composite. Chaque réflecteur consiste en une juxtaposition périodique de N bicouches (AB) ou (BA), la bicouche formant la cellule unitaire du DBR. Ici encore, A et B sont des matériaux isotropes semi-conducteurs et non magnétiques. La microcavité diffère de celle envisagée au chapitre II. Notée (CDC), elle est constituée d'une région active (amplificatrice) D prise en sandwich entre deux couches diélectriques non-magnétiques identiques C. La région active assure l'amplification des ondes électromagnétiques se propageant à travers la structure. Le milieu extérieur est l'air. Dans cette étude, une onde électromagnétique pénètre dans la structure sous incidence normale.

Les couches de matériaux A et B (d'épaisseurs respectives d_A et d_B adaptées à la vérification de la condition de Bragg qui gouverne la position spectrale des bandes interdites photoniques) qui forment les réflecteurs sont respectivement constituées de GaAs et d'arséniure d'aluminium (AlAs). Classiquement, en l'absence de la microcavité (CDC), le spectre de transmission du cristal photonique formé par la juxtaposition de ces deux réflecteurs symétriques présente une bande interdite photonique avec un pic étroit de transmissivité, ou mode de défaut, centré exactement sur la longueur d'onde de Bragg, car la couche centrale de cette structure $(AB)^N (BA)^N$, de largeur $2 d_B$, casse la périodicité de la structure et constitue donc une couche défaut. De même, la présence d'une couche défaut constituée cette fois-ci de la microcavité (CDC) introduit typiquement un ou plusieurs modes de défaut au sein de la bande interdite photonique. Cette microcavité est ici constituée de deux couches de gaine identiques en GaAs entourant une région active. Cette dernière consiste en un VCSEL à puits quantiques multiples à base de GaAs dans lequel quatre puits quantiques de structure $\text{Ga}_{0.591}\text{In}_{0.409}\text{N}_{0.028}\text{As}_{0.89}\text{Sb}_{0.08}$ sont séparés par des couches barrières de structure $\text{GaN}_{0.047}\text{As}$.

L'épaisseur et la constitution des éléments C et D qui forment la microcavité ont été précisément déterminées pour qu'elle introduise un unique mode de défaut au sein de la bande interdite photonique du cristal photonique $(AB)^N (BA)^N$, et que ce mode de défaut soit spectralement positionné à la même longueur d'onde que celui de ce cristal photonique dépourvu de microcavité. Dans nos calculs, la région active D est traitée, dans le cadre du formalisme des matrices de transfert, comme une couche équivalente de permittivité relative effective ε_D .

À la différence de l'hétérostructure décrite au chapitre II, celle étudiée ici en vue de l'obtention d'un polariseur plasmonique repose sur l'insertion d'une ou plusieurs monocouches de nanoparticules métalliques, c'est-à-dire d'un ou de plusieurs réseau(x) bidimensionnels de particules, au lieu d'un nanocomposite tridimensionnel massif placé dans la couche défaut. Dans ces réseaux, les nanoparticules sont agencées périodiquement, avec une cellule unitaire carrée. Comme au chapitre précédent, toutes les particules métalliques sont supposées avoir la même forme sphéroïdale et les mêmes dimensions, et être alignées de la même manière.

Dans la section III.3 du chapitre, l'impact du positionnement d'un unique réseau bidimensionnel de nanoparticules sur la réponse spectrale de la structure est discuté. Les calculs des caractéristiques spectrales du seul réseau de particules sont présentés et discutés dans la section III.4, et ceux relatifs aux caractéristiques spectrales de l'ensemble de la structure sont présentés dans la section III.5. La section III.6 résume et conclut ce chapitre.

L'insertion d'un ou plusieurs réseau(x) bidimensionnels de nanoparticules métalliques dans un cristal photonique présentant un mode de défaut permet le contrôle, via l'état de polarisation de l'onde électromagnétique, de l'amplification de ce mode. L'intérêt du choix de réseaux bidimensionnels, par rapport à celui d'un composite épais, est notamment que cela permet de limiter la dissipation thermique dans la structure.

En pratique, ce contrôle peut être réalisé par un choix adapté de la forme des nanoparticules (sphéroïdales, afin d'obtenir une anisotropie prononcée), de leurs dimensions (facteur de forme), et de la distance qui sépare deux particules voisines (la période spatiale du réseau). Dans l'étude présentée ici, ces paramètres ont été ajustés de manière à ce que la résonance plasmonique exploitée coïncide avec la longueur d'onde du mode de défaut du cristal photonique, les épaisseurs d_A et d_B étant choisies pour que ce dernier soit centré sur la longueur d'onde de 1550 nm.

Les calculs présentés dans ce chapitre mettent en lumière l'importance de la position du ou des réseau(x) de nanoparticules dans la structure multicouches pour l'obtention de la suppression du mode de défaut. L'efficacité de cette dernière est accrue lorsque le ou les réseau(x) sont positionnés à des emplacements de localisation maximale du champ optique dans la région active de la structure. Si la polarisation de l'onde incidente excite une résonance plasmonique située loin du mode de défaut (dans la bande interdite photonique, voire en dehors), ce dernier est au contraire amplifié.

L'approche décrite dans ce chapitre, en combinaison avec d'autres solutions récemment proposées (basées par exemple sur l'utilisation de cristaux liquides ou de matériaux fonctionnels dont les propriétés peuvent être contrôlées magnétiquement ou électriquement), peut considérablement élargir les possibilités de contrôle de la polarisation de la lumière émise par des lasers à semiconducteurs.

Dans le chapitre IV, le principe général du contrôle, *via* la polarisation de la lumière, de la transmission de cette lumière par une structure alliant propriétés photoniques et plasmoniques, est encore élargi. Ce qui est visé ici est le principe de réalisation d'un filtre dichroïque polarisant basé sur l'emploi d'un seul réseau bidimensionnel de nanoparticules sphéroïdales métalliques inséré dans une couche défaut d'un cristal photonique complexe. Le principe de fonctionnement d'un tel filtre est le suivant. La structure du système photonique multicouche formé de deux réflecteurs, ainsi que la forme anisotrope des nanoparticules, sont choisies de sorte que deux modes de défaut (centrés sur les deux longueurs d'onde de fonctionnement du filtre dichroïque visé) situés dans deux bandes interdites distinctes coïncident avec deux résonances plasmoniques excitées lorsque l'onde incidente est polarisée selon l'un ou l'autre des axes principaux des particules sphéroïdales. Si par ailleurs l'intervalle spectral entre ces deux modes (et donc entre les deux résonances plasmoniques) est suffisamment grand, on peut obtenir séparément la suppression presque totale de l'un ou de l'autre de ces modes de défaut, et donc réaliser un filtre dichroïque contrôlé par l'état de polarisation de l'onde incidente.

La section IV.2 du chapitre présente le type de réflecteurs choisi — des cristaux photoniques aperiodiques mais néanmoins construits selon une règle déterministe précise. L'avantage de tels réflecteurs est qu'ils permettent d'ajuster le nombre, l'emplacement et la largeur des bandes interdites et des modes de défaut, ainsi que de faire coïncider deux de ces modes de défauts avec deux modes de résonance plasmonique induits dans le réseau de

particules métalliques pour deux états de polarisation mutuellement orthogonaux.

Dans la section IV.3, la géométrie et les paramètres structuraux de l'hétérostructure étudiée sont présentés. Il s'agit d'une cavité photonique résonnante composée de deux réflecteurs aperiodiques diélectriques multicouches symétriques l'un de l'autre et séparés par une couche diélectrique défaut D. Un réseau bidimensionnel de nanoparticules métalliques sphéroïdales est situé au centre de la couche D, et donc au centre de la structure tout entière. Contrairement aux chapitres précédents, les couches des réflecteurs sont ici faites de matériaux diélectriques non magnétiques, isotropes et uniformes, l'oxyde de zirconium ZrO_2 et l'oxyde de silicium SiO_2 . La couche défaut est en SiO_2 .

Ici encore, le réseau de nanoparticules est un réseau périodique carré, et toutes les particules sont identiques, d'une forme sphéroïdale qui leur confère une forte anisotropie. Les dimensions typiques des nanoparticules et la période du réseau sont beaucoup plus petites que la longueur d'onde typique de l'onde optique dans la couche D.

La section IV.4 présente et discute les spectres de transmission et de réflexion de l'hétérostructure, tandis que la section IV.5 conclut le chapitre en résumant les caractéristiques et les avantages de cette structure.

Comme pour la structure étudiée au chapitre III, le choix d'un réseau bidimensionnel de nanoparticules, plutôt que d'une dispersion tridimensionnelle de ces mêmes nanoparticules se prête à un processus de fabrication moins complexe et permet aussi une dissipation d'énergie beaucoup moins importante. L'utilisation d'un cristal photonique aperiodique déterministe permet d'adapter la position spectrale des bandes interdites et des modes de défaut de cette structure de telle manière que deux de ces modes de défaut (ici, aux longueurs d'onde de 375 nm et 609 nm), situés dans des bandes interdites séparées, peuvent être ajustés et fournir les deux fenêtres étroites de transmissivité requises pour un filtre dichroïque. La suppression non simultanée de ces fenêtres, en fonction de l'état de polarisation de l'onde incidente, est obtenue grâce à l'inclusion, au centre de la structure photonique, d'une couche composite intégrant un réseau de particules métalliques anisotropes dans lequel deux résonances plasmoniques spectralement distinctes peuvent être excitées pour deux états de polarisation linéaires mutuellement orthogonaux de l'onde incidente. Pour des valeurs bien choisies des paramètres structuraux du cristal photonique ainsi que du réseau de nanoparticules métalliques, chacune des deux résonances plasmoniques de ce dernier peut être amenée à englober un des deux modes de défaut du premier, ce qui assure une extinction totale de l'un ou l'autre de ces modes selon l'état de polarisation du faisceau lumineux incident.

Parmi les différents paramètres régissant la position précise des fenêtres de transmissivité de ce filtre dichroïque, la forte influence de l'épaisseur de la couche composite défaut dans laquelle est inséré le réseau de nanoparticules métalliques a été établie. D'autres paramètres structuraux constituent cependant autant de degrés de liberté pour la conception d'un tel filtre, notamment la géométrie du cristal photonique, la nature de ses constituants, la période du réseau de particules métalliques, le facteur de forme des particules elles-mêmes, ou encore la nature du métal dont elles sont constituées.

D'autres moyens de contrôle des caractéristiques spectrales et de polarisation de ce filtre pourraient être envisagés, comme l'utilisation de plusieurs réseaux de nanoparticules métalliques, ou la combinaison de réseau(x) de nanoparticules avec d'autres types de milieux anisotropes (cristaux liquides à colorants dichroïques, verres dichroïques, etc.). De plus, les principes décrits dans cette étude restent valables dans d'autres régions spectrales, à condition que les fréquences de résonance plasmon puissent coïncider avec les modes de défaut dans une structure photonique multicouche, par exemple pour les systèmes de communications optiques dans le domaine du proche infrarouge. D'autres applications potentielles de tels filtres dichroïques sensibles à la polarisation incluent par exemple le développement de détecteurs à photon unique sensibles à la polarisation, ou d'absorbeurs plasmoniques et de nano-capteurs.

Le chapitre V de mon manuscrit, enfin, traite d'une méthode de contrôle d'une onde électromagnétique, non pas par le biais d'une hétérostructure photonique et/ou plasmonique comme dans les chapitres précédents, mais *via* la manipulation des propriétés de l'onde elle-même.

Plus précisément, il s'agit ici de contrôler la réflexion *non-spéculaire* d'un faisceau gaussien sur une surface diélectrique. Les effets non spéculaires se produisant lors de la réflexion de paquets d'ondes lumineuses sur diverses structures optiques ont été intensivement étudiés au cours des deux dernières décennies. Ces effets incluent des décalages aussi bien latéraux que transversaux des faisceaux réfléchis par rapport à la position prédite par l'optique géométrique — de tels effets ont été initialement décrits dans le contexte de la réflexion totale interne sur une interface unique et sont dans ce cas respectivement appelés effet Goos-Hänchen et effet Imbert-Fedorov, mais ces deux appellations ont depuis été souvent étendues à des situations de réflexion partielle, y compris sur des structures plus complexes que de simples surfaces. À ces décalages latéraux s'ajoutent en général des décalages angulaires, là

aussi par rapport aux prédictions de l'optique géométrique, observés dans le plan d'incidence ou perpendiculairement à ce dernier.

Dans ce chapitre, je présente une étude analytique du décalage spatial à la surface d'un milieu diélectrique, couplée à une étude numérique (par le biais du solveur Comsol Multiphysics) de la propagation après réflexion, d'un faisceau gaussien peu divergent dont la phase est modulée spatialement dans un plan transverse à la direction de propagation incidente. Plus précisément, il s'agit de comprendre comment l'ajustement de cette modulation de phase peut permettre de contrôler, d'exalter ou de réduire les décalages spatial et angulaire que ce faisceau subit lors de sa réflexion à la surface d'une couche diélectrique isotrope. La distorsion du faisceau est également prise en compte. L'étude est menée dans le domaine spectral des micro-ondes, pour lequel les décalages prennent des valeurs notables qui facilitent leur mesure et leurs applications potentielles.

Après une présentation du contexte et des objectifs de cette étude en section V.1, je décris dans la section V.2 la géométrie du problème et j'introduis un modèle analytique qui permet de déterminer le décalage spatial du faisceau à la surface de la couche diélectrique en quartz fondu.

Je considère dans mes calculs un faisceau gaussien bidimensionnel monochromatique (de longueur d'onde dans le vide de 2.912 mm) qui parvient sur cette surface en incidence oblique. Le choix d'un modèle de faisceau bidimensionnel — dans lequel le profil transversal du champ électrique de l'onde ne dépend pas de la coordonnée repérant la direction perpendiculaire au plan d'incidence — se justifie par le fait que cette étude est concentrée sur les effets non spéculaires que l'on peut observer dans ce plan. Le paramètre réel qui gouverne et quantifie le degré de modulation de phase du faisceau gaussien est ici noté ξ . Cette modulation spatiale de la phase peut être vue comme un analogue du chirp d'un faisceau dans le domaine fréquentiel.

Dans la section V.3 du chapitre, je montre comment la détermination analytique de la répartition spatiale du champ électrique de l'onde à la surface du film diélectrique peut être utilisée pour le calcul du décalage latéral du faisceau gaussien, aussi bien en fonction de l'angle d'incidence que du paramètre de modulation de phase ξ du faisceau gaussien.

La section V.4 s'intéresse à la problématique pratique de l'obtention de la modulation de phase souhaitée pour le faisceau gaussien incident. Deux méthodes purement optiques (c'est-à-dire ne faisant pas appel à un modulateur électro-optique, par exemple), et plus précisément

réfractives, sont proposées. La première consiste à focaliser sur le film diélectrique un faisceau gaussien classique (c'est-à-dire ne présentant pas de modulation spatiale de phase) à l'aide d'une lentille asphérique dont la forme est adaptée pour produire la modulation de phase requise. En l'occurrence, pour une modulation spatiale de dépendance parabolique, la lentille doit elle-même avoir un profil de surface parabolique. La deuxième méthode proposée consiste à faire se réfracter un faisceau gaussien à travers une lamelle diélectrique à faces planes et parallèle dont l'indice de réfraction présente un gradient parabolique dans la direction perpendiculaire à la direction de propagation du faisceau. J'ai déterminé, en fonction du paramètre de modulation de phase ξ souhaité, les paramètres géométriques qui définissent entièrement, selon la méthode choisie, le profil spatial de la surface de la lentille parabolique ou le profil du gradient d'indice de réfraction de la lamelle.

Dans la section V.5, je montre les résultats des simulations numériques (effectuées à l'aide de Comsol Multiphysics) de la propagation du faisceau gaussien avant et après réflexion sur le film diélectrique, et je discute de l'influence de la modulation spatiale de la phase de ce faisceau sur les décalages latéral et angulaire subis par le faisceau réfléchi que ces simulations permettent de quantifier. La distorsion du faisceau qui accompagne ces décalages est également présentée et commentée.

La section V.6 du chapitre, enfin, rassemble les conclusions de cette étude. Elle a tout particulièrement permis de montrer, par une approche théorique étayée par un modèle de simulation numérique, qu'une modulation spatiale de la phase d'un faisceau gaussien est un moyen intéressant de contrôler l'amplitude et la direction du décalage latéral et angulaire de type Goos-Hänchen (c'est-à-dire dans le plan d'incidence) que subit ce faisceau lorsqu'il se réfléchit sur une simple surface diélectrique. Les calculs menés ont montré que l'on peut envisager un décalage spatial latéral du faisceau réfléchi de l'ordre d'une longueur d'onde du faisceau gaussien si ce dernier n'est pas modulé en phase, et que ce décalage peut être multiplié d'un facteur pouvant atteindre 2,5 si on introduit une modulation spatiale de la phase dans le faisceau incident. Pour le faisceau peu divergent retenu pour nos calculs, et pour une longueur d'onde de 2,912 mm dans le domaine des micro-ondes, cela se traduit par exemple par un accroissement du décalage spatial de 2,9 mm à 7,3 mm, valeurs importantes de nature à grandement faciliter leur mesure dans le cadre d'applications pratiques.

Comme indiqué précédemment, ce décalage spatial s'accompagne d'un décalage angulaire (toujours par rapport à la direction de réflexion spéculaire, et toujours dans le plan d'incidence). Les calculs présentés dans le manuscrit montrent que le décalage angulaire peut

être multiplié par plus de quatre par la modulation de phase du faisceau gaussien et peut atteindre jusqu'à 9° , ce qui, là encore, facilite la mesure d'un tel décalage.

Les simulations numériques réalisées ont permis de déterminer la plage optimale de valeurs du paramètre ξ régissant la modulation de la phase, c'est-à-dire les valeurs de ce paramètre qui permettent d'obtenir un décalage latéral sensiblement plus important que celui qu'on peut atteindre avec un faisceau gaussien non modulé, tout en satisfaisant deux conditions importantes : que le taux de réflexion en intensité soit élevé (c'est-à-dire que la réflexion non-spéculaire se produise dans des conditions qui facilitent la détection du décalage), et, qui plus est, que la distorsion du faisceau réfléchi qui accompagne ces effets non-spéculaires ne constitue pas un obstacle à sa détection.

L'exaltation et le contrôle de ces décalages de faisceaux peuvent être utilisés, comme l'illustrent de nombreux travaux publiés ces dernières décennies, pour par exemple optimiser l'efficacité et la sensibilité de capteurs, ou encore pour concevoir des routeurs ou des dé/multiplexeurs pour les communications. La modulation de la phase du faisceau proposée dans ce manuscrit apporte un degré de liberté supplémentaire pour cette exaltation et ce contrôle. Il est par ailleurs à noter que le principe et les modèles présentés restent valables pour d'autres domaines spectraux, par exemple dans le visible ou dans le proche infrarouge.

Enfin, dans la dernière section du manuscrit, **Conclusions et perspectives**, je reprends les principaux résultats obtenus et discute des perspectives de mon travail.

TABLE OF CONTENTS

Acknowledgements	5
Résumé	7
List of acronyms	21
List of symbols	23
Introduction	25
I. Context, state of the art and methods	29
I.1. Photonic crystals	31
I.1.1 One-dimensional photonic crystals	32
I.1.2 Two-dimensional and three-dimensional photonic crystals	34
I.1.3 Photonic crystals with defects	36
I.2. Plasmonic nanostructures	39
I.2.1 Surface plasmons.....	39
I.2.2 Localized surface plasmon resonance	41
I.3. Combination of photonic crystals and plasmonic nanostructures	44
I.4. Methods.....	45
I.4.1 Transfer matrix method	45
I.4.1.A <i>General principle</i>	45
I.4.1.B <i>Simple case of homogeneous layers</i>	48
I.4.1.C <i>Simple case of interfaces between homogeneous layers</i>	49
I.4.1.D <i>Composite layers</i>	51
I.4.1.E <i>Interfaces made of monolayers of particles</i>	51
I.4.2. Effective medium approximations	51
I.4.2.A. <i>Maxwell Garnett model</i>	52
I.4.2.B <i>Bruggeman model</i>	57
I.4.2.C <i>Domains of validity</i>	58
I.4.3 Coupled dipole method.....	60
I.5. List of references	65
II. Optical amplification in a photonic crystal with an embedded nanocomposite polarizer	69
II.1. Introduction.....	71
II.2. Geometry and materials of the structure	71
II.3. Results and discussion	75
II.3.1 Dependence of the permittivity spectra of the nanocomposite layer on its structural parameters.....	75
II.3.2 Transmission spectra of the amplifying photonic crystal with a nanocomposite defect layer.....	79

II.4. Conclusions.....	87
II.5. List of references.....	88
III. Polarization-selective defect mode amplification in a photonic crystal with intracavity 2D arrays of metallic nanoparticles.....	91
III.1. Introduction	93
III.2. Geometry of the structure	94
III.3. Transfer matrix calculations	97
III.4. Transmission of a 2D array of nanoparticles.....	100
III.5. Transmission spectra of the photonic structure and suppression of the defect mode	104
III.6. Conclusions	110
III.7. List of references	111
IV. Deterministic aperiodic photonic crystal with a 2D array of metallic nanoparticles as a polarization-sensitive dichroic filter	115
IV.1. Introduction	117
IV.2. Aperiodic photonic reflectors	118
IV.3. Geometry of the composite photonic structure	124
IV.4. Results and discussion.....	128
IV.5. Conclusions	134
IV.6. List of references	136
V. Non-specular reflection of a narrow spatially phase-modulated microwave Gaussian beam.....	139
V.1. Introduction	141
V.2. Analytical description.....	143
V.3. Analytical study of the effect of phase modulation on the reflected beam at the surface of the plate	148
V.4. Obtention of a spatially phase-modulated Gaussian beam	152
V.5. Numerical simulation of the propagation of the reflected phase-modulated Gaussian beam	155
V.6. Conclusions	162
V.7. List of references	163
Conclusions and perspectives	167
List of figures.....	171
List of tables	177
List of publications.....	179

LIST OF ACRONYMS

1. PC – photonic crystal
2. NP – nanoparticle
3. DBR – distributed Bragg reflector
4. VCSEL – vertical-cavity surface-emitting laser
5. SEM – scanning electron microscope
6. 1D – one-dimensional
7. 2D – two-dimensional
8. 3D – three-dimensional
9. SP – surface plasmon
10. LSP – localized surface plasmon
11. SPP – surface plasmon polariton
12. LSPR – localized surface plasmon resonance
13. UV – ultraviolet
14. IR – infrared

LIST OF SYMBOLS

International System of Units (SI system) is used in the manuscript.

1. \mathbf{k} – wavevector
2. \mathbf{k}_0 – wavevector in vacuum
3. n – refractive index
4. \mathbf{E} – electric field vector
5. ε – relative permittivity
6. $\hat{\varepsilon}_{eff}$ – effective permittivity tensor
7. \hat{g} – depolarization tensor
8. η – volume fraction of the particles in matrix
9. p – interparticle distance
10. $\hat{\alpha}$ – polarizability tensor of a single particle
11. $\hat{\alpha}_{eff}$ – polarizability tensor of a 2D particle array
12. ω – angular frequency
13. c – speed of light in vacuum
14. λ – wavelength
15. λ_0 – wavelength in a vacuum
16. λ_{Br} – Bragg vacuum wavelength
17. r – reflection coefficient in amplitude
18. R – reflectivity
19. t – transmission coefficient in amplitude
20. T – transmittivity

INTRODUCTION

Optics is a general field of physics covering a wide range of topics related to the study of light. Photonics is the part of the discipline of optics concerned with the generation, detection, and control of light in the form of waves, as well as photons associated to these waves in the frame of the wave-particle dual nature of light. Its formation as a separate scientific and technical field, and then as a separate branch of high-tech industry, began in full in the 1960s and was intimately related to the development of laser technology. Depending on the source, the term “*photonics*” itself seems to have been first coined, among others, by the Soviet physicist A. N. Terenin in the preface to his book "Photonics of Dye Molecules and Related Organic Compounds" [Leningrad: Nauka, 1967. 616 p. (in Russian)] in 1967, or by the French scientist Pierre Aigrain in the same year. In the decades that followed, the term became widespread due to the rapid development of laser technology and fiber optic communications in the 1980s.

Photonics is in constant development: new directions, technologies and materials are constantly emerging, promising areas of application are opening up, and the methods and technologies created in this area are founding the widest practical domains of application. Due to their compactness, relative cheapness, and reliability, photonic devices are widely used in modern life. So, for example, the use of light-emitting diodes (LEDs) in lighting technology reduces energy consumption and heat generation compared to traditional lighting sources. Photonics is widely used in the production of modern electronics. Without it, the production of modern processor chips is impossible, and in the last decade there has been an active development of optical components for future computer technology. Various inter-chip optical interconnectors, optical controllers and filters are being created.

Among photonic structures and devices, those exploiting plasmonic effects are currently attracting a lot of interest, in particular because of the localization of the electromagnetic field in such structures, and hence the possibility of miniaturizing photonic devices even further. Plasmonics is one of the modern areas of photonics that studies the conditions of electromagnetic field localization near the interface between an insulator and a conductor at a sub-wavelength scale.

The largest part of this manuscript is devoted to the study of a few selected heterostructures which combine photonic and plasmonic principles and their use in the design

of polarizers and polarization sensitive filters. These structures combine the properties of multilayered filters that exploit the interference between the waves reflected and refracted at a large number of interfaces (one-dimensional photonic crystals) with plasmonic excitations in two-dimensional arrays or three-dimensional distributions of metallic nanoparticles. Such a combination provides the possibility of a polarization sensitive control of the reflection and transmission properties of these structures at selected wavelengths.

In Chapter I, general principles and calculation methods for the modelization of the properties of the photonic/plasmonic structures under study are described. These formalisms will be put into use in Chapters II, III, and IV.

Chapter II is devoted to the study of an amplifying photonic crystal in which a nanocomposite polarizing layer based on a three-dimensional random distribution of nonspherical metallic inclusions is embedded. The system can be considered as an active microcavity hosting the nanocomposite layer surrounded by two symmetrical distributed Bragg reflectors. The dependence of the spectral characteristics of the structure on the aspect ratio, volume fraction of the metallic inclusion and thickness of the nanocomposite layer is carefully analysed. It is shown that two mutually orthogonal linear states of polarization of light related to the main axes of the nanoparticles play a particular role: resonant amplification at the edge of the photonic bandgap can be observed for one of these polarization states, whereas for the other polarization state, the transmittivity of the structure is almost totally suppressed. As a result, the structure acts as an amplifier whose output is controlled by the polarization of the incoming light.

As a development of these studies, Chapter III is devoted to a system where polarization-selective amplification of a defect mode in a photonic crystal is involved, but this time with an intracavity including two-dimensional arrays of metallic nanoparticles, which allows a closest control of the position of the nanoparticles with respect to the electromagnetic field distribution in the structure, hence of the efficiency of the plasmonic excitation. The precise influence of the positioning of the two-dimensional array on the transmission spectrum of the structure is discussed. In particular, it is shown that the polarization-sensitive suppression of the defect mode is most efficient when the nanoparticles are embedded at locations of maximal field localization.

In Chapter IV, the goal is to obtain a polarization-sensitive dichroic filter exploiting two different defect modes in two separate bandgaps of a photonic crystal that can be

independently suppressed for two mutually orthogonal polarization states of the incident beams through plasmonic excitation in a two-dimensional array of metallic nanoparticles. The precise adjustment of photonic and plasmonic modes in this case requires an additional degree of freedom that is provided by the use of a non-periodic photonic crystal. Specifically, we propose to use a so-called *deterministic aperiodic photonic crystal* which allows an independent adjustment of the spectral positions of the bandgaps. As a result, the operating principle and governing parameters of a narrow-bandpass, polarization-sensitive dichroic filter operating in the near-UV and visible domains are described.

The last chapter of the manuscript, Chapter V, differs in its scope from the previous ones. In that Chapter, what is controlled are the lateral and angular shifts experienced by a Gaussian beam when it is reflected at a dielectric surface. Such shifts constitute generalization of the well-known Goos-Hänchen effect. The control in this study is provided by the structure of the beam itself. Specifically, a spatial modulation of the phase of the incident Gaussian beam is produced, and it is shown by way of both analytical calculations and numerical simulations that such a modulation can lead to a significant and adjustable exaltation of the lateral beam shift. We show how this phase modulation can be produced and determine the optimal modulation parameter, that is, the best compromise between large values of the lateral shift and limited deformation of the beam shape that inherently occurs upon reflection. The study is carried out in the microwave range, where the lateral shift of the reflected beam reaches several millimeters, which facilitates its experimental detection. Such an enhancement and control of the reflected beam shift can be used to optimize the efficiency and sensitivity of photonic devices such as sensors, routers or de/multiplexers.

CHAPTER I

CONTEXT, STATE OF THE ART AND METHODS

I.1. Photonic crystals

Although the term "*photonic crystal*" (PC) appeared relatively recently, PCs themselves are widely to be found in nature. Examples of such natural photonic crystals include the beautiful multicolored wings of some species of butterflies (Fig. I.1), the colored scales of some tropical fish, or the feathers of a peacock.

In a broad, general definition, a photonic crystal is a material or a multi-material structure with a periodically changing permittivity in one, two or three spatial directions. Accordingly, one speaks of one-dimensional (1D), two-dimensional (2D) and three-dimensional (3D) PCs. The term "photonic crystal" was first introduced in the work of E. Yablonovich in 1987 [1], in which he described the idea of artificially creating such a structure.

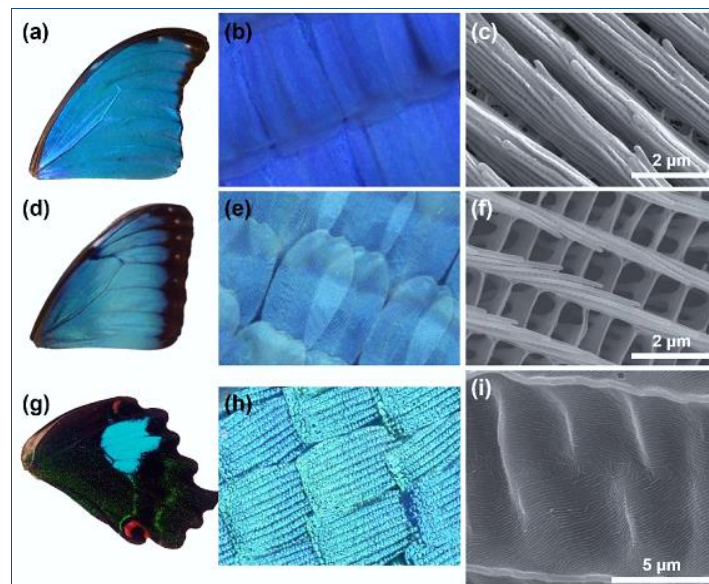


Fig. I.1. An example of a photonic crystal found in nature. Photographs of butterfly wings (left panels), optical microscope images (central panels) and scanning electron microscope images (right panels) of these wings. [2]

Photonic crystals have made a great appearance in research in optical physics for the last two to three decades [3,4]. Such periodic structures are widely used as dielectric mirrors (also known as a Bragg reflectors), which play an important role in many modern photonic systems. One-dimensional photonic crystals make it possible, among many applications, to create narrow-band light filters or amplifiers with controllable transmission and reflection bands, to obtain low-signal laser generation (so-called low-threshold and non-threshold lasers), to design media with a negative refractive index that make it possible to focus light to

a point smaller than the wavelength (“superlenses”), or to exploit the orderly nature of the phenomenon of photon confinement in a photonic crystal in order to build optical storage devices and logical devices. Variations of 2D and 3D PCs can be used, for instance, as waveguides with a complex geometry.

I.1.1 One-dimensional photonic crystals

Periodic dielectric stacks are the simplest forms of PCs, not least in terms of fabrication requirements, and have been used in photonics technology well before the introduction of the term itself. The simplest of those *one-dimensional* PCs is an alternating stack of two different dielectric materials (as presented in Fig. I.2).

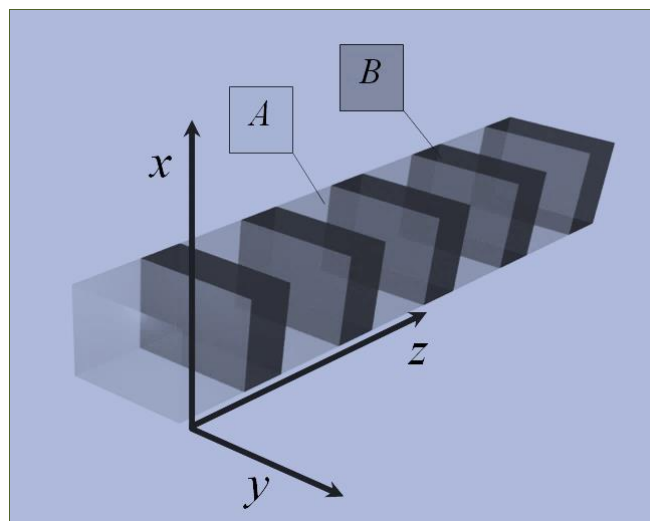


Fig. I.2. Scheme of the 1D photonic crystal.

When light impinges on such a stack in normal or oblique incidence with respect to the interfaces (those are parallel to the xy plane in Fig. I.2), each interface reflects some of the field. If the optical thickness of each layer is chosen appropriately, the reflected fields can combine in phase, resulting in constructive interference and strong reflectance, also known as Bragg reflection. Due to this, the transmittivity spectrum of such structures presents broad wavelength (or frequency) regions for which the transmittivity is almost zero. These regions are known as *stop bands* or more often *photonic bandgaps*, in reference to the electronic bandgaps in crystals after which the term photonic crystal has been coined in the first place. They are centered around a vacuum wavelength λ_0 for which the so-called Bragg condition (or quarter-wave condition) is fulfilled in all layers ($nd = \lambda_0/4$, where n is the refractive index

of a layer, and d is its thickness) [5]. An example of two such photonic bandgaps, one in the visible domain and the other in the near infrared region, is represented in Fig. I.3.

Bragg reflection occurs regardless of the refractive index (or permittivity) contrast between constituents A and B of a 1D photonic crystal such as that represented in Fig. I.2, although a larger number of periods (AB) are required to achieve a high reflectance in the bandgaps if the contrast is small. Since the absorption in dielectric optical materials used in PCs is very low, mirrors made from dielectric stacks are extremely efficient, and can be designed to reflect almost 100% of the incident light within a small range of frequencies. Also, dielectric mirrors can be constructed to operate for a predefined angle of incidence.

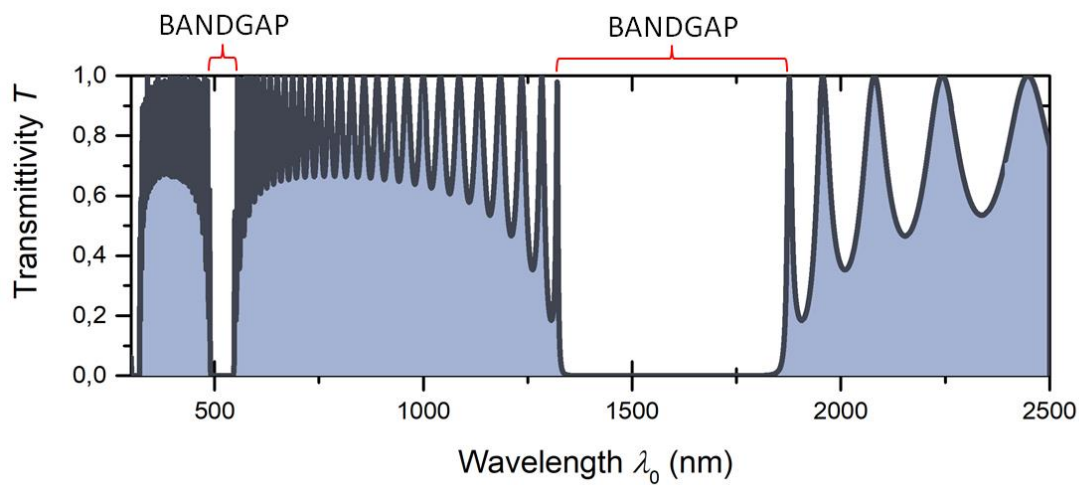


Fig. I.3. Spectrum of the 1D photonic crystal with a photonic bandgaps.

Due to the presence of the wavelength-selective reflection properties of the photonic crystals they are used in a wide range of applications, such as high-efficiency mirrors, Fabry-Perot cavities [6], optical filters [7], vertical-cavity surface-emitting lasers (VCSEL) and distributed feedback lasers [8]. An example of the PC reflectors used in a VCSEL is presented in Fig. I.4.

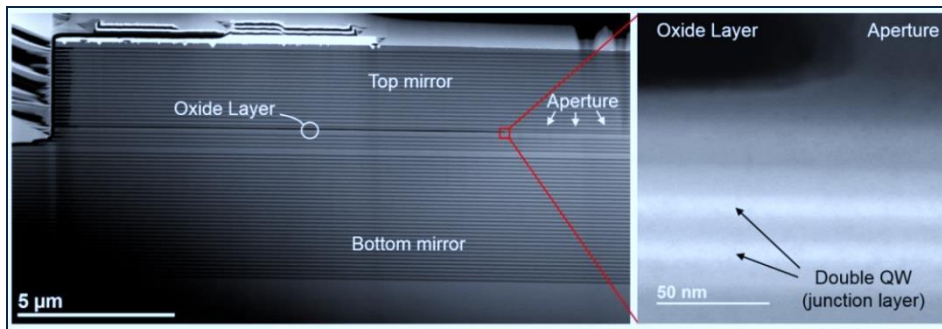


Fig. I.4. Example of a vertical-cavity surface-emitting laser (VCSEL). The top and bottom reflectors (mirrors) delimiting the active cavity of the laser are 1D photonic crystals. [8]

I.1.2 Two-dimensional and three-dimensional photonic crystals

Two-dimensional PCs can be considered as a generalization of the one-dimensional case. Instead of a set of uniform dielectric layers, 2D photonic crystal exhibit periodicity in two directions. In each of those directions, the bandgap appears if the condition of one-dimensional Bragg reflection is satisfied.

One of the most common cases in practice consists of dielectric rods periodically located in a host material, or of periodically spaced holes in a layer. An example of such arrays is presented in Fig. I.5.

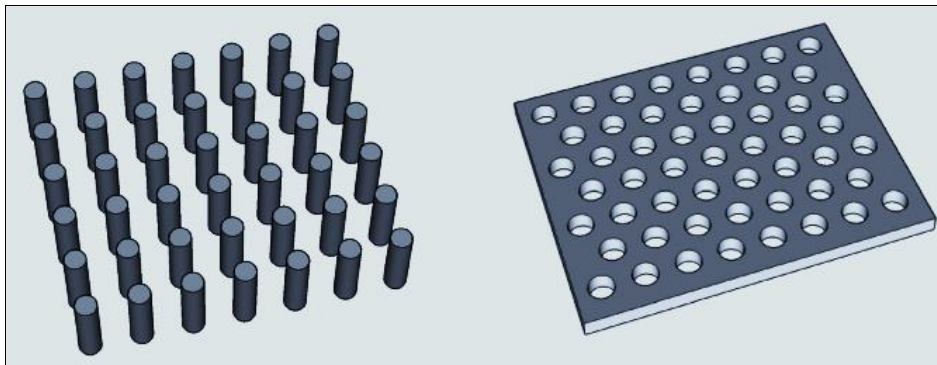


Fig. I.5. 2D photonic crystals: an array of periodically located rods (left), or periodically located holes in a host material (right). [9]

Figure I.6 shows a practical realization of such an array, with several top-view scanning electron microscope (SEM) images of periodically obtained holes in a TiO_2 matrix for increasing average hole diameters from 41 nm to 106 nm.

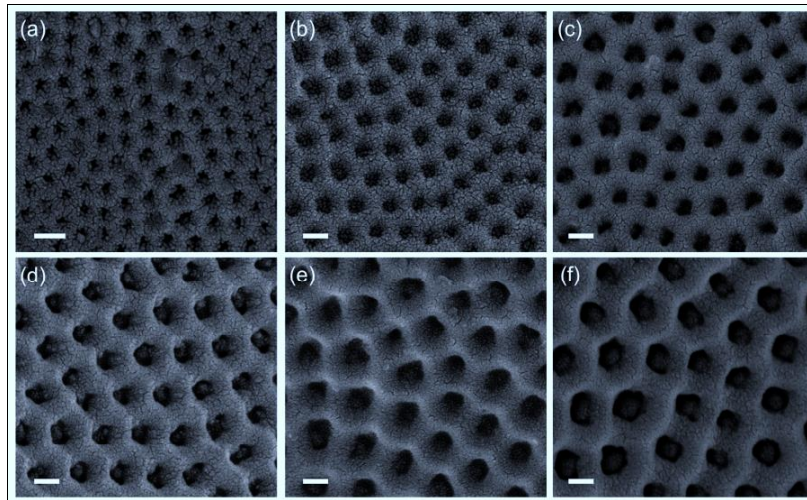


Fig. I.6. An example of a 2D photonic crystal. SEM images of arrays of holes in TiO_2 with different diameters. Scale bars indicate a length of 100 nm. [10]

Geometries of 2D photonic crystals are not limited to simple rods and holes. A variety of two-dimensional PC geometries can be practically constructed. For instance, Fig. I.7 represents cases where 2D photonic crystals are obtained by assembling multiple rings, and Fig. I.8 shows the case of a honeycomb lattice.

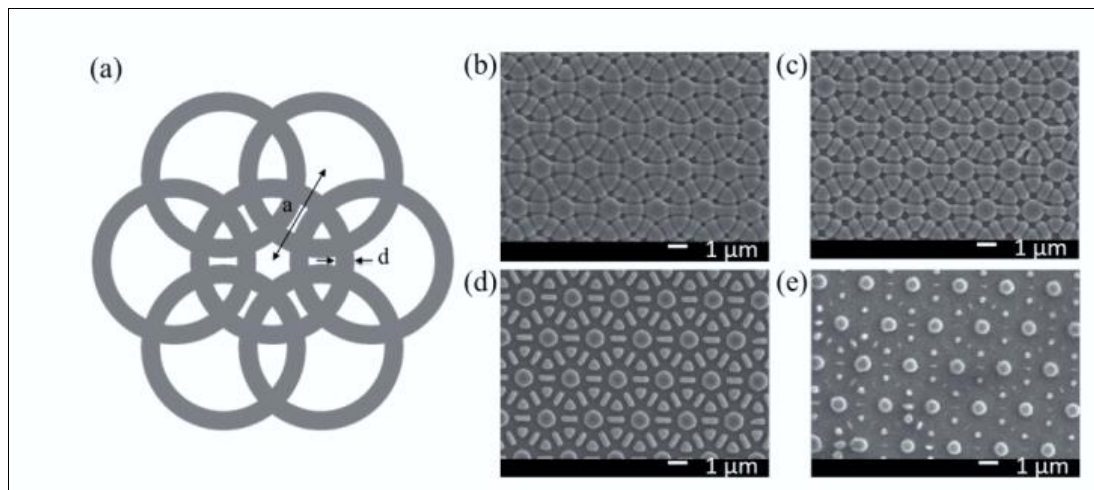
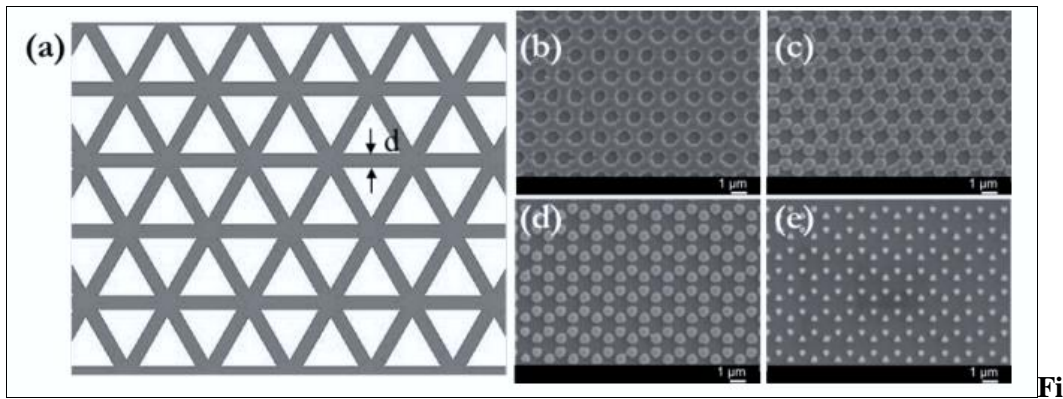


Fig. I.7. Various examples of high symmetry 2D photonic crystals obtained by assembling multiple rings. [11]



g. I.8. Example of 2D photonic crystals with a honeycomb lattice fabricated by a direct laser writing method. [11]

Three-dimensional PCs add a third dimension to the periodicity. Due to their complex geometry, they are the most challenging PC structures to fabricate. As an example, a 3D “woodpile” PC is shown in Fig. I.9.

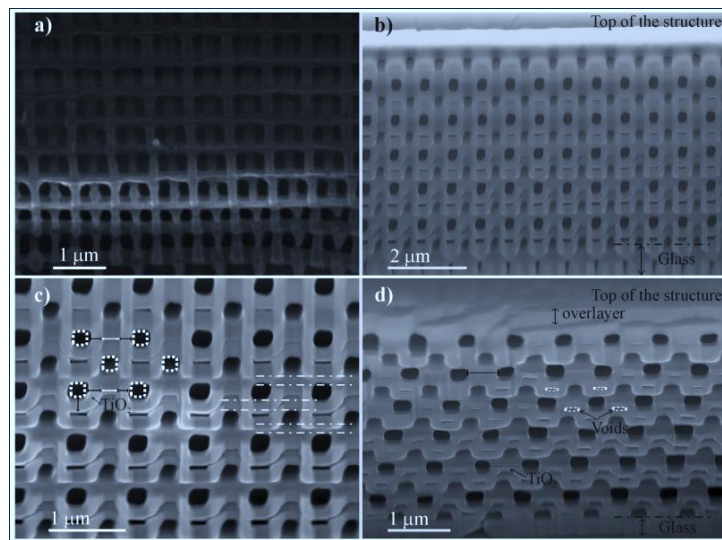


Fig. I.9. SEM images of 3D photonic crystals with a woodpile structure. [12]

I.1.3 Photonic crystals with defects

Any inhomogeneity of a photonic crystal breaking its periodicity can be considered as a defect of its structure and can radically change its properties and applications. For instance, artificially creating defects in a PC, one can form a microresonator or a waveguide with a complex geometry. An example of defects (missing holes) in a 2D photonic crystal acting as a waveguide is presented in Fig. I.10.

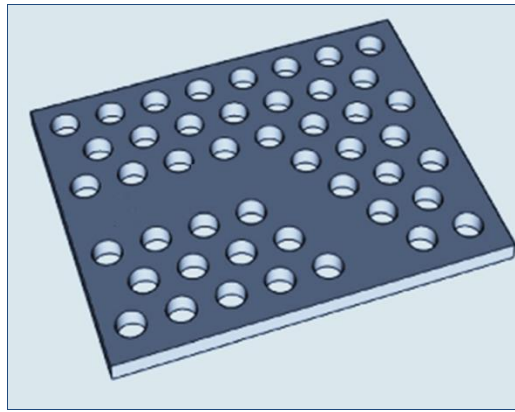


Fig. I.10. Example of a waveguide obtained with lines of missing holes in a 2D photonic crystal.

In the case of a one-dimensional photonic crystal, a defect can consist of one or more layers that break its periodicity. A typical schematic of a photonic crystal with a defect layer is presented in Fig. I.11 (in this case, the defect consists of a B layer with a thickness different from that of the other B layers).

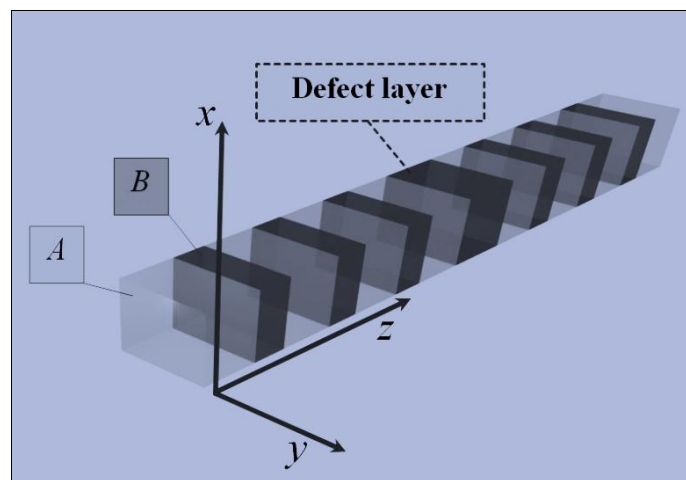


Fig. I.11. Schematic of the 1D photonic crystal with defect layer.

The presence of a defect in the structure leads to the appearance of a very narrow transmission band inside the bandgap. Such narrow transmission bands are called *defect modes*. An example of a defect mode in a photonic bandgap is presented in Fig. I.12. Its spectral position and its width strongly depend on the location, thickness, and refractive index of the defect layer in the PC.

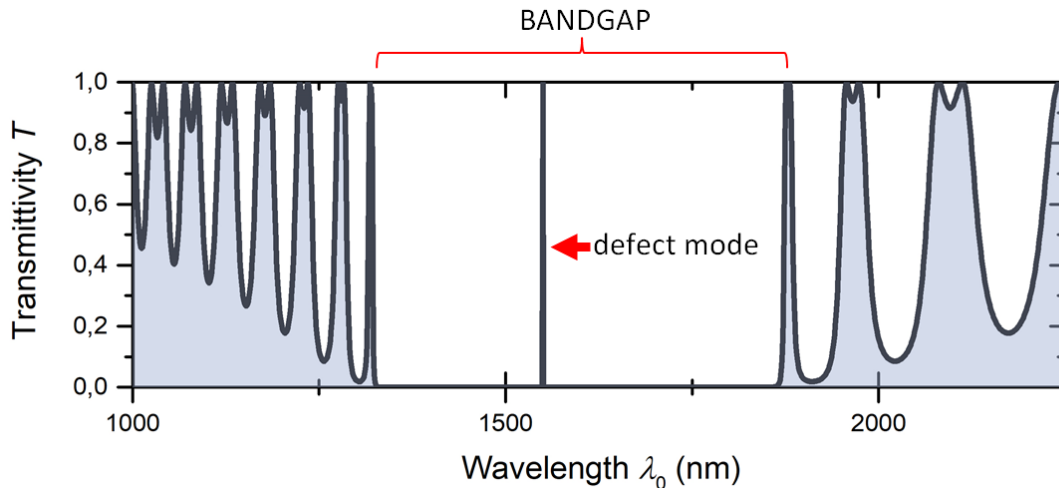


Fig. I.12. Transmittivity spectrum of a 1D photonic crystal with a defect layer. The defect mode is positioned at 1550 nm.

There are many possible ways to modify the spectrum of a photonic crystal. This can be achieved, for example, through the implantation of an additional layer in a periodic structure (implantation defect). The material of such a defect layer can coincide with or differ from the material of the layers that constitute the periodic structure. Its optical length may also differ from the optical length of the layers that constitute the structure. This type of defects can include not only single layers, but also multiple-layer combinations. Other common defects include:

- Defects obtained by inversion (mirror reflection) of a part of the structure.
- Defects obtained by transposition of two different layers in the structure.
- Defects obtained by replacement of one of the layers with another layer of different thickness or refractive index.

Regardless of the type of defect, their main goal is to bring a modification of the spectrum of the photonic structure (changing the position or width of the bandgap, or changing the position of the defect mode). In the following chapters, 1D structures with defect layers will be considered. In Chapter IV, a detailed analysis of the effect of an implanted complex defect layer thickness on the spectrum of a 1D PC will be carried out.

I.2. Plasmonic nanostructures

I.2.1 Surface plasmons

Surface plasmons (SPs) are coherent oscillations of free electrons at the boundary between a conductor and a dielectric medium. One way to excite such oscillations is through an interaction between the free electrons and an electromagnetic wave. The resulting SPs have a number of important properties.

In particular, a surface plasmon can exist only in frequency domains where the permittivities of two neighboring materials have opposite signs, which explains why they require a conductor-insulator interface.

The characteristics of a surface plasmon mainly depend on the wavelength of the electromagnetic wave that excites them and on the complex refractive indices of the media on either side of the interface. In most cases, the surface plasmon is established at the interface between a dielectric medium and a metal. The metal must have conduction band electrons capable of resonating with the incoming light at a suitable wavelength. In the visible and infrared domains, many metals satisfy such a condition. The most commonly used metals in practice are silver and gold due to their well-suited catalytic, chemical, structural, optical and electronic properties.

The most important property of surface plasmons is their strong localization near the interface, as the field amplitudes fall off exponentially with the distance from that interface.

Surface plasmons are often divided into two categories: *propagating surface plasmons* and *localized surface plasmons* (LSPs). A *propagating* surface plasmon can be represented as a bound electromagnetic wave propagating at a conductor-insulator interface and is often called surface plasmon polariton (SPP) (Fig. I.13). Historically, such surface electromagnetic waves at conductor/dielectric interfaces were studied as early as the beginning of the twentieth century (Zenneck, 1907; Sommerfeld, 1909) in relation to the problems of wireless telegraphy and therefore they are sometimes called Zenneck waves.

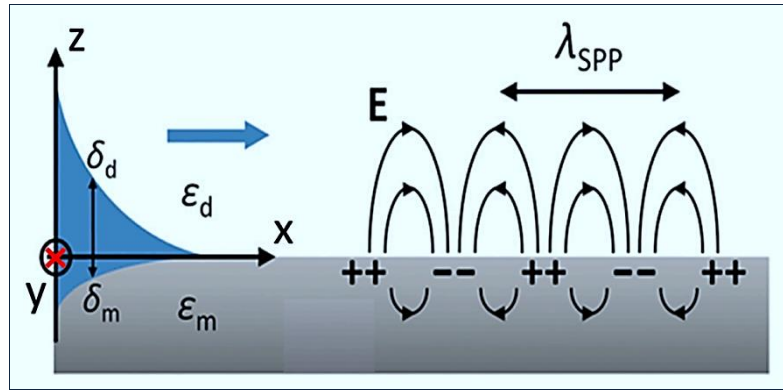


Fig. I.13. Schematic illustration of a propagating surface plasmon polariton. [13]

For a given wavelength, the wave vector of a propagating surface plasmon polariton is greater than the wave vector of a photon in free space, and therefore the excitation of a propagating surface plasmon by travelling electromagnetic waves is impossible. In practice, it can for example be obtained with a prism, or a grating, or an artificial defect (groove, ridge, etc.) on the metal surface.

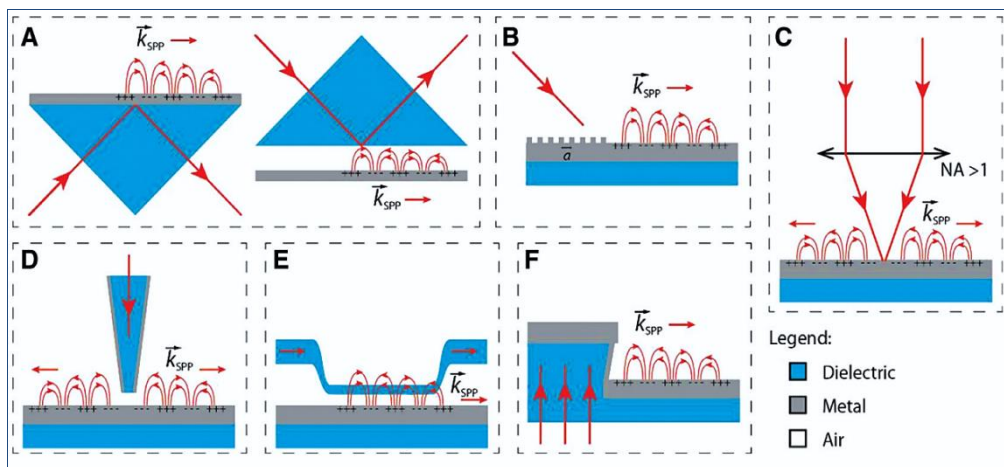


Fig. I.14. Illustration of various optical schemes for the excitation of SPPs. (A) Prism coupling schemes in the Kretschmann configuration on the left and in the Otto configuration on the right. (B) Grating coupling scheme. (C) Highly focused beam coupling scheme. (D) Near-field coupling scheme. (E) End-fire coupling scheme. (F) Step-gap leakage coupling scheme. [14]

SPPs have been used in numerous applications, including sensing, imaging, subwavelength aperture transmission, or nanoscale optical trapping.

I.2.2 Localized surface plasmon resonance

Although the term *localized surface plasmon* was introduced only in the 20th century, this unique effect of metallic nanostructures had already been used long before that. Thus, gold nanosized inclusions in glass have for a long time been widely used to give it bright colors. Church stained-glass windows can serve as examples of such an effect. Another famous example is the Lycurgus cup, which dates back to the Byzantine Empire and can be seen in the British Museum in London. The most remarkable aspect of the Cup is the dependence of its color on the direction of the light: it appears red when lit from behind and green when lit from the front. This can be explained by the presence of gold inclusions in the material of the Cup and the wavelength-dependent excitation of *localized* surface plasmons in the inclusions.



Fig. I.15. The Lycurgus cup, a Roman artefact held in the British Museum under transmitted light (left) and reflected light (right) [15]

In comparison with *propagating* surface plasmons, which were described in the previous section, in *localized* surface plasmons, the electron cloud also oscillates collectively but the spatial extension of the SP is limited by the dimensions of the nanoparticle at the surface of which it is excited, hence the name of localized surface plasmon (Fig. I.16). The appearance of a LSP in a NP is possible when the latter has free electrons able to participate in a collective oscillation (which is why LSPs are typically excited in metallic nanoparticles, as

illustrated by the historical examples mentioned above). A LSP can be qualitatively described by a simple oscillator model. When an electromagnetic wave is incident on a metallic nanoparticle, its electric field shifts the free conduction electron gas of the metal with respect to the atom lattice (see Fig. I.16). The resulting disequilibrium in the charge distribution at the surface of the particle (with an excess of negative charges on one side and a depletion of negative charges on the opposite side) creates a restoring local field inside the particle which is proportional to the displacement of the electron gas relative to the ion background in the particle. As the electric field of the electromagnetic wave oscillates, so do the movements of the charges and the resulting restoring field. The joint oscillation of the charges in the particles and the electromagnetic field constitutes what is called a localized surface plasmon. This phenomenon is a resonant one, and the resonance of these oscillations is called a *localized surface plasmon resonance (LSPR)*.

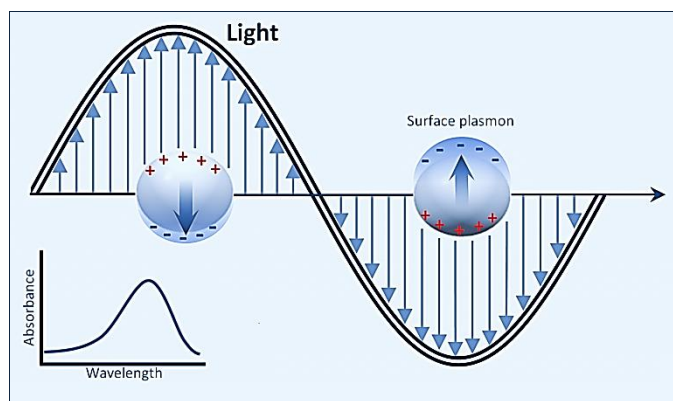


Fig. I.16. Illustration of a localized surface plasmon resonance in a nanoparticle.

The excitation of a LSP leads to a great enhancement of the electric fields near the surface of the particle and to a sharp increase of the absorption of the particle. The peak of the absorption is observed at the plasmon resonance wavelength, which depends on a number of parameters. The major parameters influencing the LSPR wavelength are:

- the dielectric function of the metal,
- the dielectric function of the surrounding medium,
- and the shape of the particle.

Figure I.17 represents the dependence of the spectral position of the LSPR wavelength on the shape and material of various nanoparticles.

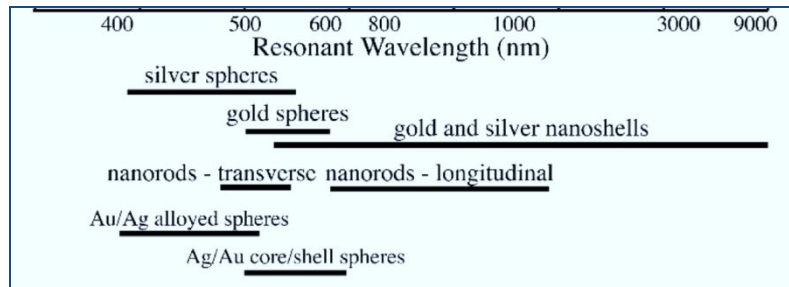


Fig. I.17. Dependence of the spectral position of the LSPR on the shape and nature of several types of nanoparticles [16].

In the case of ellipsoidal particles (which will be considered in following chapters), the position of the spectral resonance differs from the value obtained for a sphere and depends on the ratio between the lengths of the main axes of the particle. Compared to the plasmon resonance wavelength of spherical particles, the plasmon resonance wavelength of ellipsoidal particles exhibits a red shift for a polarization parallel to the longest ellipsoid axis and a blue shift for a polarization parallel to the short ellipsoid axis. An example of the influence of the LSPR on the transmission spectra for different shapes of ellipsoidal NPs is presented in Fig. I.18. This issue will be discussed in more detail in the following chapters.

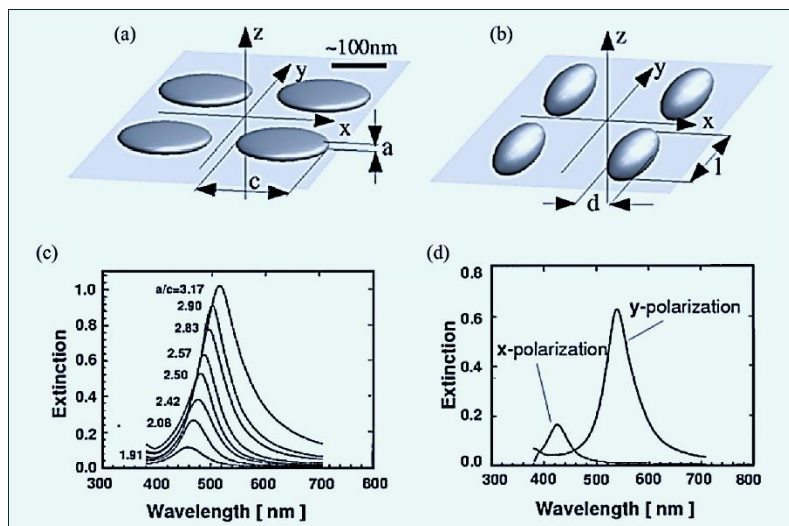


Fig. I.18. Transmission spectra of arrays of nanoparticles with different ellipsoidal shapes [16].

I.3. Combination of photonic crystals and plasmonic nanostructures

The use of localized surface plasmon resonance in arrays of nanoparticles or in nanocomposite layers embedded in photonic crystal structures is a very promising direction of research. By carefully choosing the constitutive parameters of the NPs in the array or in the nanocomposite layer, it is possible to control the optical properties of the resulting structure. The versatile optical properties of such structures can find multiple applications, for instance for the design of sensors. An example of such possibilities can be found in Ref. [17], in which a coupled photonic-plasmonic system consisting of a combination of photonic microcavities and metallic nanostructures is investigated. The authors show that it is possible to observe an exceptionally strong coupling between the resonant modes of the microcavities and the collective electron oscillations (plasmons) in the metal, and that this coupling exhibits a considerably higher sensitivity than with conventional localized plasmon sensors. In Ref. [18], an analytical and numerical study was carried out for the coupling mechanisms between a 1D photonic crystal and a 2D array of plasmonic nanodiscs embedded in a defect layer of the photonic crystal. The authors introduced a general formalism to explain and predict the emergence of the anomalies in the transmission spectra of the structure. The underlying understanding of coupling mechanisms in such hybrid systems paves the way for optimal design of sensors, light absorbers, modulators and other types of photonic devices with controllable optical properties. In Ref. [19], the dielectric properties of a nanocomposite consisting of silver NPs and a liquid crystal was investigated theoretically at different temperatures. The nanocomposite was inserted as a defect layer in a semi-finite one-dimensional PC made of alternating TiO_2 and SiO_2 layers. It was shown that the volume fraction of silver NPs and the orientations of the liquid crystal molecules significantly affect the dielectric properties of the nanocomposite. In Ref. [20] the transmission properties of one-dimensional *quasi-periodic* dielectric photonic crystals containing a plasmonic nanocomposite (Ag nanoparticles randomly immersed in a dielectric SiO_2 matrix) are theoretically investigated in the IR region. The quasi-periodicity of the photonic crystal was chosen to follow the Fibonacci sequence rule. The numerical results demonstrate the appearance of many photonic bandgaps due to the multiple periodicities of the structure. The influence of the refractive indices of the dielectric materials and the size and volume fraction of the nanoparticles on the transmission characteristics of the structure was investigated. The proposed structure could be used in many applications such as multichannel filters and optical switches.

Another promising direction of the use of such combinations is a spectral and polarization-sensitive control of the resonance modes of PC-based structures. As an example, Ref. [21] studies the transmission and reflection spectra of a structure consisting of a nanocomposite layer sandwiched between two 1D dielectric Bragg mirrors. The nanocomposite consists of metallic nanoscale inclusions of spheroidal shape, ordered with the same orientation and dispersed in a transparent matrix. It is shown that when one of the plasmon frequencies of the metallic spheroids coincides with a defect mode frequency in one of the photonic bandgaps, complete suppression of that mode in the transmission spectrum is possible for a well-chosen polarization of light. A similar structure was also considered in Ref. [22]. It is shown that the defect mode splits into two peaks with a reduced transmittivity with a strong dependence on the structural parameters and volumetric fraction of the nanospheroids.

Finally, the combination of photonics and plasmonics can be useful in order to achieve a good control of the state of polarization of the radiation generated by vertical-cavity surface-emitting lasers (VCSELs), as such a control remains a topical research subject today. As an example, in Ref. [23] authors demonstrate the polarization control of a single transverse mode VCSEL using an array of gold nanorods located on the top surface of the VCSEL.

I.4. Methods

I.4.1 Transfer matrix method

I.4.1.A General principle

Let us consider a multilayered structure which consists of N parallel plane layers made of homogeneous, nonmagnetic, isotropic materials with thickness d_j and refractive indices \tilde{n}_j ($j=1,\dots,N$), separated by $N+1$ flat interfaces (Fig. I.19.). This structure is surrounded by semi-infinite media with refractive indices \tilde{n}_0 and \tilde{n}_{N+1} . The normal to the interface planes will be the z -axis, so the interface planes are parallel to the (xy) -plane. The dimensions of the layers along the x - and y -axes are much larger than their thicknesses along the z -axis, and are thus taken to be infinite.

An incident plane electromagnetic wave impinges on the left-hand side of the structure. The time dependence of the electromagnetic fields is taken as $e^{-i\omega t}$, where $\omega = 2\pi c / \lambda_0$ is the angular frequency of the incoming plane wave of wavelength in a vacuum λ_0 and c is the velocity of light in vacuum.

The plane of incidence is the (xz) -plane, so that the wavevector of light in the structure is $\mathbf{k} = (k_x, 0, k_z)$. Due to boundary conditions that relate the field amplitudes of the incident, reflected and transmitted wave at the interfaces, k_x remains constant.

The refractive indices of the materials, which can in general be complex quantities, will be written as $\tilde{n}_j = n_j + i\kappa_j$ ($j=0, \dots, N+1$). With this choice of time dependence, negative values of the imaginary part of the complex refractive index ($\kappa_j < 0$) correspond to an amplifying medium, and positive values ($\kappa_j > 0$) to an absorbing medium.

In the following, we consider the usual s - and p -polarized components of the electromagnetic fields, where the s -component corresponds to an electric field oriented perpendicular to the plane of incidence ($E_x = E_z = 0$), and the p -component to an electric field parallel to that plane ($E_y = 0$).

In this section, the formulas are presented in the most general way, and are valid for either polarization state. Formulas specific to either s - or p -polarizations will be introduced in the next subsection.

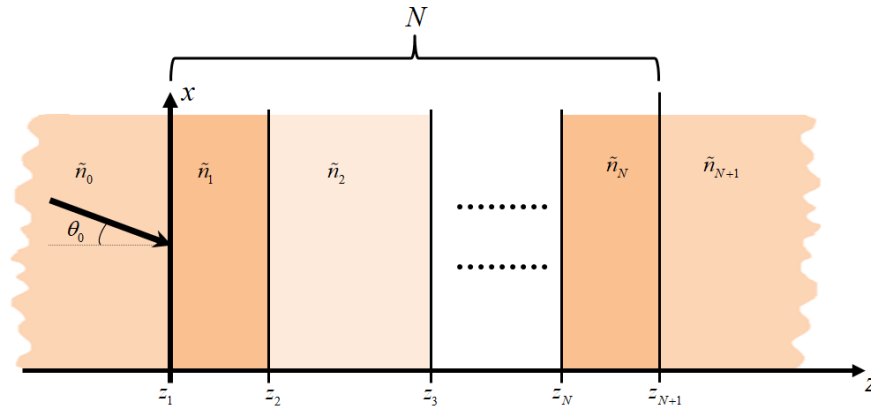


Fig. I.19. Schematic of the multilayered structure.

The complete transfer matrix \hat{G} (or T -matrix) describing wave propagation through the layered medium is defined here as the matrix that relates the complex amplitudes E_f and E_b of electric fields of forward-propagating (subscript f) and backward-propagating (subscript b) waves immediately before and immediately after the first and the last interfaces of the multilayered structure [24]:

$$\begin{pmatrix} E_f(z_1^-) \\ E_b(z_1^-) \end{pmatrix} = \hat{G} \begin{pmatrix} E_f(z_{N+1}^+) \\ E_b(z_{N+1}^+) \end{pmatrix}, \quad (\text{I.1})$$

where z_1 and z_{N+1} are the positions of the first and last interfaces along the z -axis (superscripts "-" and "+" refer to the sides before and after any interface, respectively). Equation (I.1) holds for both s - and p -polarizations. As there is no incident field from the right-hand side of the structure, Eq. (I.1) reads

$$\begin{pmatrix} E^{(i)} \\ E^{(r)} \end{pmatrix} = \hat{G} \begin{pmatrix} E^{(t)} \\ 0 \end{pmatrix}, \quad (\text{I.2})$$

where $E^{(i)}$, $E^{(r)}$ and $E^{(t)}$ are the complex electric field amplitudes of the incident, reflected and transmitted waves, respectively. For each of s - and p -polarization states this leads to two equations and two unknowns $E^{(r)}$ and $E^{(t)}$, which can easily be solved for.

The intensity reflection and transmission coefficients R and T of the structure follow from the ratios $E^{(r)} / E^{(i)}$ and $E^{(t)} / E^{(i)}$ respectively, and are defined as [24]:

$$R = \left| \frac{E^{(r)}}{E^{(i)}} \right|^2 = \left| \frac{G_{21}}{G_{11}} \right|^2, \quad (\text{I.3})$$

$$T = \frac{\tilde{n}_{N+1} \cos \theta_{N+1}}{\tilde{n}_0 \cos \theta_0} \left| \frac{E^{(t)}}{E^{(i)}} \right|^2 = \frac{\tilde{n}_{N+1} \cos \theta_{N+1}}{\tilde{n}_0 \cos \theta_0 |G_{11}|^2}. \quad (\text{I.4})$$

In general, the media constituting the structure exhibit some losses, so that an absorption coefficient A of the overall structure is defined in accordance with the principle of energy conservation as:

$$A = 1 - R - T. \quad (\text{I.5})$$

In Eq. (I.4), θ_0 is the angle of incidence of the incoming plane wave at the first interface, and θ_{N+1} is the refraction angle after the last interface of the structure.

It is worth noting that expressions of the form of Eq. (I.1) can be used to calculate the field distribution within the structure. In this case, in the left part, the column elements are replaced by the amplitudes of the local fields at the corresponding position in the structure.

In the T-matrix formalism used here, the matrix \hat{G} can be found by multiplying individual transfer matrices for wave propagation through an interface (\hat{I}_j) and wave propagation through a layer (\hat{F}_j):

$$\hat{G} = \left(\prod_{j=1}^N \hat{I}_j \hat{F}_j \right) \hat{I}_{j+1}. \quad (\text{I.6})$$

In subsections I.3.1.B and I.3.1.C we deal with propagation matrices and interface matrices in the simple case of homogeneous layers. In subsection I.3.1.D we discuss the propagation matrix of a composite layer, and in subsection I.3.1.E, we comment on the case of a 2D array of sub-wavelength-sized inclusions that will be considered as a specific case of interface.

I.4.1.B Simple case of homogeneous layers

Let us consider homogeneous layer j with thickness $d_j = z_{j+1} - z_j$ and complex refractive index \tilde{n}_j (Fig. I.20). The amplitudes of the forward and backward propagating waves at the two interfaces delimiting this layer are related in the following way:

$$\begin{aligned} E_f(z_{j+1}^-) &= E_f(z_j^+) e^{ik_{j,z}d_j}, \\ E_b(z_{j+1}^-) &= E_b(z_j^+) e^{-ik_{j,z}d_j}, \end{aligned} \quad (\text{I.7})$$

where

$$k_{j,z} = \sqrt{(\tilde{n}_j k_0)^2 - k_x^2} \quad (\text{I.8})$$

is the z -component of the wavevector in layer j , $k_0 = \omega/c$ is the wavevector in vacuum, and k_x is the x -component of the wavevector common to all layers. In matrix notation, the system of equations (I.7) takes the following form [24]:

$$\begin{pmatrix} E_f(z_j^+) \\ E_b(z_j^+) \end{pmatrix} = \hat{F}_j \begin{pmatrix} E_f(z_{j+1}^-) \\ E_b(z_{j+1}^-) \end{pmatrix}, \quad (\text{I.9})$$

where

$$\hat{F}_j = \begin{pmatrix} \exp(-i\delta_j) & 0 \\ 0 & \exp(i\delta_j) \end{pmatrix} \quad (\text{I.10})$$

is the individual transfer matrix (propagation or phase matrix) for the j -th layer, and

$$\delta_j = \text{Re}(k_{j,z})d_j. \quad (\text{I.11})$$

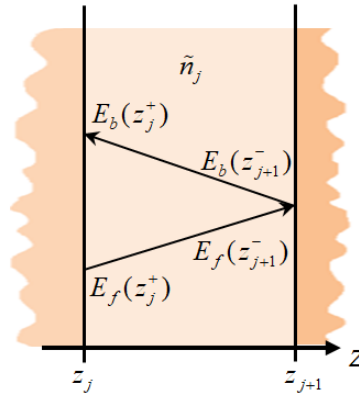


Fig. I.20. Schematic of the propagation through layer j .

I.4.1.C Simple case of interfaces between homogeneous layers

If we now consider the j -th interface between layer j and layer $j+1$ (Fig. I.21), the amplitudes of the forward and backward propagating waves on either side of the interface are related in the following way [24]:

$$\begin{pmatrix} E_f(z_j^-) \\ E_b(z_j^-) \end{pmatrix} = \hat{I}_j \begin{pmatrix} E_f(z_j^+) \\ E_b(z_j^+) \end{pmatrix}, \quad (\text{I.12})$$

where

$$\hat{I}_j = \frac{1}{t_{j-1,j}} \begin{pmatrix} 1 & -r_{j,j-1} \\ r_{j-1,j} & t_{j-1,j}t_{j,j-1} - r_{j-1,j}r_{j,j-1} \end{pmatrix} \quad (\text{I.13})$$

is the individual transfer matrix for wave propagation through the interface. Here $r_{\alpha,\beta}$ and $t_{\alpha,\beta}$ are the complex Fresnel reflection and transmission coefficients in amplitude for the interface separating two media with refractive indices n_α and n_β , when the wave is incident from the side of the medium with refractive index n_α .

The elements of the transfer matrix \hat{I}_j for the flat interface between two homogeneous, nonmagnetic, isotropic materials can be obtained with the use of Fresnel coefficients [5]. At the interface j , the Fresnel coefficients are functions of the generally

complex refractive indices \tilde{n}_{j-1} and \tilde{n}_j and of the incidence and refraction angles θ_{j-1} and θ_j (see Fig. I.21).

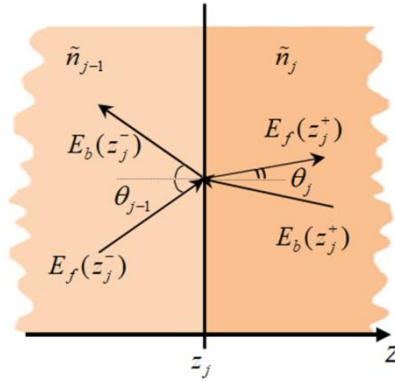


Fig. I.21. Schematic of the reflection and transmission of waves at the interface between two layers. Here θ_{j-1} , θ_j are the incidence and refraction angles at interface j for a forward propagating wave.

As is well known, Fresnel coefficients are different for s - and p -polarization states (except at normal incidence), and the angles of incidence and refraction are correlated with each other by Snell's law:

$$\tilde{n}_{j-1} \sin \theta_{j-1} = \tilde{n}_j \sin \theta_j. \quad (\text{I.14})$$

In the case of s -polarization, the Fresnel coefficients are given by [5]:

$$r_{j-1,j} = \frac{E_b(z_j^-)}{E_f(z_j^-)} = \frac{k_{j-1,z} - k_{j,z}}{k_{j-1,z} + k_{j,z}} = \frac{\tilde{n}_{j-1} \cos \theta_{j-1} - \tilde{n}_j \cos \theta_j}{\tilde{n}_{j-1} \cos \theta_{j-1} + \tilde{n}_j \cos \theta_j}, \quad (\text{I.15})$$

$$t_{j-1,j} = \frac{E_f(z_j^+)}{E_f(z_j^-)} = \frac{2k_{j-1,z}}{k_{j-1,z} + k_{j,z}} = \frac{2\tilde{n}_{j-1} \cos \theta_{j-1}}{\tilde{n}_{j-1} \cos \theta_{j-1} + \tilde{n}_j \cos \theta_j} = 1 + r_{j-1,j}, \quad (\text{I.16})$$

and in the case of p -polarization:

$$r_{j-1,j} = \frac{E_b(z_j^-)}{E_f(z_j^-)} = \frac{\tilde{n}_j^2 k_{j-1,z} - \tilde{n}_{j-1}^2 k_{j,z}}{\tilde{n}_j^2 k_{j-1,z} + \tilde{n}_{j-1}^2 k_{j,z}} = \frac{\tilde{n}_j \cos \theta_{j-1} - \tilde{n}_{j-1} \cos \theta_j}{\tilde{n}_j \cos \theta_{j-1} + \tilde{n}_{j-1} \cos \theta_j}, \quad (\text{I.17})$$

$$t_{j-1,j} = \frac{E_f(z_j^+)}{E_f(z_j^-)} = \frac{2\tilde{n}_{j-1}\tilde{n}_j k_{j-1,z}}{\tilde{n}_j^2 k_{j-1,z} + \tilde{n}_{j-1}^2 k_{j,z}} = \frac{2\tilde{n}_{j-1} \cos \theta_{j-1}}{\tilde{n}_j \cos \theta_{j-1} + \tilde{n}_{j-1} \cos \theta_j} = \frac{\tilde{n}_{j-1}}{\tilde{n}_j} (1 + r_{j-1,j}). \quad (\text{I.18})$$

Substituting (I.15) - (I.18) into (I.13), after transformations we obtain for s -polarization:

$$\hat{I}_j = \frac{1}{2\tilde{n}_{j-1} \cos \theta_{j-1}} \begin{pmatrix} 1 & \tilde{n}_{j-1} \cos \theta_{j-1} - \tilde{n}_j \cos \theta_j \\ \tilde{n}_{j-1} \cos \theta_{j-1} - \tilde{n}_j \cos \theta_j & 1 \end{pmatrix}, \quad (\text{I.19})$$

and for p -polarization:

$$\hat{I}_j = \frac{1}{2\tilde{n}_{j-1} \cos \theta_{j-1}} \begin{pmatrix} 1 & \tilde{n}_j \cos \theta_{j-1} - \tilde{n}_{j-1} \cos \theta_j \\ \tilde{n}_j \cos \theta_{j-1} - \tilde{n}_{j-1} \cos \theta_j & 1 \end{pmatrix}. \quad (\text{I.20})$$

For normal incidence ($\theta_0 = \dots = \theta_{j-1} = \theta_j = \dots = \theta_{N+1} = 0$), there is no difference between the s - and p -polarizations and the Fresnel coefficients can be written as:

$$r_{j-1,j} = \frac{\tilde{n}_{j-1} - \tilde{n}_j}{\tilde{n}_{j-1} + \tilde{n}_j}, \quad (\text{I.21})$$

$$t_{j-1,j} = \frac{2\tilde{n}_{j-1}}{\tilde{n}_{j-1} + \tilde{n}_j}. \quad (\text{I.22})$$

In this case, the interface transfer matrix takes the following form:

$$\hat{I}_j = \frac{1}{2\tilde{n}_{j-1}} \begin{pmatrix} 1 & \tilde{n}_{j-1} - \tilde{n}_j \\ \tilde{n}_{j-1} - \tilde{n}_j & 1 \end{pmatrix}. \quad (\text{I.23})$$

I.4.1.D Composite layers

The transfer matrix for a composite layer can be considered as a matrix for an homogeneous layer, because I will use in this case an effective medium approximation (which will be introduced below) for the description of the composite material properties in the case when the inclusions are much smaller than the wavelength. This case will be discussed in more detail in Chapter II.

I.4.1.E Interfaces made of monolayers of particles

A 2D array of particles can be considered as an array of interacting dipoles, and the corresponding transfer matrix will be a special type of interface matrix that will be introduced in the following Chapters.

I.4.2. Effective medium approximations

Effective-medium theory has been a tool for the evaluation of the optical properties of composite media for a long time. The main objective is the calculation of properties of the

composite from the known properties of its constituents. Effective medium methods refer to models that describe the macroscopic properties of composite materials, *i.e.*, at scales much larger than the typical wavelength of the waves that interact with these materials. These methods are based on an averaging of the multiple values of the characteristic parameters of the constituents that make up the composite material. At the constituent level, the parameters of the inhomogeneous materials vary and an exact calculation of these parameters is nearly impossible. However, theories have been developed that can yield acceptable approximations which lead to useful parameters, including the effective permittivity of a composite material as a whole. In this sense, effective medium approximations are descriptions of a composite medium based on the properties and the relative fractions of its components.

Effective permittivity is averaged dielectric characteristic of an inhomogeneous medium. It is derived in a quasi-static approximation where the electric field inside the medium may be considered as homogeneous.

Many materials fall into the broad category of composite materials whose description requires an effective medium approximation. One example that we will deal with in this manuscript, is a metal–dielectric composite consisting of a collection of metallic inclusions embedded into a dielectric matrix and arranged in some ordered or random fashion.

There are two widely used models, the Maxwell Garnett model and the Bruggeman model.

I.4.2.A. Maxwell Garnett model

Let us consider a composite medium consisting of a dielectric matrix in which identical, aligned ellipsoidal inclusions are embedded. The dielectric matrix is made of a material with relative permittivity ε_m and the inclusions are made of a material with relative permittivity ε_i . The medium is assumed to be exposed to an external electric field \mathbf{E}_e (Fig I.22). The resulting field in an inclusion can be found as

$$\mathbf{E}_i = \mathbf{E}_e + \mathbf{E}_d, \quad (\text{I.24})$$

where \mathbf{E}_d is the depolarizing field of the ellipsoidal inclusion.

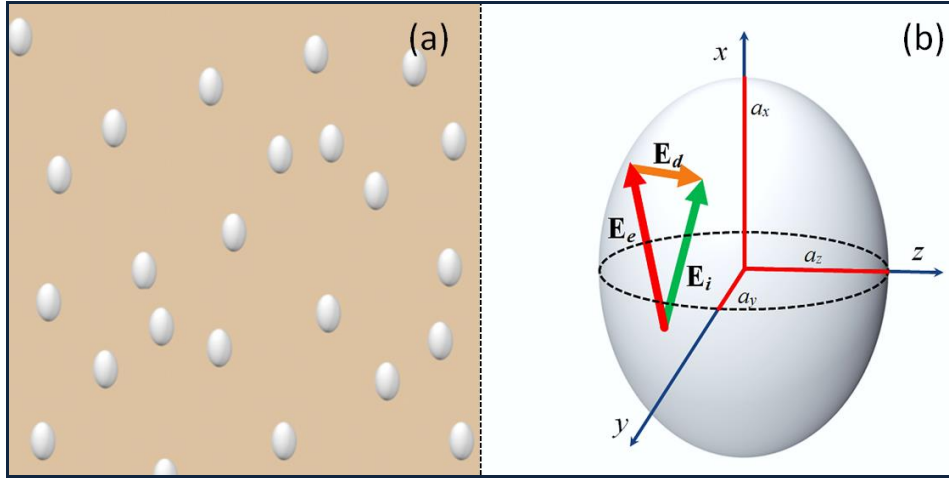


Fig. I.22. (a) Ellipsoidal inclusions in a homogeneous background (matrix) medium. The relative permittivity of the inclusions is ε_i and the relative permittivity of the medium is ε_m . (b) Geometry of an ellipsoid. Here \mathbf{E}_e and \mathbf{E}_d are an externally applied electric field and the depolarizing electric field in the inclusion, and \mathbf{E}_i is the total field in the inclusion. The Cartesian system of axes is chosen so that these axes coincide with the principal symmetry axes of the ellipsoidal inclusion, whose half-lengths are denoted a_x , a_y , and a_z .

Let us consider the case when the axes of each ellipsoidal inclusion coincide with the axes of a Cartesian coordinate system (Fig. I.22(b)). The effective macroscopic permittivity tensor $\hat{\varepsilon}_{eff}$ of this composite medium can be defined, in a linear approximation, as the following relation between the (volume)-averaged electric field \mathbf{E} and displacement vector \mathbf{D} :

$$\langle \mathbf{D} \rangle = \hat{\varepsilon}_{eff} \varepsilon_0 \langle \mathbf{E} \rangle = \begin{pmatrix} \varepsilon_{eff,x} & 0 & 0 \\ 0 & \varepsilon_{eff,y} & 0 \\ 0 & 0 & \varepsilon_{eff,z} \end{pmatrix} \varepsilon_0 \langle \mathbf{E} \rangle. \quad (\text{I.25})$$

where ε_0 is the electric permittivity of a vacuum.

Here the average electric field and displacement vector can be written by weighing the fields in the inclusions and in the matrix with the corresponding volume fractions [25-28]:

$$\langle \mathbf{D} \rangle = \eta \varepsilon_i \varepsilon_0 \mathbf{E}_i + (1 - \eta) \varepsilon_m \varepsilon_0 \mathbf{E}_e, \quad (\text{I.26})$$

$$\langle \mathbf{E} \rangle = \eta \mathbf{E}_i + (1 - \eta) \mathbf{E}_e, \quad (\text{I.27})$$

where we assume the fields \mathbf{E}_e and \mathbf{E}_i to be homogeneous, and η is the volume fraction of the inclusions in the composite medium. Then, substituting Eqs. (I.26), (I.27) to Eq. (I.25) we can write for the effective permittivity tensor elements:

$$\varepsilon_{eff,j} = \frac{\eta\varepsilon_i f_j + (1-\eta)\varepsilon_m}{\eta f_j + (1-\eta)}, \quad j = \{x, y, z\}, \quad (\text{I.28})$$

where f_j is the j -component of the diagonal tensor ($j = \{x, y, z\}$)

$$\hat{f} = \begin{pmatrix} f_x & 0 & 0 \\ 0 & f_y & 0 \\ 0 & 0 & f_z \end{pmatrix}, \quad (\text{I.29})$$

describing the ratio between the internal field and the external field: $\mathbf{E}_i = \hat{f} \mathbf{E}_e$. The components of the internal field \mathbf{E}_i can be written as [27]

$$E_{i,j} = f_j E_{e,j} = \frac{\varepsilon_m}{\varepsilon_m + g_j (\varepsilon_i - \varepsilon_m)} E_{e,j}, \quad (\text{I.30})$$

where g_j is the j -component of the depolarization tensor \hat{g} . Because of the anisotropy of an ellipsoidal inclusion, it is to be expected that the dipole moment induced by the external field in that inclusion is dependent on the direction of the field. In general, the dipole moment has a different direction to the electric field. It is only along the three principal axes directions that the field and the dipole moment it creates are aligned. If the half-lengths of the principal symmetry axes of an ellipsoidal inclusion are denoted a_x , a_y , and a_z , the depolarization tensor is the following diagonal matrix:

$$\hat{g} = \begin{pmatrix} g_x & 0 & 0 \\ 0 & g_y & 0 \\ 0 & 0 & g_z \end{pmatrix}. \quad (\text{I.31})$$

For a general ellipsoid with three different values of the half-lengths a_x , a_y , and a_z , the depolarization tensor elements have to be calculated from the integral [27].

$$g_j = \frac{a_x a_y a_z}{2} \int_0^\infty \frac{ds}{(s + a_j^2) \sqrt{(s + a_x^2)(s + a_y^2)(s + a_z^2)}}. \quad (\text{I.32})$$

The three depolarization tensor elements obey the following relation:

$$g_x + g_y + g_z = 1. \quad (\text{I.33})$$

In practice, there are often cases when the ellipsoidal inclusions have two of their three semi-axes equal in length. In this case, the inclusion has the shape of a spheroid, the size of which is characterized by only two geometric parameters. If we assume that the x -axis is the axis of rotational symmetry of such a spheroid, then we can write $a_x \neq a_y = a_z$.

Figure I.23 shows various cases of spheroids with different ratios of their polar (a_x) and equatorial ($a_y = a_z$) semi-axes. In the case when $a_x = a_y = a_z$, the inclusion will have a spherical shape.

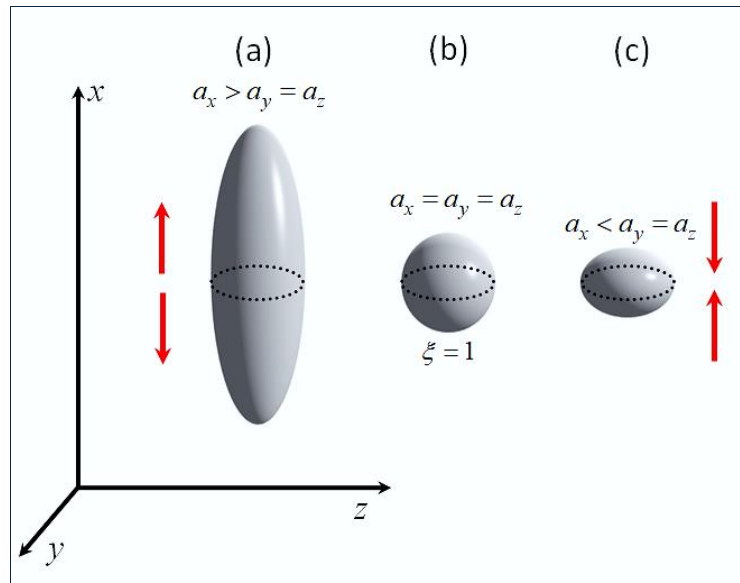


Fig. I.23. Prolate spheroids, spheres and oblate spheroids.

For prolate spheroids ($a_x > a_y = a_z$), the depolarization tensor elements are [27]

$$g_x = \frac{1-e^2}{2e^3} \left(\ln \frac{1+e}{1-e} - 2e \right), \quad (\text{I.34})$$

$$g_y = g_z = \frac{1}{2}(1 - g_x), \quad (\text{I.35})$$

where e is the eccentricity of the spheroid defined as $e = \sqrt{1 - a_y^2 / a_x^2}$.

For oblate spheroids ($a_x < a_y = a_z$), the depolarization tensor elements are [27]

$$g_x = \frac{1-e^2}{e^3} (e - \arctan e), \quad (\text{I.36})$$

$$g_y = g_z = \frac{1}{2}(1 - g_x), \quad (\text{I.37})$$

where the eccentricity is now $e = \sqrt{a_y^2 / a_x^2 - 1}$.

Both equations (I.34) and (I.36) can also be written in terms of the aspect ratio $\xi = a/b$ of the spheroid, where the polar semi-axis is $a = a_x$ and the equatorial semi-axis is $b = a_y = a_z$ [29]:

$$g_x = \frac{1}{1 - \xi^2} \left(1 - \xi \frac{\arcsin(\sqrt{1 - \xi^2})}{\sqrt{1 - \xi^2}} \right). \quad (\text{I.38})$$

The dependence of the depolarization tensor elements on the aspect ratio is shown in the Fig. I.24. In the case of a spherical inclusion ($a = b$), aspect ratio ξ is equal to 1, and the inclusion has three identical depolarization tensor elements $g_x = g_y = g_z = 1/3 \approx 0.33$.

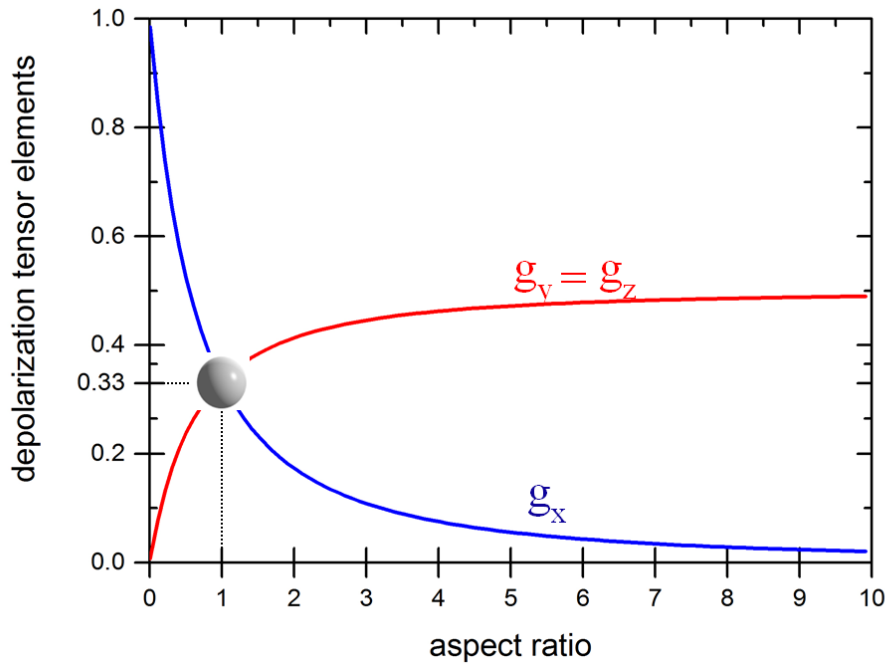


Fig. I.24. Depolarization tensor elements as a function of the aspect ratio.

After simplification, Eq. (I.28) then becomes

$$\frac{\varepsilon_{eff,j} - \varepsilon_m}{\varepsilon_m + g_j(\varepsilon_{eff,j} - \varepsilon_m)} = \eta \frac{\varepsilon_i - \varepsilon_m}{\varepsilon_m + g_j(\varepsilon_i - \varepsilon_m)}, \quad (\text{I.39})$$

which is the *Maxwell Garnett* formula for ellipsoidal inclusions for the j -component of the external field ($j = \{x, y, z\}$) [30,31].

I.4.2.B Bruggeman model

The Bruggeman mixing rule [32] presents another philosophy of homogenization. In this case host and guest are not distinguished in the mixture, and both inclusions and the environment are treated symmetrically. In the frame of this approximation both the inclusions and the surrounding medium are treated as ellipsoidal particles made of different materials with relative permittivities ε_1 and ε_2 . In this case Eq. (I.26) and (I.27) can be written as

$$\langle \mathbf{D} \rangle = \eta \varepsilon_1 \varepsilon_0 \mathbf{E}_1 + (1 - \eta) \varepsilon_2 \varepsilon_0 \mathbf{E}_2, \quad (\text{I.40})$$

$$\langle \mathbf{E} \rangle = \eta \mathbf{E}_1 + (1 - \eta) \mathbf{E}_2, \quad (\text{I.41})$$

where \mathbf{E}_1 and \mathbf{E}_2 are the local fields in the constituents of the mixture. It is considered that these constituents are immersed in an effective external field \mathbf{E}_e . Due to this the relation between local and external fields can be written as (see Eq. (I.30))

$$\begin{aligned} \mathbf{E}_1 &= \hat{f}_1 \mathbf{E}_e \\ \mathbf{E}_2 &= \hat{f}_2 \mathbf{E}_e \end{aligned} \quad (\text{I.42})$$

where the elements of tensors \hat{f}_1 and \hat{f}_2 are given by

$$f_{1,j} = \frac{\varepsilon_1}{\varepsilon_1 + g_j (\varepsilon_{eff,j} - \varepsilon_1)}, \quad (\text{I.43})$$

$$f_{2,j} = \frac{\varepsilon_2}{\varepsilon_2 + g_j (\varepsilon_{eff,j} - \varepsilon_2)}, \quad (\text{I.44})$$

with $j = \{x, y, z\}$. As a result, the following formula can be obtained for ellipsoidal scatterers [31]:

$$(1 - \eta) \frac{\varepsilon_2 - \varepsilon_{eff,j}}{\varepsilon_{eff,j} + g_j (\varepsilon_2 - \varepsilon_{eff,j})} + \eta \frac{\varepsilon_1 - \varepsilon_{eff,j}}{\varepsilon_{eff,j} + g_j (\varepsilon_1 - \varepsilon_{eff,j})} = 0. \quad (\text{I.45})$$

The distinction between the Maxwell Garnett and the Bruggeman rules is related to the symmetry property of Eq. (I.45), as compared to Eq. (I.39). The symmetry of

Eq. (I.45) means that the constituents of the mixture cannot be formally divided between matrix and inclusions and in this equation they both are weighted with their corresponding volume fraction (η for one component and $(1 - \eta)$ for the other component).

I.4.2.C *Domains of validity*

The Maxwell Garnett and Bruggeman models imply the following conditions:

- the mixture is linear, that is, none of its constitutive parameters depends on the intensity of the electromagnetic field;
- the mixture is non-parametric, that is, its parameters do not change in time according to some law as a result of external forces – electrical, mechanical, *etc.*;
- inclusions are separated by distances greater than their characteristic size;
- the characteristic size of inclusions is small compared to the wavelength in the effective medium;

There are two restrictions on the size of the inclusions (particles): from below and from above. The limitation from below is associated with the manifestation of quantum effects, when a particle containing about a thousand atoms can no longer be described similarly to a continuous medium, as is usually done in problems of classical optics. Also, the characteristic size of the particles must exceed the coherence length of an electron wave inside the particles, that is, more than approximately 1 nm [27].

The upper bound is due to the fact that, in the classical approach, an inclusion is considered as a point electric dipole. This limit for a particle can be written as $k_{eff}d \ll 1$, where k_{eff} is the amplitude of the wave vector in the effective medium and d is the characteristic size of the particle [27].

From such considerations, it is also possible to determine the limiting values of the volume fraction of particles per unit volume of the composite. The lower limit is determined by the requirement of homogeneity of the effective medium, while the upper limit is limited by the percolation threshold. The predictions of the Maxwell Garnett effective medium model are reliable for a moderate fraction of inclusions $\eta < 0.3$ [33], while for the Bruggeman theory the lower limit of the volume fraction is approximately equal to 0.33 [28].

The Maxwell Garnett and Bruggeman effective medium approximations demonstrate good results when compared to experimental measurements and numerical calculations. In Fig. I.25 taken from Ref. [33] one can see for example the simulated results of the Maxwell Garnett

effective medium approximation (triangles) and of numerical calculations carried out with the COMSOL Multiphysics solver based on finite element methods (solid and dashed lines for ordered and disordered inclusions, respectively). The results were obtained for the silver ellipsoidal inclusions in the SiO_2 medium with a volume fraction value 0.1.

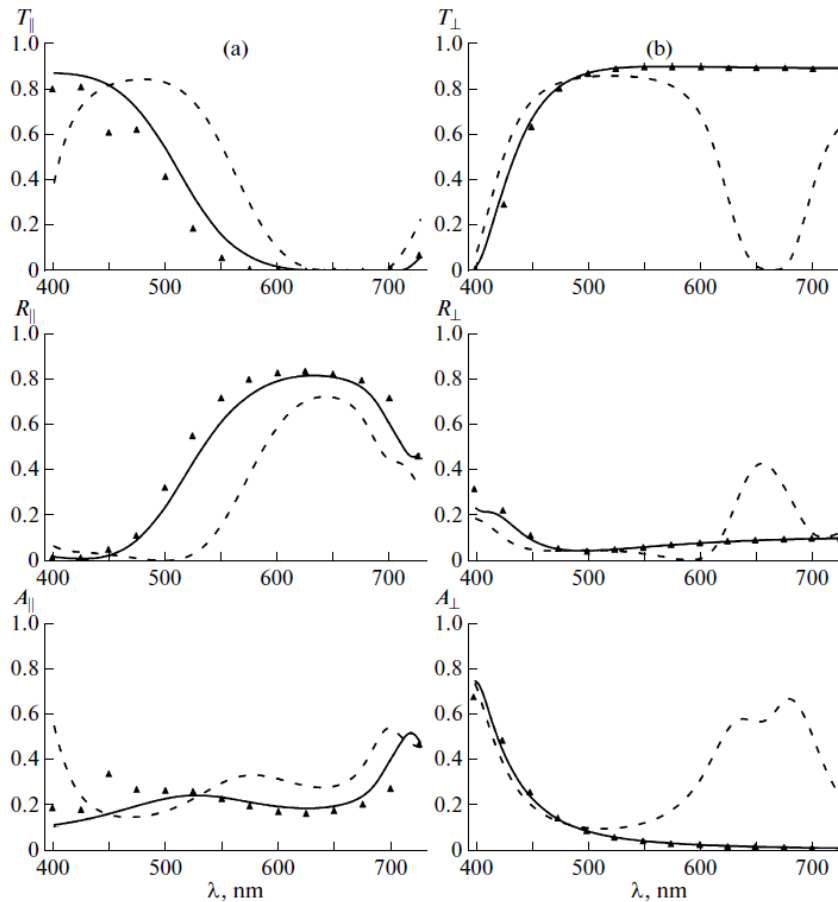


Fig. I.25. Spectral dependence of the transmittivity T , the reflectivity R , and the absorptivity A of composite films made of silver spheroidal inclusions in a SiO_2 matrix for unidirectional inclusions (solid lines) and orientationally disordered inclusions (dashed lines) for the parallel (a) and perpendicular (b) (with respect to the axis of rotation of the spheroidal inclusions) light polarizations. Triangles indicate the results of computer simulations of the composite with unidirectional inclusions. [33]

Similarly, Fig. I.26. represents the results of numerical calculations of chromatic dispersion of the effective refractive index of a $\text{Nb}_2\text{O}_5:\text{SiO}_2$ mixture (from the near-UV to near-IR) obtained with the Bruggeman model, and compared to experimental results, for volume ratios 80:20, 65:35, 50:50 35:65 and 20:80.

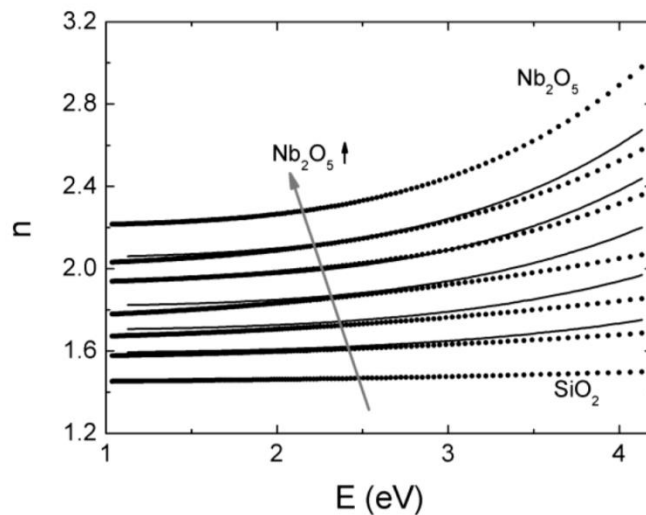


Fig. I.26. Comparison between the effective refractive index of a $\text{Nb}_2\text{O}_5:\text{SiO}_2$ mixture calculated using the Bruggeman model (solid lines) and experimentally determined (dotted lines) for different concentrations of the constituents of the mixture. [34]

In Chapter II, the Maxwell Garnett model as an effective medium approximation is used, as the Bruggeman model shows good results only for relatively large volume fractions of inclusions η , while in the systems that we study η does not exceed 0.02.

I.4.3 Coupled dipole method

The effective medium approximations described above deal with bulk composites. For low-dimensional systems these approximations do not work well, as they involve macroscopic parameters including the effective dielectric permittivity. Instead, for the description of 2D arrays of inclusions, we use the coupled dipole method whose main principles are exposed below. This method is simple to implement and allows us to speed up calculations without losing accuracy compared to numerical methods (comparisons of calculations showed that the difference in the frequencies and amplitudes of the plasmon resonance obtained with the two methods is less than 1%).

Let us consider a flat single-layer 2D array of ellipsoidal nonmagnetic inclusions in a homogeneous nonmagnetic medium. The inclusions are arranged periodically with a square unit cell whose translational invariance is directed along the x and y axes of the Cartesian coordinate system (Fig. I.27). All inclusions are assumed to have the same ellipsoidal shape and the same dimensions. In addition, all inclusions are similarly aligned, with their semi-axes coinciding with the axes of a Cartesian coordinate system.

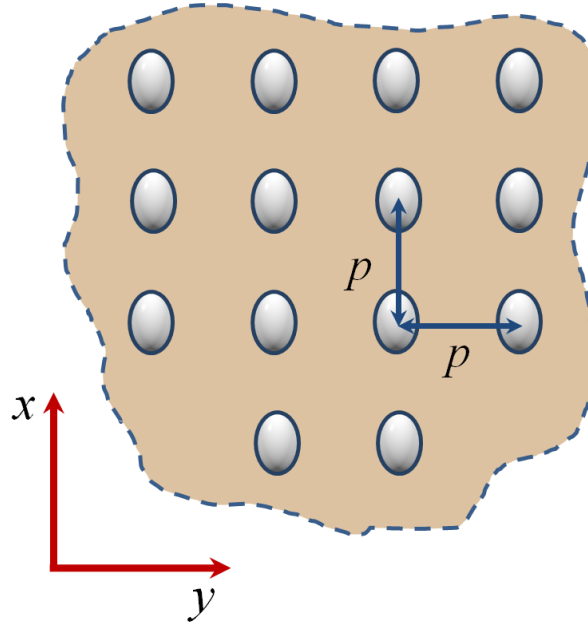


Fig. I.27. A periodic 2D array of inclusions with a square lattice. Here p is the period of the array, *i.e.* the interparticle distance.

The applied electric field \mathbf{E}_e distorts the charge distribution in the inclusions, generating electric dipoles at the nodes of the periodic lattice. Because of the anisotropy of the ellipsoids and the specific geometry of the 2D array it is to be expected that the dipole moment induced in an inclusion depends on the direction of the electric field that excites it. Let us choose a random dipole as the point of reference for the numbering of the dipoles, which will be referred to with integer numbers l and n related to their position (row and column) in the array. The reference dipole has the $(0, 0)$ index, and the total electric field at the location of that dipole can then be written as

$$\mathbf{E}'_e = \mathbf{E}_e + \sum_{(l,n) \neq (0,0)} \mathbf{E}_{d(l,n)}, \quad (\text{I.46})$$

where $\mathbf{E}_{d(l,n)}$ is the depolarizing field generated at that location by any other dipole with index (l, n) . The depolarizing field can be obtained as [5]

$$\mathbf{E}_{d(l,n)} = \frac{1}{4\pi\epsilon_m\epsilon_0} \frac{3(\mathbf{p}'_{l,n}\mathbf{r}_{l,n})\mathbf{r}_{l,n} - \mathbf{p}'_{l,n}}{r_{l,n}^3}, \quad (\text{I.47})$$

where $\mathbf{r}_{l,n}$ is the vector connecting the reference dipole to the dipole labelled by the integers (l, n) , and $\mathbf{p}'_{l,n}$ is the dipole moment of the latter. As previously, ϵ_m is the relative permittivity

of the medium surrounding the inclusion. In the linear approximation, the dipole moment of the ellipsoidal inclusion is related to the field \mathbf{E}'_e as

$$\mathbf{p}' = \hat{\alpha} \varepsilon_m \varepsilon_0 \mathbf{E}'_e, \quad (\text{I.48})$$

where $\hat{\alpha}$ is the polarizability tensor of the inclusion with diagonal elements [35]

$$\alpha_j \equiv \alpha_{jj} = \frac{4\pi a_x a_y a_z}{3} \frac{(\varepsilon_i - \varepsilon_m)}{\varepsilon_m + g_j (\varepsilon_i - \varepsilon_m)}, \quad j = \{x, y, z\} \quad (\text{I.49})$$

For a square lattice of infinite dimensions, using Eqs. (I.46)-(I.48), the components of the field \mathbf{E}'_e are given by [36,37]

$$E'_{e,j} = E_{e,j} + \frac{S_j}{4\pi p^3} \alpha_j E'_{e,j}, \quad j = \{x, y, z\}, \quad (\text{I.50})$$

where the geometric factors S_j depend on the direction of the electric field vector of the incident wave relatively to the plane of the 2D array and are calculated as the following sums:

$$S_z = \sum_{(l,n) \in \mathbb{Z}^2 \setminus (0,0)} \frac{-1}{(n^2 + l^2)^{3/2}} \approx -9.03, \quad (\text{I.51})$$

$$S_x = S_y = -\frac{1}{2} S_z \approx 4.52. \quad (\text{I.52})$$

At the same time, we can express the dipole moment in terms of the applied electric field \mathbf{E}_e and an *effective* polarizability that accounts for the influence of the entire array of inclusions. In this case, and again in the linear approximation, we can write

$$\mathbf{p}' = \hat{\alpha}_{eff} \varepsilon_m \varepsilon_0 \mathbf{E}_e, \quad (\text{I.53})$$

where $\hat{\alpha}_{eff}$ is the diagonal effective polarizability tensor of the inclusions.

From Eqs. (I.48)-(I.53) the elements of the effective electric polarizability tensor can be calculated as

$$\alpha_{eff,j} = \frac{\alpha_j}{1 - \frac{S_j \alpha_j}{4\pi p^3}}, \quad j = \{x, y, z\}, \quad (\text{I.54})$$

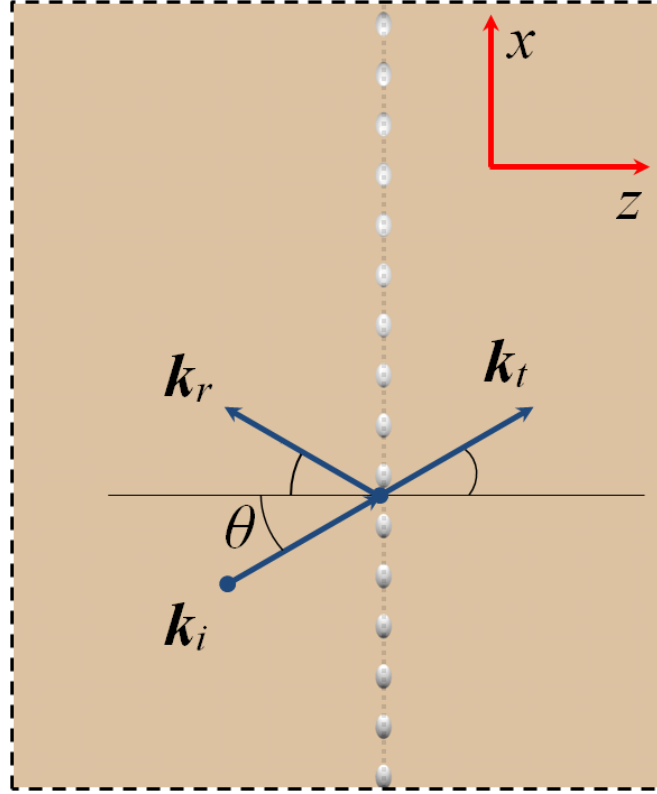


Fig. I.28. Plane wave incident onto a 2D array of inclusions parallel to the (xy) plane. The wave vectors of the incident, reflected and transmitted waves are denoted k_i , k_r , and k_t , respectively, and θ is the incidence angle.

The 2D array of inclusions embedded in the matrix can be described as a monolayer. An electromagnetic wave incident on such a monolayer at an angle θ experiences reflection and transmission. The reflection and transmission coefficients for the case of a s -polarized incident wave (*i.e.*, along the y -axis) can be expressed as [37]

$$r = \frac{-i \frac{k_0}{2p^2 \cos \theta} \sqrt{\varepsilon_m} \alpha_{eff,y}}{1 + i \frac{k_0}{2p^2 \cos \theta} \sqrt{\varepsilon_m} \alpha_{eff,y}}, \quad (\text{I.55})$$

$$t = \frac{1}{1 + i \frac{k_0}{2p^2 \cos \theta} \sqrt{\varepsilon_m} \alpha_{eff,y}}. \quad (\text{I.56})$$

In the case of a p -polarized wave (*i.e.*, parallel to the (xz) plane), these coefficients can be written as

$$r = \frac{-i \frac{k_0}{2p^2 \cos \theta} \sqrt{\varepsilon_m} (\alpha_{eff,x} \cos^2 \theta - \alpha_{eff,z} \sin^2 \theta)}{1 - \left(\frac{k_0}{2p^2}\right)^2 \varepsilon_m \alpha_{eff,x} \alpha_{eff,z} \sin^2 \theta + i \frac{k_0}{2p^2 \cos \theta} \sqrt{\varepsilon_m} (\alpha_{eff,x} \cos^2 \theta + \alpha_{eff,z} \sin^2 \theta)}, \quad (I.57)$$

$$t = \frac{1 + \left(\frac{k_0}{2p^2}\right)^2 \varepsilon_m \alpha_{eff,x} \alpha_{eff,z} \sin^2 \theta}{1 - \left(\frac{k_0}{2p^2}\right)^2 \varepsilon_m \alpha_{eff,x} \alpha_{eff,z} \sin^2 \theta + i \frac{k_0}{2p^2 \cos \theta} \sqrt{\varepsilon_m} (\alpha_{eff,x} \cos^2 \theta + \alpha_{eff,z} \sin^2 \theta)}. \quad (I.58)$$

At normal incidence ($\theta = 0$), due to the anisotropy of the 2D array we will consider two cases of linear polarization of the incoming wave, along the x and along the y axis. In this case, from Eqs. (I.55) - (I.58) we will have

$$r_x = \frac{-i \frac{k_0}{2} \sqrt{\varepsilon_m} \alpha_{eff,x}}{2p^2 + i \frac{k_0}{2} \sqrt{\varepsilon_m} \alpha_{eff,x}}, \quad t_x = \frac{2p^2}{2p^2 + i \frac{k_0}{2} \sqrt{\varepsilon_m} \alpha_{eff,x}}, \quad (I.59)$$

$$r_y = \frac{-i \frac{k_0}{2} \sqrt{\varepsilon_m} \alpha_{eff,y}}{2p^2 + i \frac{k_0}{2} \sqrt{\varepsilon_m} \alpha_{eff,y}}, \quad t_y = \frac{2p^2}{2p^2 + i \frac{k_0}{2} \sqrt{\varepsilon_m} \alpha_{eff,y}}. \quad (I.60)$$

These Fresnel-like coefficients can then be used in the transfer matrix describing a 2D array of particles, as mentioned in subsection I.3.

I.5. List of references

- [1] E. Yablonovitch, "Inhibited Spontaneous Emission in Solid-State Physics and Electronics" *Phys. Rev. Lett.* **58**, 2059 (1987).
- [2] T. Chen, T. Lu, Z. Chen, W. Wang, W. Zhang, H. Pan, X. Meng, X. Jiang and S. Zhu, "*Microstructures of responsive photonic crystals on the stimuli-responsive performance: Effects and simulation,*" *Sens. Actuators B Chem.* **305**, 127421. (2019).
- [3] J. D. Joannopoulos, S. G. Johnson, J. N. Winn, R. D. Meade, *Photonic Crystals: Molding the Flow of Light, second ed.* (Princeton University Press, Princeton, New York, 2008).
- [4] C. Sibilia, T. M. Benson, M. Marciniak, T. Szoplik, *Photonic Crystals: Physics and Technology* (Springer-Verlag, Milan, 2008).
- [5] M. Born and E. Wolf, *Principles of Optics* (Cambridge University Press, Cambridge, 1999).
- [6] V. Tolmachev, A. Baldycheva, T. Perova, "Double-cavity Fabry-Perot resonators based on one-dimensional silicon photonic crystals," *AIP Conf. Proc.* **2004**, 020001 (2018).
- [7] S.M. Musavizadeh, M. Soroosh, F. Mehdizadeh, "Optical filter based on photonic crystal," *Indian J. Pure Appl. Phys.* **53**, 736-739 (2015).
- [8] A. W. Bushmaker, Z. Lingley, M. Brodie, B. Foran, and Y. Sin, "Optical Beam Induced Current and Time Resolved Electro-Luminescence in Vertical Cavity Surface Emitting Lasers during Accelerated Aging," *IEEE Photonics Journal* PP (99), (2019)
- [9] J. E. Baker, R. Sriram and B. L. Miller, "Two-dimensional photonic crystals for sensitive microscale chemical and biological sensing," *Lab. Chip.* **15**, 971-990 (2015).
- [10] NH. Umh, S. Yu, YH. Kim, SY. Lee, and J. Yi, "Tuning the Structural Color of a 2D Photonic Crystal using a Bowl-Like Nanostructure," *ACS Applied Materials & Interfaces* **8** (24), 15802-15808 (2016).
- [11] TP. Nguyen, TQ. Tien, QC. Tong and ND. Lai, "An Optimization of Two-Dimensional Photonic Crystals at Low Refractive Index Material," *Crystals* **9** (9), 442 (2019).
- [12] C. Marichy, N. Muller, L. S. Froufe-Pérez and F. Scheffold, "High-quality photonic crystals with a nearly complete band gap obtained by direct inversion of woodpile templates with titanium dioxide," *J. Opt. Soc. Am.* **4**, 361-366 (2017).
- [13] X. Han, K. Liu and C. Sun, "Plasmonics for Biosensing," *Mater.* **12**, 1411 (2019)
- [14] F. Ye, J. M. Merlo, M. J. Burns, M. J. Naughton, "Optical and electrical mappings of surface plasmon cavity modes," *Nanophotonics* **3** (1-2), 33-49 (2014).
- [15] A. Vaughan, "Raman nanotechnology - the Lycurgus Cup - Letter to the Editor," *IEEE Electr. Insul. Mag.* **24**, 4-4 (2008).
- [16] M. L. Brongersma, P. G. Kik, *Surface Plasmon Nanophotonics* (Springer Series in Optical Sciences (SSOS, vol. **131**) 2007).
- [17] R. Ameling, H. Giessen, "Microcavity plasmonics: strong coupling of photonic cavities and plasmons," *Laser Photonics Rev.* **7**(2), 141-169 (2012).

- [18] V. S. Gerasimov, A. E. Ershov, R. G. Bikbaev, I. L. Rasskazov, I. V. Timofeev, S. P. Polyutov, and S. V. Karpov, “*Engineering mode hybridization in regular arrays of plasmonic nanoparticles embedded in 1D photonic crystal*,” *J. Quant. Spectrosc. Radiat. Transf.* **224**, 303–308 (2019).
- [19] P. Singh, K. B. Thapa, N. Kumar, D. Singh, and D. Kumar, “*Effective optical properties of the one-dimensional periodic structure of TiO₂ and SiO₂ layers with a defect layer of nanocomposite consisting of silver nanoparticle and E7 liquid crystal*,” *Pramana – J. Phys.* **93**, 50 (2019).
- [20] A. H. Aly, C. Malek, H. A. Elsayed, “*Transmittance properties of a quasi-periodic one-dimensional photonic crystals that incorporate nanocomposite material*,” *Int. J. Mod. Phys. B* **32**, 1850220 (2018).
- [21] S. G. Moiseev, V. A. Ostatochnikov, and D. I. Sementsov, “*Defect mode suppression in a photonic crystal structure with a resonance nanocomposite layer*,” *Quantum Electron.* **42**, 557–560 (2012).
- [22] S. Y. Vetrov, P. S. Pankin, and I. V. Timofeev, “*Peculiarities of spectral properties of a one-dimensional photonic crystal with an anisotropic defect layer of the nanocomposite with resonant dispersion*,” *Quantum Electron.* **44**, 881–884 (2014).
- [23] P. Babu Dayal, F. Koyama, “*Polarization control of 0.85 μm vertical-cavity surface-emitting lasers integrated with gold nanorod arrays*,” *Appl. Phys. Lett.* **91**, 111107 (2007).
- [24] C. Katsidis, D. Siapkias, “*General Transfer-Matrix Method for Optical Multilayer Systems with Coherent, Partially Coherent, and Incoherent Interference*,” *Appl. Opt.* **41**, 3978-87 (2002).
- [25] L. A. Golovan, V. Yu. Timoshenko, P. K. Kashkarov, “*Optical properties of porous-system-based nanocomposites*,” *Phys. Usp.* **50**:6, 595–612 (2007)
- [26] A. Sihvola, “*Two Main Avenues Leading To the Maxwell Garnett Mixing Rule*,” *J. Electromagn. Waves Appl.* **15**, 715–725 (2001).
- [27] A. Sihvola, *Electromagnetic Mixing Formulas and Applications* (The Institution of Engineering and Technology; 1999).
- [28] A. Sihvola, “*Mixing Rules with Complex Dielectric Coefficients*,” *Subsurface Sensing Technologies and Applications* vol. **1**, no. 4, 393-415. (2000).
- [29] J. A. Osborn, “*Demagnetizing Factors of the General Ellipsoid*,” *Phys. Rev.* **67**, 351-357 (1945)
- [30] J. C. Maxwell Garnett, “*Colours in Metal Glasses and in Metallic Films*,” *Philosophical Transactions of the Royal Society of London. Series A*,” Containing Pap. Math. Phys. Char. **203**, 385–420 (1904).
- [31] J. E. Spanier, I. P. Herman “*Use of hybrid phenomenological and statistical effective-medium theories of dielectric functions to model the infrared reflectance of porous SiC films*,” *Phys. Rev. B.* **61**, 10437 (2000).
- [32] D. A. G. Bruggeman, “*Berechnung verschiedener physikalischer Konstanten von heterogenen Substanzen. III. Die elastischen Konstanten der quasiisotropen Mischkörper aus isotropen Substanzen*,” *Annalen der Physik.* **421**, 160-178 (1937).
- [33] S.G. Moiseev, “*Nanocomposite-based ultrathin polarization beamsplitter*,” *Opt. Spectrosc.* **111**, 233-240 (2011).

- [34] J. Sancho-Parramon, V. Janicki, “*Effective medium theories for composite optical materials in spectral ranges of weak absorption: the case of Nb₂O₅- SiO₂ mixtures,*” J. Phys. D: Appl. Phys. **41**, 215304 (2008).
- [35] C. F. Bohren and D. R. Huffman, *Absorption and Scattering of Light by Small Particles* (Wiley, New York, 1983).
- [36] L. Dell'Anna, M. Merano, “*Clausius-Mossotti Lorentz-Lorenz relations and retardation effects for two-dimensional crystals,*” Phys. Rev. A **93**, 053808 (2016).
- [37] C. L. Holloway, M. A. Mohamed, E. F. Kuester and A. Dienstfrey, “*Reflection and transmission properties of a metafilm: with an application to a controllable surface composed of resonant particles,*” IEEE Trans. Electromagn. Compat. **47**, 853–865 (2005).

CHAPTER II

OPTICAL AMPLIFICATION IN A PHOTONIC CRYSTAL WITH AN EMBEDDED NANOCOMPOSITE POLARIZER

II.1. Introduction

During the last decades photonic crystals (PCs) have been intensively investigated because of their promising applications in modern photonics [1,2]. The use of PC structures with amplifying fibers opens the possibility of creating a compact semiconductor laser with a vertical cavity resonator working in optical and near-infrared regimes, or vertical cavity surface-emitting lasers [3,4]. At the same time one of the main obstacles to obtain a stable generation in such a resonator can be simultaneous amplification of waves with different polarizations, which leads to the rise of extremely undesirable polarization and amplitude instabilities [5,6] which break a stable operation of the laser. The solution of this problem can be using a thin-film subwavelength polarizer, integrated directly into the structure of the resonator PC.

This Chapter is devoted to studying the possibility of the use of a composite film with the inclusion of metallic aspherical shape nanoparticles as an integrated polarizer for amplifying PC system. As was shown in [7,8], in the region of the plasmon resonance of inclusions, such metal-dielectric composite film of subwavelength thickness may exhibit a high polarization selectivity in both reflection and transmission with moderate absorption. Resonance properties of the nanocomposite layers with metal inclusions can be used to suppress the resonance modes of the PC structures, which makes the spectra of such structure polarization-sensitive [9-12]. Thus, it would expect to obtain selective polarization amplification in the similar PC with amplification.

The Chapter is organized as follows. In Section II.2, the geometry and the structural parameters of the model are presented. Section II.3 presents the results of the calculations of the spectral properties of the structure. In subsection II.3.1 the results for the transmittivity and reflectivity of the composite layer and their dependency on its structural parameters are shown. In subsection II.3.2 the transmittivity spectrum of the entire structure (described in Section II.3) is presented and its dependence upon the structural parameters of the defect layer is discussed. Section II.4 highlights the conclusions of this Chapter.

II.2. Geometry and materials of the structure

Let us consider a symmetric PC microcavity system consisting of two distributed Bragg reflectors (DBRs) of structure $(AB)^N$ and $(BA)^N$ and a nanocomposite defect layer placed between them, surrounded by air (Fig. II.1). Alternate layers A and B , repeated N times

($N \in \mathbb{N}^*$) in each PC, have respective thicknesses d_A and d_B and are made of optically isotropic, nonmagnetic materials with relative dielectric permittivities $\varepsilon_{A,B} = \varepsilon'_{A,B} + i\varepsilon''_{A,B}$. The time dependence of the complex electric and magnetic fields of light (angular frequency ω) is taken as $\exp(-i\omega t)$, which means that positive (respectively, negative) values of $\varepsilon''_{A,B}$ correspond to the attenuation (respectively, amplification) of an electromagnetic wave upon propagation in the corresponding media. Chromatic dispersion of the relative dielectric permittivities of all media is taken into account.

In this Chapter, light is supposed to propagate under normal incidence along the z -axis of a (xyz) Cartesian system of coordinates, so that the interfaces between the layers of the structure are parallel to the (xy) plane and (xz) is the plane of incidence. A schematic of the structure is represented in Fig. II.1.

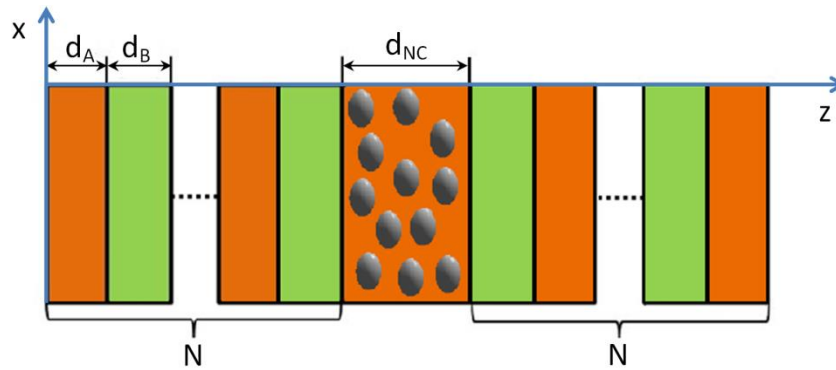


Fig. II.1. Schematic of the system: two distributed Bragg reflectors of structure $(AB)^N$ and $(BA)^N$ surround a nanocomposite layer.

The nanocomposite layer (thickness d_{NC}) consists of a semiconducting material, or matrix, hosting uniformly distributed metallic NPs of spheroidal shape and identical orientations. An effective medium approximation was used, in order to describe the optical properties of the nanocomposite. The essence of such an approximation is the assumption that a heterogeneous mixture of different materials can still retain a macroscopic optical homogeneity that can be characterized by a certain effective (averaged) relative permittivity (see Chapter I). Composite materials of various topologies have been the subject of a number of effective medium models, including the most commonly used ones, the Bruggeman, Maxwell Garnett, or Landau–Lifshitz models [13,14]. In this Chapter was considered a nanocomposite layer made of an isotropic medium with metal inclusions of sub-wavelength dimensions in the case where the volume fraction η of inclusions (defined as the ratio between the volume occupied by the

inclusions and the total volume of the composite layer) does not exceed 0.15%. The effective optical characteristics of such a composite, including in the range of the plasmon resonance frequencies of the metal NPs, are most adequately described by the Maxwell Garnett model (see discussion in Chapter I). Fig. II.2 represents a composite layer with uniformly oriented spheroidal metallic inclusions and the geometry of these inclusions.

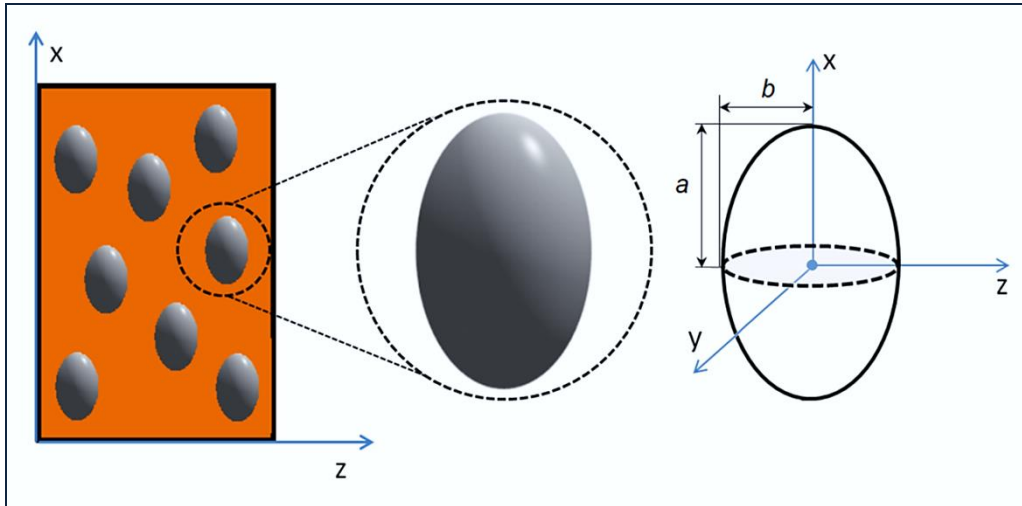


Fig. II.2. Schematic of a spheroidal metallic inclusion whose axis of symmetry is aligned parallel to the x -axis. The semi-dimensions of the spheroid are equivalent in the y and z directions.

Due to the spheroidal shape of the metal inclusions and their uniform orientation, the overall nanocomposite exhibits optical anisotropy. Here we consider spheroids whose axis of symmetry (polar axis, which is also the long axis for a prolate spheroid) is aligned parallel to the x -axis with a being their semi-dimension along this axis. The semi-dimension of the spheroid in the equivalent y and z directions, or equatorial radius, is denoted b . In this case the nanocomposite medium presents a uniaxial symmetry, and its effective relative permittivity is represented in the (xyz) system of coordinates by a diagonal (3×3) matrix with elements $\varepsilon_x = \varepsilon_{//}$ and $\varepsilon_y = \varepsilon_z = \varepsilon_{\perp}$ (the subscripts $//$ and \perp refer to two specific orientations of the electric field vector of the electromagnetic wave: parallel and perpendicular to the polar axis of the metallic NPs, respectively). In the frame of the Maxwell Garnett model these components can be calculated using the following expression (which can be obtained from Eq. I.39 in Chapter I):

$$\varepsilon_{\perp,\parallel} = \varepsilon_m \left(1 + \frac{\eta(\varepsilon_p - \varepsilon_m)}{\varepsilon_m + (1-\eta)(\varepsilon_p - \varepsilon_m) g_{\perp,\parallel}} \right), \quad (\text{II.1})$$

where ε_m and ε_p are the relative scalar permittivities of the materials forming the semiconducting matrix and the metallic inclusions, and $g_{\perp,\parallel}$ are geometric factors that account for the effect of the shape of the NPs on the dipole momentum induced in the NPs by the electromagnetic wave. These factors can be deduced from the ratio $\xi = a/b$ of the equatorial semi-axis b to the polar semi-axis a of the spheroidal inclusions as follows (see Eq. I.38):

$$g_{\parallel} = \frac{1}{1-\xi^2} \left(1 - \xi \frac{\arcsin \sqrt{1-\xi^2}}{\sqrt{1-\xi^2}} \right), \quad g_{\perp} = \frac{1}{2}(1 - g_{\parallel}). \quad (\text{II.2})$$

Note that $\xi > 1$ corresponds to prolate spheroid, whereas $\xi < 1$ corresponds to an oblate one. Different values of geometrical factors g_{\perp} and g_{\parallel} for non-spherical spheroids result in different behaviors of the relative permittivity tensor elements ε_{\perp} and ε_{\parallel} of the nanocomposite layer, which, in turn, will affect the polarization states of electromagnetic waves reflected from or transmitted through the composite layer.

The material forming the matrix of the nanocomposite is chosen to be the same as that of the layers A in the DBRs, so that $\varepsilon_m = \varepsilon_A$. To describe the spectral properties of the metallic NPs, the modified Drude model [15] was used, with:

$$\varepsilon_p(\omega) = \varepsilon_{\infty} - \frac{\omega_p^2}{\omega^2 + i\omega\gamma}, \quad (\text{II.3})$$

where ω_p is the plasmon frequency in the metal, ε_{∞} is the lattice contribution, and γ is a relaxation parameter (scattering rate).

Given that in the effective medium approximation the optical properties of the nanocomposite layer are defined by effective permittivity, to calculate the transmittivity and reflectivity of the layer and those of the entire structure, one can use the transfer matrix formalism [16,17].

II.3. Results and discussion

II.3.1 Dependence of the permittivity spectra of the nanocomposite layer on its structural parameters

In this section, the influence of the shape of the NPs and their concentration in the composite layer is studied.

The metallic spheroidal inclusions are made of silver (Ag) with the following parameters: plasmon frequency $\omega_p = 1.36 \times 10^{16} \text{ rad s}^{-1}$, $\epsilon_\infty = 5$, $\gamma = 3.04 \times 10^{13} \text{ rad s}^{-1}$ [18]. The aspect ratio ξ varies from 0 to 4, and the volume fraction η of the inclusions varies between 0.5×10^{-3} and 1.5×10^{-3} (i.e., 0.05% and 0.15%).

Let us first discuss the spectral properties of the nanocomposite layer. The calculated dependences of the real $\epsilon'_{\perp, //}$ and imaginary $\epsilon''_{\perp, //}$ parts of the nanocomposite effective permittivity tensor components on the wavelength in parts of the near-IR regime are shown in Figs. II.3(a) and II.3(b), respectively, in the case of the nanocomposite matrix (made of GaInAs) without amplification. The chromatic dispersion of GaInAs has been taken into account [19]. Here $\eta = 0.15\%$ and $\xi = 3.38$, the latter corresponding to a surface plasmon resonance wavelength around $\lambda_0 = 1550 \text{ nm}$ for the case when the polarization of the incoming light wave is parallel to the polar axis of the NPs. Note that in the remainder of this section we will particularly concentrate on wavelengths around 1550 nm because many fiber-optics-based optical devices used for optical telecommunications are designed for this specific region (telecom window).

Resonances are expected to appear in the spectral variations of $\epsilon''_{\perp, //}$ with a strong dependence upon the orientation of the long axis of the NPs with respect to the electric field vector of the electromagnetic wave [8,9]. Figure II.3 shows the spectral dispersion of the real and imaginary parts of the nanocomposite relative dielectric permittivities. It should be noted that positive values of imaginary parts $\epsilon''_{\perp, //}$ correspond to a damping of electromagnetic waves. One can see that the relative permittivity $\epsilon_{//}$ exhibits a resonant behavior at $\lambda_{//} = 1550 \text{ nm}$, which eventually leads to a significant dependence of the optical properties of the nanocomposite on the polarization of propagating waves. Due to the strong dispersion of the relative dielectric permittivity of the matrix of the nanocomposite layer, it is not possible to observe a resonance for ϵ_{\perp} for the chosen set of parameters, in particular aspect ratio

$\xi = 3.38$. The resonance peak for ε_{\perp} lies in the visible part of the spectrum, but its amplitude is small compared to the large values of absorption in the matrix.

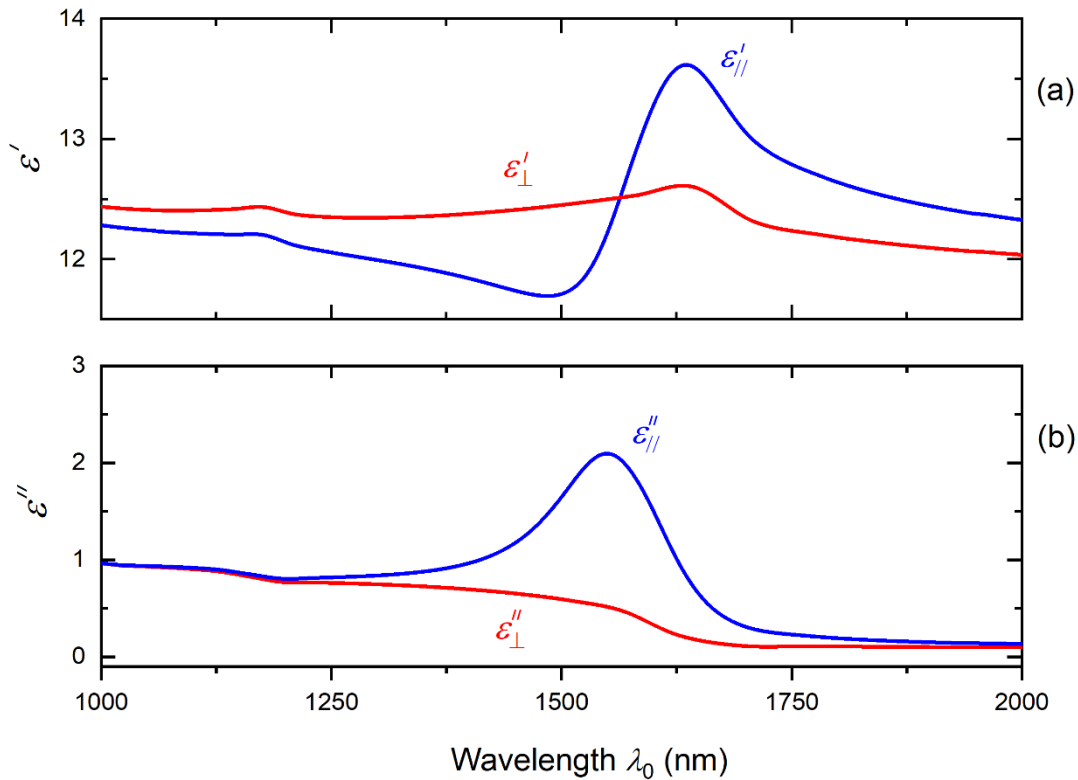


Fig. II.3. Spectral dispersion of the nanocomposite effective permittivity tensor components: (a) real parts $\varepsilon'_{\perp, \parallel}$; (b) imaginary parts $\varepsilon''_{\perp, \parallel}$ in the case of a non-amplifying nanocomposite matrix. The red and blue lines correspond to ε_{\perp} and ε_{\parallel} components, respectively. The aspect ratio of the NPs is $\xi = 3.38$.

The control of the amplitude of the plasmon resonance peak can be achieved by adjusting the volume fraction η of the NPs in the composite. Fig II.4 shows the spectral dispersion of the imaginary part of the nanocomposite effective permittivity, in the case of a non-amplifying nanocomposite matrix, as a function of η . Right and left panels correspond to the cases where light is linearly polarized along the x and y axis, respectively.

On the right panel we can see that an increase of the volume fraction of the inclusions increases the amplitude of the plasmon resonance of ε_{\parallel} , which in turn leads to increasing absorption and reflection factors of the composite layer. Thus, η can be used as a parameter for adjustment of the amplitude of the plasmon resonance peak. The position of that resonance can be also slightly affected by the value of the volume fraction of the NPs in the

composite layer, but due to the fact that small values of η were considered, the excursion of that position around 1550 nm is negligibly small. As was mentioned above, no plasmon resonance for ε_{\perp} appears in this spectral domain for this particular value of the aspect ratio, as can be seen on the left panel.

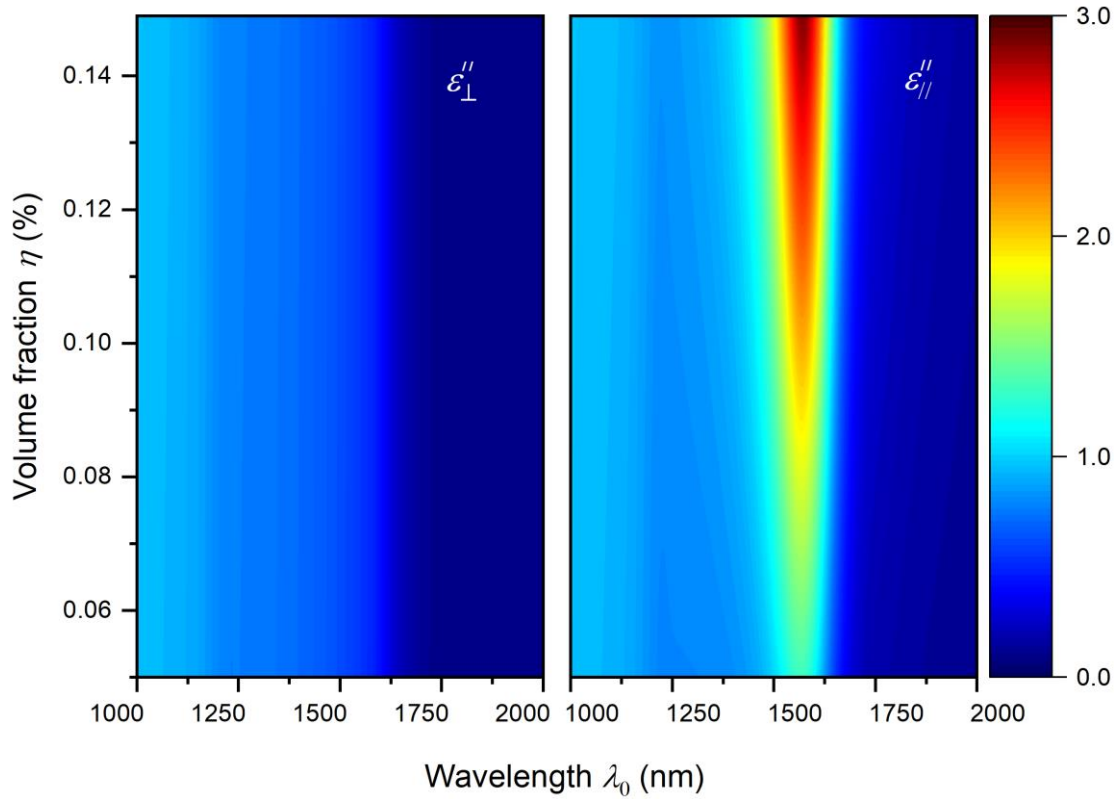


Fig. II.4. Spectral dispersion of the imaginary part of the nanocomposite effective permittivity in the case of a non-amplifying nanocomposite matrix as a function of the volume fraction η of NPs in the composite. Left and right panels correspond to ε_{\perp} and ε_{\parallel} , respectively. The aspect ratio of the NPs is $\xi = 3.38$.

Another possible way to control the plasmon resonance is to adjust aspect ratio ξ of the NPs. Fig II.5. represents the spectral dispersion of the imaginary part of the nanocomposite effective permittivities ε_{\perp} and ε_{\parallel} in the case of a non-amplifying nanocomposite matrix as a function of ξ .

For spherical NPs ($\xi = 1$), the wavelength of the plasmon resonances will be the same for any polarization state of the incoming light. For non-spherical particles ($\xi \neq 1$), both resonances can appear in the spectral range from 1 μm to 2 μm . The plasmon resonance for

$\varepsilon_{//}$ shifts towards higher wavelengths and becomes broader with an increase of the aspect ratio of the NPs. At the same time, the resonance for ε_{\perp} drifts in the opposite direction. These behaviors are mostly a consequence of the dependence of ε_{\perp} and $\varepsilon_{//}$ on g_{\perp} and $g_{//}$ in Eq. (II.2).

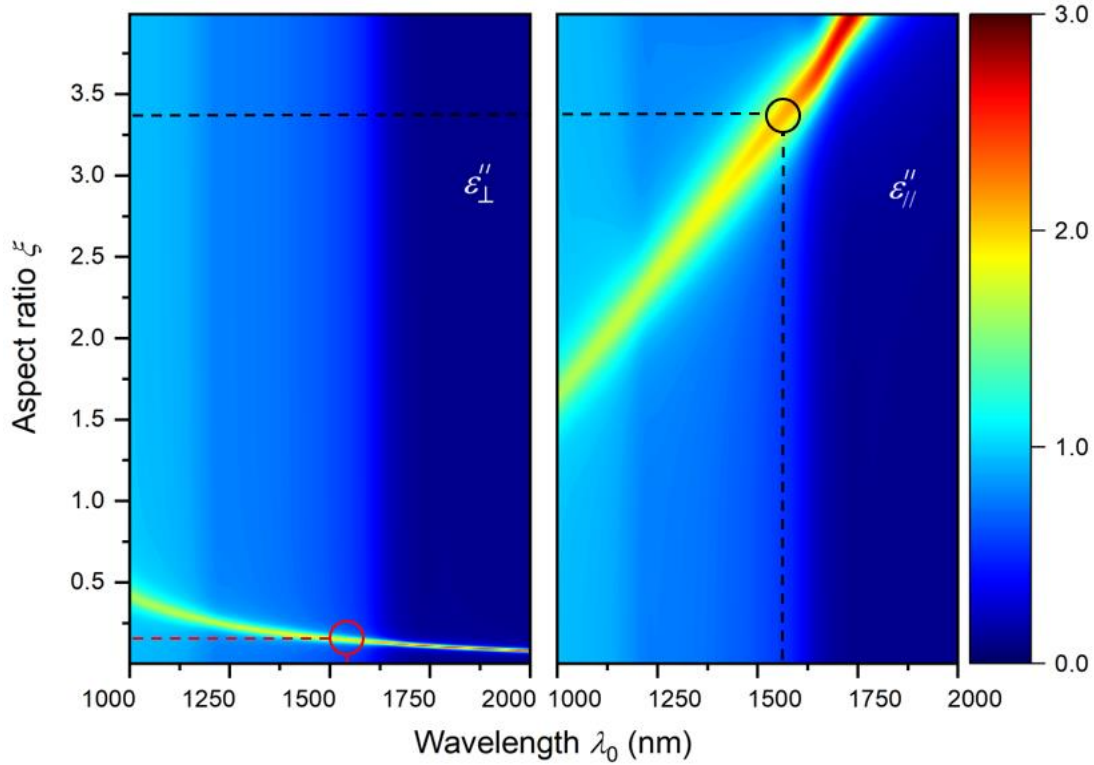


Fig. II.5. Spectral dispersion of the imaginary part of the nanocomposite effective permittivity in the case of a non-amplifying nanocomposite matrix as a function of the aspect ratio ξ of the NPs. Left and right panels correspond to ε_{\perp} and $\varepsilon_{//}$, respectively. The dashed lines correspond to $\lambda_0 = 1550$ nm. The volume fraction of the NPs is $\eta = 0.1\%$.

The dashed lines in Fig. II.5 indicate the values of aspect ratio ξ leading to maxima of the plasmon resonance peaks at 1550 nm. The black circle on the right-hand panel corresponds to a resonance of $\varepsilon_{//}''$ for a prolate spheroidal shape of the NPs ($\xi = 3.38$), whereas the red circle on the left-hand panel shows a resonance of ε_{\perp}'' for an oblate, almost disk-like, shape ($\xi \approx 0.18$).

II.3.2 Transmission spectra of the amplifying photonic crystal with a nanocomposite defect layer

In this section, the influence of the aspect ratio and volume fraction of the NPs on the spectral properties of the entire photonic structure is studied.

For the numerical calculations, let us assume layer A to be GaInAs and layer B to be GaAs. The imaginary parts of the relative dielectric permittivities of these materials are $\varepsilon_A'' = \varepsilon_B'' = -0.007$ [20]. In the narrow spectral domain under study in this Section, the spectral variations of these parameters can be neglected.

The thicknesses of the layers of the PC are $d_A = 108.5$ nm and $d_B = 111.6$ nm, and the nominal thickness of the defect nanocomposite layer is $d_{NC} = 2d_A$ (this specific choice will be discussed later). The number of periods of the PC on each side of the defect layer is $N = 100$. Thus, the thickness of the whole structure is approximately 44.24 μm . With these structural parameters a photonic bandgap appears in the region between 1550 nm and 1590 nm. Fig. II.6. represents the transmittivity spectra around the photonic bandgap for amplifying and non-amplifying PC layers and a defect layer without NPs.

The blue line in panel (a) represents the transmittivity of the structure without amplification. In this case we have a well-pronounced defect mode at 1568 nm and the edges of the bandgap at 1550 nm and 1587 nm. The red line in panel (a) is truncated to $T = 100$ and correspond to the case of the structure with amplifying reflectors. The exact values are shown in panel (b) in semi-logarithmic scale. As we can see, the amplitude of the defect mode is noticeably reduced, since the presence of amplification modifies the interference condition for forward and backward waves in the structure, but the peaks at the edges of the bandgap are significantly amplified. It is important to note that in such a distributed-feedback active cavity, light generation would take place at the frequency of an amplified photonic bandgap edge [21]. In what follows, we will concentrate on the study of the transmittivity spectrum of the photonic structure in the vicinity of its low-wavelength bandgap edge.

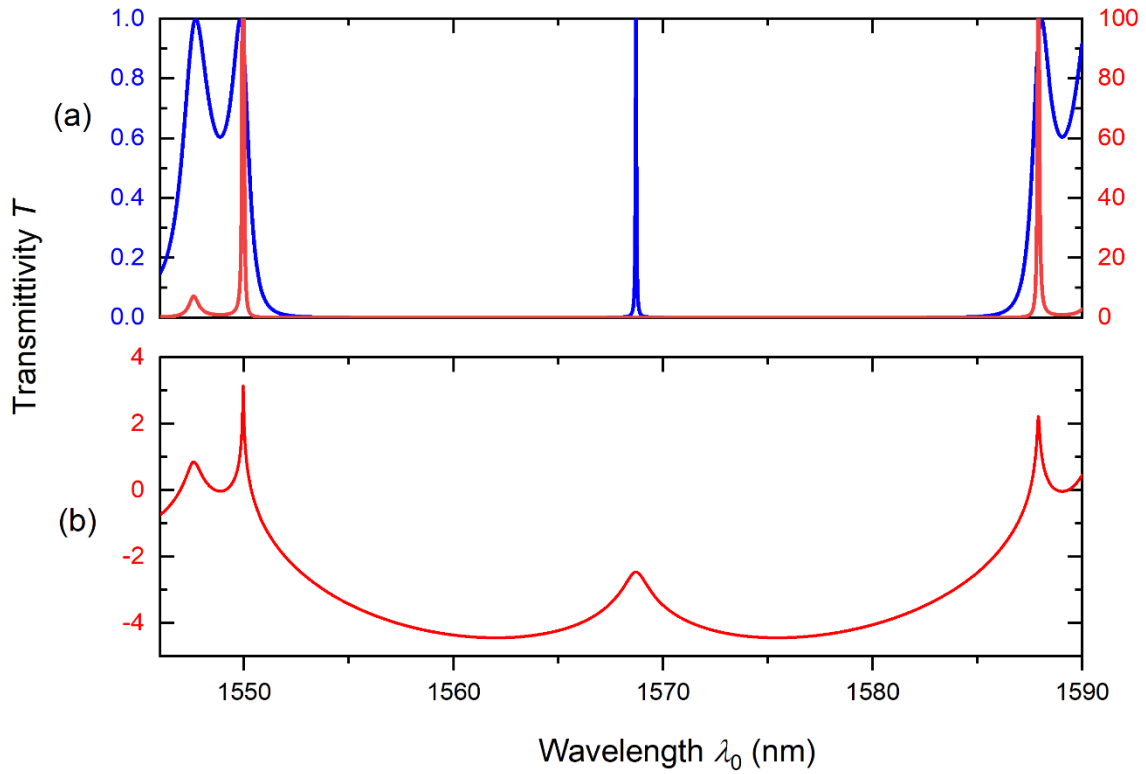


Fig. II.6. Transmittivity spectra around the photonic bandgap when the defect layer does not include NPs. Results are obtained for amplifying (red line) and non-amplifying (blue line) PC layers (panel (a)). Note the different vertical scale for the red and blue curves. The transmittivity values with amplification are limited to $T = 100$ in panel (a). Panel (b) represents the transmittivity spectrum in semi-logarithmic scale with amplification in the PC layers.

When no NPs are present in the defect layer T exhibit an identical abrupt increase at $\lambda_0 = 1550$ nm for any polarization state, *i.e.*, both components of the incoming optical electric field are equally amplified (along the x - and y -axes), and the structure does not affect the polarization state of light.

When metallic spheroids are present in the defect layer, an anisotropic element is included in the system, and the situation changes drastically for the T_{\parallel} component. Figure II.7 represents the transmittivity spectra T_{\parallel} and T_{\perp} of the structure in the vicinity of the low-wavelength photonic bandgap edge in the cases when the defect layer includes NPs. The volume fraction of the NPs is $\eta = 0.1\%$, and the aspect ratio is $\xi = 3.38$, which ensures a

plasmon resonance for $\varepsilon''_{\parallel}$ around 1550 nm. Hereafter we will focus on a small fraction of the wavelength region considered above, in the vicinity of 1550 nm.

The damping of the field component parallel to polar axis of NPs (*i.e.* along the x -axis) is strong in the vicinity of $\lambda_0 = 1550$ nm due to resonance of $\varepsilon''_{\parallel}$ (see Fig. II.3) and cancels the amplification of the PC layers and thus prevents the amplification of this component of the electromagnetic wave and slightly shifts the mod. On the other hand, ε''_{\perp} is much smaller around λ_0 , as shown in Fig. II.3(b), so that T_{\perp} almost does not change and amplification takes place (red line in Fig. II.7). As was mentioned before, ε'' which is responsible for damping of the wave component, depends on the volume fraction of the inclusions and its shape. Increase of the volume fraction of the inclusions increases the amplitude of the peak of the imaginary part of the effective permittivity at the position of the plasmon resonance, which results in decreased transmission of the structure.

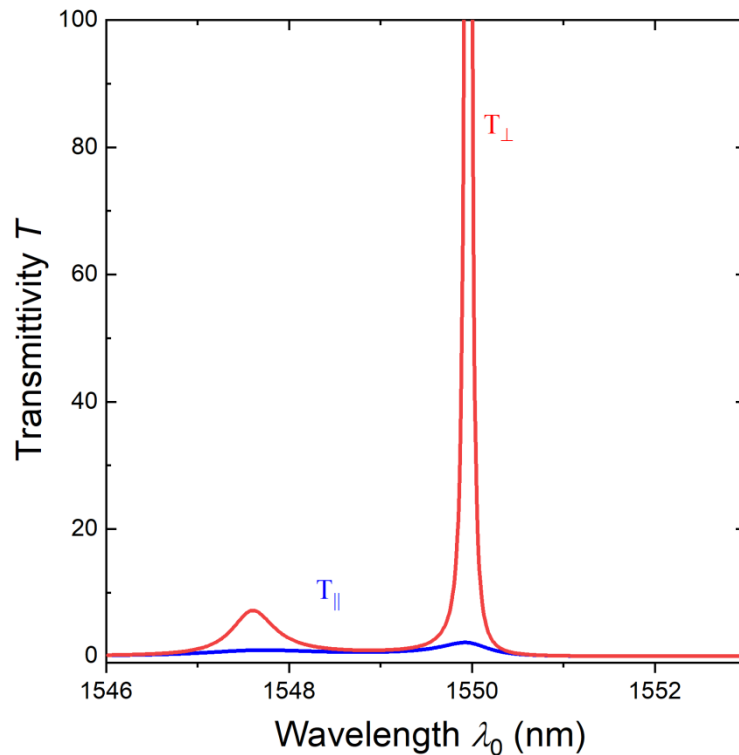


Fig. II.7. Transmittivity spectra T_{\parallel} (blue curve) and T_{\perp} (red curve) of the structure in the vicinity of the low-wavelength photonic bandgap edge when the defect layer incorporates NPs. The results are taking into account amplification in the PC layers. The aspect ratio of the NPs is $\xi = 3.38$, and the volume fraction is $\eta = 0.1\%$.

Fig. II.8 shows transmittivity spectra T_{\parallel} (incident light polarized along the x axis) and T_{\perp} (incident light polarized along the y axis) of the structure in the vicinity of the low-wavelength edge of the photonic bandgap as a function of the volume fraction η of the NPs for a fixed aspect ratio $\xi = 3.38$.

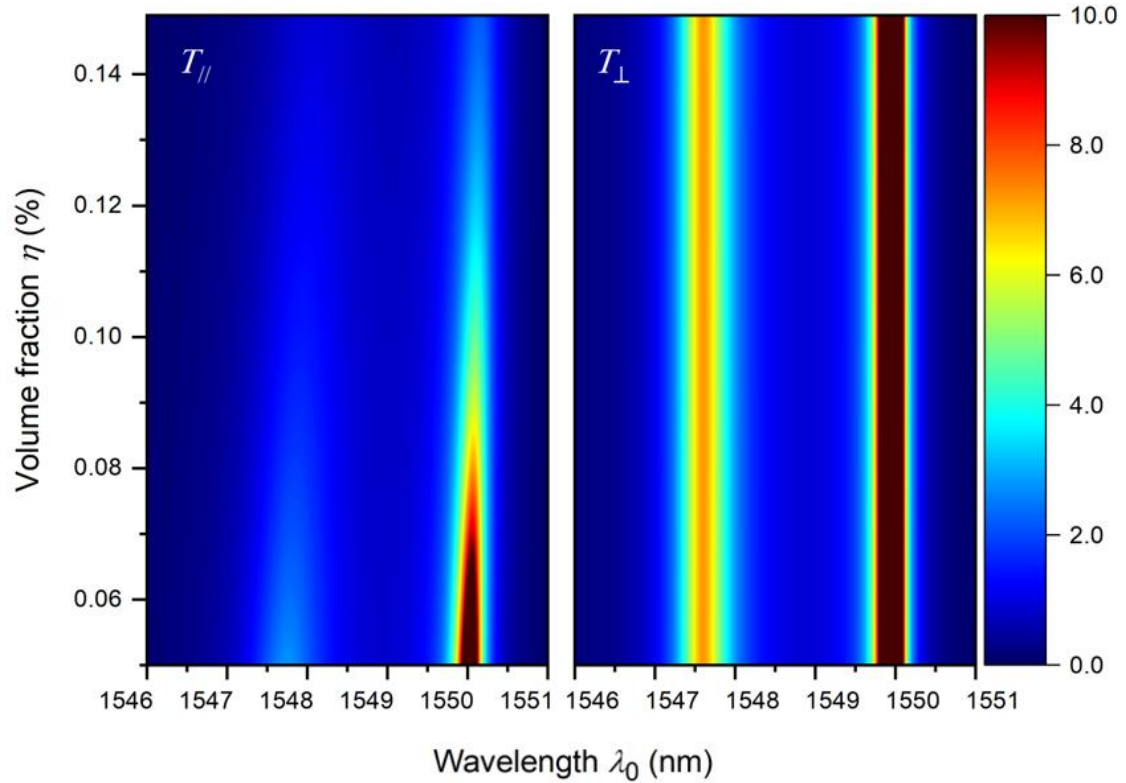


Fig. II.8. Transmittivity spectra T_{\parallel} (left panel) and T_{\perp} (right panel) of the structure in the vicinity of the low-wavelength photonic bandgap edge as a function of the volume fraction η of the NPs. Results are obtained accounting for the amplification in the PC layers. The aspect ratio of the inclusions is $\xi = 3.38$.

Another factor that can be used for the control of the suppression of the amplification of the bandgap edge is the shape of the NPs. For an effective suppression, the plasmon resonance must overlap the bandgap edge around $\lambda_0 = 1550$ nm. It means that the aspect ratio of the inclusions must be in the vicinity of $\xi = 3.38$ (see Fig. II.5). In other cases, there will be no suppression. Fig. II.9 shows the transmittivities T_{\parallel} and T_{\perp} of the structure in the vicinity of that low-wavelength photonic bandgap edge as a function of the aspect ratio ξ of the NPs. We can see a gap in the aspect ratio, in the vicinity of $\xi = 3.38$, for which the transmittivity

for the x -polarized incoming light is suppressed with a slight shift of the amplified bandgap edge due to the spectral dispersion of $\varepsilon_{\parallel}''$ (see right panel in Fig. II.5).

As a criterium for the measurement of the width of the gap in the transmittivity spectrum of the structure, we define its boundaries to correspond to 10% of the transmission peak maximum. It must also be mentioned here that the volume fraction of the inclusions is an important parameter for the width of the gap as well. In the considered case the value of the volume fraction of the inclusions is equal to 0.1%. For the chosen parameters the width of the gap will be around 0.45, with its center approximately at $\xi = 3.38$. This gap width gives a tolerance range for the variation of the shape of the NPs in order to keep observing an efficient suppression of the mode.

At the same time, due to the absence of plasmon resonance for the y -polarized incoming light, the T_{\perp} transmittivity spectrum remains the same for all aspect ratios in the considered wavelength region (Fig. II.9, right panel).

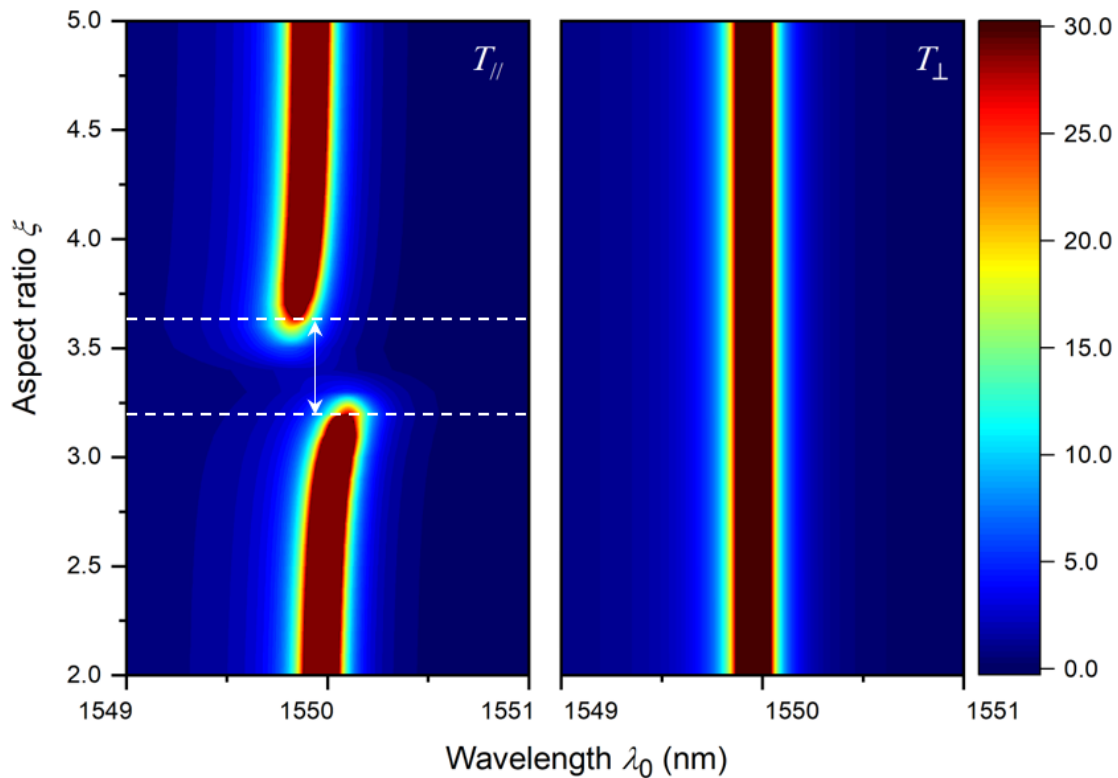


Fig. II.9. Transmittivity spectra T_{\parallel} (left panel) and T_{\perp} (right panel) around the low-wavelength photonic bandgap edge as a function of the aspect ratio of the NPs for two different polarization states of the incoming wave. Results are obtained accounting for the amplification in the PC layers. The volume fraction of the NPs is $\eta = 0.1\%$.

Figure II.10 shows the dependence of the aspect ratio gap width for T_{\parallel} on the value of the volume fraction η of the metallic inclusions in the defect layer. As we can see, the increase of η leads to a broadening of the gap in the aspect ratio (0.23, 0.45 and 0.54 for $\eta = 0.05\%$, 0.1% and 0.15% , respectively). It can be explained by the broadening of the plasmon resonance peak when η increases (see Fig. II.4).

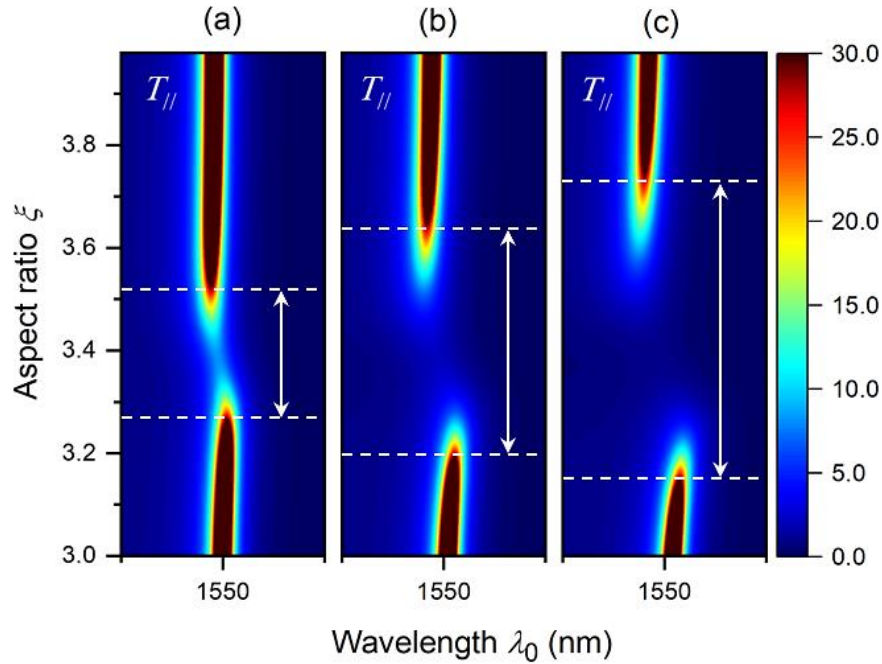


Fig. II.10. Transmittivity spectrum for the case when incoming light is polarized along the polar axis of the NPs around the low-wavelength photonic bandgap edge as a function of the aspect ratio of the NPs for different cases of the volume fraction of the inclusions in the nanocomposite (0.05%, 0.1% and 0.15% as (a), (b) and (c) respectively).

Figure II.11 represents the transmittivities T_{\parallel} and T_{\perp} at 1550 nm as functions of the volume fraction η and the aspect ratio ξ of the inclusions in the nanocomposite layer. Left and right panels correspond to the cases when light is polarized along the x - and y -axes, respectively. For clarity, some iso-transmittivity lines are shown.

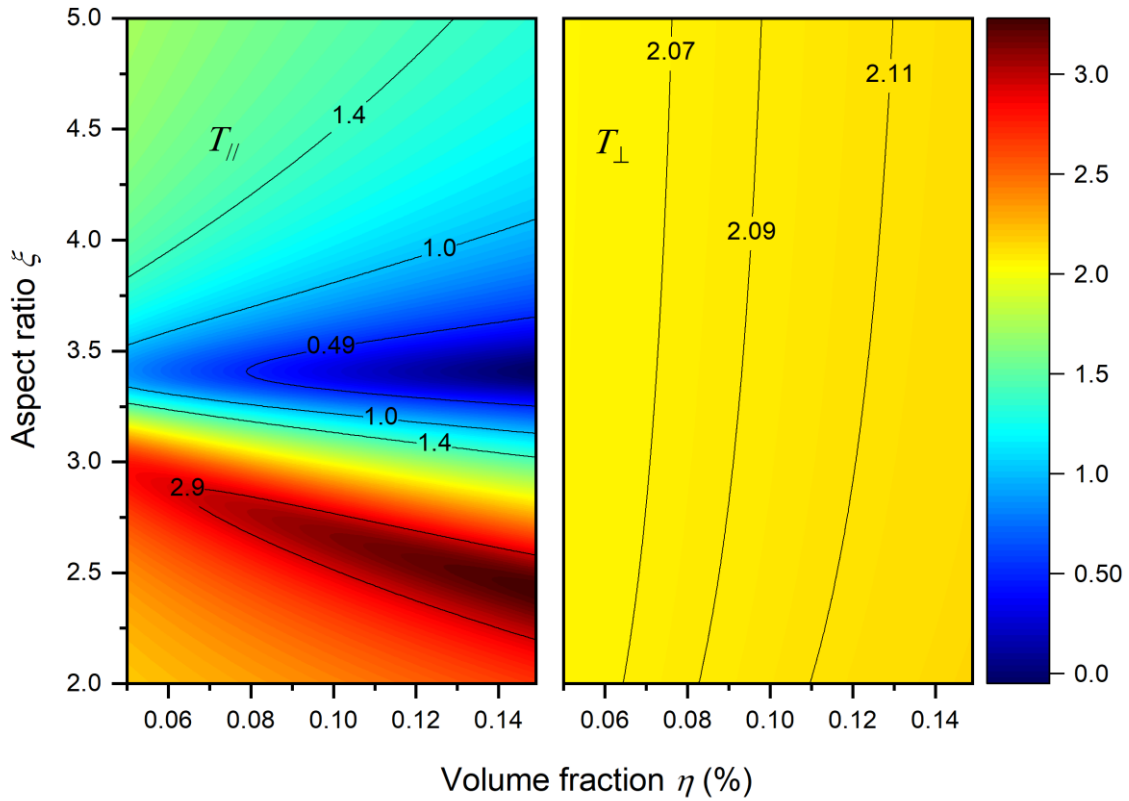


Fig. II.11. Transmittivity value as function of the volume fraction and the aspect ratio of the NPs at the 1550 nm (edge of the photonic bandgap) for two different polarizations in semi-logarithmic scale. Left and right panels correspond to the cases when incoming light is polarized along the polar axis of the NPs and perpendicular to it respectively.

For light polarized along the x axis we can see that suppression is efficient ($\log|T| < 1$) for an aspect ratio in the vicinity of 3.4 (blue zone on Fig. II.11, left panel). In that region we can also see that an increase of the volume fraction of the inclusions leads to an increase of the width and amplitude of the plasmon resonance peak (see Fig. II.4), which in turn results in a broadening of the aspect ratio range (see Fig. II.10) for which efficient suppression of the amplified mode can be achieved (the blue zone becomes wider). For light polarized along the y axis (Fig. II.11, right panel) the edge of the bandgap remains almost unchanged due to the fact that for the range of aspect ratios considered here the corresponding peak of the plasmon resonance is located in the visible part of the spectrum, as was discussed above.

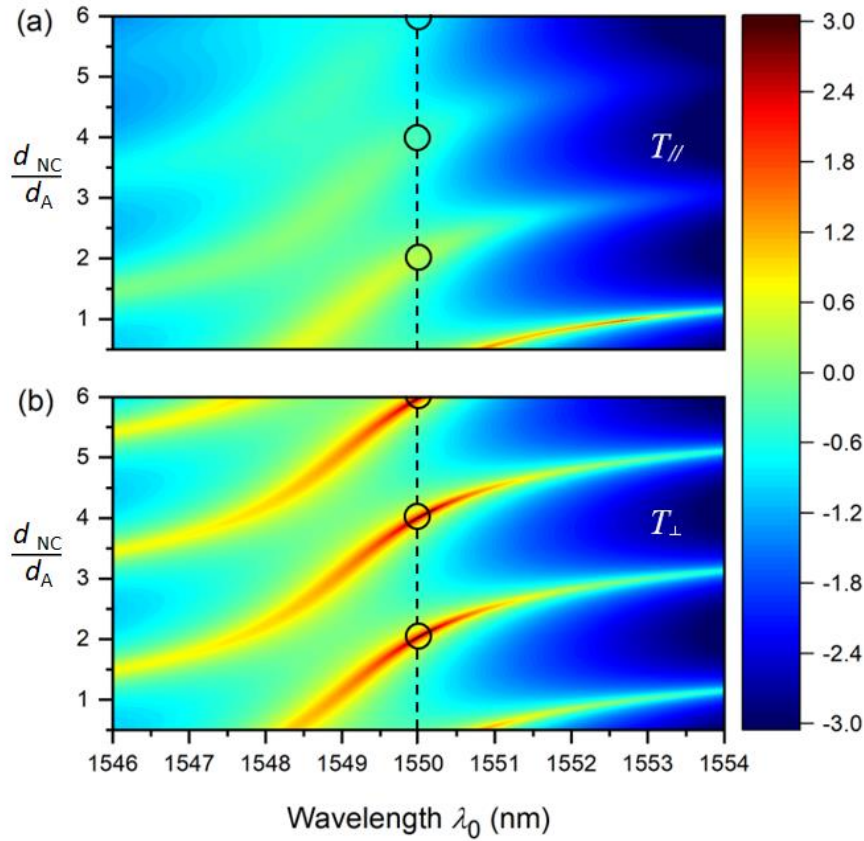


Fig. II.12. Transmittivity spectrum (in semi-logarithmic scale) around the low-wavelength photonic bandgap edge as a function of the reduced thickness d_{NC}/d_A of the nanocomposite layer for light polarized along the x (top panel) and y (bottom panel) axes. The aspect ratio of the NPs is $\xi = 3.38$, and the volume fraction is $\eta = 0.1\%$. The dashed vertical lines correspond to the working wavelength 1550 nm, and the circles correspond to the modes at 1550 nm.

A third parameter that can be used for the adjustment of the system response is the thickness of the nanocomposite defect layer. By changing that thickness, we can modify not only the position of the defect mode (as will be discussed, for instance, in the frame of Chapter IV) but also the amplitude and position of the peaks at the photonic bandgap edges. Transmittivity spectrum of the photonic crystal around its low-wavelength photonic bandgap edge (in the vicinity of 1550 nm) as a function of the reduced thickness d_{NC}/d_A of the nanocomposite layer is shown in Fig. II.12. The top and bottom panels represent the cases when light is polarized along the x and y axes, respectively.

In the picture, we can see the repetitive, periodic pattern of the peaks. Due to the fact that the concentration of NPs in the composite layer is small, and thus the real parts of the

permittivities of that layer and of layer A are almost identical, the peaks are positioned exactly at 1550 nm (black circles in Fig. II.12) for $d_{\text{NC}}/d_{\text{A}} \approx 2l$, $l \in \mathbb{N}^*$, as expected from the Bragg condition. The more the thickness of the composite layer increases, the more the transmittivity peak $T_{//}$ decreases due to absorption in the nanocomposite. This mostly affects the case of x -polarized light (Fig. II.12, top panel) due to the presence of the plasmon resonance peak at 1550 nm. As a result, a good compromise between an efficient suppression of transmittivity $T_{//}$ and high enough values of transmittivity T_{\perp} needs to be found. For that reason, the choice was made to take in this entire chapter $l = 1$, i.e. $d_{\text{NC}}/d_{\text{A}} = 2$, as mentioned above.

II.4. Conclusions

- The photonic structure studied in this chapter is a symmetric photonic crystal microcavity consisting of two distributed Bragg reflectors and a nanocomposite layer placed between them. The nanocomposite layer consists of a semiconducting material, or matrix, hosting uniformly distributed metallic NPs of spheroidal shape and identical orientations.
- The dependence of the spectral characteristics of the nanocomposite layer on the aspect ratio and volume fraction of the metallic inclusion was shown.
- The dependence of the spectral characteristics of the structure on the aspect ratio, volume fraction of the metallic inclusion and thickness of the nanocomposite layer was shown.
- It was established that mode discrimination of the structure can be achieved separately for different polarization direction of the light wave due to the anisotropy of the absorption of the nanocomposite layer.
- Thus, it was shown, that an addition of the nanocomposite layer with ellipsoidal inclusions allows separation of the polarization states of the electromagnetic waves in PC with amplification.
- Results obtained in this Chapter can be used in compact semiconductor lasers with a vertical cavity resonator working in optical and near-infrared regimes, or vertical cavity surface-emitting lasers.

II.5. List of references

- [1] J.D. Joannopoulos, S.G. Johnson, J.N. Winn, R.D. Meade, *Photonic Crystals: Molding the Flow of Light, second ed.* (Princeton University Press, Princeton, New York, 2008).
- [2]. C. Sibilia, T.M. Benson, M. Marciniak, T. Szoplik (Eds.), *Photonic Crystals: Physics and Technology* (Springer-Verlag, Milan, 2008).
- [3] S.F. Yu, *Analysis and Design of Vertical Cavity Surface Emitting Lasers* (Wiley, Hoboken, New Jersey, 2003).
- [4] C.W. Wilmsen, H. Temkin, L.A. Coldren (Eds.), *Vertical-Cavity Surface-Emitting Lasers: Design, Fabrication, Characterization, and Applications* (Cambridge University Press, Cambridge, 1999).
- [5] H.G. Winful, "Polarization instabilities in birefringent nonlinear media: application to fiber-optic devices," *Opt. Lett.* **11**, 33-35 (1986).
- [6] N.I. Zheludev, "Polarization instability and multistability in nonlinear optics," *Sov. Phys. Uspekhi* **32**, 357-375 (1989).
- [7] S.G. Moiseev, "Nanocomposite-based ultrathin polarization beamsplitter," *Opt. Spectrosc.* **111**, 233-240 (2011).
- [8] S.G. Moiseev, "Thin-film polarizer made of heterogeneous medium with uniformly oriented silver nanoparticles," *App. Phys. A* **103**, 775-777 (2011).
- [9] S.G. Moiseev, V.A. Ostatochnikov, D.I. Sementsov, "Defect mode suppression in a photonic crystal structure with a resonance nanocomposite layer," *Quant. Electron.* **42**, 557-560 (2012).
- [10] S.G. Moiseev, V.A. Ostatochnikov, D.I. Sementsov, "Influence of size effects on the optical characteristics of a one-dimensional photonic crystal with a nanocomposite defect," *JETP Lett.* **100**, 371-375 (2014).
- [11] S.Ya. Vetrov, P.S. Pankin, I.V. Timofeev, "Peculiarities of spectral properties of a one-dimensional photonic crystal with an anisotropic defect layer of the nanocomposite with resonant dispersion," *Quant. Electron.* **44**, 841-844 (2014).
- [12] V. Lozovski, M. Razumova, "Influence of inclusion shape on light absorption in thin Au/Teflon nanocomposite," *J. Opt. Soc. Am. B* **33**, 8-16 (2016).
- [13] U. Kreibitz, M. Vollmer, *Optical Properties of Metal Clusters* (Springer, Berlin, 1995).
- [14] J.E. Spanier, I.P. Herman, "Use of hybrid phenomenological and statistical effective-medium theories of dielectric functions to model the infrared reflectance of porous SiC films," *Phys. Rev.* **61**, 10437-10450 (2000).
- [15] W. Cai, V. Shalaev *Optical Metamaterials* (Springer, New York, 2009).
- [16] D.W. Berreman, "Optics in stratified and anisotropic media: 4×4 matrix formulation," *J. Opt. Soc. Am.* **62**, 502-510 (1972).
- [17] Yu.S. Dadoenkova, N.N. Dadoenkova, I.L. Lyubchanskii, D.I. Sementsov, "Reshaping of Gaussian light pulses transmitted through one-dimensional photonic crystals with two defect layers," *Appl. Opt.* **55**, 3764-3770 (2016).
- [18] P.B. Johnson, R.W. Christy, "Optical Constants of Noble Metals," *Phys. Rev.* **6**, 4370-4379 (1972).

- [19] S. Adachi. “*Optical dispersion relations for GaP, GaAs, GaSb, InP, InAs, InSb, Al_xGa_{1-x}As, and In_{1-x}Ga_xAs_yP_{1-y},*” J. Appl. Phys. **66**, 6030-6040 (1989).
- [20] P.P. Vasil'ev, “*Role of a high gain of the medium in superradiance generation and in observation of coherent effects in semiconductor lasers,*” Quant. Electron. **29**, 842–846 (1999).
- [21] A. Yariv, *Quantum electronics* (Wiley, New York, 1991).

CHAPTER III

POLARIZATION-SELECTIVE DEFECT MODE AMPLIFICATION IN A PHOTONIC CRYSTAL WITH INTRACAVITY 2D ARRAYS OF METALLIC NANOPARTICLES

III.1. Introduction

A metallic nanoparticle interacting with an electromagnetic wave can support a localized surface plasmon resonance that gives rise to a characteristic peak in its extinction spectrum [1]. When metallic NPs are arranged in 2D or 3D arrays, they can efficiently modify the amplitude and the phase of an electromagnetic wave whose frequency is close to the plasmon resonance of the NPs [2-5]. It has been shown that the optical properties of such NP arrays depend on such factors as the nature of the metal, the size, shape and surface/volume ratio of the NPs, as well as the periodicity of the array. The versatile plasmonic properties of metallic NP arrays have found many applications in the design of, among others, photonic crystals (PCs) [6-10], biological or medical sensors [11,12], antireflective coatings [13,14], or absorbers [15,16].

The polarimetric characteristics of light interaction with NP arrays have also been the topic of recent investigations [17-19]. For instance, the use of composite media with non-spherical metal inclusions has been shown to allow a polarization-sensitive control of the resonance modes of PC-based structures [20,21].

Such results can be useful in order to achieve a good control of the state of polarization of the radiation generated by vertical-cavity surface-emitting lasers (VCSELs), as such a control remains a topical research subject. Indeed, because of the inherent symmetry of the resonant cavities of VCSELs, the light waves they emit do not have a well-defined state of polarization [22]. This results in the emission of radiation with uncontrolled polarization states and in intensity instabilities. Various solutions have been put forward in order to eliminate such polarization-unstable behavior, notably inserting PCs, dielectric gratings, and plasmonic elements such as metallic films with nanoholes and metallic nanorod arrays in the aperture area of the VCSEL [23-28].

As is well known, PCs have been the subject of intensive theoretical and experimental investigations in the past decades because the control of electromagnetic waves they provide can find many applications in modern photonics and optoelectronics [29,30]. Artificial PCs are one-, two-, or three-dimensional (1D, 2D, or 3D) structures that exhibit a periodic modulation of their permittivity and/or permeability (*e.g.*, through the alternate juxtaposition of materials with different refractive indices). The interaction between counterpropagating waves in such structures ensures the existence of their most prominent feature, photonic bandgaps in their transmittivity spectra, *i.e.*, spectral domains for which the transmittivity is vanishingly small and the incident radiation is almost totally reflected. It is also well known that introducing elements into the PC that destroy their periodicity leads to the appearance of narrow peaks of high transmittivity (so-called defect modes) at frequencies located

inside the photonic bandgap. In the previous Chapter, I demonstrated the possibility of polarization-selective amplification in a 1D PC *via* the use of an embedded composite film as a defect layer, consisting of an amplifying medium with prolate metallic inclusions. In that case, polarization selectivity was achieved due to the different absorption of the electromagnetic wave depending on the relative orientation of the anisotropy axes of the inclusions and the polarization direction of the wave.

In this Chapter, I intend to show that a control of the polarization of an amplified defect mode transmitted through an active multilayered PC can be obtained by introducing one or several ordered 2D arrays of metallic (silver) NPs at well-chosen locations in the structure. The spectral and polarimetric characteristics of the heterostructure are calculated using the transfer matrix formalism, in which an embedded 2D NP array is associated with a matrix whose polarization-dependent elements are obtained within the frame of the coupled-dipole approximation approach. The influence of the geometry and location of the NP array(s) on the efficiency of polarization-selective defect mode amplification are discussed.

The Chapter is organized as follows. Section III.2 presents the geometry of the photonic structure and defines its material parameters. In Section III.3, the positioning of a 2D array of NPs in the structure is discussed. The numerical simulations of the spectral characteristics of the sole NP array are discussed in Section III.4. The numerical simulations of the spectral characteristics of the whole structure are then presented in Section III.5, and Section III.6 summarizes the conclusions of this Chapter.

III.2. Geometry of the structure

Let us first consider the photonic structure without NP arrays. It is composed of two distributed Bragg reflectors (DBRs) surrounding a composite microcavity (Fig. III.1). The DBRs are made of N unit cells (AB) and (BA), respectively, where A and B are layers of non-magnetic dielectric isotropic materials. The microcavity, denoted (CDC), consists of an active (amplifying) region D sandwiched between two identical non-magnetic dielectric layers C . The active region ensures the amplification of electromagnetic waves propagating through the structure, which is surrounded by vacuum.

In the following, an incident plane wave in the near-infrared regime impinges under normal incidence on the left-hand side of the structure, at abscissa $z=0$ of a Cartesian coordinate system whose z -axis is perpendicular to the interfaces of the system. As in the previous chapter, the time dependence of the electromagnetic fields is taken as $\exp(-i\omega t)$, where $\omega=2\pi c/\lambda_0$ is the angular frequency of the incoming plane wave of wavelength in vacuum λ_0 . The dimensions of the layers along the x - and y -axes are much larger than their thicknesses along the z -axis, and are thus taken to be

infinite in the calculations.

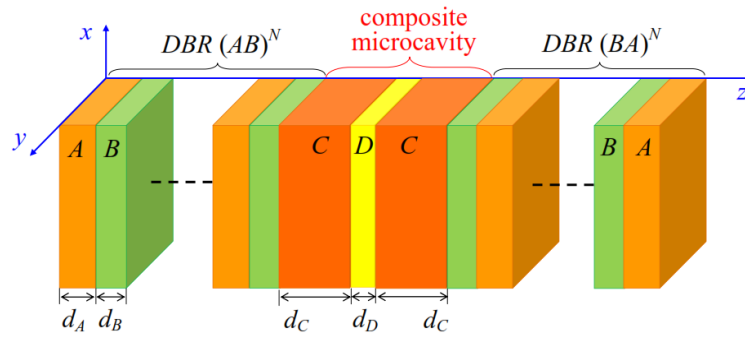


Fig. III.1. Schematic of the structure: two DBRs $(AB)^N$ and $(BA)^N$ are separated by a composite microcavity consisting of an amplifying layer D surrounded by two identical cladding layers C .

Layers A and B (with thicknesses d_A and d_B , respectively) are made of isotropic, non-magnetic semiconductor materials GaAs and AlAs. Their thicknesses d_A and d_B satisfy the Bragg condition of resonant reflection at vacuum wavelength $\lambda_{Br} = 1550$ nm:

$$d_A \sqrt{\text{Re}[\varepsilon_A]} = d_B \sqrt{\text{Re}[\varepsilon_B]} = \frac{\lambda_{Br}}{4} = 387.5 \text{ nm}. \quad (\text{III.1})$$

Each DBR consists of $N = 20$ GaAs/AlAs bilayers. As is well-known, in the absence of the (CDC) microcavity, the transmission spectrum of the PC formed by the juxtaposition of those DBRs exhibits a photonic bandgap with a peak of transmittivity, or defect mode, centered on wavelength $\lambda_{Br} = 1550$ nm because the central layer of a $(AB)^N(BA)^N$ PC (a defect layer with thickness $2d_B$), breaks the periodicity of the structure. Similarly, the presence of a defect layer consisting of the (CDC) microcavity typically introduces one or several defect modes inside the photonic bandgap. Here, the cavity consists of two identical GaAs cladding layers surrounding an active region with an overall thickness d_D . The active region is a GaAs-based multiple quantum well VCSEL in which four $\text{Ga}_{0.591}\text{In}_{0.409}\text{N}_{0.028}\text{As}_{0.89}\text{Sb}_{0.08}$ quantum wells are separated by $\text{GaN}_{0.047}\text{As}$ barrier layers, similar to that described in Ref. [31]. In our calculations, it will be considered as an equivalent layer with effective permittivity ε_D . Specifically, the constitution of the microcavity and its thickness are chosen such that it introduces a single defect mode centered on wavelength $\lambda_0 = 1550$ nm. The values of the material parameters and layer thicknesses used for our calculations are gathered in Table III.1.

In comparison with what was described in Chapter II, here the principle of a plasmonic polarizer is based on the use of one or several monolayers of metallic NPs, *i.e.*, 2D array(s) of NPs instead of a 3D bulk nanocomposite.

Medium		Permittivity at $\lambda_0 = 1550 \text{ nm}$		Layer thickness (nm)	
Layer A (GaAs)		$\varepsilon_A \approx 11.255 + i0.027$ [34]		$d_A = 115.5$	
Layer B (AlAs)		$\varepsilon_B \approx 8.36$ [29]		$d_B = 134$	
Layer C (GaAs)		$\varepsilon_C \approx 11.255 + i0.027$ [34]		$d_C = 404$	
Active layer D	quantum well	$\varepsilon_D \approx 12.869 - i0.214$	13.610 [33]	$d_D = 104$	8 [33]
	barrier		12.557 [33]		24 [33]

Table III.1. Material permittivities and layer thicknesses used for the numerical calculations. If, as is the case here, the thicknesses of the layers composing the active region are much smaller than the radiation wavelength, the region *D* can be described with good accuracy by an average dielectric permittivity $\varepsilon_D = \varepsilon'_D + i\varepsilon''_D$ obtained within an effective medium approximation [32]. The amplification of an electromagnetic wave in this active equivalent layer, despite the optical absorption taking place in some of the layers of the structure, is described by $\varepsilon''_D < 0$.

In such 2D arrays, the NPs are arranged periodically with a square unit cell whose translational invariance is directed along the *x* and *y* axes of the Cartesian coordinate system (see Fig. III.1). As in the previous chapter (see Fig. II.2), all metallic NPs are assumed to have the same spheroidal shape and the same dimensions. In addition, all NPs are similarly aligned, with their polar axis parallel to the *x*-axis. Their dimensions are characterized by their aspect ratio $\xi = a/b$, where *a* and *b* are the half-lengths of their polar and equatorial axes, respectively. The typical dimensions of the NPs and the period *p* (interparticle distance) of the square lattice are supposed to be much smaller than the wavelength of the optical wave in the layers where the NP arrays are embedded, *i.e.*, $\{2a, 2b, p\} \ll \lambda_0 / \text{Re}[\sqrt{\varepsilon_m}]$, $m \in \{C, D\}$. Such a structure exhibits pronounced anisotropic optical properties, and its reflection and transmission spectra, in particular, are expected to depend significantly on the direction of polarization of the incident radiation [18,20].

III.3. Transfer matrix calculations

Let us consider and compare two different cases for the positioning of the 2D arrays (Fig. III.2). The first one has the NP array at the center of the active layer D , *i.e.*, the geometric center of the structure. In the second case, two identical NP arrays are embedded in the microcavity, one in each layer C , at a distance Δ from the center of the structure. The choice of the position(s) of the monolayer(s) will be discussed below (see Section III.4).

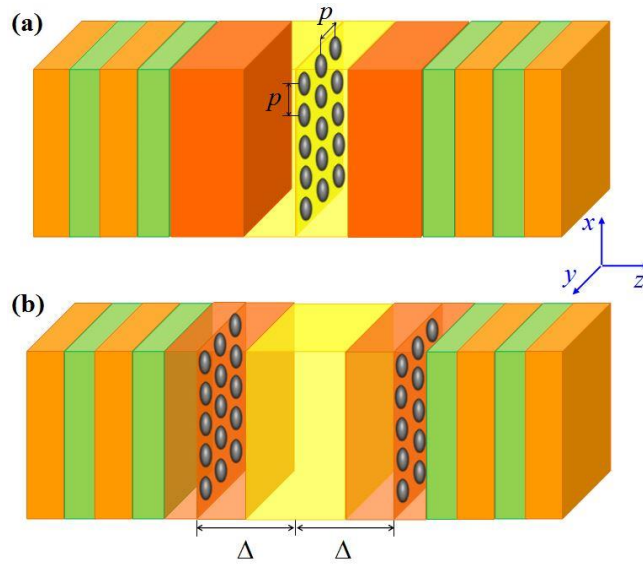


Fig. III.2. Schematic of the photonic structure with embedded 2D metallic NP arrays placed (a) at the center of the active region, and (b) on both sides of the active region at the distance Δ from its center. The period of the NP array is denoted p .

As in the previous Chapter, the transfer matrix formalism is used for the determination of the optical response of the structure.

In the first case, depicted in Fig. III.2(a), a total of $(4N + 4)$ layer-layer interfaces and one 2D array of NPs must thus be taken into account, as well as $(4N + 4)$ layers (note that the central D layer is divided in two identical sub-layers by the NP array).

In the second case (Fig. III.2(b)), the number of layer-layer interfaces again amounts to $(4N + 4)$, the number of 2D NP arrays to two, and the number of layers to $(4N + 5)$.

In both cases, the first and the last interfaces separate a layer A from the vacuum. Hereinafter, the interfaces (including the 2D array(s) of NPs) internal to the heterostructure are numbered by the integer index j (with $2 \leq j \leq 4N + 3$ in the first case, and $2 \leq j \leq 4N + 4$ in the second case) and the layers they separate are numbered $(j - 1)$ and j , following the positive direction of the z -axis.

Denoting L the total thickness of the system and applying Eqs. (I.6), (I.10) and (I.13) to the entire PC, the following relation between the amplitudes of the incident $E^{(i)} = E^{(f)}(0^-)$, reflected $E^{(r)} = E_b(0^-)$ and transmitted $E^{(t)} = E_f(L^+)$ optical fields is obtained:

$$\begin{pmatrix} E_{\perp, //}^{(i)} \\ E_{\perp, //}^{(r)} \end{pmatrix} = \hat{G}_{\perp, //} \begin{pmatrix} E_{\perp, //}^{(t)} \\ 0 \end{pmatrix}, \quad (\text{III.2})$$

where $\hat{G}_{\perp, //} = \hat{G}_{x, y}$ is the overall transfer matrix of the structure. As in Chapter II, the subscripts $//$ and \perp refer to the linear polarization directions respectively parallel and perpendicular to the main (polar) axis of the NPs, *i.e.*, to the x -axis. The overall transfer matrix is obtained with

$$\hat{G}_{\perp, //} = \left(\prod_{j=1}^{2N+2} \hat{I}_j^F \hat{F}_j \right) \hat{I}_{\perp, //}^{\text{NP}} \left(\prod_{j=2N+3}^{4N+4} \hat{F}_j \hat{I}_{j+1}^F \right) \quad (\text{III.3})$$

for the structure shown in Fig. III.2(a) and

$$\hat{G}_{\perp, //} = \left(\prod_{j=1}^{2N+1} \hat{I}_j^F \hat{F}_j \right) \hat{I}_{\perp, //}^{\text{NP}} \left(\prod_{j=2N+2}^{2N+3} \hat{F}_j \hat{I}_{j+1}^F \right) \hat{F}_{2N+4} \hat{I}_{\perp, //}^{\text{NP}} \left(\prod_{j=2N+5}^{4N+5} \hat{F}_j \hat{I}_{j+1}^F \right) \quad (\text{III.4})$$

for the structure depicted in Fig. II.3(b), where $\hat{I}_{\perp, //}^{\text{NP}}$ is the matrix for a 2D NP array seen as an interface separating two layers. Note that Eq. (III.4) is indeed written for the case of two identical 2D arrays. Propagation matrices \hat{F}_{2N+2} and \hat{F}_{2N+3} in Eq. (III.3) are obtained for a geometric thickness equal to $d_D/2$. Similarly, propagation matrices \hat{F}_{2N+1} , \hat{F}_{2N+2} , \hat{F}_{2N+4} and \hat{F}_{2N+5} in Eq. (III.4) correspond to layers whose geometric thicknesses are equal to $(d_D/2 + d_C - \Delta)$, $(\Delta - d_D/2)$, $(\Delta - d_D/2)$ and $(d_D/2 + d_C - \Delta)$, respectively. As was mentioned above, the active layer D is approximated as a homogeneous layer whose effective permittivity takes into account its fine structure [31].

The matrix for a 2D NP array can be considered as a matrix for an interface surrounded by two layers and is written as [33]

$$\hat{I}_{\perp, //}^{\text{NP}} = \frac{1}{t_{\perp, //}^{\text{NP}}} \begin{pmatrix} 1 & -r_{\perp, //}^{\text{NP}} \\ r_{\perp, //}^{\text{NP}} & 1 + 2r_{\perp, //}^{\text{NP}} \end{pmatrix}, \quad (\text{III.5})$$

where $r_{\perp, //}^{\text{NP}}$ and $t_{\perp, //}^{\text{NP}}$ are the complex reflection and refraction coefficients of a 2D NP array for the two mutually orthogonal \perp and $//$ linear polarizations. Within the frame of the coupled-dipole approximation and for normal incidence, these coefficients can be obtained from Eqs. (I.59, I.60) with

use of Eqs. (I.51, I.52, I.54) as:

$$r_{\perp, //}^{\text{NP}} = t_{\perp, //}^{\text{NP}} - 1 = -i \frac{k_0 \sqrt{\varepsilon_m} \alpha_{\perp, //}}{2p^2 - 0.72 \alpha_{\perp, //} / p - ik_0 \sqrt{\varepsilon_m} \alpha_{\perp, //}}, \quad (\text{III.6})$$

where $k_0 = 2\pi / \lambda_0$ is the wavevector in free space, and

$$\alpha_{\perp, //} = V \frac{\varepsilon_p - \varepsilon_m}{g_{\perp, //} (\varepsilon_p - \varepsilon_m) + \varepsilon_m} \quad (\text{III.7})$$

is the complex polarizability of an individual spheroidal NP. Here ε_p and ε_m are the relative permittivity of the metallic NPs and relative permittivity of the isotropic layer into which the array is embedded, respectively. In Eq. (III.7), $V = 4\pi ab^2 / 3$ is the volume of the NP, and $g_{\perp, //}$ is a geometric factor accounting for the influence of the shape of the NP on its induced dipolar moment (see Chapter II, Eq. (II.2)).

The reflectivities $R_{\perp, //}$ and transmittivities $T_{\perp, //}$ of the entire photonic structure for the longitudinal and transverse light polarizations are deduced from transfer matrix elements as

$$R_{\perp, //} = \left| \frac{E_{\perp, //}^{(r)}}{E_{\perp, //}^{(i)}} \right|^2 = \left| \frac{(\hat{G}_{\perp, //})_{21}}{(\hat{G}_{\perp, //})_{11}} \right|^2, \quad T_{\perp, //} = \left| \frac{E_{\perp, //}^{(t)}}{E_{\perp, //}^{(i)}} \right|^2 = \frac{1}{|(\hat{G}_{\perp, //})_{11}|^2}. \quad (\text{III.8})$$

With the same transfer matrix formalism, it is also possible to obtain the field distribution inside the structure. For any given position z_1 , applying Eqs. [I.2] to the part of the structure located between $z = z_1$ and $z = L$, and denoting $E'^{(i)} = E_f(z_1^-)$ and $E'^{(r)} = E_b(z_1^-)$ the amplitudes of the incident and reflected optical fields at z_1 , respectively, we have, similarly to Eq. (III.2):

$$\begin{pmatrix} E'_{\perp, //}{}^{(i)} \\ E'_{\perp, //}{}^{(r)} \end{pmatrix} = \hat{G}'_{\perp, //} \begin{pmatrix} E_{\perp, //}^{(t)} \\ 0 \end{pmatrix}, \quad (\text{III.9})$$

where $\hat{G}'_{\perp, //}$ is the transfer matrix of the fraction of the structure under consideration, obtained in a similar fashion to Eqs. (III.3) or (III.4).

The modulus of the total optical field at position z_1 in this case can be deduced from

$$|E'_{\perp, //}{}^{(r)} + E'_{\perp, //}{}^{(i)}| = \left| \left[(\hat{G}'_{\perp, //})_{11} + (\hat{G}'_{\perp, //})_{12} \right] T_{\perp, //} \right|. \quad (\text{III.10})$$

Figure III.3 represents the longitudinal distribution of the normalized field modulus in the photonic

structure *without NP array*.

As we can see, the field intensity exhibits three particularly interesting antinodes within the (CDC) microcavity: one local maximum at the center of the active layer *D* (hence at the center of the photonic structure as a whole) and two larger maxima symmetrically located at the distance $\Delta = 225$ nm from that center. The intensity maxima are different due to the difference in permittivity in layers *C* and *D*. As will be justified below, those are the locations that will be chosen for the NP arrays embedded in the structure (see Fig. III.2).

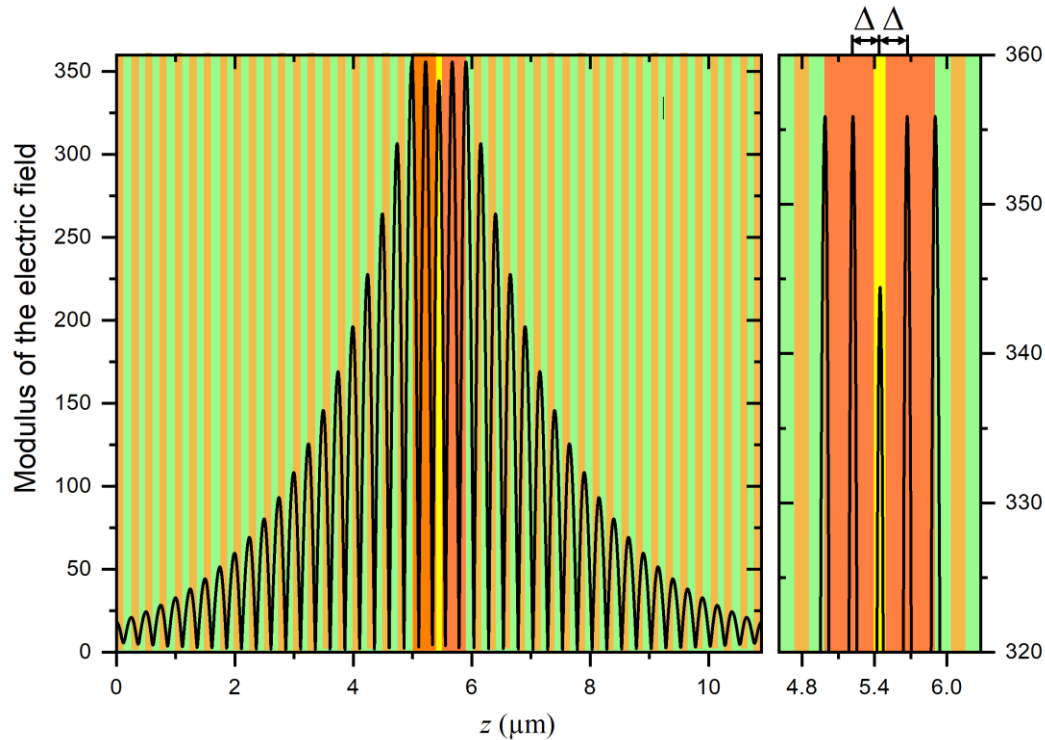


Fig. III.3. Longitudinal distribution of the normalized optical field modulus in the photonic structure shown in Fig. III.1 (*i.e.*, without NP array). The colors of the vertical bars correspond to those of the layers in the schematic of the structure. The right panel zooms in on the area immediately surrounding the composite microcavity. Here Δ is the distance from the center of layer *D* to two symmetrical absolute field maxima in the layers *C*.

III.4. Transmission of a 2D array of nanoparticles

Let us first discuss the transmission properties of a 2D metallic NP array as described above. In order to assess its sole contribution, calculations in this sub-section are carried out with two semi-infinite GaAs layers surrounding the array made of silver (Ag) particles.

The NPs have the shape of prolate (*i.e.*, elongated) spheroids (thus with $a > b$, *i.e.*, $\xi > 1$) with a half-length of their polar axis $a = 10$ nm. The distance between the centers of the particles (period p of the array) varies from 60 nm to 120 nm. Their relative permittivity is taken to follow the modified Drude model (see Chapter II, Eq. (II.3)) where the plasma frequency in silver is $\omega_p = 1.35 \times 10^{16}$ rad \cdot s $^{-1}$, the contribution of its crystal lattice to the relative permittivity is $\varepsilon_\infty = 5$, and the relaxation rate describing the effective electron scattering rate is $\gamma = 5.5 \times 10^{13}$ s $^{-1}$ [34]. The calculations are carried out taking into account the frequency dispersion of the dielectric permittivity of GaAs [35].

Figure III.4 shows the transmittivity $|t_{||}^{\text{NP}}|^2$ of the 2D NP array surrounded by identical media for the longitudinal polarization state (where the optical electric field is directed along the polar axis of the metallic spheroids, *i.e.*, along the x -axis) of the incoming light for three different values of the aspect ratio of the nanoparticles.

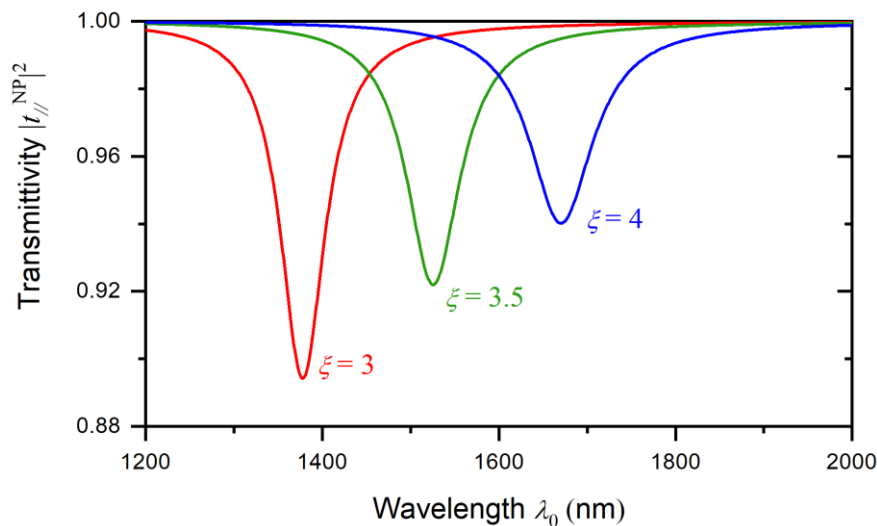


Fig. III.4. Transmission spectra of an Ag NP array embedded in a GaAs matrix for the longitudinal polarization state of the incoming light and for different values of the aspect ratio of the NPs. Red, green and blue curves correspond to ξ equal to 3.0, 3.5 and 4.0, respectively. The period of the NP array is $p = 120$ nm. The length of the polar axis of the NPs is $2a = 20$ nm.

One can see that the transmittivity exhibits a resonant behavior, and it can be shown that the position of the transmittivity minimum is associated with the localized plasmon resonance in Ag particles. The excitation of that resonance induces indeed a dip in the transmittivity spectrum. With an increase of the aspect ratio of the NPs, the plasmon resonance (and the dip in the transmittivity) moves

towards higher wavelengths. This behavior coincides with the one that was observed in Chapter II for a 3D nanocomposite.

Increasing the value of the aspect ratio ζ reduces the amplitude of the dips. This can be related to the fact that for a given value of the half-length a of the polar axis, the volume of the prolate spheroidal NPs decreases when ζ increases. As a result, according to Eq. (III.7), the polarizability of the NPs decreases, thus reducing the scattering of light by the array, which in turn reduces the overall efficiency of surface plasmon excitation.

It should also be noted that due to the anisotropy of the shape of the particles ($\zeta \neq 1$), the plasmon resonances for longitudinal and transverse polarization states do not occur at the same wavelength. As in Chapter II, the plasmon resonance for the transverse polarization state is positioned at lower wavelengths than for the longitudinal polarization state (in this case, it occurs in the visible domain, below 700 nm). Reducing the value of aspect ratio ζ would bring the surface plasmon resonances for transverse and longitudinal incoming states of polarization closer to each other (hence a red shift for the former and a blue shift for the latter), as the spheroids thus tend towards an isotropic spherical shape, for which transverse and longitudinal resonances are expected to merge.

Let us now discuss the influence of the period p of the array on its transmittivity spectrum. Figure III.5 shows the transmittivity spectra of the monolayer for the longitudinal polarization state of incoming light and for three different values of that period ($p = 60$ nm, 90 nm, and 120 nm). The value of the aspect ratio is equal to 3.5 in all three cases.

Here again, we can see similarities in the behaviors of the NP monolayer and of the 3D nanocomposite with randomly distributed NPs that was discussed in Chapter II. An increase of the value of p reduces the overall volume of the NPs in the monolayer, which leads to a decrease of the amplitude of the transmission dips. On the other hand, for small NP concentrations, which is the case here, modifying the value of the array period almost does not affect the spectral position of its transmittivity dip. This, again, is similar to the behavior of the spectral properties of the 3D nanocomposite in Chapter II.

So, as was already discussed in Chapter II for the case of the nanocomposite layer with randomly distributed NPs, the main parameters that allow us to control the position and the amplitude of the plasmon resonance for the 2D NP array are the aspect ratio ζ of the NPs and the period p of the array (which determines the concentration of the NPs in the array).

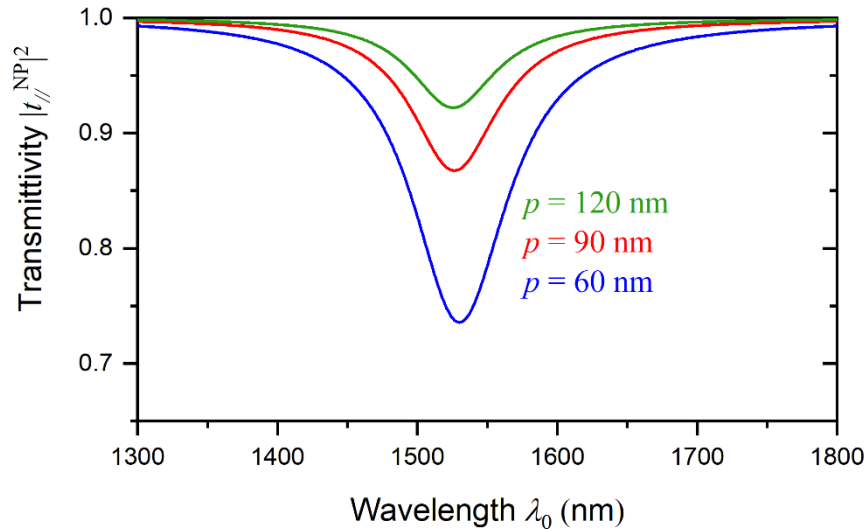


Fig. III.5. Transmission spectra of an Ag NP array embedded in a GaAs matrix for the longitudinal polarization state of the incoming light and for different values of the period p of the NP array. Green, red and blue curves correspond to p equal to 60 nm, 90 nm, and 120 nm, respectively. The aspect ratio of the NPs is $\xi = 3.5$. The length of the polar axis of the NPs is $2a = 20$ nm.

However, it should be noted that the spectral characteristics of the NP array are bound to vary with the location of the array within the structure — in the active layer D or in the GaAs cladding layers C of the microresonator — due to their different dielectric permittivities (as mentioned above, the spectra shown in Figs. III.5 and III.6 have been obtained for a semi-infinite GaAs layer on either side of the array). In the following, we will consider values of the aspect ratio ξ that ensure that the collective *longitudinal* surface plasmon resonance of the 2D silver NPs array(s) coincides with $\lambda_0 = 1550$ nm for both situations described in Section III.3. Specifically, using Eqs. (III.6)-(III.7) it was determined that this condition is achieved for $\xi = 3.6$ when NPs are embedded in a cladding layer C , and for $\xi = 3.2$ when they are located in the active region D .

Also, the precise positioning of the 2D array matters (unlike in the case of the bulk nanocomposite), because the monolayer is considered as an interface between layers, since the size of the NPs is much smaller than the wavelength and the thicknesses of the layers. Placed at a minimum of the field amplitude, the monolayer will almost not affect the transmission spectrum of the structure. On the other hand, the impact of the NP array will be strongest when its position coincides with a peak value of the field amplitude (this will be discussed in more details in section III.5, see also Fig. III.10). As was shown in Fig. III.3, there are three such peaks in the microcavity: one central peak at the center

of the layer D and two lateral peaks in the layers C at distance $\pm\Delta = \pm 225$ nm from the center of the structure. Embedding a single NP array at the location of the central peak corresponds to the case shown in Fig. III.2(a), whereas embedding two identical NP arrays at the locations of the two lateral peaks corresponds to the case shown in Fig. III.2(b).

Here I want to say a few words about why the idea of embedding NPs in the passive region of the microcavity (*i.e.*, in either of the layers C) is considered instead of inserting them in the active layer D . In the case with a NP array at the center of the system (Fig. III.2(a)), the layer D experiences heating from the absorption in the NPs in addition to that due to pumping process necessary for the amplification, which can lead to undesirable temperature effects on the stability of the structure. Locating the NPs in the passive region of the microcavity mitigates this issue by spreading the heating in the resonator. Furthermore, distributing the NPs over several arrays facilitates this spreading even more. In this study, the choice was made to consider the case of two identical NP arrays symmetrically located in layers C on either side of the active layer D (Fig. III.2(b)).

III.5. Transmission spectra of the photonic structure and suppression of the defect mode

Let us first consider the active structure without embedded 2D NP array, as presented on Fig. III.1. As shown in Fig. III.6, in this case the transmittivity spectrum exhibits a photonic bandgap extending from 1465 nm to 1645 nm. Due to the presence of the active composite microcavity (constituting a defect layer), a defect mode (large transmittivity peak) appears in the bandgap, centered at 1550 nm for the chosen structural parameters. As we can see on the right inset panel, due to the amplification in the central layer, the amplitude of that defect mode greatly exceeds 1. This structure does not include any anisotropic element, so that the efficiency of the amplification of the defect mode does not depend on the state of polarization of the incoming electromagnetic wave.

The next step consists in introducing a NP array. It will introduce anisotropy and thus polarization dependence of the optical response of the structure. As was shown in Figs. III.4 and III.5, the spectral characteristics of the 2D array of NPs significantly depend on both the shape of the NPs (through the aspect ratio ξ) and their surface density (through the period p).

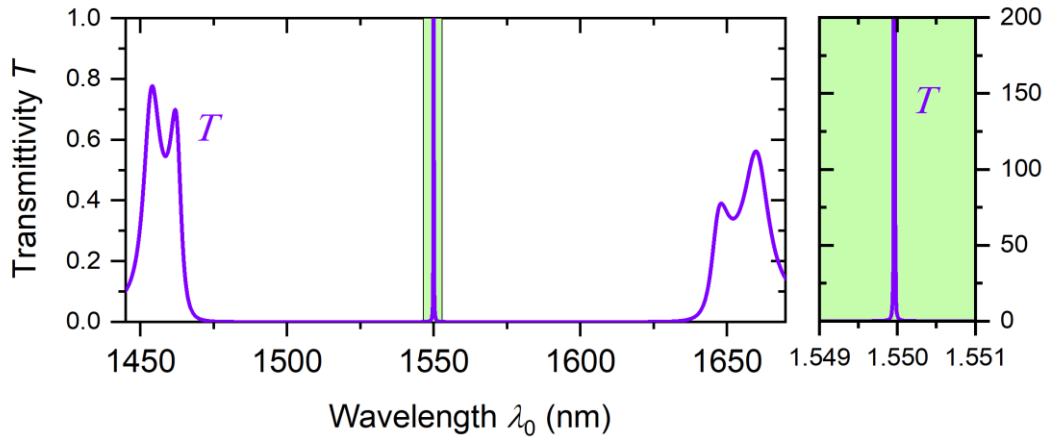


Fig. III.6. Transmission spectrum of the photonic structure without NP array. The spectrum is identical for any state of polarization of the incident light wave. The right inset zooms in on the spectrum around the defect mode (note the different vertical scale in the inset and in the main figure. The curve in the inset is truncated to $T = 200$).

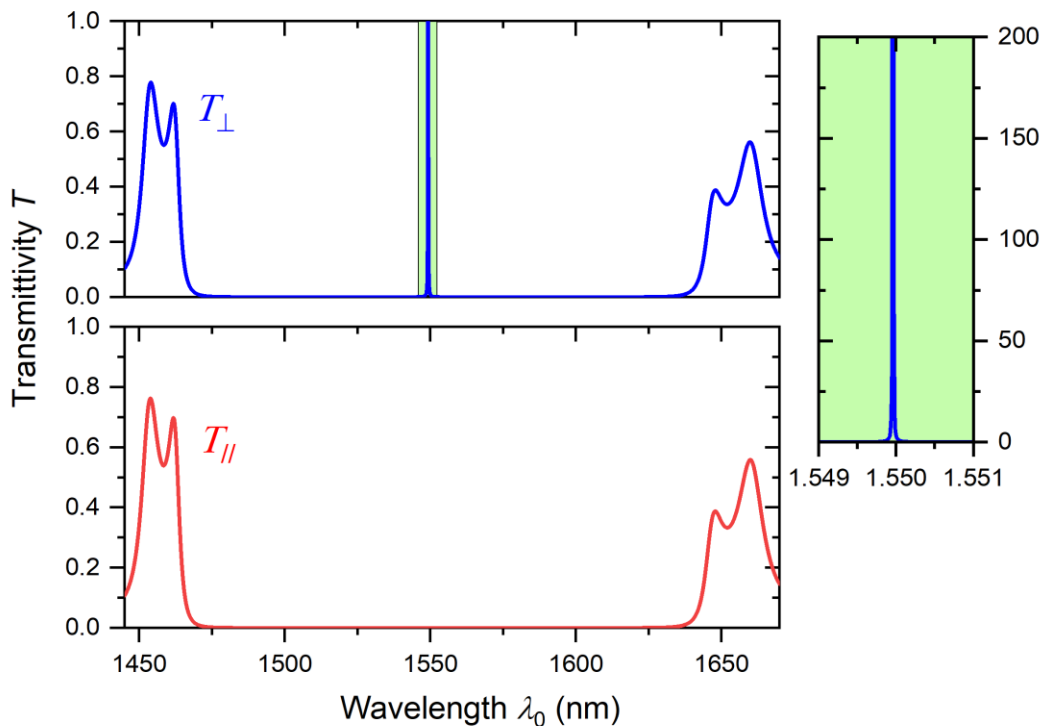


Fig. III.7. Transmission spectra T_{\perp} and T_{\parallel} (top and bottom panels, respectively) of the amplifying PC with one embedded silver 2D NP array at the center of the defect layer. The inset (truncated to $T = 200$) zooms in on the amplified defect mode. The interparticle distance p is equal to 90 nm, and the aspect ratio of the NPs is $\xi = 3.6$.

On the basis of simulation results such as those presented in these figures, the structural parameters of the 2D NP array were determined that ensure the coincidence of the surface plasmon resonance in the NP array and the defect mode centered at wavelength $\lambda_0 = 1550$ nm. In addition, as was mentioned in the previous Section, the precise positioning of the monolayer(s) really matters.

Let us first consider the case with only one NP array positioned at the center of the structure (see Fig. III.2(a)). The calculated transmission spectra T_{\perp} and T_{\parallel} are shown in Fig. III.7. The bottom panel of Fig. III.7 shows that the excitation of a longitudinal surface plasmon resonance in silver NPs (along their polar axis) results in a drastic decay of T_{\parallel} , *i.e.* an almost complete suppression of the defect mode, for x -polarized light. In the top panel, due to the fact that in this case, the wavelength of the incoming light wave is much too distant from the plasmon resonance, the spectrum of T_{\perp} appears virtually identical to that of the PC structure without 2D array of silver NPs (see Fig. III.6).

The structural properties of the NP arrays play an important part in the suppression of the defect mode. In particular, the effect of the period p is addressed in Figs. III.8 and III.9.

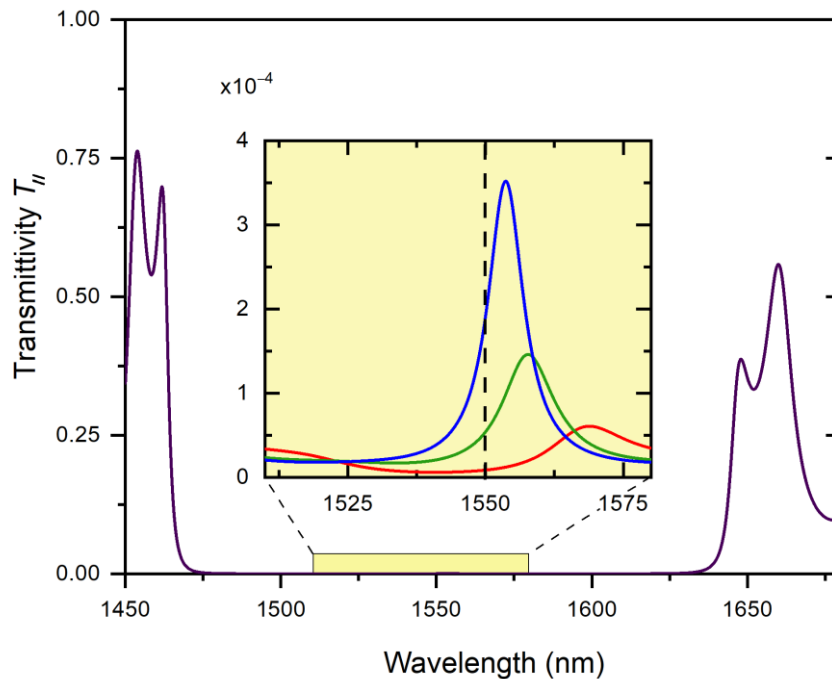


Fig. III.8. Transmission spectra T_{\parallel} of the amplifying PC with a single embedded silver 2D NP array at the center of the defect layer. Red, green and blue curves in the inset correspond to a period p equal to 60 nm, 90 nm, and 120 nm, respectively. The aspect ratio of the NPs is $\xi = 3.6$. The dashed vertical line in the inset denotes wavelength $\lambda_0 = 1550$ nm.

Figure III.8 represents transmission spectrum $T_{//}$ (i.e. for a longitudinal polarization of the incoming light) of the structure with a single NP array located at its center, for three different values of the period p considered in Fig. III.5.

The main figure (purple curve) shows a spectrum, away from the spectral domain immediately surrounding $\lambda_0 = 1550$ nm, that does not depend much on the value of p . The effect of the NP array is by design mostly visible near λ_0 , in the vicinity of the defect mode, and the impact of period p in this spectral domain can be seen in the inset. The efficiency of the defect mode suppression decreases when the period increases, which is consistent with the fact that the amount of metal also decreases, and, in turn, the transmittivity of the array increases (see Fig. III.5). Also, a red shift of the strongly depleted defect mode appears when the interparticle distance p decreases, so that the longitudinal transmittivity $T_{//}$ at wavelength $\lambda_0 = 1550$ nm actually becomes close to zero. This shift can qualitatively be attributed to the shift introduced by the presence of the NP array to the phases of the forward and backward electromagnetic waves in the multilayered PC, which affects the constructive interference condition responsible for the defect mode in the transmission spectrum.

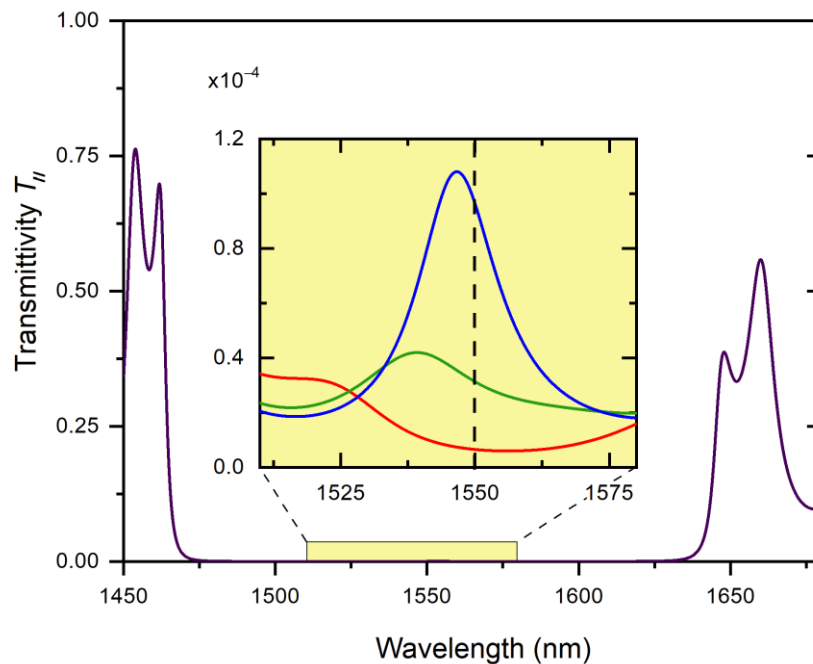


Fig. III.9. Transmission spectra $T_{//}(\lambda_0)$ of the amplifying PC with two identical embedded 2D silver NP arrays at the distances $\pm\Delta = \pm 225$ nm from the center of the structure (in the layers C). Red, green and blue curves in the inset correspond to a period p of the array equal to 60 nm, 90 nm, and 120 nm, respectively. The aspect ratio of the NPs is $\xi = 3.2$. The dashed vertical line in the inset denotes wavelength $\lambda_0 = 1550$ nm.

Figure III.9 addresses the same issue, but for the structure with two identical NP arrays positioned at distances $\pm\Delta = \pm 225$ nm from the center (see Fig. III.2(b)). Contrary to what was observed in Fig. III.8, the complex interplay between the additional phase shifts introduced by the arrays leads this time to a *blue shift* of the defect mode when period p decreases. In addition, the amplitude of what remains of the defect mode peak, when it is nearly suppressed by two identical NP arrays symmetrically placed in layers C , is about three times smaller than when a single NP array is introduced at the center of the PC. This can be related to the larger number of scattering centers (surface plasmons excited in the NPs), which results in a stronger absorption of light, in the former case. However, even in the latter case, the intensity of the transmitted wave at λ_0 is almost negligible, and in both cases, the reduction rate of the intensity is of the order of 100 with respect to the structure without NP array.

As was discussed above, two NP arrays embedded into passive layers C allow us to distribute the heating without losing the efficiency of the suppression/amplification processes of the defect mode (see Fig. III.9).

Of course, other schemes with NP arrays positioned in various locations in layers C and (or) D are also possible. This versatility significantly expands the possibilities for the polarization-dependent control of the transmission spectra of the structure. In addition, it is possible to consider several NP arrays with different periods, aspect ratios or orientations of their axes in order to obtain a photonic structure in which the selection of *different* modes with *different* polarizations can be achieved. The two cases considered in this Chapter are nevertheless sufficient to establish the validity of the principle of a polarization-selective amplifier exploiting the combination of a photonic crystal-based cavity and plasmonic excitations in metallic inclusions.

The previous simulations and discussions assumed a perfect positioning of the NP array(s) with respect to the optical field maxima in layers C and D shown in Fig. III.3. It can be expected that the efficiency of the defect mode suppression will be reduced if the position of the NP array(s) departs from that optimal situation. We can ask ourselves what tolerance range can be allowed for that position for which the suppression of the defect mode remains acceptable for any arbitrary efficiency criterium. Figure III.10 gives some insight into this question: it shows the evolution of the $T_{//}$ transmittivity spectrum in the vicinity of the defect mode when the position z_a of a single NP array varies along the width of the C and D layers forming the microcavity.

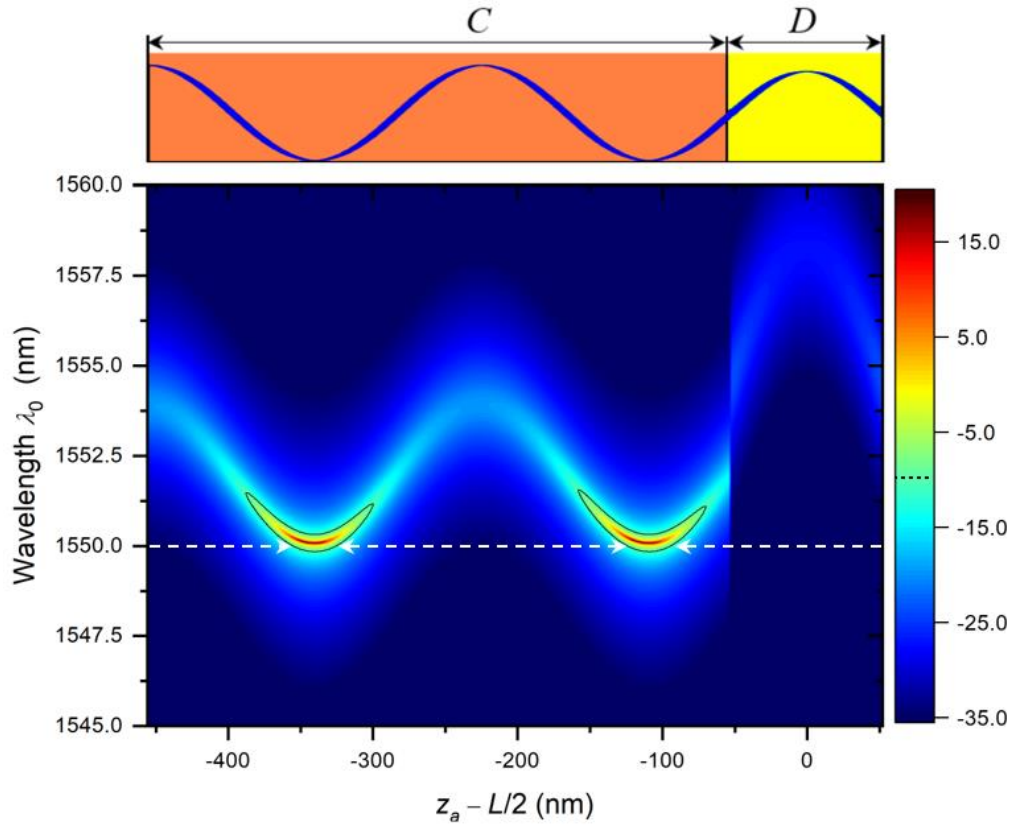


Fig. III.10. Transmittivity spectrum $T_{//}(\lambda_0)$ (in semi-logarithmic scale) of the amplifying PC in the vicinity of the defect mode as a function of the position of the monolayer relative to the center of the structure. The period of the NP array is taken as $p = 90$ nm. The aspect ratio of the NPs is $\xi = 3.6$ in the layer C and $\xi = 3.2$ in the layer D . The top panel represents the longitudinal distribution of the optical field modulus (blue curve) at defect mode wavelength 1550 nm. Colors on the top panel correspond to the layer colors in Fig. III.3 (orange for layer C and yellow for layer D).

The bright zone on the picture shows the evolution of the position of the defect mode. Black lines are iso-transmission curves that delimit “transmission islands” where the defect mode is not suppressed. As a criterion for the efficiency of the defect mode suppression, we chose $T_{//} \leq 0.001$. The blue curve on the top panel of Fig. III.10 represents the optical field distribution at wavelength $\lambda_0 = 1550$ nm. As we can see, the positions of the “transmission islands” on the main panel of the figure coincide with regions of minimal optical field localization.

Indeed, the closer the location of the NP array is to the position of a local minimum of the optical field, the less efficient the excitation of the plasmon resonance will be. This results in a large amplification of the defect mode visible as red spots at the center of the “transmission islands”.

Moving towards the maxima of the optical field localization increases the efficiency of the NP monolayer as a defect mode suppressor. Moreover, we can see that the closer the location of the NP array is to the position of a local maximum of the field, the more pronounced is the red shift of the defect mode (the same shift that could be observed in Fig. III.8 for a single NP array at the center of the layer D). As a result of this shift and suppression, we observe wide ranges of positions for the NP array (shown by white dotted arrows) in which the criterion of the defect mode suppression at 1550 nm can be satisfied. This constitutes also a criterion for the tolerance on the positioning of the NP array inside the microcavity. A similar discussion can be led for the case of two or more NP arrays embedded in the structure, as for instance in the geometry of Fig. III.2(b).

III.6. Conclusions

- In this Chapter, the demonstration was made that polarization-controlled amplification of a defect mode can be achieved in an amplifying photonic crystal in which periodic 2D arrays of metallic nanoparticles are embedded.
- It was shown, that the presence of one or several 2D nanoparticle arrays embedded in the multilayered heterostructure provides a polarization-dependent way to suppress the defect mode. This can be achieved if the dimensions and mutual distance of the spheroidal nanoparticles are chosen so that a surface plasmon resonance will be excited in them by an incoming light beam of 1550 nm vacuum wavelength coinciding with the defect mode.
- It was also shown, that the suppression of the defect mode in the former case depends on the position of the NP array. Suppression is the most efficient when the array is embedded at locations of maximal optical field localization in the amplifying region of the structure.
- The approach described in this Chapter, in combination with other recently proposed solutions (based for instance on the use of liquid crystals [34,36-37] or of materials whose properties can be magnetically or electrically controlled [38-42]), can significantly expand the possibilities of controlling the polarization of light emitted by semiconductor lasers.

III.7. List of references

- [1] L. Novotny and N. van Hulst, "Antennas for light," *Nature Photonics* **5**, 83–90 (2011).
- [2] F. Ding, A. Pors, and S. I. Bozhevolnyi, "Gradient metasurfaces: a review of fundamentals and applications," *Rep. Prog. Phys.* **81**, 026401 (2018).
- [3] R. Kulllock, S. Grafström, P. R. Evans, R. J. Pollard, and L. M. Eng, "Metallic nanorod arrays: negative refraction and optical properties explained by retarded dipolar interactions," *J. Opt. Soc. Am. B* **27**, 1819–1827 (2010).
- [4] S. G. Moiseev, "Active Maxwell–Garnett composite with the unit refractive index," *Physica B* **405**, 3042–3045 (2010).
- [5] A. I. Rahachou and I. V. Zozoulenko, "Light propagation in nanorod arrays," *J. Opt. A: Pure Appl. Opt.* **9**, 265–270 (2007).
- [6] S. G. Moiseev and V. A. Ostatochnikov, "Defect modes of one-dimensional photonic-crystal structure with a resonance nanocomposite layer," *Quantum Electron.* **46** (8), 743–748 (2016).
- [7] S. Ya. Vetrov, R. G. Bikbaev, and I. V. Timofeev, "The optical Tamm states at the edges of a photonic crystal bounded by one or two layers of a strongly anisotropic nanocomposite," *Opt. Commun.* **395**, 275–281 (2016).
- [8] H. A. Elsayed, "Transmittance properties of one dimensional ternary nanocomposite photonic crystals," *Mater. Res. Express* **5**, 036209 (2018).
- [9] A. H. Aly, C. Malek, and H. A. Elsayed, "Transmittance properties of a quasi-periodic one-dimensional photonic crystals that incorporate nanocomposite material," *Int. J. Mod. Phys. B* **32**, 1850220 (2018).
- [10] V. S. Gerasimov, A. E. Ershov, R. G. Bikbaev, I. L. Rasskazov, I. V. Timofeev, S. P. Polyutov, and S. V. Karpov, "Engineering mode hybridization in regular arrays of plasmonic nanoparticles embedded in 1D photonic crystal," *J. Quant. Spectrosc. Radiat. Transf.* **224**, 303–308 (2019).
- [11] P. Alivisatos, "The use of nanocrystals in biological detection," *Nature Biotechnology* **22**, 47–52 (2004).
- [12] S. Unser, I. Bruzas, J. He, and L. Sagle, "Localized surface plasmon resonance biosensing: current challenges and approaches," *Sensors* **15**, 15684–15716 (2015).
- [13] S. G. Moiseev, "Composite medium with silver nanoparticles as an anti-reflection optical coating," *Appl. Phys. A* **103**, 619–622 (2011).
- [14] A. S. Shalin and S. G. Moiseev, "Controlling interface reflectance by a monolayer of nanoparticles," *Quantum Electron.* **39**, 1175–1181 (2009).
- [15] X. Tang, L. Zhou, X. Du, and Y. Yang, "Enhancing absorption properties of composite nanosphere and nanowire arrays by localized surface plasmon resonance shift," *Results in Physics* **7**, 87–94 (2017).
- [16] T. P. Otanicar, P. E. Phelan, R. S. Prasher, G. Rosengarten, and R. A. Taylor, "Nanofluid-based direct absorption solar collector," *J. Renew. Sust. Energy* **2**, 033102 (2010).
- [17] S. G. Moiseev, "Nanocomposite-based ultrathin polarization beamsplitter," *Opt. Spectrosc.* **111**, 233–240 (2011).

- [18] Ö. Sepsi, T. Gál, and P. Koppa, "Polarized light emitting diodes using silver nanoellipsoids," *Opt. Express* **22**, A1190–A1196 (2014).
- [19] V. Lozovski and M. Razumova, "Influence of inclusion shape on light absorption in thin Au/Teflon nanocomposite films," *J. Opt. Soc. Am. B* **33**, 8–16 (2016).
- [20] S. G. Moiseev, V. A. Ostatochnikov, and D. I. Sementsov, "Defect mode suppression in a photonic crystal structure with a resonance nanocomposite layer," *Quantum Electron.* **42**, 557–560 (2012).
- [21] S. Ya. Vetrov, P. S. Pankin, and I. V. Timofeev, "Peculiarities of spectral properties of a one-dimensional photonic crystal with an anisotropic defect layer of the nanocomposite with resonant dispersion," *Quantum Electron.* **44**, 881–884 (2014).
- [22] R. Michalzik (Ed.), *VCSELs. Fundamentals, Technology and Applications of Vertical-Cavity Surface-Emitting Lasers* (Springer-Verlag, Berlin, 2013).
- [23] D.-S. Song, S.-H. Kim, H.-G. Park, C.-K. Kim, and Y.-H. Lee, "Single-fundamental-mode photonic-crystal vertical-cavity surface-emitting lasers," *Appl. Phys. Lett.* **80**, 3901–3903 (2002).
- [24] M. A. Arteaga, M. López-Amo, H. Thienpont, and K. Panajotov, "Role of external cavity reflectivity for achieving polarization control and stabilization of vertical cavity surface emitting laser," *Appl. Phys. Lett.* **90**, 031117 (2007).
- [25] Y. Hong, R. Ju, P. S. Spencer, and K. A. Shore, "Investigation of polarization bistability in vertical-cavity surface-emitting lasers subjected to optical feedback," *IEEE J. Quantum Electron.* **41**, 619–624(2005).
- [26] J. M. Ostermann, P. Debernardi, and R. Michalzik, "Optimized integrated surface grating design for polarization-stable VCSELs," *IEEE J. Quantum Electron.* **42**, 690–698(2006).
- [27] J. Hashizume and F. Koyama, "Transverse and polarization mode controlled vertical cavity surface emitting laser with metal nano-aperture array for optical near-field," 18th Annual Meeting of the IEEE Lasers and Electro-Optics Society, LEOS2005, WK3, pp. 467–468, Oct. 2005.
- [28] P. Babu Dayal and F. Koyama, "Polarization control of 0.85 μm vertical-cavity surface-emitting lasers integrated with gold nanorod arrays," *Appl. Phys. Lett.* **91**, 111107 (2007).
- [29] J. D. Joannopoulos, R. D. Meade, and J. N. Winn, *Photonic Crystals* (Princeton University Press, Princeton, 1995).
- [30] K. Inoue and K. Ohtaka (Eds.), *Photonic Crystals: Physics, Fabrication and Applications* (Springer-Verlag, Berlin, 2004).
- [31] M. A. Rahman, M. R. Karim, J. Akhtar, and M. I. Reja, "Performance characterization of a GaAs based 1550 nm Ga_{0.591}In_{0.409}N_{0.028}As_{0.89}Sb_{0.08} MQW VCSEL," *Int. J. of Photonics and Optical Technology* **4**, 14–18 (2018).
- [32] A. Sihvola, *Electromagnetic Mixing Formulas and Applications* (The Institution of Electrical Engineers, London, 1999).
- [33] C. C. Katsidis and D. I. Siapkas, "General transfer-matrix method for optical multilayer systems with coherent, partially coherent, and incoherent interference," *Appl. Opt.* **41**, 3978–3987 (2002).

- [34] H. U. Yang, J. D'Archangel, M. L. Sundheimer, E. Tucker, G. D. Boreman, and M. B. Raschke, "Optical dielectric function of silver," *Phys. Rev. B* **91**, 235137 (2015).
- [35] A. D. Rakić and M. L. Majewski, "Modeling the optical dielectric function of GaAs and AlAs: Extension of Adachi's model," *J. Appl. Phys.* **80**, 5909–5914 (1996).
- [36] L. Frasukiewicz, T. Czyszanowski, H. Thienpont, and K. Panajotov, "Electrically tunable VCSEL with intra-cavity liquid crystal: Design, optimization, and analysis of polarization- and mode-stability," *Opt. Commun.* **427**, 271–277 (2018).
- [37] H. Mehrzad and E. Mohajerani, "Liquid crystal mediated active nano-plasmonic based on the formation of hybrid plasmonic-photonic modes," *Appl. Phys. Lett.* **112**, 061101 (2018).
- [38] V. A. Gunyakov, I. V. Timofeev, M. N. Krakhalev, W. Lee, and V. Ya. Zyryanov, "Electric field-controlled transformation of the eigenmodes in a twisted-nematic Fabry–Pérot cavity," *Sci. Rep.* **8**, 16869 (2018).
- [39] C.-J. Wu, J.-J. Liao, and T.-W. Chang, "Tunable multilayer Fabry-Perot resonator using electro-optical defect layer," *J. of Electromagn. Waves and Appl.* **24**, 531–542 (2010).
- [40] L. He, Y. Hu, H. Kim, J. Ge, S. Kwon, and Y. Yin, "Magnetic assembly of nonmagnetic particles into photonic crystal structures," *Nano Lett.* **10**, 4708–4714 (2010).
- [41] T. Goto, H. Sato, H. Takagi, A. V. Baryshev, and M. Inoue, "Novel magnetophotonic crystals controlled by the electro-optic effect for non-reciprocal high-speed modulators," *J. Appl. Phys.* **109**, 07B756 (2011).
- [42] V. G. Arkhipkin, V. A. Gunyakov, S. A. Myslivets, V. Ya. Zyryanov, V. F. Shabanov, and Wei Lee, "Electro- and magneto-optical switching of defect modes in one-dimensional photonic crystals," *J. Exp. Theor. Phys.* **112**, 577–587 (2011).

CHAPTER IV

DETERMINISTIC APERIODIC PHOTONIC CRYSTAL WITH A 2D ARRAY OF METALLIC NANOPARTICLES AS A POLARIZATION-SENSITIVE DICHROIC FILTER

IV.1. Introduction

Dichroic filters possess the ability to selectively transmit or reject two separate spectral bands of an incident light beam. The rejected band is usually reflected, but the concept can be extended to cases where it is absorbed. A few common applications of dichroic filters include heat control in lighting appliances, liquid-crystal-based projectors [1], fluorescence microscopy or photovoltaic [2]. They can also be used as high-pass filters in laser frequency multipliers, e.g., by separating the spectral components of higher harmonic generators [3].

Dichroic filtering can be obtained in various ways, including the use of multilayered structures such as unidimensional photonic crystals (PCs). Indeed, the transmission spectrum of such structures made of periodically (but also quasi-periodically) alternating layers is known to exhibit photonic bandgaps, i.e., frequency ranges in which the propagation of electromagnetic waves is prohibited [4,5]. Moreover, breaking the periodicity of a PC by introducing one or several defect layers (made of a different material from those constituting the periodically alternating layers, or simply having a different thickness) leads to the appearance of narrow peaks of high transmittivity (so-called defect modes) at frequencies located inside the photonic bandgaps. These well-established properties have been put to use in the last decades for the design of many types of PC-based reflectors and filters [6], and the inclusion in them of, among others, reflective coatings [7,8], all-dielectric metasurfaces [9-12] or metallic composites [13-15] has been shown to allow further control of their spectral characteristics or to introduce an additional control of those characteristics by the state of polarization of light.

In this Chapter, I propose the design of a polarization-controlled dichroic filter based on the use of a single 2D array of metallic spheroidal NPs embedded in a defect layer surrounded by two reflectors. Using a 2D array simplifies the fabrication of such a filter and reduces energy dissipation at frequencies away from the plasmon resonances of the NPs. The working principle of such a filter is as follows. The prolate spheroidal shape of the NPs ensures that they can sustain two plasmon resonances excited at different frequencies for two mutually orthogonal polarizations of light respectively parallel and perpendicular to their long axis. As a result, the absorption of light at a frequency where a photonic defect mode coincides with a plasmon resonance frequency in the NP array substantially depends on its polarization. The structure of the multilayered photonic system and the anisotropic shape of the NPs are chosen so that two defect modes located in two separate bandgaps coincide with two plasmon resonances and that the spectral interval between them is large enough to separately achieve the nearly complete suppression of either defect modes for one of two mutually orthogonal states of polarization.

A crucial requirement of this scheme is the ability to adjust the number, location and width of the bandgaps and defect modes of the PC in order to allow the necessary coincidence between surface plasmonic modes in the NP array and photonic defect modes in separate bandgaps. Various methods have been devised to that effect, including the design of PCs with complex defect layers [16,17], or the external control of transmission spectra with magnetic or electric fields [18,19,20]. Another route consists in playing with the geometry of the PC. In comparison to regular, periodic, 1D PCs, multilayered structures with a complex periodicity (e.g., multi-periodic [21-24] or quasi-periodic PCs [25-29], or even disordered multilayered structures [30]) can exhibit more bandgaps in a given frequency region of interest, as well as several defect modes in those bandgaps, which greatly expands the possibilities for their use. In this Chapter, I propose the use of a deterministic aperiodic PC whose complex architecture follows a set of mathematical rules [31,32] that enable the adjustment of the location of photonic bandgaps and defect modes around frequencies of plasmon resonances of NPs.

The Chapter is organized as follows. Section IV.2 presents the chosen type of aperiodic photonic structure and demonstrates its advantages. In Section IV.3, the geometry and structural parameters of the investigated model are presented. Section IV.4 presents the results of the calculations for the transmittivity and reflectivity spectrum of the structure. Section IV.5 concludes the Chapter.

IV.2. Aperiodic photonic reflectors

First, let us discuss configuration of the distributed reflectors that will be used in the composite photonic structure. The main idea in this Chapter is to achieve polarization-sensitive control, and as a result, alternate suppression of two different defect modes in neighboring bandgaps. To achieve this, the coincidence of plasmonic and photonic resonance modes can be used, in a similar way as what was described in the two previous Chapters. Due to the spheroidal shape of the nanoparticles in the 2D NP array, two plasmon resonances appear at different wavelengths for incoming linear polarization states of light respectively parallel and perpendicular to the main axis of the NPs (see the schematic of the structure in Fig. IV.6 below). Here both plasmon resonances will be used to control two separate defect modes, located in two adjacent bandgaps, in such a way that one defect mode can be suppressed whereas the other one is left intact). Unlike the case described in Chapter III, where only one defect mode and one plasmon resonance were made to coincide, it is much harder to achieve the coincidence of two different plasmon resonances with two different defect modes in neighboring bandgaps. The position and the amplitude of the plasmonic resonances can be adjusted by changing the shape of the NPs in the array, the period of the array, or even the material surrounding the array, but the main problem here is the fact that the positions of these resonances cannot be changed separately. So, in this

case, an additional control over the positions of the bandgaps and defect modes of the photonic structure will be needed.

Let us first consider a single periodic photonic reflector $(AB)^N$ without defect layer and without NP array. Calculations hereafter are carried out for A and B layers made of ZrO_2 ($n_A = 2.02$) and SiO_2 ($n_B = 1.45$), respectively [33], and for $N=20$. For the case of the normal incidence angle of the incoming light the positions of the bandgaps of such DBR are determined by the thicknesses d_A and d_B of layers A and B , which are chosen to obey the usual Bragg condition [34]

$$n_A d_A = \frac{\lambda_{Br}}{4}, \quad n_B d_B = \frac{\lambda_{Br}}{4}, \quad (\text{IV.1})$$

where λ_{Br} is the Bragg vacuum wavelength of the incoming light and thus corresponds to the center of the first bandgap of the photonic crystal.

Figure IV.1. shows the evolution of the positions of the photonic bandgaps of the periodic DBR for three different values of $\lambda_{Br} = 700, 750$ and 800 nm.

The pink and green rectangular panels indicate two neighboring bandgaps of the DBR. We can see that the change of λ_{Br} is shifting simultaneously the positions of both bandgaps. Indeed, with a periodic structure as a reflector, these positions cannot be modified separately.

To achieve more control on positions of the bandgaps, the choice is made to use an aperiodic reflector instead of a periodic one. The chosen aperiodic structure is obtained through the overlap of two periodic DBRs $(AB)^N$ and $(AB)^{N'}$ made of alternate layers of materials A and B (Figs. IV.2(a) and IV.2(b)). The layer thicknesses (d_A and d_B) of the first DBR and those (d'_A and d'_B) of the second DBR are chosen to satisfy the Bragg condition Eq. (VI.1.) for two different vacuum wavelengths λ_{Br} and λ'_{Br} , so that $d_{A,B} = \lambda_{Br}/(4n_{A,B})$ and $d'_{A,B} = \lambda'_{Br}/(4n_{A,B})$. Specifically, the combination of the periodic DBRs is chosen such that the spatial variation of the refractive index in the resulting aperiodic structure can be written as

$$n_{aper}(z) = \bar{n} + \Delta n \max[F(z), F'(z)], \quad 0 \leq z \leq L, \quad (\text{IV.2})$$

where L is the total length of DBRs as well as that of the resulting reflector, and with

$$\bar{n} = \frac{n_A + n_B}{2}, \quad \Delta n = \frac{n_A - n_B}{2}, \quad (\text{IV.3})$$

and

$$F(z) = \operatorname{sgn} \left[\sin \left(\frac{2\pi}{\lambda_{0Br}} \frac{\bar{n}^2 - \Delta n^2}{\bar{n}} z \right) \cos \left(\frac{2\pi}{\lambda_{0Br}} \frac{\bar{n}^2 - \Delta n^2}{\bar{n}} z + \frac{\pi}{2} \frac{\Delta n}{\bar{n}} \right) \right] \quad (\text{IV.4})$$

and a similar expression for $F'(z)$ (replacing λ_{Br} with λ'_{Br}).

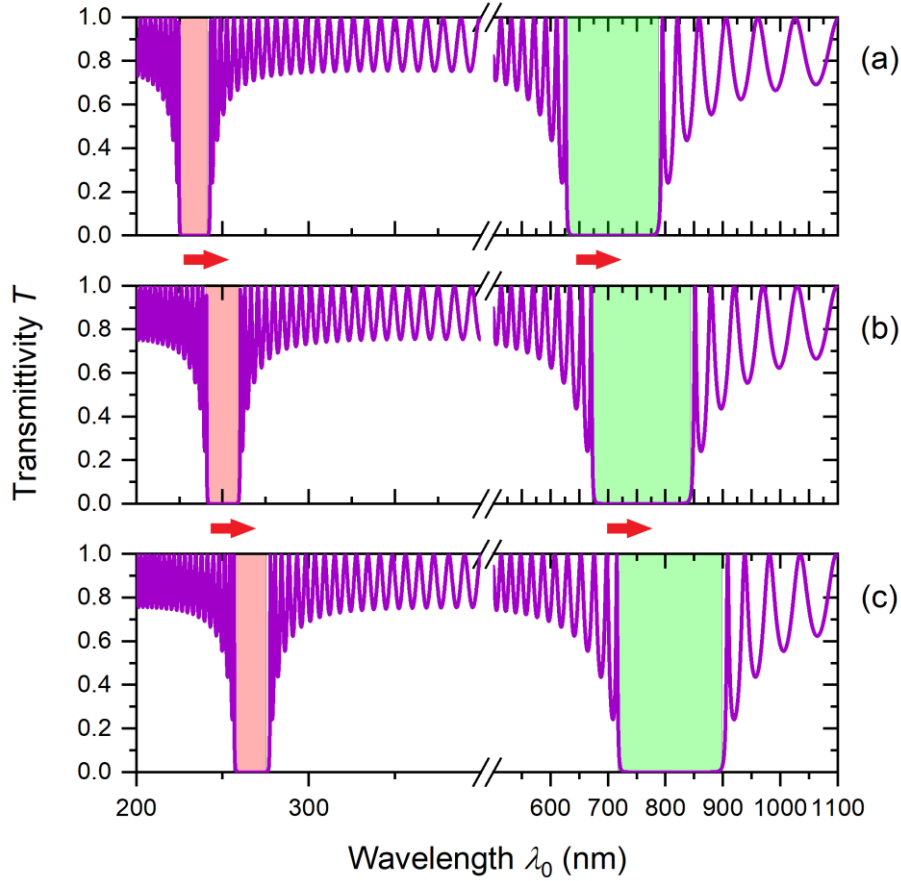


Fig. IV.1. Transmissivity spectrum of the periodic DBR. Top, central and bottom panels represent the cases with Bragg vacuum wavelengths equal to 700, 750 and 800 nm respectively. Red and green rectangles represent two neighboring bandgaps.

The combination process described by Eqs. (IV.2)–(IV.4) is a logical (Boolean) OR operation between the high index regions of the two periodic DBRs. Because of this precise mathematical definition, the reflector can be called deterministic (as opposed to random). A schematic of the result of such a combination is shown in Fig. IV.2(c).

Such a construction rule of the reflector gives us more parameters to play with. In particular, Bragg vacuum wavelengths λ_{Br} and λ'_{Br} will be used to adjust the spectral position of the photonic bandgaps of the reflector with great versatility.

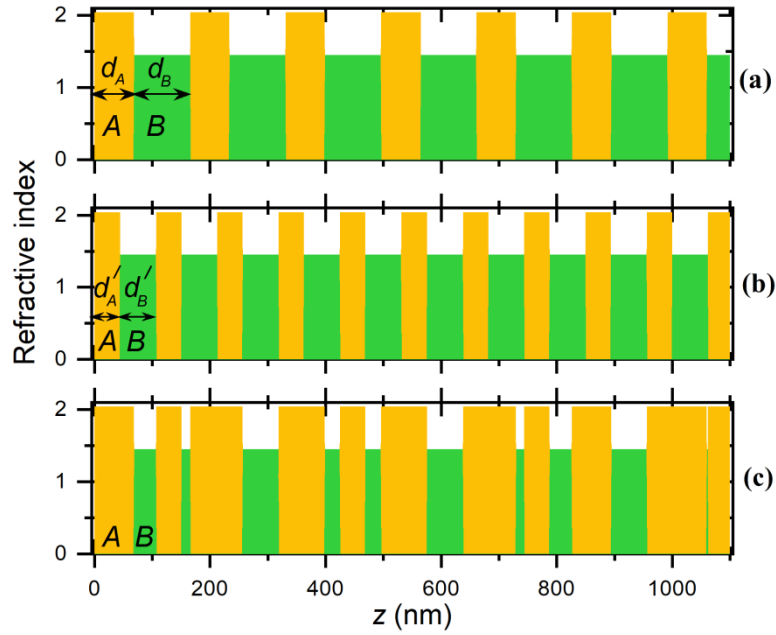


Fig. IV.2. (a) DBR $(AB)^N$ with thicknesses d_A and d_B for layers A and B ; (b) DBR $(AB)^{N'}$ with thicknesses d'_A and d'_B for layers A and B ; (c) deterministic aperiodic reflector obtained by the overlap of these periodic DBRs as described in Eqs. (IV.2)–(IV.4).

As an illustration, the transmittivity spectrum of the aperiodic reflector obtained with mathematical rule Eqs. (IV.2)–(IV.4) is shown in Fig. IV.3 for a fixed Bragg vacuum wavelength $\lambda_{Br} = 560$ nm for the first DBR and several choices of Bragg vacuum wavelength λ'_{Br} for the second DBR. Specifically, λ'_{Br} is taken as 340 nm in panel (a), 360 nm in panel (b), and 380 nm in panel (c), respectively.

Red and green regions denote two neighboring bandgaps. As we can see, changing the Bragg vacuum wavelength of one of the DBRs constituting the aperiodic reflector modifies the position of one of the bandgaps only (in red), whereas the second bandgap (in green) remains at the same spectral position. So λ_{Br} and λ'_{Br} can be used to gain independent control over the spectral positions of the bandgaps. In this case, the position of the lower-wavelength bandgap (in red) was controlled by the adjustment of the lower value of Bragg wavelengths λ_{Br} and λ'_{Br} . If one wishes to adjust the position of the higher-wavelength bandgap (in green), the higher value of λ_{Br} and λ'_{Br} should be modified.

The next logical step consists in considering a resonant structure with two such aperiodic reflectors facing each other, which will be called the left-hand side and the right-hand side reflectors.

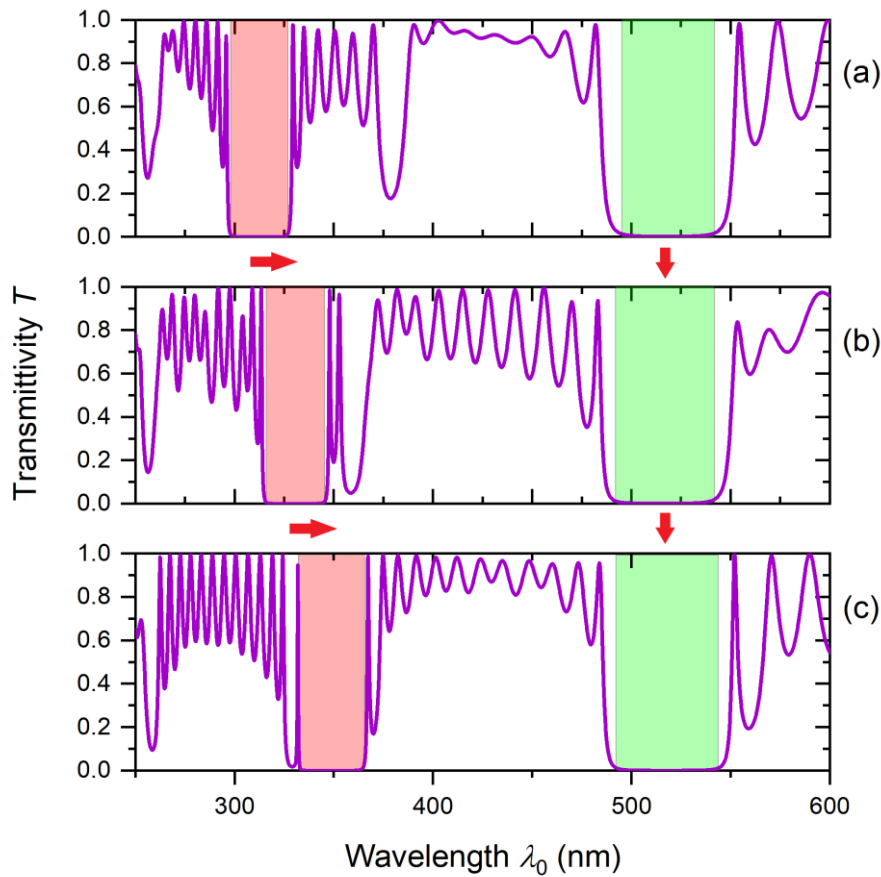


Fig. IV.3. Transmittivity spectrum of the aperiodic reflector. The first Bragg vacuum wavelengths λ_{Br} is fixed and equal to 560 nm. Panels (a), (b), and (c) correspond to values of the second Bragg vacuum wavelength λ'_{Br} equal to 340 nm, 360 nm and 380 nm, respectively.

The left-hand side reflector obeys the rules given by Eqs. (IV.2 – IV.4), so that $n_{left}(z) = n_{aper}(z)$, and the right-hand side one is its mirror image, so that the spatial dependence of its refractive index can be written as $n_{right}(z) = n_{left}(2L - z)$ for $L \leq z \leq 2L$, where L is the length of both reflectors.

Figure IV.4 shows the transmittivity spectrum of this structure in three cases, where Bragg vacuum wavelength λ_{Br} is fixed at 360 nm, and second Bragg vacuum wavelength λ'_{Br} is equal to 480 nm, 520 nm and 560 nm in panels (a), (b), and (c), respectively. As mentioned above, the position of the first bandgap (in red) remains the same for all three panels, whereas the second bandgap (in green) undergoes a red shift. Additionally, narrow transmittivity peaks similar to defect modes can appear in the bandgaps.

A further step towards the final structure consists in introducing a spacer between the reflectors,

made of a homogeneous SiO₂ layer (as in layers B), so that the structure is now a Fabry-Perot-like cavity.

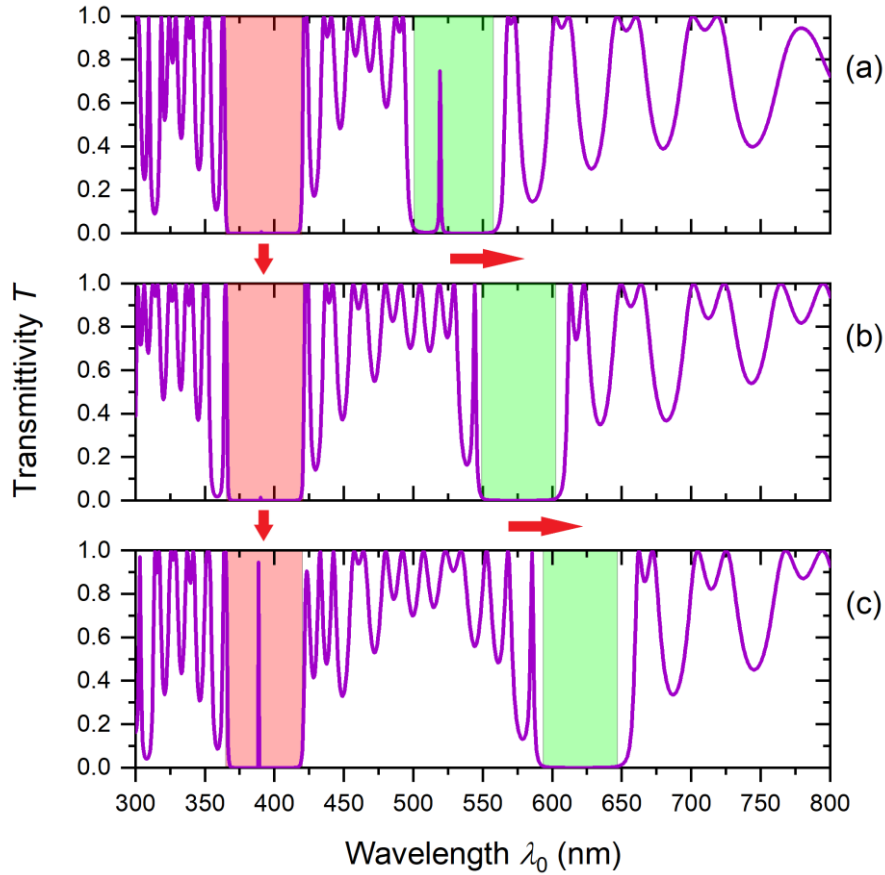


Fig. IV.4. Transmittivity spectrum of a structure consisting of two aperiodic reflectors mirroring each other. In each reflector, the first Bragg vacuum wavelengths λ_{Br} is fixed and equal to 360 nm. Panels (a), (b), and (c) correspond to values of the second Bragg vacuum wavelength λ'_{Br} equal to 480 nm, 520 nm, and 560 nm, respectively.

Figure IV.5 represents the transmittivity spectrum of the resulting structure in the vicinity of the higher-wavelength bandgap, for $\lambda_{Br} = 360$ nm and $\lambda'_{Br} = 560$ nm, and for a thickness d_D of the spacer (henceforth called layer D) varying between 0 and d_A .

This region of the spectrum corresponds to the green region of Fig. IV.4(c). Because of the presence of the central layer, a narrow defect mode appears in the bandgap, whose position varies with d_D . Figure IV.5 shows the superposition of the transmittivity spectrum for values of d_D varying between 0 (thick curve) and d_B with a step of $0.1d_B$. An increase of d_D induces a shift of the spectral position of the defect mode towards longer wavelengths (see red arrow in the figure). A similar behavior can be observed for defect modes in all bandgaps of the structure. As a result, the thickness

of the central spacer can be used as a control parameter that allows the adjustment of the defect modes inside the photonic bandgaps, while keeping the same spectral positions of these bandgaps.

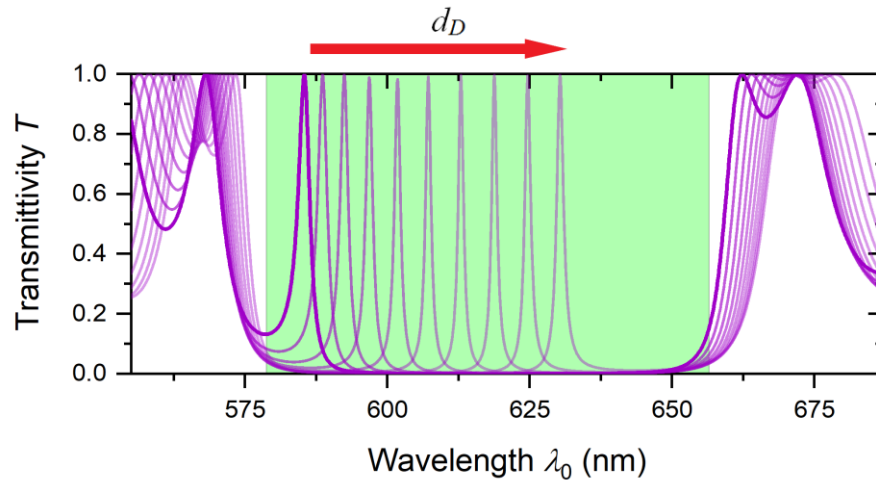


Fig. IV.5. Evolution of the higher-wavelength photonic bandgap of a Fabry-Perot-like cavity consisting of a central A layer surrounded by two mirroring aperiodic reflectors, for different thickness d_D of the central layer (from 0 to d_A with a step of $0.1d_A$). The thick curve corresponds to $d_D = 0$. The red arrow shows the direction of the shift of the defect mode with an increase of d_D .

It should be noted that there are other ways to combine two (or more) DBRs in order to design a deterministic aperiodic reflector and thus to define a Fabry-Perot-like cavity similar to the one described above. Other mathematical rules for the design of an aperiodic reflector could also be considered [35,36], provided of course the transmittivity spectrum of the resulting structure exhibits the desired spectral features, in particular, defect modes.

The final step will now consist in introducing a layer of metallic nanoparticles in the central layer in order to obtain a polarization-sensitive filter.

IV.3. Geometry of the composite photonic structure

The final structure under the study is a resonant photonic cavity consisting of two multilayered dielectric aperiodic reflectors separated by a dielectric layer D made of SiO_2 with thickness d_D , as shown in Fig. IV.6. A 2D array of spheroidal metallic NPs is located at the center of layer D . The reflector to the right of the layer D is the mirror image of the reflector to the left of that layer, so that the position of the NP array coincides with the center of the structure as a whole. As previously, the boundaries of all the layers are perpendicular to the z -axis of a Cartesian system of coordinates, so that

$z = 0$ is the position of the first interface and the whole structure is located in the region $z \geq 0$.

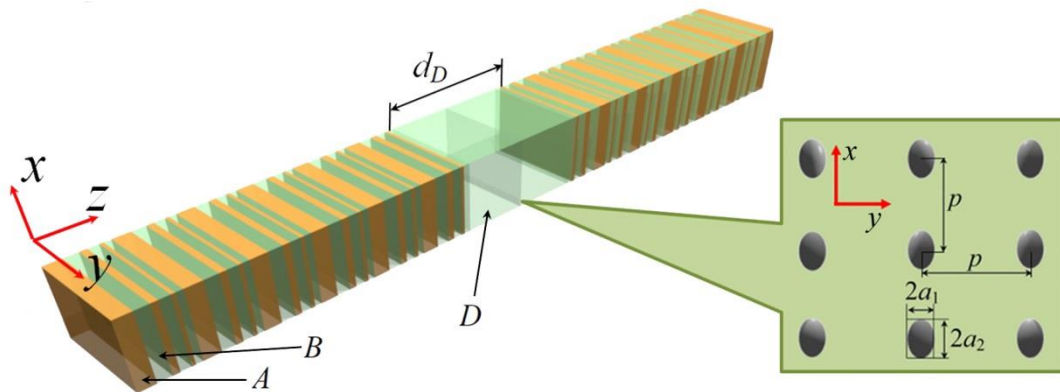


Fig. IV.6. Schematic of the composite photonic structure. Two symmetrical deterministic aperiodic multilayered reflectors consisting of alternate A (in orange) and B (in green) layers are separated by a layer D (thickness d_D). A 2D array of spheroidal metallic nanoparticles, characterized by the dimensions $2a_1$ and $2a_2$ of the particles and the interparticle distance p , is located at the center of the structure.

As it was in the structure discussed in Fig. IV.5, the Bragg vacuum wavelengths for the DBRs $(AB)^N$ and $(AB)^{N'}$ constituting the aperiodic reflectors are chosen as $\lambda_{Br} = 360$ nm and $\lambda'_{Br} = 560$ nm. Thus, the thicknesses of the layers in these DBRs are $d_A \approx 44.55$ nm, $d_B \approx 62$ nm and $d'_A \approx 69.3$ nm, $d'_B \approx 96.55$ nm, respectively, so that the thickness of the unit cell is smaller in $(AB)^N$ than in $(AB)^{N'}$. The number of periods N' in DBR $(AB)^{N'}$ was chosen so that the length $L = 2131$ nm of that reflector is the same as that of DBR $(AB)^N$ for $N = 20$.

It should be noted that for the chosen value $N = 20$, the resulting multilayered reflector does not exhibit translational symmetry, *i.e.*, the total length of this reflector is smaller than its periodic cell (it can be shown that a periodic cell of this photonic structure is obtained for $N = 28$). However, as one can see from the results discussed below, even with $N = 20$, this deterministic aperiodic PC (and its counterpart on the right-hand side of layer D) is enough to ensure the existence of photonic bandgaps in the spectral regions encompassing the plasmon resonances in the metallic NPs. The number of layers of the dielectric reflectors surrounding the cavity was chosen on the basis of a standard criterion: it should be sufficient to allow sufficiently pronounced photonic bandgaps, *i.e.*, bandgaps approaching ideal features (vertical boundaries and zero transmittivity). In a structure with fewer layers the features

of the photonic bandgaps are degraded – in particular, full reflectivity is not achieved. Moreover, reducing the number of layers in the reflectors leads to a decrease in the amplitude of the defect modes due to a reduction of the quality factor of the cavity.

The NPs located at the center of layer D are placed at the nodes of a 2D square lattice with period p that exhibits translational invariance along the x - and y -axes of the (xyz) Cartesian coordinate system (see Fig. IV.6). All NPs are identical prolate spheroids and are similarly aligned, with their long axis parallel to the x -axis, and their shape is characterized by aspect ratio $\xi = a/b$, where a and b are the half-lengths of their polar and equatorial axes, respectively ($a > b$). The typical dimensions of the NPs and the period p of the square lattice are much smaller than the typical wavelength of the optical wave in layer D , i.e., $\{2a, 2b, p\} \ll \lambda_0 / n_B$, where λ_0 is the wavelength in vacuum.

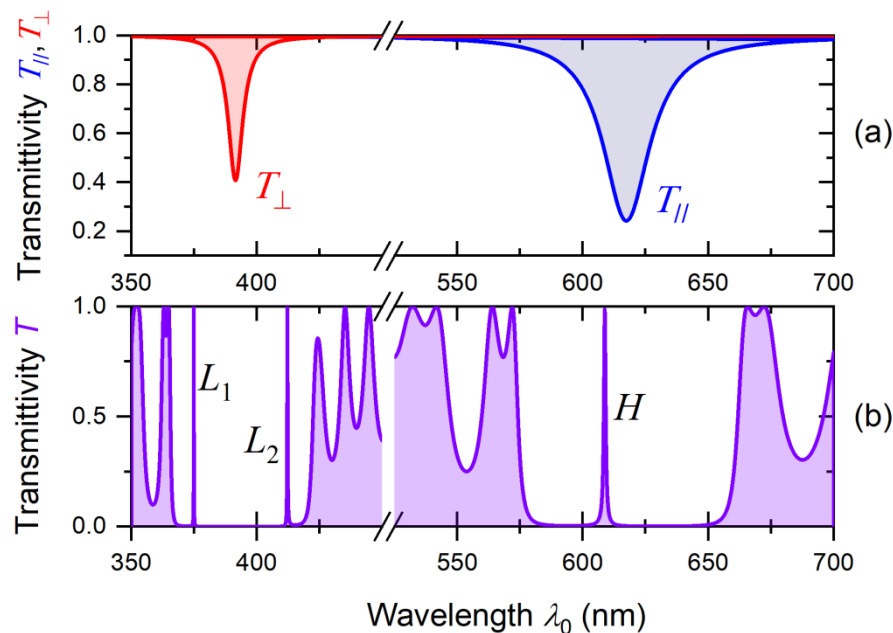


Fig. IV.7. (a) Transmittivity spectra of the NP array embedded in a SiO_2 matrix for the x -polarized (blue curve) and y -polarized (red curve) incoming light. The dips are due to surface plasmon resonances in the NPs. (b) Transmittivity spectrum of the photonic structure without NP array. The two defect modes in the lower-wavelength bandgap and the defect mode in the higher-wavelength bandgap are denoted L_1 , L_2 , and H , respectively.

In the following, let us consider an incident plane wave in the visible regime that impinges under normal incidence on the left-hand side of the structure, at abscissa $z = 0$. The time dependence of the electromagnetic fields is taken as $\exp(-i\omega t)$, where $\omega = 2\pi c/\lambda_0$ is the angular frequency of the

incoming plane wave and c is the velocity of light in vacuum. The dimensions of the layers along the x - and y -axes are much larger than their thicknesses along the z -axis, and are thus taken to be infinite in the calculations.

Parameters are chosen to have two neighboring bandgaps and two plasmon resonances to coincide with each of the bandgap. In the first bandgap there are two defect modes (the reasons for that will be discussed later). Fig. IV.7. shows the transmittivity spectrum of the photonic structure without 2D NP array and the transmittivity dips due to surface plasmon resonances in the sole 2D NP array embedded in SiO_2 .

As in Chapters II and III, the subscripts $//$ and \perp refer to the linear polarization directions respectively parallel and perpendicular to the main (polar) axis of the NPs, *i.e.*, to the x -axis.

Panel (a) in Fig. IV.7 shows the transmittivity spectrum of the sole 2D NP array embedded in a SiO_2 matrix. The array consists of silver (Ag) particles, and the interparticle distance and aspect ratio of the NPs are taken as $p = 15$ nm and $\xi = 2.5$, respectively. For $a_1 = 5$ nm, each NP is a prolate nanospheroid whose principal axes are 10 nm \times 4 nm \times 4 nm in length. The periodicity of the array and the dimensions of the NPs have been chosen so that this spectrum exhibits a broad dips inside two neighboring bandgaps. Those dips correspond to the polarization-sensitive excitation of a localized surface plasmon resonance in the 2D array of metallic NPs. As was already shown in Chapter III, the width of the transmission dip due to the excitation of a plasmon resonance in the 2D array of nanoparticles depends on the strength of the interaction between particles and the optical wave, which in turn depends on a number of parameters, including material parameters, the distance between neighboring particles, their shape, and their orientation relative to the optical field. For the parameters used in this Chapter, the strength of the interaction between the NPs and the optical wave at plasmonic resonance frequency is indeed expected to be significantly higher for x -polarized light, as that direction coincides with the axis of revolution of the NPs, for which their electric dipole moments are larger. As a result, the transmission dip for x -polarized light (FWHM ≈ 22 nm) is broader than the dip observed for y -polarized light (FWHM ≈ 7 nm).

Panel (b) in Fig. IV.7 shows the transmittivity spectrum of the aperiodic structure without NPs in layer D . Unless otherwise indicated, the thickness of the central layer is taken as $d_D \approx 485.4$ nm. This value (as well as those of the thicknesses and refractive indices of all the layers of the structure) is chosen so that two defect modes (hereinafter called L_1 and L_2 , located at approximately 375 nm and 412 nm, respectively) appear in the lower-wavelength bandgap and one (denoted H , at 609 nm) in the higher-wavelength one, in both cases away from the bandgap edges. The lower-wavelength bandgap

is narrower (with a width of approximately 56 nm) than its higher-wavelength counterpart (width approximately equal to 86 nm). It should be noted that in this case the spectrum of the photonic structure does not depend on the state of polarization of the incoming electromagnetic wave, as the structure does not include any anisotropic element. The reason for choosing a configuration where one of the bandgaps exhibits two defect modes whereas the other exhibits only one defect mode will be discussed below.

IV.4. Results and discussion

In the following, the calculated transmittivity spectra of the structure for x - and y -polarized incident light are discussed in relation with the respective spectral positions of two of its defect modes and the surface plasmon resonances in the NP array. The crucial roles played by the position of the latter within layer D and the thickness of that layer are highlighted, and the mechanism of a polarization-dependent suppression of the defect modes is detailed.

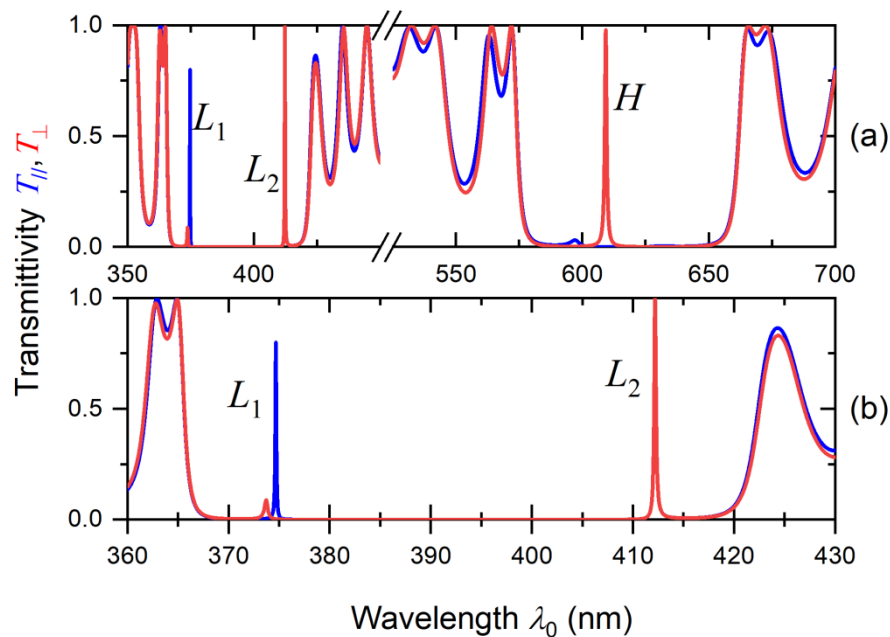


Fig. IV.8. (a) Transmittivity spectra of the photonic structure with 2D array of NPs for x -polarized (blue curve) and y -polarized (red curve) incoming lightwave; (b) zoom on the lower-wavelength bandgap. Two defect modes in the lower-wavelength bandgap and the defect mode in the higher-wavelength bandgap are denoted L_1 , L_2 , and H , respectively.

Figure IV.8 represents the transmittivity spectra of the photonic structure under consideration in a near-UV and visible spectral range encompassing two neighboring photonic bandgaps when 2D NP array is placed at its center (see Fig. IV.6) for x - and y -polarization states of the incoming wave.

Parameters of the structure are the same as for Fig. IV.7.

For either of these polarization states, the plasmon resonance excited in the NPs is broad enough to encompass a defect mode of the structure, which leads to a significant decay and a slight blue shift of that mode. Specifically, the defect mode affected by the presence of the NPs is the one (denoted H in Figs. IV.7 and IV.8) in the higher-wavelength bandgap for x -polarized light, whereas it is the defect mode L_1 in the lower-wavelength bandgap for y -polarized light (Figs. IV.7 and IV.8). The reason for which the defect mode L_2 remains unchanged in the presence of the NP array will be discussed below, in relation to Figs. IV.9 and IV.10.

The attenuation of defect modes L_1 and H results from the absorption of light following from the excitation of a plasmon resonance in the NPs. The spectral blue shift they exhibit is caused by the influence of the NP array on the phase of the electromagnetic field in layer D .

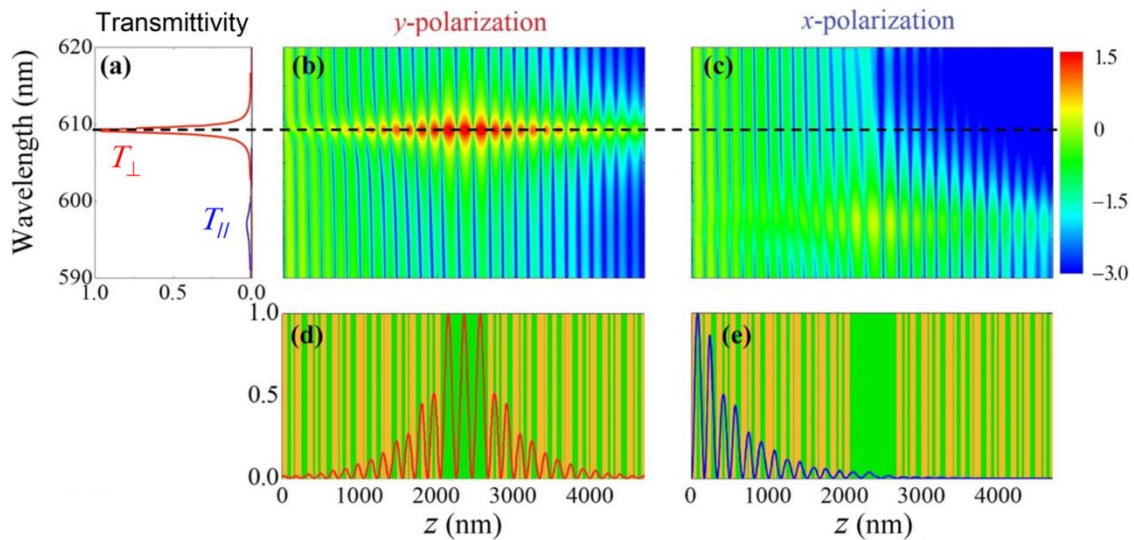


Fig. IV.9. Spectral characteristics of the aperiodic structure in the vicinity of defect mode H in the higher-wavelength bandgap: (a) Zoom on the transmittivity spectra for x - and y -polarized light; (b) and (c) distribution of the square of the normalized optical field magnitude $|E(z)/E(0)|^2$ (in logarithmic scale) in the structure for y - and x -polarized light, respectively; (d) and (e) square of the optical field magnitude normalized to its maximum value ($|E(z)/\max[E(z)]|^2$) at wavelength $\lambda_0 = 609$ nm (see black dashed line in the top panels) for y - and x -polarized light, respectively. As in Figs. IV.2 and IV.6, the vertical color bars in panels (d) and (e) denote the alternate layers of the structure.

In Fig. IV.9, panel (a) represents the transmittivity spectra $T_{//}$ and T_{\perp} for x - and y -polarized light in

the vicinity of defect mode H in the higher-wavelength bandgap, whereas panels (b) and (c) show the spatial distribution of the square of the normalized optical field magnitude $|E(z)/E(0)|^2$ in the same spectral domain. Finally, panels (d) and (e) represent the square of the optical field magnitude normalized to its maximum value ($|E(z)/\max[E(z)]|^2$) at the wavelength $\lambda_0 = 609$ nm of defect mode H . For y -polarized light (panels (b) and (d)), a strong field localization is observed in layer D at this wavelength, with three almost equal optical field amplitude maxima. The thickness of that layer is chosen so that one of these maxima coincides with the position of the NP array (at the center of the layer). In comparison, for x -polarized light (panels (c) and (e)), field localization at the position of NP array appears at the lower wavelength of approximately 597 nm corresponding to the reduced and frequency-shifted defect mode (as discussed above), and the field maxima are significantly smaller than for y -polarized light (compare the transmission spectra in panel (a)).

Similar distributions of the optical field take place around the wavelength $\lambda_0 = 375$ nm of defect mode L_1 , but with a reversed polarization dependence of the mode suppression as in the case of mode H (see Fig. IV.8). Namely, L_1 is almost completely absorbed as a result of plasmon excitation for y -polarized incident light. For x -polarized light, defect mode L_1 experiences a weak influence of the tail of the broad plasmon resonance centered in the higher-wavelength bandgap, which is why it is only slightly attenuated.

As mentioned above, the plasmon resonance of the NP array for y -polarized light (red curve in Fig. IV.7) is located between the two defect modes L_1 and L_2 . However, only the former is suppressed due to localized surface plasmon excitation. This can be explained in light of Fig. IV.10, where the spatial distribution of the optical field in the photonic structure without NP array is shown at the wavelength $\lambda_0 = 375$ nm of defect mode L_1 (Fig. IV.10 (a)) and at the wavelength $\lambda_0 = 412$ nm of defect mode L_2 (Fig. IV.10(b)) for any polarization state.

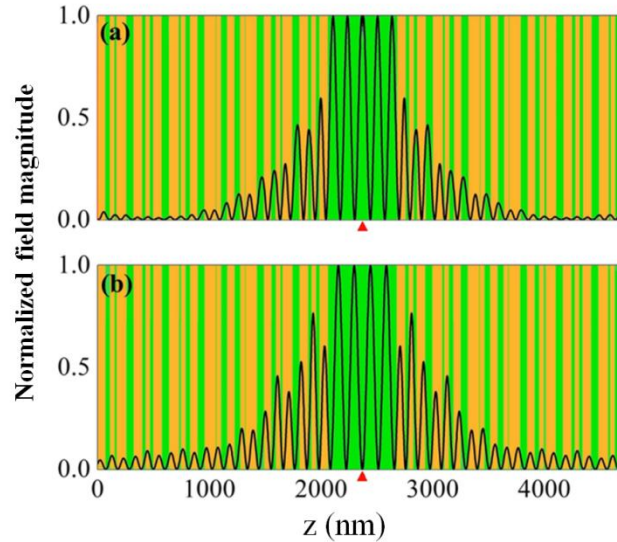


Fig. IV.10. Square of the optical field magnitude normalized on its maximum value ($|E(z)/\max[E(z)]|^2$) in the photonic structure without NP array (a) at wavelength $\lambda_0 = 375$ nm of defect mode L_1 and (b) at wavelength $\lambda_0 = 412$ nm of defect mode L_2 for any state of polarization. The red triangles indicate the center of the photonic structure.

In the first case, the optical field exhibits a maximum at the center of the structure (shown by a red triangle in the figure), which, when a 2D NP array is embedded at that position, results in a very efficient excitation of a collective oscillation of the free conduction electrons in the NPs, hence a very strong suppression of defect mode L_1 . In the second case, the field is almost zero at that location and the impact of the metallic NPs on the optical field is negligible. As a consequence, defect mode L_2 is not affected by the presence of the NP array. Note that the optical field is also has a maximum in the plane of the NP array at the wavelength $\lambda_0 = 609$ nm of defect mode H for y -polarized light (as can be seen from Fig. IV.9(d)), but in that case, that mode is not suppressed by plasmon resonance, as the resonance in the NPs for y -polarized light occurs far away from 609 nm, in the lower-wavelength bandgap of the structure (see red curve in Fig. IV.7). Unlike what was discussed above about L_1 , defect mode H does not experience much influence from the tail of the plasmon resonance centered in the lower-wavelength bandgap, as that resonance is significantly narrower than that centered in the higher-wavelength bandgap.

In effect, Figs. IV.8 and IV.9 thus show that the polarization-dependent spectral behavior of the structure is determined both by matching the plasmon and optical defect modes and by adjusting the spatial position of the nanoparticles with respect to the antinodes of the optical field in the photonic crystal.

Figure IV.11 illustrates the polarization-sensitive dependence of the transmittivity spectra $T_{//}$ and T_{\perp} in both photonic bandgaps as functions of the thickness of layer D . As mentioned above, that thickness has until now assumed the nominal value $d_D \approx 485.4$ nm. The spectral variations of $T_{//}$ and T_{\perp} are represented for thicknesses of layer D ranging from approximately $0.25 d_D$ to $2.25 d_D$.

The behavior of the narrow transmission passbands (defect modes in the photonic bandgaps) is identical in all the cases presented in Fig. IV.11: as the thickness of the D layer increases, they form at the short-wavelength edge of the bandgap and shift to its long-wavelength edge, where they subsequently vanish. In each of the bandgaps, up to two defect modes can be formed simultaneously. Of particular interest is the fact that intervals of layer D thickness can be found for which defect modes are simultaneously suppressed in the lower-wavelength bandgap for x -polarized light and in the higher-wavelength bandgap for y -polarized light. This makes it possible to achieve the polarization-dependent transmittivity response required in a polarization-sensitive dichroic filter. In Fig. IV.11, this selective suppression of the defect modes due to the hybridization of plasmonic and photonic modes in the structure manifests itself through the absence, for a given thickness of layer D , of every second S -shaped transmission line, either for x -polarized light (Fig. IV.11(a)) or for y -polarized light (Fig. IV.11(d)), but not for both simultaneously. Note that with an increase of the strength of the interaction between the plasmonic and photonic subsystems, the suppression and shift of the photonic modes take place (see also Fig. IV.8).

The dependence of the transmittivity spectra on the thickness of layer D deserves further discussion. For a thickness of layer D equal to d_D (vertical dashed white lines), previously discussed defect modes L_1 and L_2 in the lower-wavelength bandgap can be seen (dashed white circles) in Fig. IV.11(c), and the suppression of L_1 (but not L_2) for a y -polarized incident light beam is visible in Fig. IV.11(d).

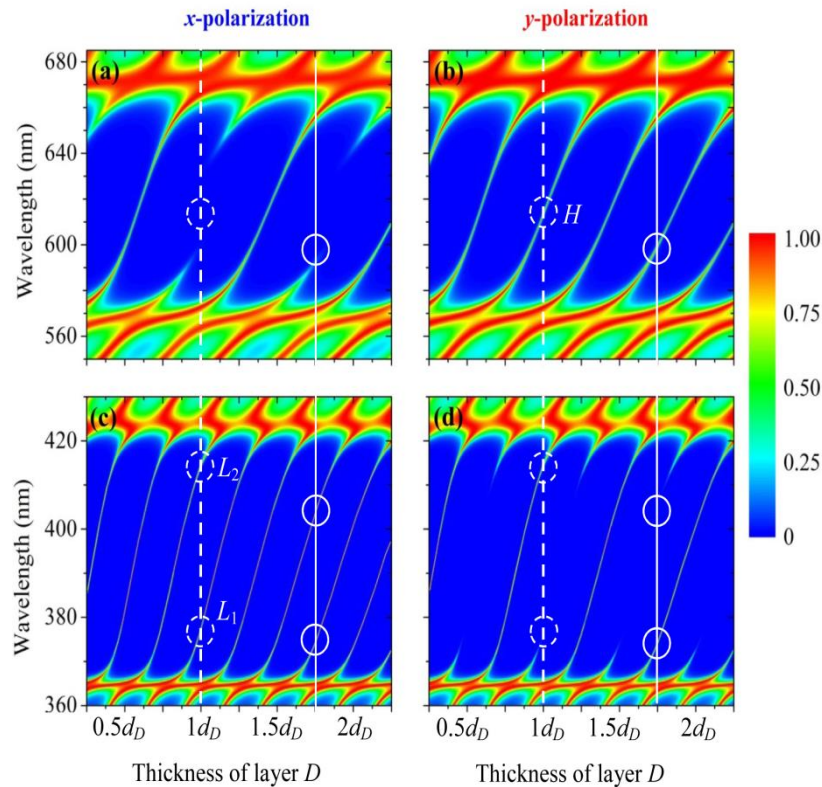


Fig. IV.11. Evolution of transmittivity spectra $T_{//}$ [panels (a) and (c)] and T_{\perp} [panels (b) and (d)] in the higher-wavelength bandgap (top panels) and lower-wavelength bandgap (bottom panels) as functions of the thickness of layer D expressed in terms of nominal thickness d_D . The white dashed lines represent the case where that thickness is exactly equal to d_D , as in Figs. IV.8 to IV.10. The white solid lines represent the case where layer D thickness is equal to $1.75d_D$. The white circles denote the spectral positions of the defect modes L_1 , L_2 and H discussed in the paper for these two thicknesses. The 2D array of NPs is located at the center of layer D .

Similarly, the existence of defect mode H in the higher-wavelength bandgap (dashed white circle) and its suppression for an x -polarized light beam are clearly visible in Figs. IV.11(a) and IV.11(b), respectively. The cross-sections of the transmittivity spectra along the vertical white dashed lines shown in Fig. IV.11 correspond to the curves presented in Fig. IV.8.

What Figs. IV.11 also shows is that a similar polarization-sensitive behavior in the lower-wavelength bandgap can be observed when the thickness of layer D slightly increases from d_D up to approximately $1.25 d_D$. Obviously, in so doing, the spectral positions of the defect modes change. In addition, defect mode L_2 disappears, and defect mode L_1 shifts towards larger wavelengths. As for defect mode H in the higher-wavelength bandgap, its successful suppression can be achieved for a

thickness of layer D ranging from $0.9 d_D$ to $1.1 d_D$ approximately. In effect, the structure can thus be considered as a polarization-controlled dichroic filter when those intervals overlap, *i.e.*, for values of the layer D thickness in the interval $[d_D, 1.1 d_D]$.

As a matter of fact, such a polarization-dependent suppression of defect modes can also occur for other thicknesses of layer D , in which case the relative spectral positions of the relevant defect modes can be different. In particular, this situation can be observed in the thickness range $[1.75 d_D, 1.85 d_D]$, as highlighted with solid vertical white lines and solid white circles in Figs. IV.11.

Finally, it must be pointed out that the spectral characteristics of the composite photonic structure under study, based on the use of aperiodic dielectric reflectors, can vary over a rather wide range due to the large number of independent constitutive parameters that define its design (nature of the materials, layer thicknesses, rules governing the way they alternate, etc.). Thus it is also possible to design the photonic structure so that it exhibits a single defect mode in each of two neighboring bandgaps, and to obtain a spatial distribution of the optical field such that the excitation of plasmon resonances in the 2D array of nanoparticles allows polarization-selective suppression of these defect modes. In this Chapter, however, we elected to consider a structure exhibiting two defect modes in one of the photonic bandgaps. This deliberate choice has made it possible, on the one hand, to demonstrate the significance of the spatial overlap of the nanoparticle array with a region of high optical field localization in the structure, and, on the other hand, to point out the possibility of selective cancellation of one of two defect modes within the same photonic bandgap.

IV.5. Conclusions

- A new design for a dichroic filter combining a 2D array of metallic nanoparticles and aperiodic dielectric reflectors has been proposed.
- The choice of a 2D nanoparticle array, rather than a 3D nanoparticle dispersion, lends itself to a less complex fabrication process and to much less energy dissipation.
- The use of a deterministic aperiodic photonic crystal makes it possible to tailor the spectral position of the bandgaps and defect modes of that structure in such a way that two of these defect modes, located in separate bandgaps, can be adjusted and provide the required narrow transmittivity windows of the filter. Their non-simultaneous, polarization-sensitive suppression is achieved through the inclusion of a composite resonant layer at the center of the photonic structure. Two surface plasmon resonances

excited, for two mutually orthogonal linear states of polarization of the incoming light, in a two-dimensional array of prolate, spheroidal metallic nanoparticles embedded in that layer, can be exploited to that effect. For well-chosen values of the structural parameters of both the photonic crystal and the array of metallic nanoparticles, each of the two plasmon resonances of the latter can be made to encompass one of the two selected defect modes of the former, thus ensuring a nearly total extinction of one or the other of these modes — depending on the polarization state of the incoming light beam.

- Among the various parameters governing the precise position of the transmittivity windows of the structure as a dichroic filter, the strong influence of the thickness of the composite defect layer in which the array of metallic nanoparticles is embedded was established. Other structural parameters, however, constitute as many degrees of freedom for the design of such a filter, including the geometry of the photonic crystal, the nature of its layers, the period of the metallic nanoparticle array, the aspect ratio of the nanoparticles themselves, or the nature of the metal.
- Further ways of controlling the spectral and polarization-related characteristics of that filter could be envisioned, such as the use of several metallic nanoparticle arrays, or the combination of nanoparticle array(s) with other types of anisotropic media (liquid crystals with dichroic dyes, dichroic glasses, etc.). Moreover, the principles described in this study remain valid in other spectral regions, provided plasmon resonance frequencies can be made to coincide with defect modes in a multilayered photonic structure, for instance for optical communication systems in the near-infrared domain. Other potential applications of such polarization-sensitive dichroic filters include for instance the development of polarization-sensitive single-photon detectors [37,38], or plasmonic absorbers [39] and nano-sensors.

IV.6. List of references

- [1] F.-J. Ko and H.-P. David Shieh, “High-efficiency micro-optical color filter for liquid-crystal projection system applications,” *Appl. Opt.* **39**, 1159 (2000).
- [2] M. Peters, J. C. Goldschmidt, P. Löper, B. Groß, J. Üpping, F. Dimroth, R. B. Wehrspohn, and B. Bläsi, “*Spectrally-selective photonic structures for PV applications*,” *Energies* **3**, 171 (2010).
- [3] J. W. Archer, “A novel quasi-optical frequency multiplier design for millimeter and submillimeter wavelengths,” *IEEE Trans. Microwave Theory Tech.* **32**, 421 (1984).
- [4] J. D. Joannopoulos, R. D. Meade, and J. N. Winn, *Photonic Crystals* (Princeton University Press, Princeton, 1995).
- [5] K. Inoue and K. Ohtaka (Eds.), *Photonic Crystals: Physics, Fabrication and Applications* (Springer-Verlag, Berlin, 2004).
- [6] Q. Gong and X. Hu, *Photonic Crystals: Principles and Applications* (Pan Stanford, 2014).
- [7] D. D. Nolte, A. E. Lange, and P. L. Richards, “Far-infrared dichroic bandpass filters,” *Appl. Opt.* **24**, 1541-1545 (1985).
- [8] N. Sharma, N. Destouches, C. Florian, R. Serna, and J. Siegel, “Tailoring metal-dielectric nanocomposite materials with ultrashort laser pulses for dichroic color control,” *Nanoscale* **11**, 18779 (2019).
- [9] C.-S. Park, I. Koirala, S. Gao, V. R. Shrestha, S.-S. Lee, and D.-Y. Choi, “Structural color filters based on an all-dielectric metasurface exploiting silicon-rich silicon nitride nanodisks,” *Opt. Express* **27**, 667-679 (2019).
- [10] I. Koirala, S.-S. Lee, and D.-Y. Choi, “Highly transmissive subtractive color filters based on an all-dielectric metasurface incorporating TiO₂ nanopillars,” *Opt. Express* **26**, 18320-18330 (2018).
- [11] V. E. Babicheva, M. I. Petrov, K. V. Baryshnikova, and P. A. Belov, “Reflection compensation mediated by electric and magnetic resonances of all-dielectric metasurfaces [Invited],” *J. Opt. Soc. Am. B* **34**, D18-D28 (2017).
- [12] V. I. Zakomirnyi, A. E. Ershov, V. S. Gerasimov, S. V. Karpov, H. Ågren, and I. L. Rasskazov, “Collective lattice resonances in arrays of dielectric nanoparticles: a matter of size,” *Opt. Lett.* **44**, 5743-5746 (2019).
- [13] S. G. Moiseev, “Nanocomposite-based ultrathin polarization beamsplitter,” *Opt. Spectrosc.* **111**, 233-240 (2011).
- [14] H. Yu, Z. Liang, D. Meng, J. Tao, J. Liang, X. Su, Y. Luo, X. Xu, and Y. Zhang, “Polarization-selective dual-band infrared plasmonic absorber based on sub-wavelength gaps,” *Optics Communications* **446**, 156-161 (2019).
- [15] A. Muravitskaya, A. Movsesyan, S. Kostcheev, and P.-M. Adam, “Polarization switching between parallel and orthogonal collective resonances in arrays of metal nanoparticles,” *J. Opt. Soc. Am. B* **36**, E65-E70 (2019).
- [16] Y. H. Lu, M. D. Huang, S. Y. Park, P. J. Kim, T.-U. Nahm, Y. P. Lee, and J. Y. Rhee, “Controllable switching behavior of defect modes in one-dimensional heterostructure photonic crystals,” *J. Appl. Phys.* **101**, 036110 (2007).

- [17] N. Ouchani, D. Bria, B. Djafari-Rouhani, and A. Nougaoui, “*Defect modes in one-dimensional anisotropic photonic crystal*,” J. Appl. Phys. **106**, 113107 (2009).
- [18] P. Singh, K. B. Thapa, N. Kumar, D. Singh, and D. Kumar, “*Effective optical properties of the one-dimensional periodic structure of TiO₂ and SiO₂ layers with a defect layer of nanocomposite consisting of silver nanoparticle and E7 liquid crystal*,” Pramana – J. Phys. **93**, 50 (2019).
- [19] J.-X. Liu, H.-Y. Xu, Z.-K. Yang, X. Xie, Y. Zhang, and H.-W. Yang, “*A research of magnetic control ferrite photonic crystal filter*,” Plasmonics **12**, 971–976 (2017).
- [20] S. Isaacs, F. Placido, and I. Abdulhalim, “*Investigation of liquid crystal Fabry–Perot tunable filters: design, fabrication, and polarization independence*,” Appl. Opt. **53**, H91-H101 (2014).
- [21] J. W. Klos, M. Krawczyk, Yu. S. Dadoenkova, N. N. Dadoenkova, and I. L. Lyubchanskii, “*Photonic-magnonic crystals: Multifunctional periodic structures for magnonic and photonic applications*”, J. Appl. Phys. **115**, 174311 (2014).
- [22] Y. S. Dadoenkova, N. N. Dadoenkova, I. L. Lyubchanskii, J. W. Klos, and M. Krawczyk, “*Confined states in photonic-magnonic crystals with complex unit cell*”, J. Appl. Phys. **120**, 073903 (2016).
- [23] N. N. Dadoenkova, Y. S. Dadoenkova, I. S. Panyaev, D. G. Sannikov, and I. L. Lyubchanskii, “*One-dimensional dielectric bi-periodic photonic structures based on ternary photonic crystals*,” J. Appl. Phys. **123**, 043101 (2018).
- [24] I. S. Panyaev, L. R. Yafarova, D. G. Sannikov, N. N. Dadoenkova, Y. S. Dadoenkova, and I. L. Lyubchanskii, “*One-dimensional multiperiodic photonic structures: A new route in photonics (four-component media)*,” J. Appl. Phys. **126**, 103102 (2019).
- [25] D. Qi, X. Wang, Y. Cheng, F. Chen, L. Liu, and R. Gong, “*Quasi-periodic photonic crystal Fabry–Perot optical filter based on Si/SiO₂ for visible-laser spectral selectivity*,” J. Phys. D: Appl. Phys. **51**, 225103 (2018).
- [26] C. A. A. Araújo, M. S. Vasconcelos, P. W. Mauriz, and E. L. Albuquerque, “*Omnidirectional band gaps in quasiperiodic photonic crystals in the THz region*,” Opt. Mater. **35**, 18-24 (2012).
- [27] A. M. Vyunishev, P. S. Pankin, S. E. Svyakhovskiy, I. V. Timofeev, and S. Ya. Vetrov, “*Quasiperiodic one-dimensional photonic crystals with adjustable multiple photonic bandgaps*,” Opt. Lett. **42**, 3602-3605 (2017).
- [28] M. Tavakoli and Y. S. Jalili, “*One-dimensional Fibonacci fractal photonic crystals and their optical characteristics*,” J. Theor. Appl. Phys **8**, 113 (2014).
- [29] Y. Wang, and S. Jian, S. Han, S. Feng, Z. Feng, B. Cheng, and D. Zhang, “*Photonic band-gap engineering of quasiperiodic photonic crystals*,” J. Appl. Phys. **97**, 106112 (2005).
- [30] M. Bellingeri, A. Chiasera, I. Kriegel, and F. Scotognella, “*Optical properties of periodic, quasi-periodic, and disordered one-dimensional photonic structures*,” Opt. Mat. **72**, 403-421 (2017).
- [31] J. Xavier, J. Probst, and C. Becker, “*Deterministic composite nanophotonic lattices in large area for broadband applications*,” Sci. Reports **6**, 38744 (2016).

- [32] L. Dal Negro and S. V. Boriskina, “*Deterministic aperiodic nanostructures for photonics and plasmonics applications*,” *Laser and Photonics Reviews* **6**, 178-218, (2012).
- [33] M. Jerman, Z. Qiao, and D. Mergel, “*Refractive index of thin films of SiO₂, ZrO₂, and HfO₂ as a function of the films’ mass density*,” *Appl. Opt.* **44**, 3006-3012 (2005).
- [34] M. Born and E. Wolf, *Principles of Optics* (Cambridge University Press, Cambridge, 1999).
- [35] M. Bellingeri, A. Chiasera, I. Kriegel, F. Scotognella, “*Optical properties of periodic, quasi-periodic, and disordered one-dimensional photonic structures*”, *Opt. Mater.* **72**, 403-421 (2017).
- [36] J. Wei, F. Sun, B. Dong, Y. Ma, Y. Chang, H. Tian, C. Lee, “*Deterministic aperiodic photonic crystal nanobeam supporting adjustable multiple mode-matched resonances*”, *Opt. Lett.* **43**, 5407-5410 (2018).
- [37] D. Li and R. Jiao, “*Design of a low-filling-factor and polarization-sensitive superconducting nanowire single photon detector with high detection efficiency*,” *Photon. Res.* **7**, 847-852 (2019).
- [38] F. Zheng, X. Tao, M. Yang, G. Zhu, B. Jin, L. Kang, W. Xu, J. Chen, and P. Wu, “*Design of efficient superconducting nanowire single photon detectors with high polarization sensitivity for polarimetric imaging*,” *J. Opt. Soc. Am. B* **33**, 2256-2264 (2016).
- [39] F. Chen, L. Sun, H. Zhang, J. Li, and C. Yu, “*Plasmonic absorber and nanosensor assisted by metal films coupled with hexagonal holes array*,” *Optik* **181**, 115-122 (2019).

CHAPTER V

NON-SPECULAR REFLECTION OF A NARROW SPATIALLY PHASE-MODULATED MICROWAVE GAUSSIAN BEAM

V.1. Introduction

Non-specular effects occurring upon the reflection of light wavepackets from various optical structures have been intensively studied in the last two decades. These effects include both lateral and transverse shifts of the reflected beams relative to the position predicted by ray optics (first described, in the context of the total internal reflection, as the Goos-Hänchen [1] and the Imbert-Fedorov [2], [3] effects, respectively) [4], as well as the corresponding angular shifts in the plane of incidence or perpendicular to it, i.e., deviations of the reflection angle from the value it takes in the frame of geometric optics [5,6].

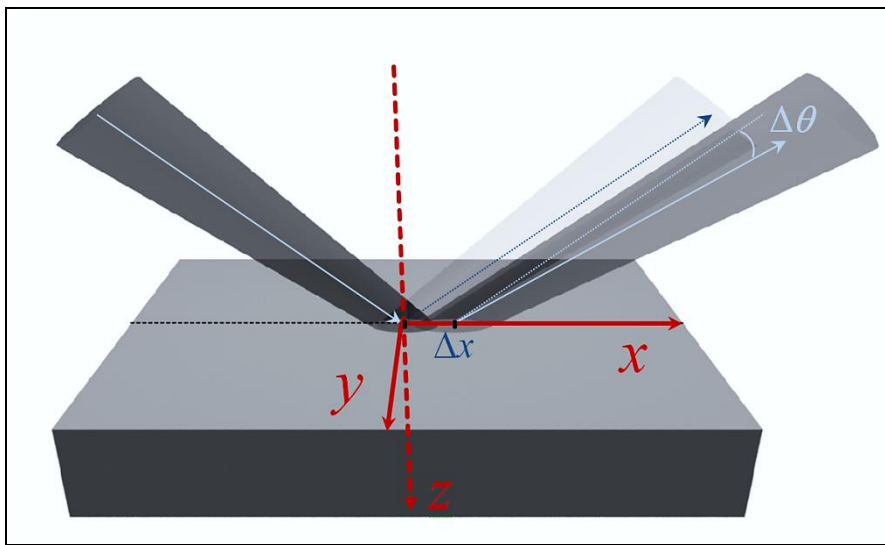


Fig. V.1. Schematic illustration of the lateral beam shifts (spatial shift Δx and angular shift $\Delta\theta$) upon reflection on a planar interface.

Although these effects are, as a rule, rather small, the beam shifts have nevertheless been reported to take potentially significant values in many configurations, including upon total internal reflection [1], [7], but also at the vicinity of minima of the reflection coefficient, for instance at Brewster and pseudo-Brewster incidence angles [8-10], near the edges of photonic bandgaps in photonic crystals [11], or in a nanophotonic cavity [12]. In all cases, measurements of the beam shifts can be made using conventional methods based on position sensitive detectors, while charge-coupled device can give more detailed information about the profile of the reflected beam [13]. More precise detection techniques include interferometric set-ups [14,15] or signal enhancement techniques, [7,10,16-19].

Here I need to mention that, despite the Goos-Hänchen effect has historically been observed and discussed for a long time as the shift experienced by a light beam upon its reflection at a single interface under the conditions of total internal reflection, and is related to the dispersion of the reflection coefficient, in the last two decades in particular, lateral beam shifts have been described and exploited at partial reflection on a single surface, but also with multilayered or complex structures, including photonic crystals or metasurfaces, both in reflection and in transmission. So in the scientific community, the term “Goos-Hänchen shift” has experienced a semantic shift and been generalized to all these types of lateral shifts, whose physical origin can indeed be related to mechanisms similar to those governing the “original” Goos-Hänchen effect.

Far from being mere curiosities, such beam shifts can obviously be exploited in order to yield information about the material(s) constituting the optical structure from which reflection takes place or about the medium surrounding that structure. Indeed, as they can be shown to be extremely sensitive to tiny variations of material properties (in particular, the permittivity) upon any kind of external excitations (electric or magnetic fields, pressure, temperature, mechanical strain,...), these effects are good candidates for the design of very precise sensors in particular, which is one of the main reasons they have attracted much attention lately. To that intent, however, it is also desirable to be able to enhance, and particularly, control in a reversible way the beam shifts, as well as relate the values they assume with the changes of permittivity of the materials the light beam encounters.

The control of Goos-Hänchen beam shifts has been studied in a variety of functional materials and structures. For instance, an external magnetic field can tune the Goos-Hänchen shift in magnetic media [17], [20-25]. Similarly, in combined magneto-optic and electro-optic systems the shift can be controlled via external electric and magnetic fields [20], [26-28]. A GH shift can be induced through the electro-optic effect [29] or by misfit strain [8]. As a consequence, measurements of changes in lateral shifts can thus be used for the monitoring of local electric and magnetic fields [30]. The sensitivity of the GH shift to tiny changes of the refractive indices in various systems can be put to use for the design of bio- or chemical sensors [31,32], surface plasmon resonance sensors [33] or simply for the precise measurement of refractive indices [34]. In some systems, the dependence of GH shift to temperature can be used for the design of thermal sensors [26,35]. Beyond sensing applications, the principles of optical switches [36], beam splitters [37], de/multiplexers [38],

or optical differential operation and image edge detection [39] have been proposed on the basis of the GH effect.

In all these instances, the focus has for the most part been set on ways to design the optical system in which the beam shifts take place, as well as to select the properties of its constituents, in order to achieve the desired control and enhancement of the effect and possibly use it for applications. More rarely the focus has been set on the properties of the beam itself, specifically on the way it can be tailored for an enhanced control of the Goos-Hänchen effect, but also on the way the reflected beam can be distorted as a corollary to that effect. Among those rarer studies, let us note the demonstration that the lateral Goos-Hänchen shift of light beams reflected and transmitted through a layered dielectric structure can be effectively controlled by the focusing (and defocusing) of the incident beam [40], with an increase of the shift when the beam is narrower. A significant reshaping of the reflected light beam has been discussed in a number of studies [41-44], including the observation that it can even split into two beams when a giant shift occurs [45]. As a rule, beam distortion is also more noticeable for narrow beams with waists of the same order of magnitude as their wavelength. Thus reshaping of the beam upon reflection requires additional studies.

In this Chapter, I present analytical and numerical calculations carried out in order to investigate the effect of a transverse spatial modulation of the phase of a narrow Gaussian beam on the lateral and angular shifts (as well as the reshaping) it undergoes in its plane of incidence upon reflection off a simple dielectric isotropic plate. Those calculations were carried out in the microwave domain. The Chapter is organized as follows. In Section V.2, I provide an analytical derivation of the electric field of the reflected wave at the upper surface of the plate. In Section V.3, I show how it can be used for the calculation of the lateral beam shift for various degrees of phase modulation of the incoming wavepacket. Section V.4 describes ways to achieve the desired phase modulation of the incoming Gaussian beam. In Section V.5, I show the results of the numerical simulations of beam propagation before and after reflection from the plate and discuss the influence of the spatial phase modulation on the lateral and angular shifts undergone by the reflected beam, as well as its reshaping. Section V.6 contains the conclusions of this Chapter.

V.2. Analytical description

In this study, the reflection of a microwave Gaussian beam from a simple, homogeneous, isotropic, dielectric, non-magnetic plate of refractive index n_p and thickness d was considered,

as shown in Fig. V.2. The refractive index of the surrounding medium is n_S . The upper and lower surfaces of the plate are parallel to the (xy) plane of a Cartesian system of coordinates.

A two-dimensional (2D) monochromatic Gaussian s-polarized beam (wavelength λ_0 in vacuum and angular frequency $\omega = 2\pi c/\lambda_0$) impinges on the top surface of the plate. The propagation direction of the beam is determined by its central wavevector k_c with $k_c = k_0 n_S$, where $k_0 = 2\pi/\lambda_0$ is the wavenumber of the beam in vacuum. The incidence angle θ is defined as the angle between k_c and the normal to the surface parallel to the z -axis. In the (xz) plane of incidence, a system of x' and z' axes (obtained through a rotation of the x and z -axes by a rotation of angle θ around the y -axis) is associated to the beam, so that its central wavevector is parallel to the z' -axis. The lateral dimensions of the plate, along the x - and y -axes, are supposed to be much larger than the diameter of the Gaussian beam, so that side effects can be neglected. The choice of a 2D beam description, in which the electric field profile does not depend on the y coordinate in the direction perpendicular to the plane of incidence (see Eq. (V.1) below) is justified by the fact that this study is devoted to the non-specular effects (in particular the beam shifts) that can be observed in that plane. Indeed, upon reflection, a Gaussian beam undergoes a Goos-Hänchen lateral shift Δx in its plane of incidence (Fig. V.2) that can be seen as a translation of the central wavevector of the reflected beam (solid red arrow) with respect to the direction of specular reflection (dashed red arrow).

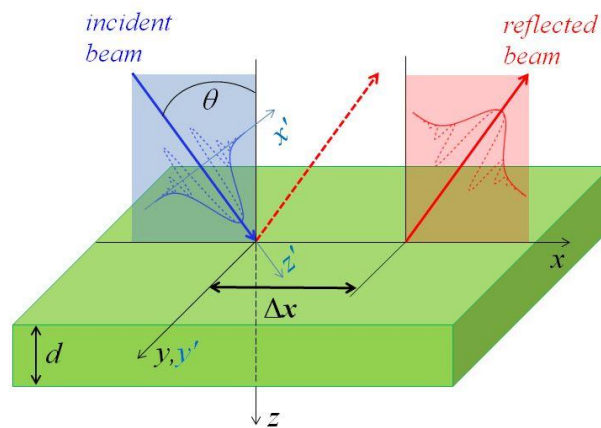


Fig. V.2. Schematic of the system. A 2D Gaussian microwave beam impinges on the upper surface of a dielectric plate of thickness d . The incidence plane is (xz) and θ is the incidence angle. The lateral shift of the reflected beam is denoted Δx . Solid and dashed curves respectively show the profiles of the modulus and real part of the electric fields of the incident (blue curves) and reflected (red curves) beams. The dashed red arrow shows the direction of specular reflection without lateral shift.

In this Chapter, the effect of a spatial modulation of the phase of an incident Gaussian beam on the lateral (as well as angular) shift and the simultaneous reshaping of its reflected beam is specifically studied. This modulation is quantified by the additional (in comparison with the expression of the field for a usual Gaussian beam) complex exponential factor that depends on the real-valued coefficient ξ in the following expression of the transverse electric field amplitude distribution $E_y^{(i)}(x', z')$, in which the origin common to the (xyz) and $(x'y'z')$ Cartesian systems of axes coincides with the center of the incident 2D Gaussian beam in the plane of its waist, and the time dependence of the propagating wavepacket is chosen as $\exp(i\omega t)$:

$$E_y^{(i)}(x', z') = E_0 \sqrt{\frac{w_0}{w(z')}} \exp\left[-\left(\frac{1}{w^2(z')} + i\frac{\xi}{w_0^2}\right)x'^2\right] \exp\left[i\eta(z') - ik_c\left(z' + \frac{1}{2R(z')}x'^2\right)\right]. \quad (\text{V.1})$$

In Eq. (V.1), z' is the algebraic axial distance from the waist, $w(z')$ is the beam radius (defined as the distance from the z' -axis for which the field amplitude falls to $1/e$ of its axial value), $w_0 = w(0)$ is the waist radius, and E_0 is the axial value of the field amplitude at the waist. An important characteristic parameter of the Gaussian beam is its Rayleigh length $z'_R = k_0 w_0^2 / 2$, from which the z' -dependent beam parameters in Eq. (V.1) can be deduced, namely the beam radius at position z' ,

$$w(z') = w_0 \sqrt{1 + \left(\frac{z'}{z'_R}\right)^2}, \quad (\text{V.2})$$

the radius of the wavefront curvature at position z'

$$R(z') = \frac{z'^2 + z'^2_R}{z'}, \quad (\text{V.3})$$

and its Gouy phase

$$\eta(z') = \arctan\left(\frac{z'}{z'_R}\right). \quad (\text{V.4})$$

It should be noted that although similar at first glance, factors $\exp\{-i\xi x'^2 / w_0^2\}$ and $\exp\{-ik_c x'^2 / 2R(z')\}$ in Eq. (V.1) are not equivalent, since the latter varies with the position z' along the propagation axis of the incident beam and explicitly depends on the curvature

radius of the wavefront, especially so at large distances from the beam waist, and thus does not yield a parabolic modulation of the phase.

With the choice of origin for both systems of axes mentioned above, the center line of the Gaussian incident beam crosses the upper surface of the plate at the point $\{x = x' = 0, y = y' = 0, z = z' = 0\}$ and the center of the beam in the waist plane thus coincides with $z' = 0$ on that surface. In oblique incidence (for $\theta \neq 0$), the other points of the beam waist are located above or below the upper surface of the dielectric plate. Using Eq. (V.1) and the relations

$$x' = x \cos \theta, \quad z' = x \sin \theta, \quad (\text{V.5})$$

the complex amplitude of the electric field on the upper surface of the plate ($z = 0$) in the (x, y, z) system of coordinates is:

$$E_y^{(i)}(x, z = 0) = E_0 \sqrt{\frac{w_0}{w(x)}} \exp \left[- \left(\frac{1}{w^2(x)} + i \frac{\xi}{w_0^2} \right) x^2 \cos^2 \theta \right] \times \exp \left[i \eta(x) - i k_c \left(x \sin \theta + \frac{1}{2R(x)} x^2 \cos^2 \theta \right) \right], \quad (\text{V.6})$$

where $w(x)$, $R(x)$, $\eta(x)$ are thus calculated for $x = z' / \sin \theta$.

In the paraxial approximation, in the vicinity of the beam waist (i.e., when $z' \ll z'_R$), one can see from Eqs. (V.2)–(V.4) that $w(z') \approx w_0$, $R(z') \rightarrow \infty$, and $\eta(z') \approx 0$ for all points inside the beam spot at the upper surface of the plate (i.e., for $z = 0$). Thus, the electric field distribution of the incident beam on that surface can be written as

$$E_y^{(i)}(x) = E_G^{(i)} \exp(-i k_{cx} x), \quad (\text{V.7a})$$

with

$$E_G^{(i)} = E_0 \exp \left[- \frac{(1 + i \xi) x^2 \cos^2 \theta}{w_0^2} \right], \quad (\text{V.7b})$$

and where $k_{cx} = k_c \sin \theta$ is the x -component of the central wavevector of the incident beam in the surrounding medium.

The spatial profile $E_y^{(r)}(x)$ of the reflected beam at the upper surface of the plate can be obtained using the following inverse spatial Fourier transform [8,26]:

$$E_y^{(r)}(x) = \frac{1}{\sqrt{\pi}} \int_{-\infty}^{\infty} E_y^{(i)}(K) \Re(K + k_{cx}) \exp(iKx) dK, \quad (\text{V.8})$$

where

$$E_y^{(i)}(K) = \int_{-\infty}^{\infty} E_y^{(i)}(x) \exp(-iKx) dx = E_0 \sqrt{\pi} \sqrt{\frac{w_0^2}{(1+i\xi)\cos^2\theta}} \exp\left[-\frac{1}{4} \frac{w_0^2 K^2}{(1+i\xi)\cos^2\theta}\right] \quad (\text{V.9})$$

is the incident field distribution in the spatial frequency domain. In Eqs. (V.8) and (V.9), the spatial Fourier variable K is defined as $K = k_x - k_{cx}$, where k_x is the x -component of the wavevector \mathbf{k} of any given spatial Fourier component of the incoming field distribution $E_y^{(i)}(x)$, and the corresponding $\Re(K + k_{cx}) = \Re(k_x)$ is the complex reflection coefficient of the system at a given position x across the beam at the surface of the plate. This reflection coefficient \Re is deduced from Maxwell's equations and from the boundary conditions at each interface in the system as [46]:

$$\Re = r \frac{1 - \exp(2ik_{tz}d)}{1 - r^2 \exp(2ik_{tz}d)} \quad \text{with} \quad r = \frac{k_z - k_{tz}}{k_z + k_{tz}}, \quad (\text{V.10})$$

where, for any given spatial Fourier component of the incoming field distribution, $k_z = k_0 n_s \cos\theta'$ and $k_{tz} = k_0 n_p \cos\theta'_t$ are the components along the z -axis of its wavevector \mathbf{k} and of its corresponding refracted wavevector \mathbf{k}_t , and θ' and θ'_t are the incidence angle and the refraction angle in the plate respectively associated to \mathbf{k} and \mathbf{k}_t and related by Snell's law $n_s \sin\theta' = n_p \sin\theta'_t$. The spread of values assumed by the angles θ' and θ'_t reflects the divergence of the incoming Gaussian beam. Equations (V.8)–(V.10) lead to the determination of the reflected beam intensity profile from which, after comparison with the incoming beam intensity profile, the value of the lateral shift at the upper surface of the plate, denoted Δx , can be numerically deduced. As a rule, an angular shift $\Delta\theta$ with respect to the specular geometry can also be observed. Its value cannot be deduced from the analytical approach described above and discussed below in Section V.3 (as that approach yields the field distribution at the surface of the plate only), but it can be obtained from numerical simulations of the propagation of the Gaussian beam after reflection (see Section V.5).

V.3. Analytical study of the effect of phase modulation on the reflected beam at the surface of the plate

In this Section, the analytical description from the previous Section is applied to a Gaussian beam in the microwave domain, for which the lateral and angular beam shifts are expected to reach large and easily measurable values. Note that the intermediate Fourier transforms expressed in Eqs. (V.8) and (V.9) require numerical calculations.

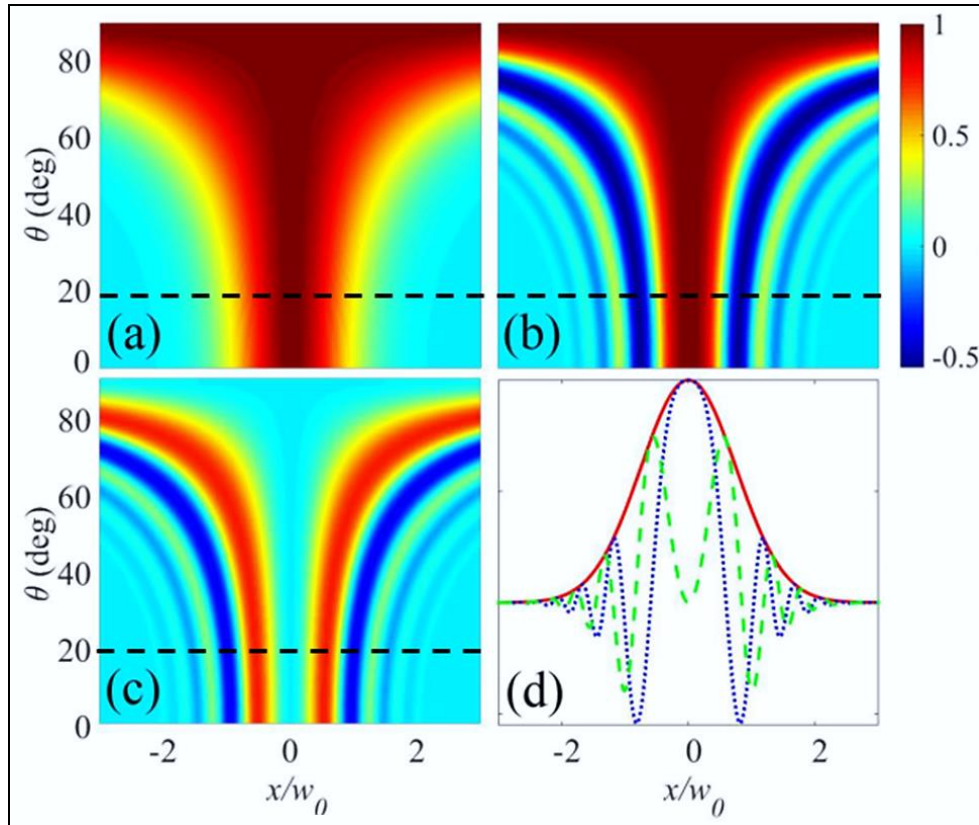


Fig. V.3. Normalized distribution of the amplitude of the incident spatially modulated Gaussian beam at the upper surface of the plate (at $z = 0$) as a function of the incidence angle and for spatial modulation parameter $\zeta = -5$: (a) modulus $|E_G^{(i)} / E_0|$, (b) real part $\text{Re}[E_G^{(i)} / E_0]$, and (c) imaginary part $\text{Im}[E_G^{(i)} / E_0]$. Panel (d) shows the cross-section of panels (a)-(c) for incidence angle $\theta = 20^\circ$ (horizontal black dashed lines), where the red solid, blue dotted and green dashed curves denote the modulus, real and imaginary parts of the normalized field, respectively.

Our simulations were carried out for a dielectric plate made of fused quartz (relative permittivity $\varepsilon_p = n_p^2 = 3.8$ at vacuum wavelength $\lambda_0 = 2.912$ mm [44], and thickness

$d = 8.33$ mm) surrounded by air ($n_S = 1$). For that value of thickness d , the reflection coefficient \Re deduced from Eq. (V.10) can be shown to reach a zero minimum at an incidence angle of approximately 18.5° . Around that incidence angle, for small but non-zero values of \Re , beam shifts are known to reach large values [9]. The waist of the incident Gaussian beam is chosen as $w_0 = 3\lambda_0$. In this case, the Rayleigh length is $z'_R \approx 84.5$ mm, so that the variations of the beam diameter across the thickness of the plate can be neglected.

The transverse spatial distribution of the normalized Gaussian amplitude $E_G^{(i)}(x)/E_0$ of the electric field at the upper surface of the plate ($z = 0$) is shown in Fig. V.3 as a function of the incidence angle and for the spatial modulation parameter $\xi = +5$.

Panels (a), (b), and (c) present the modulus $|E_G^{(i)}/E_0|$, real part $\text{Re}[E_G^{(i)}/E_0]$, and imaginary part $\text{Im}[E_G^{(i)}/E_0]$ of the normalized amplitude, respectively, and panel (d) shows the cross-sections of distributions (a)-(c) for an incidence angle $\theta = 20^\circ$. As expected from Eq. (V.7b), the distribution of the Gaussian field amplitude is symmetrical with respect to the x -axis (position $x = 0$ corresponds to the center of the incident beam waist). Although the phase modulation of the Gaussian beam (for $\xi \neq 0$) does not affect the envelope (the modulus) of the field amplitude it does, however, modify the real and imaginary parts of $E_G^{(i)}(x)$, and an increase of the modulation parameter ξ leads to increasingly fast oscillations of $\text{Re}[E_G^{(i)}/E_0]$ and $\text{Im}[E_G^{(i)}/E_0]$ along the x -axis. In accordance with Eq. (V.7b), a reversal of the sign of ξ reverses the sign of the imaginary part of the Gaussian field amplitude. As a whole, the phase modulation of the field can be expected to exert a noticeable influence on the overall reflected beam, as the latter results from the interference between multiple waves reflected from the upper and lower surfaces of the dielectric plate.

This is clearly illustrated in Fig. V.4, where the transverse distribution along the x -axis of the normalized modulus $|E^{(r)}/E_0|$ of the reflected electric field at the upper surface of the plate ($z = 0$), deduced from Eqs. (V.1)-(V.10), is shown as a function of incidence angle θ and for different values of the spatial modulation parameter ξ . The black curves follow the position of the maximum of the beam intensity, *i.e.*, a departure of those lines from $x = 0$ indicates and quantifies the lateral beam shift Δx .

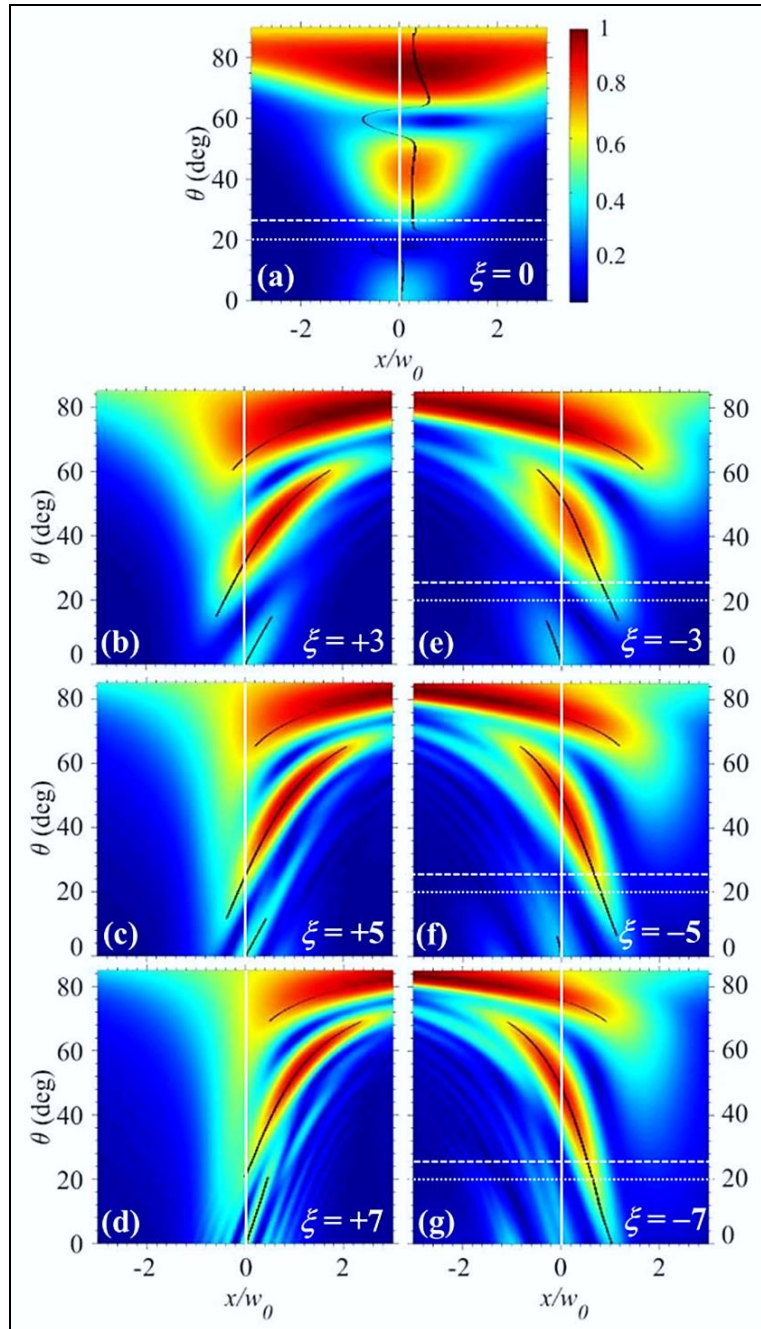


Fig. V.4. Distribution of the normalized modulus $|E_y^{(r)} / E_0|$ of the reflected field at the upper surface of the plate (at $z=0$) as a function of the x -coordinate and the incidence angle θ for values of the spatial phase modulation parameter equal to: (a) $\xi=0$, (b) $\xi=+3$, (c) $\xi=+5$, (d) $\xi=+7$, (e) $\xi=-3$, (f) $\xi=-5$, and (g) $\xi=-7$. Black lines follow the position of the absolute maximum of the field amplitude when θ varies. The horizontal dotted and dashed lines in panels (a), (e), (f), and (g) correspond to incidence angles $\theta=20^\circ$ and $\theta=25^\circ$ and refer to the cases depicted in Fig. V.8 and discussed in Section V.5. The vertical white lines show the position of the center of the incident beam ($x=0$).

In the absence of spatial modulation ($\xi=0$, Fig. V.4(a)), the reflected beam already exhibits a significant distortion, with respect to the Gaussian profile of the incident beam, in particular in the vicinity of incidence angles corresponding to minima of the modulus of reflection coefficient \mathfrak{R} — specifically, around $\theta=18.5^\circ$ and $\theta=60^\circ$ (the precise values of those angles are determined using Eqs. (V.10)). Indeed, near $\theta=18.5^\circ$, the reflected wave splits into two beams with almost equal maxima. With an increase of the absolute value of the spatial phase modulation parameter ξ (Fig. V.4(b)-(g)), the distortion of the reflected field becomes stronger, and larger intervals of θ appear for which the profile of the reflected field is split and exhibits two peaks. Due to this beam reshaping, the determination of the lateral shift, as calculated analytically at the surface of the plate, is sometimes ambiguous, since both maxima of the split beam can be of comparable amplitudes — this is especially true in the case of a non-modulated beam, as evidenced by the black lines in Fig. V.4.

This ambiguity, however, is less of a difficulty for incidence angles far from those for which $|\mathfrak{R}|$ nears a minimum. In this case, the reflected field is still split in two, but one maximum is visibly larger than the other one (see for example Figs. V.4(e)-V.4(g), as well as the discussion of Fig. V.4 in the Section V.5), and for all intents and purposes the lateral beam shift Δx can be defined as the shift in position of the brighter part of the reflected wave. The analytical calculations depicted in Fig. V.4 show that, for such incidence angles, an increase of the spatial phase-modulation (increase of $|\xi|$) leads to an increase of the lateral beam shift. It can also be noted that for $0 < \theta < 15^\circ$ and $\theta > 20^\circ$, the lateral shift experienced upon reflection by a spatially phase-modulated beam is coupled with significantly larger values of the reflected electric field than in the case with a non-modulated beam ($\xi=0$). This fact makes spatially phase-modulated beams particularly useful for so-called weak measurements of the lateral beam shifts [7,17,19]. For increasing absolute values of the modulation parameter, however, the reflected beam also experiences an increased reshaping – see Figs. V.3(d) and V.3(g), so that a compromise, when choosing the value of the phase modulation parameter, must be found between increased lateral shift, large reflected intensity and distortion of the beam.

Finally, Fig. V.4 also shows that the general tendency for the dependence of the lateral shift on the angle of incidence is that its evolution when θ increases is reversed (although non-symmetrically with respect to $x=0$) upon a sign reversal of the spatial modulation parameter ξ , as can readily be seen when comparing Figs. V.4(b) and V.4(e), Figs. V.4(c) and V.4(f), or

Figs. V.4(d) and V.4(g). However, as should be expected, for incidence angles around normal incidence ($\theta = 0$), calculations show that the distribution of the Gaussian beam field is symmetric with respect to $x = 0$ for any ξ .

Overall, the results shown in Fig. V.4 clearly highlight the marked sensitivity of the lateral shift of the Gaussian beam upon a spatial modulation of its phase and the way a thoughtful choice of the parameter governing that modulation provides a control of both the amplitude and the sign of the shift.

It must be noted, however, that the lateral GH beam shift upon reflection is, as mentioned earlier, coupled to an angular shift, also in the plane of incidence, with respect to the purely specular direction, for which the central wavevector of the reflected beam would make the exact same angle θ (in absolute value) with the normal to the surface as the central wavevector of the incoming beam. In reality, the reflection of the beam departs from this simple behaviour familiar to ray optics, and an angular shift $\Delta\theta$ is indeed observed, that can, in some cases, reach several degrees and thus cannot be neglected, as it must be taken into account for the design of any device exploiting the measurement of the GH effect for sensing purposes. The analytical calculations presented in this Section do not allow a simple evaluation of $\Delta\theta$. Estimates based on numerical simulations of the propagation of the reflected beam, however, can be carried out, and are presented and discussed below.

V.4. Obtention of a spatially phase-modulated Gaussian beam

Before moving to the next section with numerical simulations, let us discuss two ways of achieving a transverse spatial phase modulation of a Gaussian beam that will be used. A first way consists in focusing a conventional (*i.e.*, without phase modulation) Gaussian beam with a non-spherical lens tailored to yield the required phase modulation. Let us consider such a 2D lens, made of a transparent material with refractive index n_L and immersed in an homogeneous medium with refractive index n_S (with $n_S < n_L$, which is the case when the surrounding medium is vacuum or air). Its optical axis coincides with the z' -axis (the central axis of the incoming beam, see Fig. V.2), *i.e.*, the incoming conventional Gaussian beam is incident along the axis of the lens. The lens is located close to the waist of the beam, that can thus be considered collimated and its wavefront to be plane across the lens, provided the latter's thickness at all points is much smaller than the Rayleigh length z'_R of the beam.

Let us first consider the case of a symmetrical biconvex 2D lens (Fig. V.5(a)), introduce the function $\rho_{bc}(x')$ describing the lens thickness profile and denote $\rho_{bc}(0) = \rho_{bc0}/2$ its total thickness on the optical axis. In the paraxial approximation, the additional transverse spatial phase modulation introduced by the lens verifies:

$$\frac{\xi}{w_0^2} x'^2 + 2m\pi \approx 2k_0(n_L - n_S)\rho_{bc}(x'), \quad m \in \mathbb{Z}. \quad (\text{V.10})$$

As a result, the dependence of ρ_{bc} on the distance x' from the optical axis is thus parabolic (for $-h/2 \leq x' \leq h/2$, where h is the height of the lens), with

$$\rho_{bc}(x') \approx \frac{\xi x'^2 + 2m\pi w_0^2}{4\pi(n_L - n_S)w_0^2} \lambda_0 = \frac{\lambda_0}{4\pi(n_L - n_S)w_0^2} \xi x'^2 + \frac{\rho_{bc0}}{2}. \quad (\text{V.11})$$

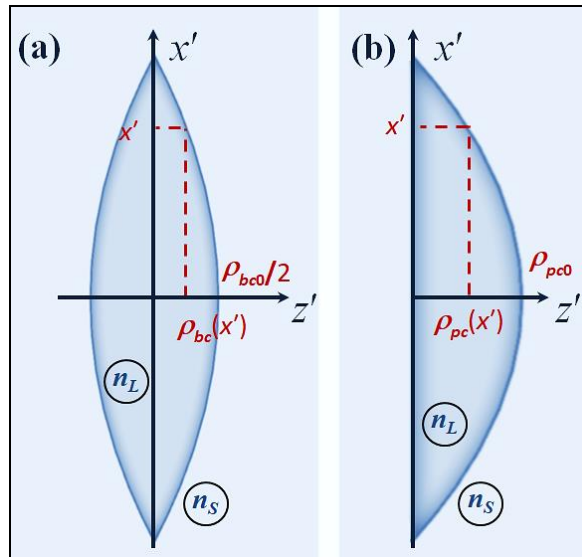


Fig. V.5. Schematic of (a) a biconvex lens and (b) a plano-convex lens with refractive index n_L surrounded by a medium with refractive index n_S . Note that the actual origin of the $(x'y'z')$ Cartesian system of axes is the same as in Fig. V.2.

For $\xi < 0$, the lens is at its thickest at its center and it is thus converging. The numerical simulations discussed in Section V.5 (Figs. V.7 and V.8) were carried out for such a symmetrical biconvex lens, made of the same fused quartz as the dielectric plate ($n_L = n_P$) and surrounded with air ($n_S = 1$) as well.

Of course, other types of converging lenses can be considered in order to obtain the required phase modulation, for instance a plano-convex lens (Fig. V.5(b)). Now the lens profile function, denoted $\rho_{pc}(x')$, verifies, in the paraxial approximation:

$$\frac{\xi}{w_0^2} x'^2 + 2m\pi \approx k_0(n_L - n_S)\rho_{pc}(x'), \quad m \in \mathbb{Z}, \quad (\text{V.12})$$

which yields

$$\rho_{pc}(x') \approx \frac{\xi x'^2 + 2m\pi w_0^2}{2\pi(n_L - n_S)w_0^2} \lambda_0 = \frac{\lambda_0}{2\pi(n_L - n_S)w_0^2} \xi x'^2 + \rho_{pc0}. \quad (\text{V.13})$$

where $\rho_{pc}(0) = \rho_{pc0}$ is a thickness of the lens on its optical axis. Again, for $\xi < 0$, the lens is converging.

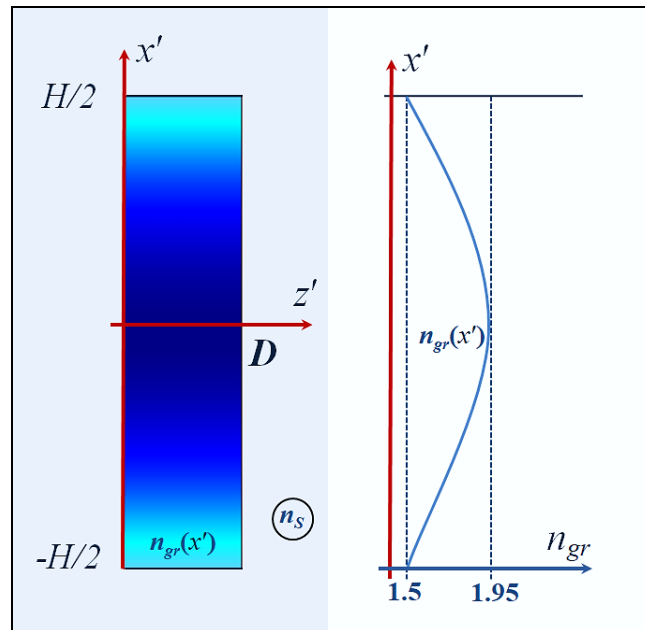


Fig. V.6. Schematic of a flat dielectric lamella (thickness D , and parabolic gradient $n_{gr}(x')$ of its refractive index) acting as a converging lens and surrounded by a medium with refractive index n_s . The color variations inside the lamella schematically illustrate the change in the refractive index along the x' -axis. Right panel shows the dependency between refractive index and the x' axis.

Yet another way to achieve the desired spatial modulation of the phase of the incident Gaussian beam is to use a flat dielectric lamella whose refractive index n_{gr} exhibits a

parabolic gradient in the direction x' perpendicular to the beam propagation direction z' (Fig. V.6). It is assumed that the local refractive index $n_{gr}(x')$ exceeds the ambient refractive index n_s . In order to induce the desired parabolic phase term in Eq. (V.1), $n_{gr}(x')$ must vary as

$$n_{gr}(x') = n_{gr,c} + \frac{\lambda_0}{2\pi w^2 D} \xi x'^2, \quad (\text{V.14})$$

where D is the thickness of the lamella and $n_{gr,c}$ is its refractive index at $x' = 0$. The minimal size of such a graded flat lens along the x' axis is dependent on the waist radius w of the incident Gaussian beam. As can be seen from Eq. (V.14), the rate of change in the local refractive index along the lamella $n_{gr}(x') - n_{gr,c} / x'^2$ is determined by both the beam parameters (λ_0, w, ξ) and the lamella thickness (D).

For $\xi < 0$ the local refractive index decreases with the distance $|x'|$ from the plane $x' = 0$, which is the plane of symmetry of the lamella. The calculations which are shown and discussed in Section V.5 (Fig. V.9) were made for $n_{gr,c} = n_p = 1.95$ and $D = 9.2$ mm. In this case, the value of the refractive index at a distance $|x'| = 16,72$ mm is 1.5.

Such a graded index flat lens can be obtained for different spectral ranges by using additive manufacturing technologies (3D-printing) resulting in the fabrication of a composite material, or a perforated gradient index lamella that provide the required refractive index gradient [47-51].

V.5. Numerical simulation of the propagation of the reflected phase-modulated Gaussian beam

This Section presents the results of numerical simulations of the production of a phase-modulated Gaussian beam and its propagation after reflection on the dielectric plate. These simulations were carried out using the COMSOL Multiphysics solver.

As was presented in the previous section, two different approaches have been used in order to obtain the transverse spatial phase modulation of the form $\exp(-i\xi x'^2)$ that appears in Eq. (V.1) in addition to the longitudinal phase term $\exp(-ik_0 n_s z')$ of a conventional Gaussian beam.

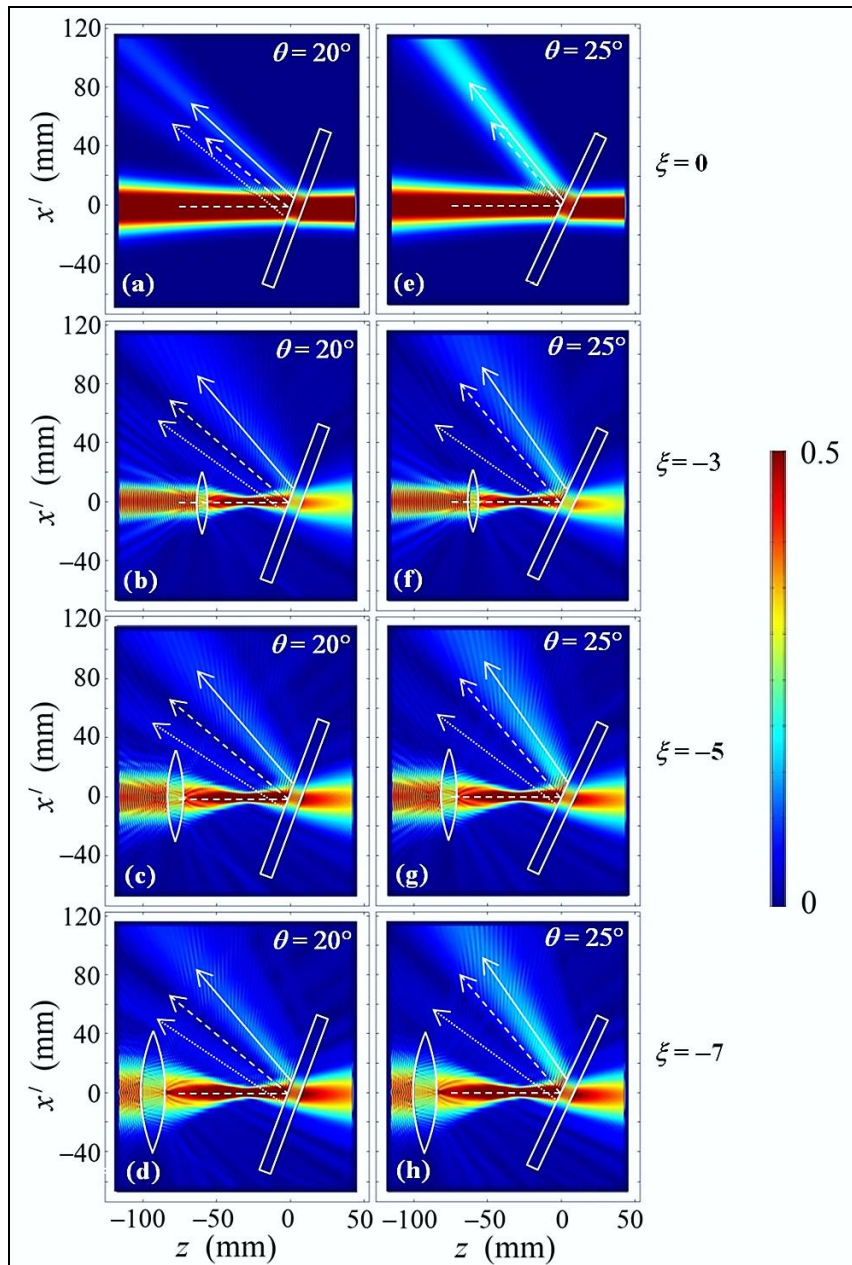


Fig. V.7. Numerical simulation of the total electric field amplitude distribution (normalized with respect to E_0) for values of the spatial phase modulation parameter equal to (a) and (e) $\zeta = 0$, (b) and (f) $\zeta = -3$, (c) and (g) $\zeta = -5$, (d) and (h) $\zeta = -7$, and for incidence angle $\theta = 20^\circ$ (top panels) and $\theta = 25^\circ$ (bottom panels), in the case where the phase of the incident Gaussian beam is spatially modulated using a parabolically-shaped biconvex lens. The white dashed line denotes the center of the incoming beam and the white dashed arrow indicates the direction of its specular reflection. The solid and dotted arrows show the propagation directions of the first and second reflected beams, respectively. Note that, the color scale for the normalized field amplitude has been truncated to the $[0; 0.5]$ interval in order to enhance the readability of the graphs.

Two ways of achieving that goal by focusing a non-modulated Gaussian beam are proposed: 1) with a lens with one (plano-convex lens) or two (biconvex lens) parabolically-shaped surface profile(s) in the $(x'z')$ plane; or 2) with a flat-surfaced thin lamella exhibiting a parabolic gradient of its refractive index also acting as a converging lens. In both cases, the constitutive parameters of the lens were chosen so that it produces a spatially phase-modulated beam with a negative modulation parameter ($\xi < 0$).

Figure V.7 shows the results of numerical simulations where a spatial phase modulation is added to an initially non-modulated Gaussian beam when it is focused with a symmetrical biconvex lens whose thickness (in the direction of the z' -axis) follows a parabolic dependence as a function of x' (see Eq. (V.13) in the Section V.4).

In order to properly assess the influence of the resulting phase modulation, the position of the lens relatively to the plate as well as the waist of the incoming (non-modulated) Gaussian beam were adapted for each value of the resulting negative modulation parameter ξ , in such a way that the focused (phase-modulated) beam keeps the same waist radius w at the upper surface of the dielectric plate in all cases. Note that the height h of the lens should be significantly larger than the diameter $2w$ of the incoming beam in order to reduce non-paraxial aberrations. Thus, for each value of ξ , the height of the lens must be adapted in addition to its curvature.

In practice, the lateral beam shift measurements are easier to realize at relatively small incidence angles. Figure. V.7 shows the reflection of the Gaussian beam simulated for two values of the incidence angle: $\theta = 20^\circ$ (left panels) and $\theta = 25^\circ$ (right panels). The first of these values is close to the minimum of reflectivity $|\mathfrak{R}|$ of the plate, as was discussed above, whereas for the second value reflection is characterized by both large values of the lateral shift and large values of $|\mathfrak{R}|$. The analytically calculated profiles of the electric field modulus at the surface of the plate for those angles of incidence correspond to the horizontal dotted and dashed white lines in Fig. V.4.

As was predicted by the calculations based on the analytical model described in Section V.3, the Gaussian beam undergoes a reshaping of its field profile even when its phase is not spatially modulated ($\xi = 0$, Figs. V.7(a) and V.7(e)). As can be seen in all panels of Fig. V.7, the reflected intensity is split between two beams as a result of this reshaping, one of which corresponds to a negative lateral shift Δx (dotted arrows) with respect to the specular direction (dashed arrows) and the other corresponds to a positive lateral shift Δx (solid

arrows). In what follows, these two beams will be referred as the first and second reflected beams, respectively.

At incidence angle $\theta = 20^\circ$ (Fig. V.7(b)-(d)), these two beams are of comparable amplitudes for all values of the modulation parameter ξ (with the first reflected beam corresponding to $\Delta x > 0$ only slightly brighter), but as mentioned above, the overall reflected intensity is low, as this incidence angle coincides with low values of $|\Re|$.

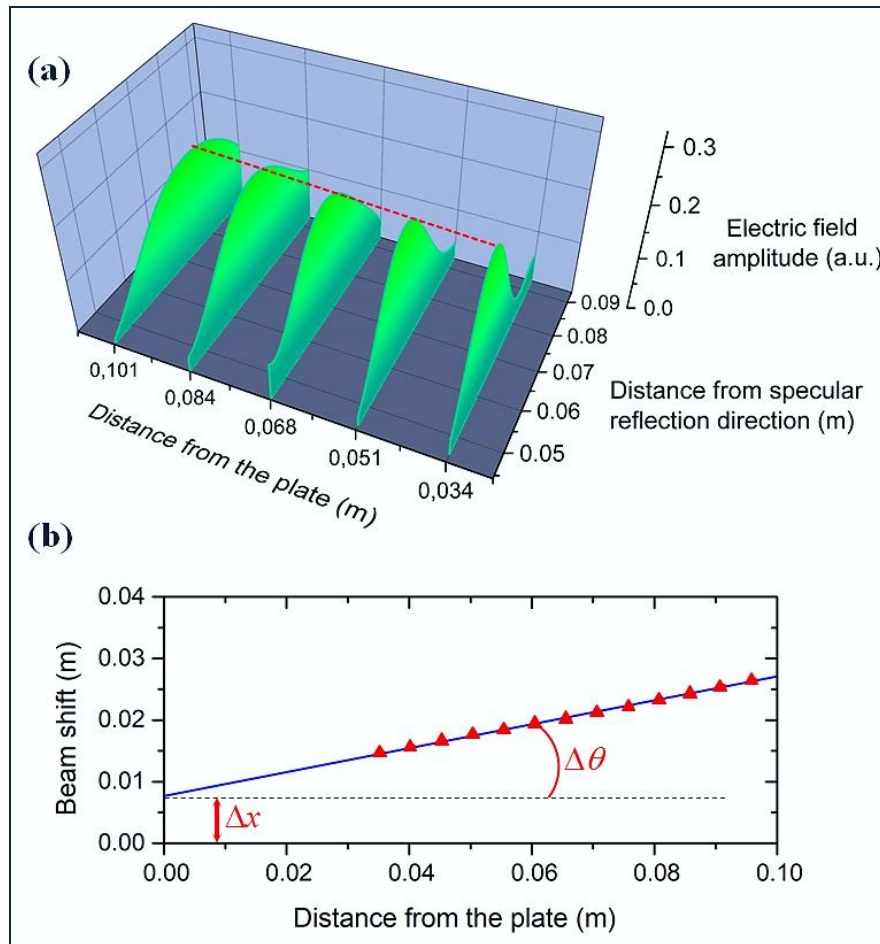


Fig. V.8. (a) Profile of the electric field amplitude of the reflected beam at different distances from the plate. The red dotted line corresponds to the position of the maximum of the electric field amplitude. (b) Linear extrapolation (solid blue line) of the determined maxima positions (red dots). The data correspond to an incidence angle equal to 20° and a modulation parameter $\xi = -5$.

For all intents and purposes, the case where incidence angle θ is equal to 25° (Fig. V.7(f)-(h)) is more interesting, since the detection of beam shifts is bound to be easier in this case due to the larger values of the reflected intensity. At that incidence angle, the intensities of the

two reflected beams greatly differ, with the first beam (solid arrow, for $\Delta x > 0$) much brighter than the second one (dotted arrow, for $\Delta x < 0$), and thus more suitable to potential applications. The position of the center (defined as the location where intensity is maximum) of the first reflected beam at the surface of the plate can be numerically deduced from the simulations and its comparison with that of the incoming beam yields the positive value of the lateral shift Δx it undergoes.

In order to calculate the position of the center of the reflected beam and its reflection angle, the electric field amplitude was determined on a series of cross-sections along the direction of the specular reflection (see Fig. V.8(a)) and in each case, the position of the maximum value of that amplitude was numerically estimated. A linear extrapolation of the corresponding points leads to the estimated direction of the reflected beam. The intersection of that direction with the upper surface of the plate differs from the position predicted by geometric optics, which leads to the value of the spatial shift Δx at the surface of the plate (see Fig. V.8(b)). Similarly, the comparison of that line with the specular reflection direction yields the value of the angular shift $\Delta\theta$. The dashed horizontal line in Fig. V.8(b) corresponds to the position of the beam maximum if there were no angular shift.

Similarly, the direction of propagation of either first or second reflected beam, obtained through a numerical determination of its center, can be compared to the specular direction, which leads to the value of the angular shift $\Delta\theta = \theta_r - \theta$, where θ_r denotes the absolute value of the angle between the central propagation axis of a reflected beam and the normal to the top surface of the plate. The angular shift thus determined is positive for the first reflected beam, whereas it is negative for the less bright second reflected beam — meaning that $\theta_r > \theta$ and $\Delta\theta > 0$ for the first reflected beam, and $\theta_r < \theta$ and $\Delta\theta < 0$ for the second one (whereas $\theta_r = \theta$ in the case of the specular reflection).

The results of the analytical and numerical determinations of the normalized lateral spatial shift $\Delta x/\lambda_0$ of the brighter first reflected beam are compared in Fig. V.9(a) as functions of ξ for $-7 \leq \xi \leq 0$ and for $\theta = 25^\circ$. The error bars are those of the numerical procedure used for the determination of the reflected beam center at the upper surface of the plate ($z = 0$), with an uncertainty related to the reshaping of that beam (as shown in Fig. V.4).

The values of Δx obtained with both approaches are in a satisfactorily good agreement for all values of ξ considered in our calculations, and, for $-3 \leq \xi \leq 0$, indicate a steady increase of the shift (by a factor that can slightly exceed 2) when the absolute value of parameter ξ

increases, i.e., when the transverse modulation of the phase of the incoming Gaussian optical electric field increases. For larger values of $|\xi|$, both methods seem to indicate a general tendency for Δx to decrease slightly. This can be related to the fact that the reshaping undergone by the reflected beam becomes markedly stronger when the modulation parameter increases in absolute value. Thus, for an effective control of the enhancement of the lateral shift, one should retain values of the modulation parameter within the interval $-5 \leq \xi \leq -2$. Overall, our calculations show that the lateral shift Δx can exceed twice the value of the wavelength in vacuum of the incoming beam, that is, reach values of the order of 1 cm.

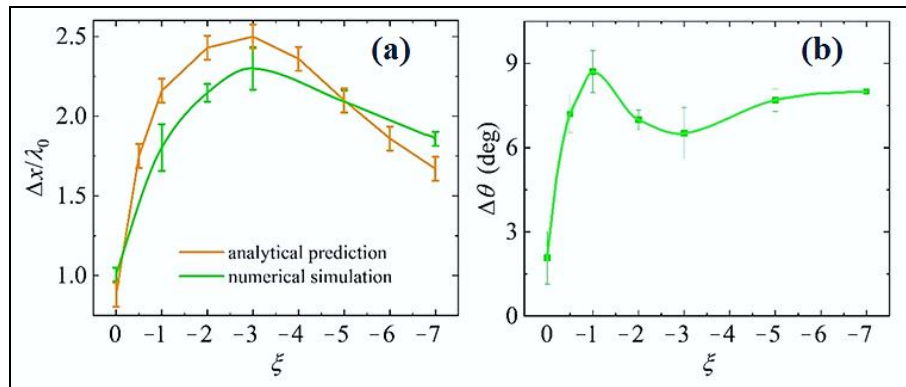


Fig. V.9. (a) Comparison of the normalized lateral spatial shifts $\Delta x/\lambda_0$ of the first reflected beam as a function of the phase modulation parameter ξ (for $-7 \leq \xi \leq 0$) obtained with the analytical calculation (orange curve) and with the numerical simulation (green curve). (b) Angular beam shift $\Delta\theta$ for the same set of values of ξ obtained using the numerical simulation. The incidence angle is $\theta = 25^\circ$.

Similarly, Fig. V.9(b) represents the variations of the angular shift $\Delta\theta$ of the first reflected beam for the same incidence angle $\theta = 25^\circ$ and over the same range $-7 \leq \xi \leq 0$ of the phase modulation parameter. Here again, the error bars stem from the procedure used for the determination of the central axis of the primary reflected beam. The angular shifts deduced from the numerical simulations are noticeably enhanced when the incoming Gaussian beam is phase-modulated (by a factor larger than 4 when ξ increases from 0 to 7 in absolute value) and reach several degrees, which makes them easy to detect for potential applications of lateral shift measurements.

As mentioned earlier, similar results can be obtained when the spatial modulation of the Gaussian beam is achieved using a flat-surfaced thin lamella with a spatial gradation of its

refractive index $n_{gr}(x')$ obeying a parabolic law along the x' -axis. For the case $\xi < 0$, the refractive index profile of such a thin lamella is described by Eq. (V.14) in Section V.4. Again, simulations show a split of the reflected electric field in two separate beams with different propagation directions (on either side of the specular direction), one being markedly more intense than the other. Figure V.10 illustrates this approach with the example of numerical simulations of beam propagation carried out when the refractive index at the center of such a focusing lamella is $n_{gr,c} = n_P$ and for $\xi = -3$. The other parameters are identical to those used in Figs. V.4 and V.7. In this case the refractive index in the lamella decreases parabolically along the x' -axis from the center of the lamella to its extremities, so that $n_{gr}(x' = \pm H/2) = 1.5$, where $H = 33.4$ mm is the total height of the lamella, whose thickness is chosen as $D = 9.2$ mm. For this set of structural parameters, calculations lead to values of the lateral spatial shift Δx of the first (i.e., brighter) reflected beam, estimated as previously at the surface of the plate coinciding with the (xy) plane, approximately equal to $2.82 \lambda_0$ for incidence angle $\theta = 20^\circ$ and $2.33 \lambda_0$ for $\theta = 25^\circ$, which is in a good agreement with the corresponding values estimated with a parabolic lens.

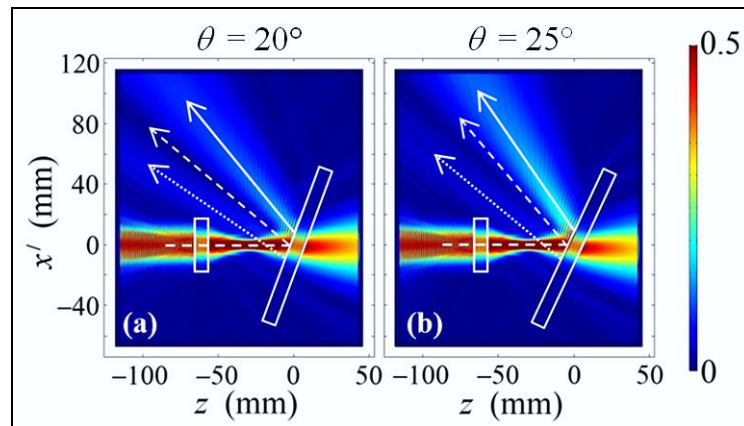


Fig. V.10. Numerical simulation of the electric field amplitude distribution (normalized with respect to E_0) for spatial phase modulation parameter $\zeta = -3$ and for incidence angle (a) $\theta = 20^\circ$ and (b) $\theta = 25^\circ$ in the case where the phase of the incident Gaussian beam is spatially modulated with the help of a focusing thin lamella with a parabolic refractive index gradient. The white dashed line denotes the central axis of the incoming beam and the normal to the surfaces of the focusing lamella. The white dashed arrow indicates the direction of the specular reflection, and the solid and dotted arrows show the central axes of the first (brighter) and second reflected beams, respectively. As in Fig. V.7, the color scale for the normalized field amplitude has been truncated to the $[0; 0.5]$ interval in order to enhance the readability of the graphs.

V.6. Conclusions

- It was shown theoretically and numerically that a spatial modulation of the phase of the incident Gaussian beam is an interesting way to control the amplitude and direction of the Goos-Hänchen shift to which the reflected beam is subjected. In practice, such a modulation can be achieved by placing a parabolic convex (for $\xi < 0$) or concave (for $\xi > 0$) lens, or a dielectric lamella with a parabolic gradient of its refractive index distribution, in front of a non-modulated Gaussian incident beam.
- The spatial lateral shift of the reflected beam is of the order of one wavelength of the incoming non-modulated Gaussian beam, and it can be increased up to 2.5 times by introducing a spatial modulation to the beam. For the chosen waist of the microwave beam used for the calculations, this translates into an exaltation of the spatial shift from 2.9 mm to 7.3 mm, which would facilitate its detection in the context of practical applications.
- The spatial Goos-Hänchen shift is accompanied by an angular shift in the plane of incidence. The angular shift is also sensitive to the modulation of the phase of the beam. It can be increased more than four times by the phase modulation of the Gaussian beam and can reach up to 9° , which makes the measurement of such a shift easier.
- The optimal range $[-5, -1]$ of the parameter governing the phase modulation was established for which the lateral shift of the reflected beam is significantly larger than that of a non-modulated beam and takes place at large values of the reflection coefficient, and for which the reshaping of the reflected beam is not crucial.
- The enhancement and control of the reflected beam shift can be used to optimize the efficiency and sensitivity of sensors, routers, de / multiplexers...

V.7. List of references

- [1] F. Goos, H. Hänchen, “*Ein neuer und fundamentaler Versuch zur Totalreflexion*,” *Ann. der Phys.* **1**, 333 (1947).
- [2] I. Fedorov, “*On the theory of total internal reflection*,” *Dokl. Akad. Nauk SSSR* **105**, 465 (1955) (in Russian).
- [3] C. Imbert, “*Calculation and experimental proof of the transverse shift induced by total internal reflection of a circularly polarized light beam*,” *Phys. Rev. D* **5**, 787 (1972).
- [4] K. Y. Bliokh, A. Aiello, “*Goos–Hänchen and Imbert–Fedorov beam shifts: an overview*,” *J. Opt.* **15**, 14001 (2013).
- [5] R. P. Riesz, R. Simon, “*Reflection of a Gaussian beam from a dielectric slab*,” *J. Opt. Soc. Am. A* **2**(11), 1809-1817 (1985).
- [6] L. I. Perez, “*Reflection and non-specular effects of 2D Gaussian beams in interfaces between isotropic and uniaxial anisotropic media*,” *J. Modern Optics* **47**, 1645-1658 (2000).
- [7] G. Jayaswal, G. Mistura, and M. Merano, “*Weak measurement of the Goos–Hänchen shift*,” *Opt. Lett.* **38**, 1232-1234 (2013).
- [8] Y. S. Dadoenkova, F. F. L. Bentivegna, N. N. Dadoenkova, I. L. Lyubchanskii, and Y. P. Lee, “*Influence of misfit strain on the Goos–Hänchen shift upon reflection from a magnetic plate on a nonmagnetic substrate*,” *J. Opt. Soc. Am. B* **33**, 393 (2016).
- [9] A. Aiello, J. P. Woerdman, “*Theory of angular Goos-Hänchen shift near Brewster incidence*,” arXiv:0903.3730 (2009).
- [10] L. Xie, X. Zhou, X. Qiu, L. Luo, X. Liu, Z. Li, Y. He, J. Du, Z. Zhang, and D. Wang, “*Unveiling the spin Hall effect of light in Imbert-Fedorov shift at the Brewster angle with weak measurements*,” *Opt. Express* **26**, 22934-22943 (2018).
- [11] Y. S. Dadoenkova, N. N. Dadoenkova, J. W. Kłos, M. Krawczyk, I. L. Lyubchanskii, “*Goos–Hänchen effect in light transmission through biperiodic photonic-magnonic crystals*,” *Phys. Rev. A* **96**, 043804 (2017).
- [12] K. V. Sreekanth, Q. L. Ouyang, S. Han, K.-T. Yong, and R. Singh, “*Giant enhancement in Goos–Hänchen shift at the singular phase of a nanophotonic cavity*,” *Appl. Phys. Lett.* **112**, 161109 (2018).
- [13] O. J. S. Santana and L. E. E. de Araujo, “*Direct measurement of the composite Goos–Hänchen shift of an optical beam*,” *Opt. Lett.* **43**, 4037-4040 (2018).
- [14] C. Prajapati, D. Ranganathan, and J. Joseph, “*Interferometric method to measure the Goos–Hänchen shift*,” *J. Opt. Soc. Am. A* **30**, 741-748 (2013).
- [15] W. Zhang and Z. Zhang, “*Collinear heterodyne interferometer technique for measuring Goos–Hänchen shift*,” *Appl. Opt.* **57**, 9346-9350 (2018).
- [16] J. B. Götte and M. R. Dennis, “*Generalized shifts and weak values for polarization components of reflected light beams*,” *New J. Phys.* **14**, 073016 (2012).
- [17] T. Tang, J. Li, L. Luo, J. Shen, C. Li, J. Qin, L. Bi, and J. Hou, “*Weak measurement of magneto-optical Goos-Hänchen effect*,” *Opt. Express* **27**, 17638-17647 (2019).

- [18] O. J. S. Santana, S. A. Carvalho, S. De Leo, and L. E. E. de Araujo, “*Weak measurement of the composite Goos–Hänchen shift in the critical region,*” *Opt. Lett.* **41**, 3884-3887 (2016).
- [19] O. J. S. Santana, L. E. E. de Araujo, “*Weak measurement of the Goos–Hänchen shift of partially coherent light beams,*” *J. Opt. Soc. Am. B* **36**, 533-540 (2019).
- [20] Y. S. Dadoenkova, F. F. L. Bentivegna, N. N. Dadoenkova, R. V. Petrov, I. L. Lyubchanskii, and M. I. Bichurin, “*Controlling the Goos–Hänchen shift with external electric and magnetic fields in an electro-optic/magneto-electric heterostructure,*” *J. Appl. Phys.* **119**, 203101 (2016).
- [21] R. Macêdo, R. L. Stamps, and T. Dumelow, “*Spin canting induced nonreciprocal Goos–Hänchen shifts,*” *Opt. Express* **22**, 28467-28478 (2014).
- [22] T. Tang, J. Qin, J. Xie, L. Deng, and L. Bi, “*Magneto-optical Goos–Hänchen effect in a prism-waveguide coupling structure,*” *Opt. Express* **22**, 27042-27055 (2014).
- [23] H. Wu, Q. Luo, H. Chen, Y. Han, X. Yu, and S. Liu, “*Magnetically controllable nonreciprocal Goos–Hänchen shift supported by a magnetic plasmonic gradient metasurface,*” *Phys. Rev. A* **99**, 033820 (2019).
- [24] H. Ma and R.-X. Wu, “*Nonreciprocal normal-incidence lateral shift for transmitted wave beams through the magnetic photonic crystal slab,*” *Appl. Phys. Lett.* **116**, 071104 (2020).
- [25] W. Yu, H. Sun, and L. Gao, “*Magnetic control of Goos–Hänchen shifts in a yttrium-iron-garnet plate,*” *Sci. Rep.* **7**, 45866 (2017).
- [26] Y. S. Dadoenkova, F. F. L. Bentivegna, R. V. Petrov, and M. I. Bichurin, “*Thermal dependence of the lateral shift of a light beam reflected from a liquid crystal cell deposited on a magnetic plate,*” *J. Appl. Phys.* **123**, 033105 (2018).
- [27] H. F. Wang, Z. X. Zhou, H. Tian, D. J. Liu, and Y. Q. Shen, “*Electric control of enhanced lateral shift owing to surface plasmon resonance in Kretschmann configuration with an electro-optic crystal,*” *J. Opt.* **12**, 045708 (2010).
- [28] A. Madani, S. R. Entezar, “*Tunable enhanced Goos–Hänchen shift in one-dimensional photonic crystals containing graphene monolayers,*” *Superlattices Microstruct.* **86**, 105-110 (2015).
- [29] X. Jiao, Z. Wang, and Y. Cai, “*Goos–Hänchen shift in single crystal silicon induced by the electro-optic effects,*” *Phys. Stat. Solidi B* **256**(10), 1900188 (2019).
- [30] L. Luo, T. Tang, J. Shen, C. Li, “*Electro-optic and magneto-optic modulations of Goos–Hänchen effect in double graphene coating waveguide with sensing applications,*” *J. Magn. Mater.* **491**(7-8), 165524 (2019).
- [31] Y. S. Dadoenkova, F. F. L. Bentivegna, V. V. Svetukhin, A. V. Zhukov, R. V. Petrov, M. I. Bichurin, “*Controlling optical beam shifts upon reflection from a magneto-electric liquid-crystal-based system for applications to chemical vapor sensing,*” *Appl. Phys. B* **123**, 107 (2017).
- [32] T. Tang, L. Luo, W. Liu, X. He, and Y. Zhang, “*Goos–Hänchen effect in semiconductor metamaterial waveguide and its application as a biosensor,*” *Appl. Phys. B* **120**, 497-504 (2015).
- [33] X. Yin, L. Hesselink, “*Goos–Hänchen shift surface plasmon resonance sensor,*” *Appl. Phys. Lett.* **89**, 261108 (2006).

- [34] J. Hou, T. Tang, G. Chen, H. Yang, “*Refractive index detection via magneto-optical Goos-Hänchen effect in multilayer structure containing magnetic plate,*” *Superlattices Microstruct.* **120**, 766-770 (2018).
- [35] B. Zhao and L. Gao, “*Temperature-dependent Goos-Hänchen shift on the interface of metal/dielectric composites,*” *Opt. Express* **17**, 21433-21441 (2009).
- [36] A. Farmani, A. Mir, Z. Sharifpour, “*Broadly tunable and bidirectional terahertz graphene plasmonic switch based on enhanced Goos-Hänchen effect,*” *Appl. Surf. Sci.* **453**, 358-364 (2018).
- [37] P. Han, X. Chang, W. Li, H. Zhang, A. Huang, Z. Xiao, “*Tunable Goos-Hänchen shift and polarization beam splitting through a cavity containing double ladder energy level system,*” *IEEE Photonics J.* **11**, 6101013 (2019).
- [38] H. Sattari, S. Ebadollahi-Bakhtevan, M. Sahrai, “*Proposal for a 1×3 Goos-Hänchen shift-assisted de/multiplexer based on a multilayer structure containing quantum dots,*” *J. Appl. Phys.* **120**, 133102 (2016).
- [39] D. Xu, S. He, J. Zhou, S. Chen, S. Wen, and H. Luo, “*Goos-Hänchen effect enabled optical differential operation and image edge detection,*” *Appl. Phys. Lett.* **116**, 211103 (2020).
- [40] A. A. Zharov, N. A. Zharova, and A. A. Zharov Jr., “*Phase control of the giant resonant Goos-Hänchen shift,*” *JETP Letters* **112**, 65-70 (2020).
- [41] W. Nasalski, “*Modified reflectance and geometrical deformations of Gaussian beams reflected at a dielectric interface,*” *J. Opt. Soc. Am. A* **6**(9), 1447-1454 (1989).
- [42] Yu. F. Nasedkina, D. I. Sementsov, “*Longitudinal shift and transformation of a Gaussian beam upon reflection from a thin plate,*” *Opt. Spectrosc.* **102**(5), 777-784 (2007).
- [43] Yu. F. Nasedkina, D. I. Sementsov, and O. V. Mosin, “*Modification of Gaussian Beams Reflected by a Thin Amplifying Plate,*” *J. Commun. Technol. Electron.* **53**(12), 1391-1398 (2008).
- [44] V. B. Yurchenko, M. Ciydem, M. L. Gradziel, and J. A. Murphy, “*Major reshaping of narrow beams by resonant multilayer structures,*” *Opt. Express* **28**, 8211-8222 (2020).
- [45] P. Xiao, “*Beam reshaping in the occurrence of the Goos-Hänchen shift,*” *J. Opt. Soc. Am. B* **28**, 1895-1898 (2011).
- [46] M. Born, E. Wolf, *Principles of Optics* (Cambridge University Press, Cambridge, 1999).
- [47] A. Camposeo, L. Persano, M. Farsari, and D. Pisignano, “*Additive manufacturing: Applications and directions in photonics and optoelectronics,*” *Adv. Optical Mater.* **7**, 180041 (2019).
- [48] Y. Wu, P. S. Grant, and D. Isakov, “*3D-printed $\lambda/4$ phase plate for broadband microwave applications,*” *Opt. Express* **26**, 29068-29073 (2018).
- [49] A. Petosa A. Ittipiboon, “*Design and performance of a perforated dielectric Fresnel lens,*” *IEE Proceedings - Microwaves, Antennas and Propagation* **150**, 309-314 (2003).
- [50] S. Zhang, “*Design and fabrication of 3D-printed planar Fresnel zone plate lens,*” *Electronics Letters* **52**, 833-835 (2016).

- [51] A. P. Haring, A. U. Khan, G. Liu, and B. N. Johnson, “*3D printed functionally graded plasmonic constructs*,” *Adv. Optical Mater.* **5**, 1700367 (2017).

CONCLUSIONS AND PERSPECTIVES

This work was devoted to several ways of controlling the spectrum, the state of polarization, and/or the propagation of an electromagnetic wave using either the combination of photonic heterostructures and plasmonic inclusions (Chapters II to IV) or the properties of the wave itself (Chapter V).

The combination of an *amplifying photonic crystal* with a *nanocomposite, anisotropic, plasmonic layer* based on a three-dimensional distribution of nonspherical metallic inclusions for the polarization sensitive control of an amplified electromagnetic wave was, to the best of our knowledge, proposed for the first time in this work. The ellipsoidal shape of the nanoparticles makes it possible to adjust, in a wide domain ranging from UV to near-IR wavelengths, the spectral position of the surface plasmon resonance taking place in the nanoparticles and exploited in order to achieve the required polarization sensitivity. As a result, the bandgap edge of the photonic crystal (here, around the 1550 nm telecom wavelength) can be amplified or not depending on the direction of polarization of a linearly polarized incident light with respect to the main axes of the ellipsoidal particles.

In a further development, the combination of a *narrow amplifying spectral photonic filter* with a *plasmonic polarizer*, based on the excitation of localized plasmon resonances in *ordered monolayers* (2D arrays) of metallic anisotropic nanoparticles embedded into a photonic microcavity was, also to the best of our knowledge, described for the first time in this work in order to achieve polarization-sensitive narrow-band amplification. Again, this study was carried out for near-IR light around the 1550 nm wavelength, which in this case corresponds to a defect mode of the photonic crystal. Depending on the polarization state of the linearly polarized incident light, this defect mode is either amplified or suppressed. Contrary to the previous study with a bulk nanocomposite plasmonic layer, a 2D array of nanoparticles can be considered as a single interface, and the use of such a monolayer gives more flexibility for the precise positioning of the metallic particles in the structure necessary to achieve the best possible efficiency for the suppression of the amplified defect mode.

For this study, an extension of the transfer matrix method was proposed for the description of a 2D plasmonic monolayer (considered as an interface) with a transfer matrix whose elements are derived on the basis of the coupled-dipole approximation. An interesting perspective of this approach would be a further extension of the transition matrix method

including resonant elements for the description of waveguide structures with various types of plasmonic resonators [1].

Another development presented in this work is a new design for a *polarization sensitive dichroic filter* involving a 2D array of metallic nanoparticles surrounded by two *deterministic aperiodic dielectric reflectors*. The use of deterministic aperiodic photonic crystals as reflectors makes it possible to tailor the spectral position of the photonic bandgaps and defect modes of that structure in such a way that two of these modes, located in separate bandgaps, can be independently adjusted and provide the two required narrow transmittivity windows of the dichroic filter. A crucial part of the work consists in adjusting the spectral position of two surface plasmon resonances excited in the 2D array of metallic nanoparticles so that they coincide with the two selected defect modes of the photonic structure. Depending on the polarization state of a linearly polarized incoming beam, one or the other plasmon resonance is excited, thus ensuring a nearly total extinction of one or the other of the defect modes.

The main idea proposed in these studies — i.e., the insertion of an anisotropic resonant plasmonic inclusion in a cavity surrounded by two photonic-crystal-based resonators — opens the way to a family of similar optical devices exploiting the combination of photonic and plasmonic effects. For instance, the results presented here can significantly expand the possibilities of controlling the polarization of the radiation emitted by compact vertical cavity surface emitting semiconductor lasers (VCSELs). Indeed, because of the inherent symmetry of the resonant cavities of VCSELs, the light waves they emit do not have a well-defined state of polarization. This results in the emission of radiation with uncontrolled polarization states and in intensity instabilities. In comparison with other solutions proposed in the literature in order to address this issue (with polarizers positioned outside the VCSEL), the use of 2D arrays of nanoparticles embedded within the resonant area of the VCSEL itself would allow a much higher degree of freedom for the adjustment of the system. In addition to prevent laser emission of unwanted polarization state, this solution can also help to reduce the problems caused by heating in the VCSEL. In a further expansion of the idea of using an embedded 2D array of nanoparticles, a properly selected combination of several such monolayers located at different positions in the structure can spread the heat over the structure and reduce the laser emission instability inherent to heating in a laser cavity.

The results obtained in the course of these studies have already been published and attracted some interest in the photonics community. Citations of these publications (see List of publications, pp. 179 *et seq.*) can be found in papers devoted to plasmon resonances in

arrays of nanoparticles [2,3,4,5], in works devoted to the investigation of Tamm states [6], or in studies where the combination of plasmonic resonances with a photonic structure was used for the creation of absorbers [7,8]. They were also cited in connection with the use of an aperiodic photonic crystal in order to obtain a broadband absorber [8], or multichannel and passband filters [9]. Finally, they were cited in [10], where a 1D photonic crystal with an anisotropic defect layer is used to lift the degeneracy of TE and TM mode resonances, which can be used for the design of polarization sensitive filters.

In addition to these studies, where plasmonic and photonic properties are efficiently combined for polarization-sensitive spectral control of a light beam, a chapter of this work was devoted to a way to control the non-specular reflection of a Gaussian wavepacket with a spatial modulation of the phase of the electromagnetic field. Such non-specular effects (resulting in lateral as well as angular shifts of the reflected beam with respect to the predictions of geometric optics) belong to the same general category as the well-known Goos-Hänchen and Imbert-Fedorov effects. Far from being mere curiosities, such beam shifts can obviously be exploited in order to yield information about the material(s) constituting the optical structure from which reflection takes place or about the medium surrounding that structure. Among many other potential applications, the measurements of beams shifts are intensively used in different kinds of sensors, thus an efficient exaltation of the shifts is highly desirable in order to facilitate their detection. The majority of the studies devoted to that topic consider an enhancement of the beam shifts due to specific (for instance, resonant or anisotropic) properties of the structure they interact with. In this work, a transverse spatial modulation of the phase of a narrow microwave Gaussian beam was proposed to enhance the lateral and angular shift it undergoes in its plane of incidence upon reflection off a simple dielectric isotropic plate. It was demonstrated that the lateral shift of the reflected modulated beam is significantly larger than that of a non-modulated one, and that the lateral shift can reach up to several millimeters, which facilitates its experimental detection. A possible physical realization of the transverse spatial modulation of the phase of the incident beam was suggested (using either a parabolic shaped lens or a flat lamella with a parabolic gradient of refractive index). The proposed structure has the potential to improve the quality of sensors based on the beam shift effect [11,12]. Beyond the optimization of the efficiency and sensitivity of sensors, mentioned before, the principles of optical switches, beam splitters, de/multiplexers, the monitoring of local electric and magnetic fields can, among others, be proposed on the basis of this effect.

- [1] Y. Fan, X. Le Roux, A. Korovin, A. Lupu, A. de Lustrac, “*Integrated 2D-Graded Index Plasmonic Lens on a Silicon Waveguide for Operation in the Near Infrared Domain*,” ACS Nano. **11**(5), 4599-4605 (2017).
- [2] A.D. Utyushev, V.I. Zakomirnyi, I.L. Rasskazov, “*Collective lattice resonances: Plasmonics and beyond*,” Rev. Phys. **6**, 100051, 2021,
- [3] A.S. Fedorov, P. Krasnov, M.A. Visotin, F.N. Tomilin, S. Polyutov, “*Thermoelectric and Plasmonic Properties of Metal Nanoparticles Linked by Conductive Molecular Bridges*,” Phys. Status Solidi B **257**(12), 202000249 (2020).
- [4] V.I. Zakomirnyi, A.E. Ershov, V.S. Gerasimov, S.V. Karpov, H. Ågren, & I.L. Rasskazov, “*Collective lattice resonances in arrays of dielectric nanoparticles: a matter of size*,” Opt. let. **44**(23), 5743-5746 (2019).
- [5] A.S. Fedorov, M.A. Visotin, V.S. Gerasimov, S.P. Polyutov, & P.A. Avramov, “*Charge transfer plasmons in the arrays of nanoparticles connected by conductive linkers*,” Chem. Phys. **154**(8), 084123 (2021).
- [6] P.S. Pankin, S.Y. Vetrov, & I.V. Timofeev, “*Tamm plasmon in a structure with the nanocomposite containing spheroidal core-shell particles*,” J Opt. **21**(3), 035103 (2019).
- [7] J. Han, J. Jiang, T. Wu, Y. Gao, and Y. Gao, “*Multi-Channel High-Performance Absorber Based on SiC-Photonic Crystal Heterostructure-SiC Structure*,” J. Nanomater. **12**(2):289, (2022).
- [8] Y. Yu, H. Da, “*Broadband and perfect absorption of monolayer MoS₂ with Octonacci quasi-photonic crystal*,” Physica B Condens. Matter PHYSICA B, **604**, 412684 (2021).
- [9] H.A. Elsayed, & M.M. Abadla, “*Transmission investigation of one-dimensional Fibonacci-based quasi-periodic photonic crystals including nanocomposite material and plasma*,” Phys. Scr. **95**(3), 035504 (2020).
- [10] A.T. Jervakani, & B.S. Darki, “*An ultracompact optical polarizer based on the one-dimensional photonic crystals containing anisotropic layers*,” Opt. Commun. **526**, 128884 (2023).
- [11] T. Tang, L. Luo, W. Liu, X. He, and Y. Zhang, “*Goos-Hänchen effect in semiconductor metamaterial waveguide and its application as a biosensor*,” Appl. Phys. B **120**, 497-504 (2015).
- [12] X. Yin, L. Hesselink, “*Goos-Hänchen shift surface plasmon resonance sensor*,” Appl. Phys. Lett. **89**, 261108 (2006).

LIST OF FIGURES

- I.1.** An example of a photonic crystal found in nature. Photographs of butterfly wings (left panels), optical microscope images (central panels) and scanning electron microscope images (right panels) of these wings.
- I.2.** Scheme of the 1D photonic crystal.
- I.3.** Spectrum of the 1D photonic crystal with a photonic bandgaps.
- I.4.** Example of a vertical-cavity surface-emitting laser (VCSEL). The top and bottom reflectors (mirrors) delimiting the active cavity of the laser are 1D photonic crystals.
- I.5.** 2D photonic crystals: an array of periodically located rods (left), or periodically located holes in a host material (right).
- I.6.** An example of a 2D photonic crystal. SEM images of TiO₂ arrays of holes in TiO₂ with different diameters. Scale bars indicate a length of 100 nm.
- I.7.** Various examples of high symmetry 2D photonic crystals obtained by assembling multiple rings.
- I.8.** Example of 2D photonic crystals with a honeycomb lattice fabricated by a direct laser writing method.
- I.9.** SEM images of 3D photonic crystals with a woodpile structure.
- I.10.** Example of a waveguide obtained with lines of missing holes in a 2D photonic crystal.
- I.11.** Schematic of the 1D photonic crystal with defect layer.
- I.12.** Transmittivity spectrum of a 1D photonic crystal with a defect layer. The defect mode is positioned at 1550 nm.
- I.13.** Schematic illustration of a propagating surface plasmon polariton.
- I.14.** Illustration of various optical schemes for the excitation of SPPs. (A) Prism coupling schemes in the Kretschmann configuration on the left and in the Otto configuration on the right. (B) Grating coupling scheme. (C) Highly focused beam coupling scheme. (D) Near-field coupling scheme. (E) End-fire coupling scheme. (F) Step-gap leakage coupling scheme.
- I.15.** The Lycurgus cup, a Roman artefact held in the British Museum under transmitted light (left) and reflected light (right).
- I.16.** Illustration of a localized surface plasmon resonance in a nanoparticle.
- I.17.** Dependence of the spectral position of the LSPR on the shape and nature of several types of nanoparticles.
- I.18.** Transmission spectra of arrays of nanoparticles with different ellipsoidal shapes.
- I.19.** Schematic of the multilayered structure.
- I.20.** Schematic of the propagation through layer j .
- I.21.** Schematic of the reflection and transmission of waves at the interface between two layers. Here θ_{j-1} , θ_j are the incidence and refraction angles at interface j for a forward propagating wave.
- I.22.** (a) Ellipsoidal inclusions in a homogeneous background (matrix) medium. The permittivity of the inclusions is ϵ_i and the permittivity of the medium is ϵ_m . (b) Geometry of an ellipsoid. Here \mathbf{E}_e and \mathbf{E}_d are an externally applied electric field and the depolarizing electric field in the inclusion, and \mathbf{E}_i is the total field in the inclusion. The Cartesian system of axes is chosen so

- that these axes coincide with the principal symmetry axes of the ellipsoidal inclusion, whose half-lengths are denoted α_x , α_y , and α_z .
- I.23.** Prolate spheroids, spheres and oblate spheroids.
- I.24.** Depolarization tensor elements as a function of the aspect ratio.
- I.25.** Spectral dependence of the transmittivity T , the reflectivity R , and the absorptivity A of composite films made of silver spheroidal inclusions in a SiO_2 matrix for unidirectional inclusions (solid lines) and orientationally disordered inclusions (dashed lines) for the parallel (a) and perpendicular (b) (with respect to the axis of rotation of the spheroidal inclusions) light polarizations. Triangles indicate the results of computer simulations of the composite with unidirectional inclusions.
- I.26.** Comparison between the effective refractive index of a $\text{Nb}_2\text{O}_5:\text{SiO}_2$ mixture calculated using the Bruggeman model (solid lines) and experimentally determined (dotted lines) for different concentrations of the constituents of the mixture.
- I.27.** A periodic 2D array of inclusions with a square lattice. Here p is the period of the array, *i.e.* the interparticle distance.
- I.28.** Plane wave incident onto a 2D array of inclusions parallel to the (xy) plane. The wave vectors of the incident, reflected and transmitted waves are denoted \mathbf{k}_i , \mathbf{k}_r , and \mathbf{k}_t , respectively, and θ is the incidence angle.
- II.1.** Schematic of the system: two distributed Bragg reflectors of structure $(AB)^N$ and $(BA)^N$ surround a nanocomposite layer.
- II.2.** Schematic of a spheroidal metallic inclusion whose axis of symmetry is aligned parallel to the x -axis. The semi-dimensions of the spheroid are equivalent in the y and z directions.
- II.3.** Spectral dispersion of the nanocomposite effective permittivity tensor components: (a) real parts $\varepsilon'_{\perp,\parallel}$; (b) imaginary parts $\varepsilon''_{\perp,\parallel}$ in the case of a non-amplifying nanocomposite matrix. The red and blue lines correspond to ε_{\perp} and ε_{\parallel} components, respectively. The aspect ratio of the NPs is $\xi = 3.38$.
- II.4.** Spectral dispersion of the imaginary part of the nanocomposite effective permittivity in the case of a non-amplifying nanocomposite matrix as a function of the volume fraction η of NPs in the composite. Left and right panels correspond to ε_{\perp} and ε_{\parallel} , respectively. The aspect ratio of the NPs is $\xi = 3.38$.
- II.5.** Spectral dispersion of the imaginary part of the nanocomposite effective permittivity in the case of a non-amplifying nanocomposite matrix as a function of the aspect ratio ξ of the NPs. Left and right panels correspond to ε_{\perp} and ε_{\parallel} , respectively. The dashed lines correspond to $\lambda_0 = 1550$ nm. The volume fraction of the NPs is $\eta = 0.1\%$.
- II.6.** Transmittivity spectra around the photonic bandgap when the defect layer does not include NPs. Results are obtained for amplifying (red line) and non-amplifying (blue line) PC layers (panel (a)). Note the different vertical scale for the red and blue curves. The transmittivity values with amplification are limited to $T = 100$ in panel (a). Panel (b) represents the transmittivity spectrum in semi-logarithmic scale with amplification in the PC layers.
- II.7.** Transmittivity spectra T_{\parallel} (blue curve) and T_{\perp} (red curve) of the structure in the vicinity of the low-wavelength photonic bandgap edge when the defect layer incorporates NPs. The results are taking into account amplification in the PC layers. The aspect ratio of the NPs is $\xi = 3.38$, and the volume fraction is $\eta = 0.1\%$.
- II.8.** Transmittivity spectra T_{\parallel} (left panel) and T_{\perp} (right panel) of the structure in the vicinity of the low-wavelength photonic bandgap edge as a function of the volume fraction η of the NPs.

- Results are obtained accounting for the amplification in the PC layers. The aspect ratio of the inclusions is $\xi = 3.38$.
- II.9.** Transmittivity spectra $T_{//}$ (left panel) and T_{\perp} (right panel) around the low-wavelength photonic bandgap edge as a function of the aspect ratio of the NPs for two different polarization states of the incoming wave. Results are obtained accounting for the amplification in the PC layers. The volume fraction of the NPs is $\eta = 0.1\%$.
- II.10.** Transmittivity spectrum for the case when incoming light is polarized along the polar axis of the NPs around the low-wavelength photonic bandgap edge as a function of the aspect ratio of the NPs for different cases of the volume fraction of the inclusions in the nanocomposite (0.05%, 0.1% and 0.15% as (a), (b) and (c) respectively).
- II.11.** Transmittivity value as function of the volume fraction and the aspect ratio of the NPs at the 1550 nm (edge of the photonic bandgap) for two different polarizations in semi-logarithmic scale. Left and right panels correspond to the cases when incoming light is polarized along the polar axis of the NPs and perpendicular to it respectively.
- II.12.** Transmittivity spectrum (in semi-logarithmic scale) around the low-wavelength photonic bandgap edge as a function of the reduced thickness d_{NC}/d_A of the nanocomposite layer for light polarized along the x (top panel) and y (bottom panel) axes. The aspect ratio of the NPs is $\xi = 3.38$, and the volume fraction is $\eta = 0.1\%$. The dashed vertical lines correspond to the working wavelength 1550 nm, and the circles correspond to the modes at 1550 nm.
- III.1.** Schematic of the structure: two DBRs $(AB)^N$ and $(BA)^N$ are separated by a composite microcavity consisting of an amplifying layer D surrounded by two identical cladding layers C .
- III.2.** Schematic of the photonic structure with embedded 2D metallic NP arrays placed (a) at the center of the active region, and (b) on both sides of the active region at the distance Δ from its center. The period of the NP array is denoted p .
- III.3.** Longitudinal distribution of the normalized optical field modulus in the photonic structure shown in Fig. III.1 (*i.e.*, without NP array). The colors of the vertical bars correspond to those of the layers in the schematic of the structure. The right panel zooms in on the area immediately surrounding the composite microcavity. Here Δ is the distance from the center of layer D to two symmetrical absolute field maxima in the layers C .
- III.4.** Transmission spectra of an Ag NP array embedded in a GaAs matrix for the longitudinal polarization state of the incoming light and for different values of the aspect ratio of the NPs. Red, green and blue curves correspond to ζ equal to 3.0, 3.5 and 4.0, respectively. The period of the NP array is $p = 120$ nm. The length of the polar axis of the NPs is $2a = 20$ nm.
- III.5.** Transmission spectra of an Ag NP array embedded in a GaAs matrix for the longitudinal polarization state of the incoming light and for different values of the period p of the NP array. Green, red and blue curves correspond to p equal to 60 nm, 90 nm, and 120 nm, respectively. The aspect ratio of the NPs is $\xi = 3.5$. The length of the polar axis of the NPs is $2a = 20$ nm.
- III.6.** Transmission spectrum of the photonic structure without NP array. The spectrum is identical for any state of polarization of the incident light wave. The right inset zooms in on the spectrum around the defect mode (note the different vertical scale in the inset and in the main figure. The curve in the inset is truncated to $T = 200$).
- III.7.** Transmission spectra T_{\perp} and $T_{//}$ (top and bottom panels, respectively) of the amplifying PC with one embedded silver 2D NP array at the center of the defect layer. The inset (truncated to $T = 200$) zooms in on the amplified defect mode. The interparticle distance p is equal to 90 nm, and the aspect ratio of the NPs is $\xi = 3.6$.
- III.8.** Transmission spectra $T_{//}$ of the amplifying PC with a single embedded silver 2D NP array at the center of the defect layer. Red, green and blue curves in the inset correspond to a period p

- equal to 60 nm, 90 nm, and 120 nm, respectively. The aspect ratio of the NPs is $\xi = 3.6$. The dashed vertical line in the inset denotes wavelength $\lambda_0 = 1550$ nm.
- III.9.** Transmission spectra $T_{//}(\lambda_0)$ of the amplifying PC with two identical embedded 2D silver NP arrays at the distances $\pm\Delta = \pm 225$ from the center of the structure (in the layers *C*). Red, green and blue curves in the inset correspond to a period p of the array equal to 60 nm, 90 nm, and 120 nm, respectively. The aspect ratio of the NPs is $\xi = 3.2$. The dashed vertical line in the inset denotes wavelength $\lambda_0 = 1550$ nm.
- III.10.** Transmittivity spectrum $T_{//}(\lambda_0)$ (in semi-logarithmic scale) of the amplifying PC in the vicinity of the defect mode as a function of the position of the monolayer relative to the center of the structure. The period of the NP array is taken as $p = 90$ nm. The aspect ratio of the NPs is $\xi = 3.6$ in the layer *C* and $\xi = 3.2$ in the layer *D*. The top panel represents the longitudinal distribution of the optical field modulus (blue curve) at defect mode wavelength 1550 nm. Colors on the top panel correspond to the layer colors in Fig. III.3 (orange for layer *C* and yellow for layer *D*).
- IV.1.** Transmissivity spectrum of the periodic DBR. Top, central and bottom panels represent the cases with Bragg vacuum wavelengths equal to 700, 750 and 800 nm respectively. Red and green rectangles represent two neighboring bandgaps.
- IV.2.** (a) DBR $(AB)^N$ with thicknesses d_A and d_B for layers *A* and *B*; (b) DBR $(AB)^{N'}$ with thicknesses d'_A and d'_B for layers *A* and *B*; (c) deterministic aperiodic reflector obtained by the overlap of these periodic DBRs as described in Eqs. (IV.2)–(IV.4).
- IV.3.** Transmittivity spectrum of the aperiodic reflector. The first Bragg vacuum wavelengths λ_{Br} is fixed and equal to 560 nm. Panels (a), (b), and (c) correspond to values of the second Bragg vacuum wavelength λ'_{Br} equal to 340 nm, 360 nm and 380 nm, respectively.
- IV.4.** Transmittivity spectrum of a structure consisting of two aperiodic reflectors mirroring each other. In each reflector, the first Bragg vacuum wavelengths λ_{Br} is fixed and equal to 360 nm. Panels (a), (b), and (c) correspond to values of the second Bragg vacuum wavelength λ'_{Br} equal to 480 nm, 520 nm, and 560 nm, respectively.
- IV.5.** Evolution of the higher-wavelength photonic bandgap of a Fabry-Perot-like cavity consisting of a central *A* layer surrounded by two mirroring aperiodic reflectors, for different thickness d_D of the central layer (from 0 to d_A with a step of $0.1d_A$). The thick curve corresponds to $d_D = 0$. The red arrow shows the direction of the shift of the defect mode with an increase of d_D .
- IV.6.** Schematic of the composite photonic structure. Two symmetrical deterministic aperiodic multilayered reflectors consisting of alternate *A* (in orange) and *B* (in green) layers are separated by a layer *D* (thickness d_D). A 2D array of spheroidal metallic nanoparticles, characterized by the dimensions $2a_1$ and $2a_2$ of the particles and the interparticle distance p , is located at the center of the structure.
- IV.7.** (a) Transmittivity spectra of the NP array embedded in a SiO_2 matrix for the x -polarized (blue curve) and y -polarized (red curve) incoming light. The dips are due to surface plasmon resonances in the NPs. (b) Transmittivity spectrum of the photonic structure without NP array. The two defect modes in the lower-wavelength bandgap and the defect mode in the higher-wavelength bandgap are denoted L_1 , L_2 , and H , respectively.
- IV.8.** (a) Transmittivity spectra of the photonic structure with a 2D array of NPs for x -polarized (blue curve) and y -polarized (red curve) incoming lightwave; (b) zoom on the lower-wavelength bandgap. The two defect modes in the lower-wavelength bandgap and the defect mode in the higher-wavelength bandgap are denoted L_1 , L_2 , and H , respectively.

- IV.9.** Spectral characteristics of the aperiodic structure in the vicinity of defect mode H in the higher-wavelength bandgap: (a) Zoom on the transmittivity spectra for x - and y -polarized light; (b) and (c) distribution of the square of the normalized optical field magnitude $|E(z)/E(0)|^2$ (in logarithmic scale) in the structure for y - and x -polarized light, respectively; (d) and (e) square of the optical field magnitude normalized to its maximum value ($|E(z)/\max[E(z)]|^2$) at wavelength $\lambda_0 = 609$ nm (see black dashed line in the top panels) for y - and x -polarized light, respectively. As in Figs. IV.2 and IV.6, the vertical color bars in panels (d) and (e) denote the alternate layers of the structure.
- IV.10.** Square of the optical field magnitude normalized on its maximum value ($|E(z)/\max[E(z)]|^2$) in the photonic structure without NP array (a) at wavelength $\lambda_0 = 375$ nm of defect mode L_1 and (b) at wavelength $\lambda_0 = 412$ nm of defect mode L_2 for any state of polarization. The red triangles indicate the center of the photonic structure.
- IV.11.** Evolution of transmittivity spectra $T_{//}$ [panels (a) and (c)] and T_{\perp} [panels (b) and (d)] in the higher-wavelength bandgap (top panels) and lower-wavelength bandgap (bottom panels) as functions of the thickness of layer D expressed in terms of nominal thickness d_D . The white dashed lines represent the case where that thickness is exactly equal to d_D , as in Figs. IV.8 to IV.10. The white solid lines represent the case where layer D thickness is equal to $1.75d_D$. The white circles denote the spectral positions of the defect modes L_1 , L_2 and H discussed in the paper for these two thicknesses. The 2D array of NPs is located at the center of layer D .
- V.1.** Schematic illustration of the lateral beam shifts (spatial shift Δx and angular shift $\Delta\theta$) upon reflection on a planar interface.
- V.2.** Schematic of the system. A 2D Gaussian microwave beam impinges on the upper surface of a dielectric plate of thickness d . The incidence plane is (xz) and θ is the incidence angle. The lateral shift of the reflected beam is denoted Δx . Solid and dashed curves respectively show the profiles of the modulus and real part of the electric fields of the incident (blue curves) and reflected (red curves) beams. The dashed red arrow shows the direction of specular reflection without lateral shift.
- V.3.** Normalized distribution of the amplitude of the incident spatially modulated Gaussian beam at the upper surface of the plate (at $z = 0$) as a function of the incidence angle and for spatial modulation parameter $\zeta = -5$: (a) modulus $|E_G^{(i)} / E_0|$, (b) real part $\text{Re}[E_G^{(i)} / E_0]$, and (c) imaginary part $\text{Im}[E_G^{(i)} / E_0]$. Panel (d) shows the cross-section of panels (a)-(c) for incidence angle $\theta = 20^\circ$ (horizontal black dashed lines), where the red solid, blue dotted and green dashed curves denote the modulus, real and imaginary parts of the normalized field, respectively.
- V.4.** Distribution of the normalized modulus $|E_y^{(r)} / E_0|$ of the reflected field at the upper surface of the plate (at $z = 0$) as a function of the x -coordinate and the incidence angle θ for values of the spatial phase modulation parameter equal to: (a) $\zeta = 0$, (b) $\zeta = +3$, (c) $\zeta = +5$, (d) $\zeta = +7$, (e) $\zeta = -3$, (f) $\zeta = -5$, and (g) $\zeta = -7$. Black lines follow the position of the absolute maximum of the field amplitude when θ varies. The horizontal dotted and dashed lines in panels (a), (e), (f), and (g) correspond to incidence angles $\theta = 20^\circ$ and $\theta = 25^\circ$ and refer to the cases depicted in Fig. V.8 and discussed in Section V.5. The vertical white lines show the position of the center of the incident beam ($x = 0$).
- V.5.** Schematic of (a) a biconvex lens and (b) a plano-convex lens and refractive index n_L surrounded by a medium with refractive index n_S . Note that the actual origin of the $(x'y'z')$ Cartesian system of axes is the same as in Fig. V.2.
- V.6.** Schematic of a flat dielectric lamella (thickness D , and parabolic gradient $n_{gr}(x')$ of its refractive index) acting as a converging lens and surrounded by a medium with refractive

index n_s . The color variations inside the lamella schematically illustrate the change in the refractive index along the x' -axis. Right panel shows the dependency between refractive index and the x' axis.

- V.7.** Numerical simulation of the total electric field amplitude distribution (normalized with respect to E_0) for values of the spatial phase modulation parameter equal to (a) and (e) $\xi = 0$, (b) and (f) $\xi = -3$, (c) and (g) $\xi = -5$, (d) and (h) $\xi = -7$, and for incidence angle $\theta = 20^\circ$ (top panels) and $\theta = 25^\circ$ (bottom panels), in the case where the phase of the incident Gaussian beam is spatially modulated using a parabolically-shaped biconvex lens. The white dashed line denotes the center of the incoming beam and the white dashed arrow indicates the direction of its specular reflection. The solid and dotted arrows show the propagation directions of the first and second reflected beams, respectively. Note that the color scale for the normalized field amplitude has been truncated to the $[0; 0.5]$ interval in order to enhance the readability of the graphs.
- V.8.** (a) Profile of the electric field amplitude of the reflected beam at different distances from the plate. The red dotted line corresponds to the position of the maximum of the electric field amplitude. (b) Linear extrapolation (solid blue line) of the determined maxima positions (red dots). The data correspond to an incidence angle of the plate equal to 20° and a modulation parameter $\xi = -5$.
- V.9.** (a) Comparison of the normalized lateral spatial shifts $\Delta x/\lambda_0$ of the first reflected beam as a function of the phase modulation parameter ξ (for $-7 \leq \xi \leq 0$) obtained with the analytical calculation (orange curve) and with the numerical simulation (green curve). (b) Angular beam shift $\Delta\theta$ for the same set of values of ξ obtained using the numerical simulation. The incidence angle is $\theta = 25^\circ$.
- V.10.** Numerical simulation of the electric field amplitude distribution (normalized with respect to E_0) for spatial phase modulation parameter $\xi = -3$ and for incidence angle (a) $\theta = 20^\circ$ and (b) $\theta = 25^\circ$ in the case where the phase of the incident Gaussian beam is spatially modulated with the help of a focusing thin lamella with a parabolic refractive index gradient. The white dashed line denotes the central axis of the incoming beam and the normal to the surfaces of the focusing lamella. The white dashed arrow indicates the direction of the specular reflection, and the solid and dotted arrows show the central axes of the first (brighter) and second reflected beams, respectively. As in Fig. V.7, the color scale for the normalized field amplitude has been truncated to the $[0; 0.5]$ interval in order to enhance the readability of the graphs.

LIST OF TABLES

- III.1.** Material permittivities and layer thicknesses used for the numerical calculations. If, as is the case here, the thicknesses of the layers composing the active region are much smaller than the radiation wavelength, the region D can be described with good accuracy by an average dielectric permittivity $\varepsilon_D = \varepsilon_D' + i\varepsilon_D''$ obtained within an effective medium approximation. The amplification of an electromagnetic wave in this active equivalent layer, despite the optical absorption taking place in some of the layers of the structure, is described by $\varepsilon_D'' < 0$.

LIST OF PUBLICATIONS

Scientific journals

1. Yu.S. Dadoenkova, I.A. Glukhov, S.G. Moiseev, V. Svetukhin, A. Zhukov & I. Zolotovskii, “*Optical generation in an amplifying photonic crystal with an embedded nanocomposite polarizer,*” *Opt. Commun.*, **389**, 1-4 (2017), doi: 10.1016/j.optcom.2016.12.017.
2. S.G. Moiseev, I.A. Glukhov, V.A. Ostatochnikov, A.P. Anzulevich & S.N. Anzulevich, “*Spectra of the photonic crystal structure with a monolayer of metallic nanoparticles,*” *Appl. Spectrosc.*, **85**(3), 511-516 (2018), doi: 10.1007/s10812-018-0681-x.
3. S.G. Moiseev, I.A. Glukhov, Yu.S. Dadoenkova & F.F.L. Bentivegna, “*Polarization-selective defect mode amplification in a photonic crystal with intracavity 2D arrays of metallic nanoparticles,*” *J. Opt. Soc. Am. B* **36** (6), 1645 (2019), doi: 10.1364/JOSAB.36.001645.
4. I.A. Glukhov, Yu.S. Dadoenkova, F.F.L. Bentivegna & S. G. Moiseev, “*Deterministic aperiodic photonic crystal with a 2D array of metallic nanoparticles as polarization-sensitive dichroic filter,*” *J. Appl. Phys.* **128**, 053101 (2020), doi: 10.1063/5.0008652.
5. Yu.S. Dadoenkova, I.A. Glukhov, S.G. Moiseev & F.F.L. Bentivegna, “*Non-specular reflection of a narrow spatially phase-modulated Gaussian beam,*” *J. Opt. Soc. Am. A* **39** (11), 2073 (2022), doi: 10.1364/JOSAA.470180.

Conference proceedings

6. I.A. Glukhov, S.G. Moiseev. “*Spectra and field distribution of photonic-crystal structure with inclusions of metal nanoparticles,*” *CEUR Workshop Proceedings*, **1900**, 43-47 (2017), doi : 10.18287/1613-0073-2017-1900-43-47.
7. I.A. Glukhov, S.G. Moiseev, “*Optical generation in an amplifying photonic crystal with metal nanoparticles,*” *J. Phys.: Conf. Ser.* **1096**, 012005 (2018), doi : 10.1088/1742-6596/1096/1/012005.
8. S.G. Moiseev, Yu.S. Dadoenkova, I.A. Glukhov, T.A. Vartanyan, A.A. Fotiadi & F.F.L. Bentivegna, “*Selective polarization generation in an amplifying photonic crystal with a 2D array of metal nanoparticles,*” *Proc. SPIE* **11031**, Integrated Optics: Design, Devices, Systems, and Applications V, 1103114 (2019), doi: 10.1117/12.2520788.
9. I.A. Glukhov, S.G. Moiseev, Yu.S. Dadoenkova & F.F.L. Bentivegna, “*Exploiting plasmon resonances in a composite photonic crystal for polarization-sensitive dichroic filtering,*” *Proc. SPIE* **11368**, Photonics and Plasmonics at the Mesoscale, 113680F (2020), doi: 10.1117/12.2555761.
10. I.A. Glukhov, S.G. Moiseev, Yu.S. Dadoenkova & F.F.L. Bentivegna, “*Апериодическая плазмон-фотонная гетероструктура для поляризационно-чувствительной фильтрации (Aperiodic plasmon-photonic heterostructure for*

polarization-sensitive filtration),” Радиоэлектронная Техника (Radio-Electronic Technique), Interuniversity Collection of Scientific Papers, Ulyanovsk (Russia), 143-148 (2020).

Oral presentations at national conferences

11. I.A. Glukhov, S.G. Moiseev, Yu.S. Dadoenkova & F.F.L. Bentivegna, “Влияние положения и параметров двумерного массива металлических наночастиц на дефектную моду фотонного кристалла (*Effect of the position and parameters of a two-dimensional array of metallic nanoparticles on the defect mode of a photonic crystal*),” 22nd All-Russian Scientific School & Workshop for Young Scientists "Actual problems of physical and functional electronics", Ulyanovsk (Russia), 2019.
12. I.A. Glukhov, S.G. Moiseev, Yu.S. Dadoenkova & F.F.L. Bentivegna, “Аперриодическая плазмон-фотонная гетероструктура для поляризационно-чувствительной фильтрации (*Aperiodic plasmonic-photonic heterostructure for polarization-sensitive filtering*),” 23rd All-Russian Scientific School & Workshop for Young Scientists "Actual problems of physical and functional electronics", Ulyanovsk (Russia), 2020.
13. I.A. Glukhov, F.F.L. Bentivegna, Yu.S. Dadoenkova & S.G. Moiseev, “Управление смещением отраженного гауссова пучка посредством пространственной модуляции его фазы (*Controlling the displacement of a reflected Gaussian beam by means of spatial modulation of its phase*),” 24th All-Russian Scientific School & Workshop for Young Scientists "Actual problems of physical and functional electronics", Ulyanovsk (Russia), 2021.

Poster presentations at international conferences

14. S.G. Moiseev, Yu.S. Dadoenkova, I.A. Glukhov, T.A. Vartanyan, A.A. Fotiadi & F.F.L. Bentivegna, “Selective polarization generation in an amplifying photonic crystal with a 2D array of metal nanoparticles,” SPIE Optics + Optoelectronics 2019, Prague (Czech Republic), 2019.
15. I.A. Glukhov, S.G. Moiseev, Yu. S. Dadoenkova & F.F.L. Bentivegna, “Exploiting plasmon resonances in a composite photonic crystal for polarization-sensitive dichroic filtering,” SPIE Photonics Europe (online), 2020.
16. I.A. Glukhov, S.G. Moiseev, Yu.S. Dadoenkova & F.F.L. Bentivegna, “Polarization-selective defect mode suppression in a deterministic aperiodic photonic crystal through plasmon excitation in an embedded array of metallic nanoparticles,” European Conference on Integrated Optics (online), 2020.
17. I.A. Glukhov, Yu.S. Dadoenkova, F.F.L. Bentivegna, S.G. Moiseev & A.S. Abramov, “Усиление эффекта Гуса-Хенхен при отражении гауссова пучка от диэлектрической пластины (*Enhancement of the Goos-Hänchen effect upon reflection of a Gaussian beam from a dielectric plate*),” International Workshop on Fiber Lasers, Novosibirsk (Russia), 2022.

Poster presentations at national conferences

18. I.A. Glukhov, S.G. Moiseev, Yu.S. Dadoenkova, F.F.L. Bentivegna & P. Morel, “*Filtre amplificateur polarisant par excitation d’un plasmon de surface dans un cristal photonique actif*,” Journée du Club Optique Micro-Ondes JCOM 2019 (Société Française d’Optique), Brest (France), 2019.
19. S.G. Moiseev, I.A. Glukhov, Yu.S. Dadoenkova, F.F.L. Bentivegna & O.V. Ivanov, “*Поляризационно-селективное усиление дефектной моды в фотонно-кристаллической структуре с плазмонным метаслоем (Polarization-selective amplification of a defect mode in a photonic crystal with a plasmonic layer)*,” All-Russian Conference on Fiber Optics (ARCFO 2019), Perm (Russia), 2019.
20. I.A. Glukhov, Yu.S. Dadoenkova, S.G. Moiseev & F.F.L. Bentivegna, “*Contrôle de la réflexion d’un faisceau micro-onde gaussien par modulation spatiale de sa phase*,” Journée du Club Optique Micro-Ondes JCOM 2021 (Société Française d’Optique), Paris (France), 2021.
21. Yu.S. Dadoenkova, I.A. Glukhov, S.G. Moiseev & F.F.L. Bentivegna, “*Réflexion non-spéculaire d’un faisceau gaussien spatialement modulé en phase*,” 20ème Conférence Horizons de l’Optique (Horizons de l’Optique – Optique Dijon 2021), Dijon (France), 2021.

Titre : Manipulation d'ondes électromagnétiques dans les domaines visible, IR et micro-ondes à l'aide d'hétérostructures plasmoniques et des propriétés du faisceau.

Mots clés : Nanoplasmonique ; cristal photonique; mode de défaut ; nanoparticules ; localisation de champ ; méthode des matrices de transfert ; approximation de milieu effectif ; filtre sensible à la polarisation ; cristal photonique aperiodique déterministe ; filtre dichroïque ; décalage de Goos-Hänchen ; modulation de phase.

Résumé : Les travaux présentés sont consacrés à des méthodes de contrôle d'une onde électromagnétique par le biais d'hétérostructures photoniques et/ou plasmoniques ou *via* la manipulation des propriétés de l'onde elle-même. Après une présentation des méthodes de modélisation de l'interaction entre onde et hétérostructures, le manuscrit se consacre d'abord à l'étude d'un cristal photonique amplificateur sensible à la polarisation dans lequel est insérée une distribution aléatoire tridimensionnelle d'inclusions métalliques asphériques. Le principe d'un filtre spectral amplificateur est ensuite décrit, qui permet l'amplification sélective en polarisation d'un mode de défaut d'un cristal photonique incluant des réseaux bidimensionnels de nanoparticules métalliques. Une troisième structure étudiée est un filtre dichroïque sensible à la polarisation qui exploite les possibilités d'un cristal pho-

tonique aperiodique couplé à une inclusion bidimensionnelle de particules métalliques : deux modes de défaut dans deux bandes interdites distinctes du cristal photonique sont indépendamment supprimés pour deux états de polarisation mutuellement orthogonaux via l'excitation de résonances plasmoniques dans les particules. Enfin, ce travail s'intéresse au contrôle des décalages latéral et angulaire subis à la réflexion sur une surface diélectrique par un faisceau gaussien spatialement modulé en phase, et pouvant être exploités pour la conception de capteurs ou pour les communications optiques. La combinaison d'un modèle analytique et de simulations numériques permet d'optimiser la modulation de phase spatiale nécessaire à une exaltation significative et ajustable de ces décalages de faisceau.

Title : Manipulation of electromagnetic waves in the visible, IR and microwave domains using plasmonic heterostructures and beam properties.

Keywords : Nanoplasmonics; photonic crystal; defect mode; nanoparticles; field localization; transfer-matrix method; effective medium approximation; polarization-sensitive filter; deterministic aperiodic photonic crystal; dichroic filter; Goos-Hänchen shift; phase modulation.

Abstract : My work is devoted to the development of methods of control of an electromagnetic wave using a few selected photonic and/or plasmonic heterostructures, or manipulating the incident beam properties. In Chapter I, general principles and calculation methods for the modelization of the interaction between the wave and the photonic/plasmonic structures are described. Chapter II is devoted to the study of a polarization-sensitive amplifying photonic crystal in which a nanocomposite polarizing layer, based on a three-dimensional random distribution of nonspherical metallic inclusions, is embedded. Chapter III is devoted to a spectrally narrow amplifying filter, where the polarization-selective amplification of a defect mode in a photonic crystal is involved and in which the defect includes two-dimensional arrays of metallic nanoparticles.

In Chapter IV, a polarization-sensitive dichroic filter based on an aperiodic photonic crystal with a metallic two-dimensional array inclusion is studied. Two different defect modes in two separate bandgaps of the photonic crystal are independently suppressed for two mutually orthogonal polarization states of the incident beam through the plasmonic excitation in the metallic nanoparticles. In Chapter V, the Goos-Hänchen lateral and angular shifts experienced by a spatially phase-modulated Gaussian beam when it is reflected at a dielectric surface are described. A combined analytical and numerical derivation of the shifts leads to the determination of the optimal spatial phase modulation necessary for a significant and adjustable exaltation of the beam shift amplitudes.